Computational and Experimental Analysis of the Mechanical Performance of SLS Generated Polymer-Ceramic Bone Scaffold Materials

Heather Doyle B.E. (2010)

Supervisor: Prof. Peter McHugh

A thesis submitted to the National University of Ireland as fulfilment of the requirements for the Degree of Doctor of Philosophy.

Biomedical Engineering,

National University of Ireland, Galway.

September 2014

Contents

Abstract

The load-bearing ability of orthopaedic scaffolds in critical-sized defects is of critical importance. 3D printing methods such as selective laser sintering (SLS) have great potential for the fabrication of patient-specific scaffolds. The incorporation of ceramic particles is desirable to promote osteogenesis; however the influence of these particles on the microstructure and mechanical behaviour of SLS materials is unclear.

A multiscale modelling methodology is developed to predict the macroscale elastic properties of polymer-ceramic SLS materials with complex microstructures. The relationship between micromechanics-evaluated elastic properties and average grey-value is found to be material-specific. The macroscale elastic modulus of SLS materials with different volumes of β-TCP particles is accurately predicted when element-specific assignment of elastic properties based on grey-value is used. Increasing the ceramic content of these SLS materials is shown to result in a slight increase in stiffness but significant reductions in strength. Changes in mechanical properties under simulated physiological degradation conditions are evaluated, and are shown to be dependent on the incorporation of ceramic particles.

Computational models of critical-sized ovine tibial defects with implanted scaffolds are generated. The ability of each defect to withstand bending and compressive

loading is analysed, demonstrating the influence of callus volume and of both scaffold volume and stiffness on defect load-bearing. Clinically-used metrics for the prediction of the safety of removing external fixation are evaluated for each defect and deficiencies in these measurements are demonstrated by comparison with simulation results.

In conclusion, the use of both mechanical testing methods and computational modelling in this thesis has led to an improved understanding of the influence of ceramic content on mechanical properties as well as the development of a multiscale modelling methodology to prediction macroscale mechanical properties. Computational modelling of real defect geometries has resulted in a non-invasive method to assess defect stability and load-bearing capacity.

Acknowledgements

Firstly, I would like to express my sincere gratitude to my supervisor Prof. Peter McHugh for your patience, knowledge, support and guidance over the years. I wouldn't be here without your support and understanding.

I also wish to acknowledge the Irish Research Council for Science and Engineering Technology (IRCSET), who funded this PhD research and the Irish Centre for High End Computing (ICHEC), for the use of their computational facilities. Thank you to Stefan Lohfeld for assistance with sample fabrication and to Pat McDonnell and Noel Harrison for their valuable technical input. Thanks also to Prof. Tony Keaveny and the University of California Education Abroad Program (UCEAP) for the opportunity to study at UC, Berkeley. I would also like to thank Pat Kelly and William Kelly from the Mechanical and Biomedical Engineering Laboratory NUIG for technical assistance and to Jane Bowman and Sharon Gilmartin for all the help throughout the years.

Thank you to my friends and fellow postgraduate students who have been a greatly appreciated source of advice, help and encouragement. I would especially like to thank Caoimhe, Claire, Evelyn, Donnacha, James, Nicola and Ted for all the technical help, insightful suggestions and advice on this work. Thank you to those on

the second floor, past and present, for the lunch time entertainment. Thank you also to my friends from Galway for all of your moral support throughout these years.

To my parents, Ann and Paul, thank you for your never-ending love, support and encouragement. A special thanks to Eimear and Evan. Shane, thank you for all of your support through everything and for keeping me sane!

List of Publications

The work presented in this thesis has appeared in the following publication:

Chapter 3: H Doyle, S Lohfeld, PE McHugh. Predicting the Elastic Properties of Selective Laser Sintered PCL/β-TCP Bone Scaffold Materials Using Computational Modelling. *Annals of Biomedical Engineering*.42 (3): 661-677, 2014.

Chapter 4: H Doyle, S Lohfeld, P McDonnell, PE McHugh. Assessment of a multiscale modelling methodology to predict the mechanical properties of PCL/β-TCP scaffold materials. *Annals of Biomedical Engineering.* DOI: 10.1007/s10439-014-1199-x

Chapter 6: H Doyle, S Lohfeld, L Dürselen, PE McHugh. Computational modelling to assess the stability of critical sized tibial defects with two types of implanted scaffold. *Journal of the Mechanical Behaviour of Biomedical Materials,* Accepted 2015.

The following publication arising from work in this thesis are in submission:

Chapter 5: H Doyle, S Lohfeld, PE McHugh. Evaluating the effect of increasing ceramic content on the mechanical properties, material microstructure and degradation of selective laser sintered PCL/β-TCP materials. *Under review,* 2014.

1 Introduction

1.1 Chapter Summary

This chapter provides a background to polymer-ceramic selective laser sintered (SLS) materials, with specific focus on the application of orthopaedic scaffolds. The complexity of polymer-ceramic SLS materials and the effect of ceramic particulate inclusions on the sintering behaviour and material structure of the fabricated materials are discussed. The needs and requirements of orthopaedic scaffolds are outlined, with specific focus on structural and material property requirements as well as the *in vivo* change in properties over time as scaffold material degradation occurs. The capabilities of computational modelling are discussed with application to both scaffold materials and *in vivo* defects. The main objectives of this thesis are outlined, and an overview of the contents of each subsequent chapter in this thesis is given.

1.2 Selective Laser Sintering

Selective laser sintering (SLS) is a fully-automated rapid prototyping manufacturing method where a CO_2 laser is used to melt polymeric powders to form the required part, without the use of chemicals, blowing agents or support structures (Tan et al. 2003). The part to be fabricated is designed using CAD software to generate a 3D

model. The part is then fabricated layer by layer as a laser passes over the powdered material and material is sintered according the pattern determined by the 3D model. A new layer of powder is then moved into the part bed using rollers, and the next layer of material is sintered. This process is repeated until the full part is created.

A high degree of repeatability and conformity to the original design on the macro-scale is an advantage of this manufacturing method. The minimum possible feature size is dependent on laser spot diameter and can be a limiting factor. This limitation was addressed by Lohfeld et al. by using an "outline scan" method without a "fill scan" option (Lohfeld et al. 2010), allowing small feature sizes and high levels of macroporosity to be achieved in relatively small parts. The results of that study also demonstrated that this fabrication method is sensitive to parameters such as scan spacing, with higher laser power or greater scan spacing resulting in thicker struts (Figure 1.1). The laser power and the orientation of parts with respect to the direction of the laser path have been shown to influence the density and stiffness of fabricated parts, with increasing density and stiffness with increasing laser power and greater part stiffness in the direction parallel to the laser path (Caulfield et al. 2007). The nature of this fabrication method means that there are few geometrical limitations on the designs that can be fabricated, allowing this method to be used to fabricate replicas of complex geometries from micro-computed tomography (μ-CT) scans, such as those of trabecular bone (McDonnell et al. 2010).

SLS parts have been fabricated from a wide range of materials, from polyamide (Franco et al. 2010) to high-carbon steel (Nakamoto et al. 2009). Polymer-ceramic composite materials for bone tissue engineering applications have been fabricated

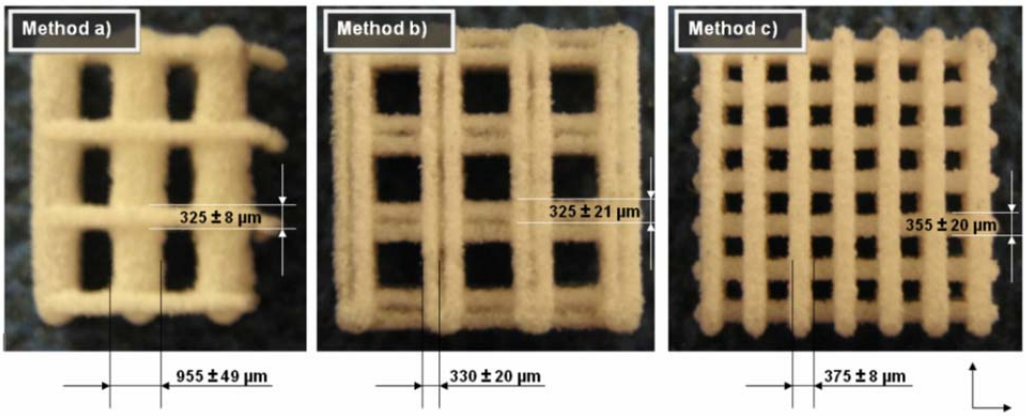

Figure 1.1: Geometrical variation in polyamide SLS scaffolds as a result of differences in fabrication settings. In method a) laser offset, scan spacing of 0.1mm and a laser power of 9 W were used, resulting in the largest strut cross-section. No laser offset or scan spacing and a laser power of 5 W were used in method b) giving the smallest strut cross-section. No scan spacing and a laser power of 5 W were used with a laser offset in method c). From (Lohfeld et al. 2010).

from Polycaprolactone (PCL) and β-Tricalcium Phosphate (β-TCP) with a range of volume fraction ratios ranging from 10% to 50% (Lohfeld et al. 2012; Lam et al. 2008; Lee and Kim 2011). The incorporation of a ceramic phase has been shown to have significant effects on the microstructure and mechanical properties of the resulting materials (Lohfeld et al. 2012; Eshraghi and Das 2012). The ceramic phase has been shown to act as a barrier to sintering, requiring increased laser powers (Lohfeld et al. 2012). Sintering of this type of composite material is carried out at temperatures above the melt temperature of the polymer phase but below the melt temperature of the ceramic phase; therefore the ceramic particles do not get sintered and act to inhibit the flow and consolidation of the polymer melt. The stiffening effect of ceramic particles in polymer-ceramic SLS materials has been shown to be less than for solid materials with the same polymer-ceramic ratio (Eshraghi and Das

2012), indicating that the stiffening effect of the ceramic particles is offset by reduced sintering caused by the presence of the ceramic particles.

The research in this thesis focuses on polymer-ceramic composite materials fabricated using SLS, specifically on the application of PCL/β-TCP orthopaedic bone tissue engineering scaffold materials. For orthopaedic scaffolds designed to be placed in critical-sized defects where a large portion of the body-weight is to be supported by the scaffold, the stiffness of the scaffold material to be implanted is a critical design factor. The influence of β-TCP particles on the sintering of PCL/β-TCP SLS materials is dependent on the volume of ceramic and on the processing parameters (Lohfeld et al. 2012). Although a preliminary study of the effects of β-TCP presence on the stiffness of the sintered PCL material has been performed (Lohfeld et al. 2014), a thorough investigation of the microstructure and stiffness of SLS materials with different volumes of β-TCP is required in order to fully understand the effect of ceramic particles on the sintering behaviour and mechanical properties of this type of material.

1.3 Orthopaedic Scaffolds

The traditional surgical treatment for skeletal defects that occur as a result of disease or injury is the use of autograft (native) or allograft (donor) bone. The major issues associated with the use of autografts are donor site morbidity and the inherent risks involved in a second surgery that is required to harvest the tissue. The risk of rejection or infection in the case of allografts is also a serious concern. For large,

critical-sized defects, the volume of tissue required and the availability of sufficient tissue for the treatment of the defect can be a limiting factor for both treatments. A critical-sized defect is a large defect in a bone that will not heal on its own without intervention. Bone tissue engineering scaffolds have been proposed as an alternative treatment for this type of defect in order to overcome the risks and shortcomings of the available treatments. The fundamental needs that orthopaedic scaffold implants must satisfy have been defined (Hollister 2009) as follows:

- *Form*: A scaffold must initially fill the geometry of the 3D bone defect.
- *Fixation*: Scaffolds must be securely attached to the neighbouring bone in order to reduce motion between the bone and scaffold that could lead to non-union and pseudoarthritis.
- *Formation*: The scaffold must enhance tissue regeneration within the defect site, providing an appropriate mass transport environment and allowing for the delivery of osteoinductive factors.
- *Function*: The scaffold must provide temporary mechanical load bearing within the defect until sufficient tissue has formed to take over this function.

The *form* of a scaffold is defined by the defect geometry, which can be determined using μ-CT scan or magnetic resonance imaging (MRI) techniques. Rapid prototyping methods such as SLS can then be used to fabricate scaffold geometries to fit a patient-specific defect, as illustrated in Figure 1.2. *Fixation* of the scaffold to the native bone surrounding the defect can be achieved surgically with sutures, screws or external fixation such as metal plates. Mechanical strains at the

scaffold/native bone interface must be minimised in order to prevent pseudoarthritis (Cheal et al. 1991).

A scaffold can enhance the *formation* of new bone within a defect by the delivery of biological factors and the provision of a suitable environment for mass transport and for bone formation. The scaffold architecture must allow for cell migration and vascular penetration in order for bone formation to occur. Optimal pore sizes of <100 μm (Jones et al. 2009), 150 to 260 μm (von Doernberg et al. 2006) and 300 to 400 μm (Tsuruga et al. 1997) have been reported, suggesting minimum requirements for scaffold macropores in order to encourage bone ingrowth. While high porosity is desirable, the resulting reduction in scaffold stiffness means that a trade-off between porosity and stiffness is required. Scaffold surface modifications to improve cell attachment have shown success, for example the addition of adhesion peptides such as RGD (Gabriel et al. 2006). Calcium-phosphate based materials such as hydroxyapatite and β-TCP are commonly used in orthopaedic scaffolding materials as they have good biocompatibility and osteoconductivity, both on their own and in combination with polymers (Dong et al. 2002; Kang et al. 2011; Wongwitwichot et al. 2010; Rai et al. 2010; Liu et al. 2007; Lu and Zreiqat 2010). For this reason, increasing the volume of β-TCP in polymer-ceramic SLS materials is considered desirable for the promotion of bone formation.

This thesis is concerned with the *function* aspect of scaffold requirements. The basic requirement for scaffold functionality is the ability to support mechanical loading of the defect site during early stages of healing. The two main aspects of the functional requirements of orthopaedic scaffolds that will be addressed in this thesis are:

1) Elastic properties of scaffold materials.
2) *In-vivo* load-bearing capabilities of the scaffold-tissue defect construct.

1.4 Functional Requirements of Orthopaedic Scaffolds

1.4.1 Influence of Local Elastic Properties on New Bone Formation

The elastic properties of scaffold materials are an important consideration as factors such as substrate stiffness and mechanical loading of cells seeded on a scaffold are known to affect the formation of new bone. Mechanical stimuli are converted to chemical stimuli within cells through a process called mechanotransduction (Wang et al. 1993). Tension that is generated in the cellular cytoskeleton is transmitted to focal adhesion sites where the cell is attached to the extra-cellular matrix (Chen and Ingber 1999), as illustrated in Figure 1.3. In the absence of mechanical loading, internal tensile forces generated in cells are dependent on substrate stiffness; large forces are typically generated on 'hard' substrates forming mature focal adhesions and a highly organised cytoskeleton, whereas smaller forces are typically generated on 'soft' substrates and an organised cytoskeleton cannot be formed (Breuls et al. 2008). This has been shown to influence the differentiation of mesenchymal stem cells (MSCs), with osteogenic differentiation occurring on substrates with stiffness values ranging from 25 kPa to 40 kPa and myogenic and neurogenic differentiation occurring on substrates with stiffness of 8 kPa to 17 kPa and 0.1 kPa to 1 kPa, respectively (Engler et al. 2006). Enhanced osteogenesis was observed on 3D gel scaffolds with a modulus of greater than 225 kPa in a study of the differentiation of

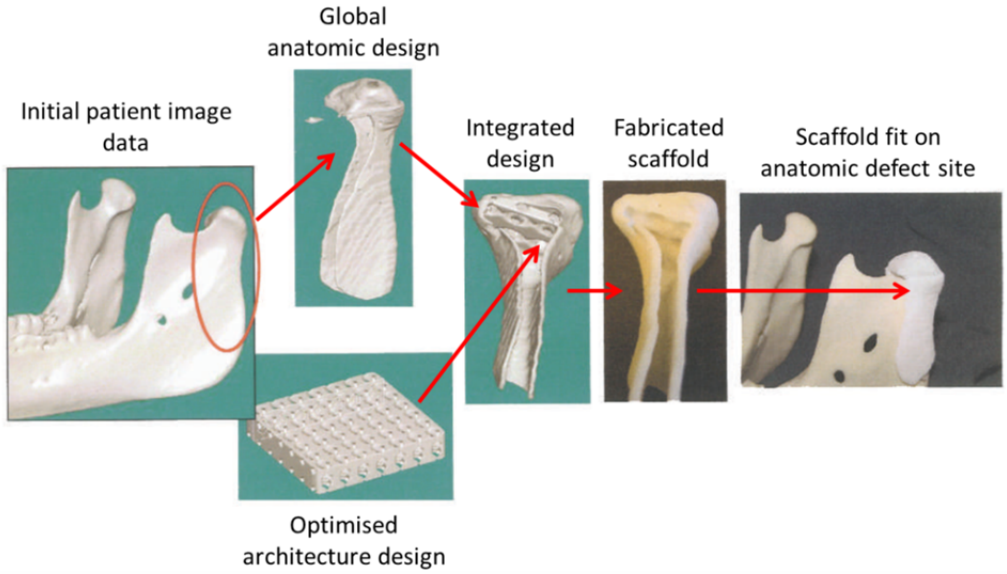

Figure 1.2: Illustration of an image-based method for designing a scaffold to fit a patient-defect. The defect geometry is obtained from μ-CT scans, from which the scaffold exterior geometry is derived. A scaffold with optimised architecture is designed and an integrated part is generated with additional features for surgical fixation. The scaffold, fabricated using SLS, fits well on the intended anatomic reconstruction site (Hollister 2005).

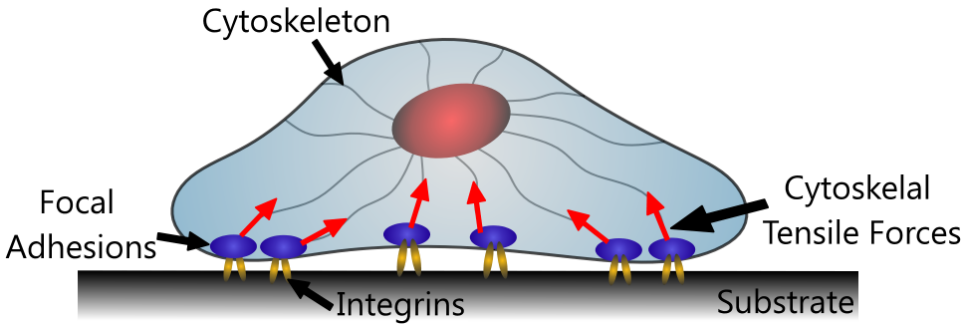

Figure 1.3: Schematic illustration of a cell attached to a substrate through transmembrane molecules called integrins. When cells attach to a substrate, integrins begin to cluster and form focal adhesions (FA). Mechanical forces, which can be generated by the cytoskeleton itself, are required for the maturation of focal adhesions.

osteoblast-like cells on gel scaffolds with a gradient of stiffness ranging from 10 kPa to 300 kPa (Chatterjee et al. 2010), confirming the 2D result. These results suggest that increased bone formation would be expected in the case of cells seeded on relatively stiff substrates in comparison with cells seeded on softer materials.

Regenerating bone tissue has been shown to respond to local mechanical strain (Baas et al. 2010). Physiologically, strains of 0.2% to 0.4% have been reported in human long bones during strenuous exercise (Burr et al. 1996), with 0.15% reported as the minimum effective strain under which bone remodelling occurs (Frost 1992). An increase in osteoblastic activities has been shown at low strain magnitudes (0.8% and 5%) *in vitro*, compared to a decrease in osteoblastic activities and an increase fibroblastic differentiation at higher strain magnitudes (10% and 15%) (Koike et al. 2005). Bone formation has been observed at sites of large local strains (in the order of thousands of micro-strains) in 3D scaffolds *in vitro* (Baas et al. 2010). These results indicate that tissue differentiation is influenced by the strains experienced by cells on a scaffold surface. When extremely stiff materials are used for scaffold materials, the strains transferred to cells seeded on the scaffold are very low as the scaffold experiences only small deformations during loading. Large strains are transferred to cells seeded on the surface of compliant scaffolds as large deformations occur during mechanical loading. The results above therefore suggest that a compromise between stiff and compliant scaffold materials is required to promote bone formation.

1.4.2 Elastic Properties of Native Bone

A schematic diagram of a long bone is shown in Figure 1.4, with regions of cortical bone and trabecular bone indicated. The elastic modulus of human cortical bone evaluated using nanoindentation testing has reported values that range from 17.8 GPa to 25.8 GPa, as shown in Table 1.1. This is slightly greater than the elastic modulus values reported for trabecular bone evaluated using nanoindentation testing of local trabecular bone structures, ranging from 13.4 GPa to 25 GPa (Table 1.2). Differences between the wet and dry evaluation of elastic modulus have been highlighted (Wolfram et al. 2010), with 25% greater values reported under dry conditions. Note that these values of elastic modulus are orders of magnitude greater than the 2D gel substrates used in the studies to evaluate the influence of substrate stiffness on cellular differentiation *in vitro*, (Section 1.4.1), and therefore may not be directly comparable.

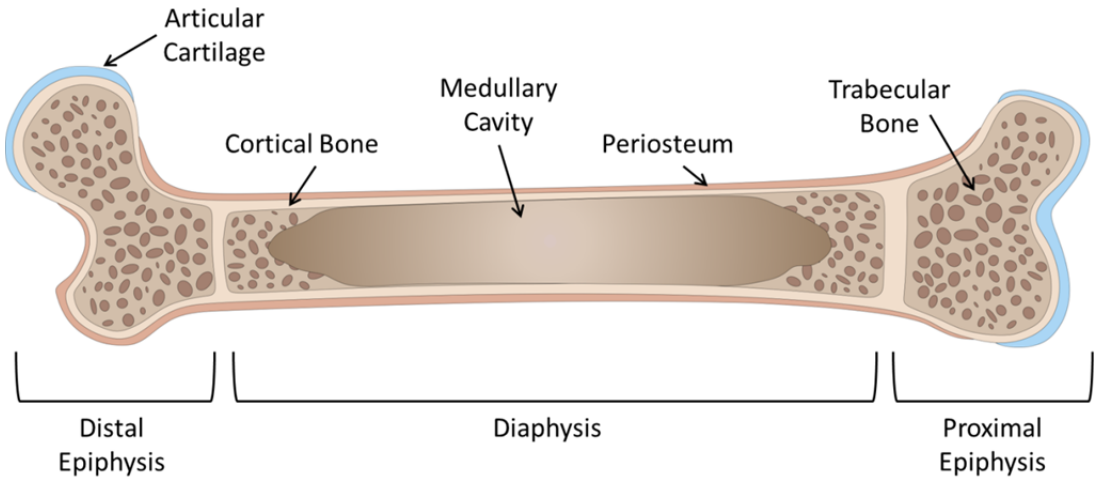

Figure 1.4: Schematic diagram of a long bone showing locations of cortical bone and trabecular bone.

Various animal models are employed in *in vivo* studies to assess the performance of orthopaedic scaffolds. The values of cortical and trabecular elastic modulus for some commonly used animal models are reported in Table 1.1 and Table 1.2; note that there are differences between the values reported for human tissue and for various animal tissues. The reported ranges of elastic modulus values for ovine cortical bone range are similar to ranges reported for human cortical bone with values ranging from 15 GPa to 25 GPa. Reported values of elastic modulus for bovine and rabbit cortical bone are also similar to human cortical bone, as shown in Table 1.1. However, values for porcine and rat cortical bone are lower than those reported for human cortical bone, and murine cortical bone has greater elastic modulus than human cortical bone with values ranging from 27.5 GPa to 36.4 GPa, as shown in Table 1.1. The values of ultimate strength for cortical and trabecular for some commonly used animal models are reported in Table 1.3 and Table 1.4. Cortical bone has higher strength than trabecular bone. Similar values of cortical bone ultimate strength have been reported for human and ovine cortical bone (Table 1.3), however the values in Table 1.4 indicate that ovine trabecular bone ultimate strength is greater than the values reported for human trabecular bone.

The elastic modulus of cortical bone (Fan et al. 2002) and trabecular bone (Keaveny et al. 2001; Mittra et al. 2005) are known to be anisotropic with greatest stiffness in the loading, or axial, direction. The elastic modulus of cortical bone in the axial direction has been shown to be greater than in the transverse direction using nanoindentation (Feng et al. 2012). The elastic modulus in the axial direction has been shown to be greater than in the mediolateral and anteroposterior directions for ovine trabecular bone (Nafei et al. 2000).

Table 1.1: Summary of values for the elastic modulus (E) of cortical bone for different animal models as reported in the literature.

Animal	Location	Test method	E (GPa)	σ_U (MPa)	Reference
Human	Tibia	FEA	20		(Gardner et al. 2000)
	Femur	Nanoindentation	20.1		(Rho et al. 2000)
	Tibia	Nanoindentation	22.5-25.8		(Rho et al. 1997)
	Femur	Tension/FEA	17.8		(Bayraktar et al. 2004)
Ovine	Tibia	FEA (2D)	15.75		(Steiner et al. 2012)
	Tibia	Nanoindentation	20.8		(Cipitria et al. 2012)
	Tibia	Nanoindentation	15-25		(Grant et al. 2014)
	Tibia	3-Point Bending	25.6		(Schorlemmer et al. 2005)
Bovine	Tibia	Nanoindentation	16.03		(Shepherd et al. 2011)
	Tibia	Nanoindentation	19.8		(Wang et al. 2006)
	Tibia	Nanoindentation	16.3-22.51		(Carnelli et al. 2011)
	Femur	Nanoindentation	21.88		(Isaksson et al. 2010)
Pig	Femur	Nanoindentation	11.4-25.29		(Feng and Jasiuk 2011)
Rabbit	Tibia	Nanoindentation	20.66		(Vayron et al. 2012)
Rat	Femur	FEA	15		(Shefelbine et al. 2005)
	Femur	Nanoindentation	7.2		(Leong and Morgan 2009)
Mouse	Femur Tibia	Nanoindentation	31.4-3.7 30.8-33.1		(Silva et al. 2004)
	Tibia	Nanoindentation	27.5-36.4		(Rodriguez-Florez et al. 2013)

Table 1.2: Summary of values for trabecular bone elastic modulus (E) from the literature.

Animal	Location	Test method	E (GPa)	Reference
Human	Vertebrae	Nanoindentation	13.4	(Rho et al. 1997)
	Femoral Neck	Nanoindentation	19.6-22.3	(Chevalier et al. 2007)
	Femoral Neck	Nanoindentation	21-25	(Hengsberger et al. 2002)
	Vertebrae	Nanoindentation (Wet) Nanoindentation (Dry)	12.3 15.4	(Wolfram et al. 2010)
	Femoral Neck	Compression/FEA	18	(Bayraktar et al. 2004)
Ovine	Vertebrae	Nanoindentation	8.33	(Harrison et al. 2008)
Bovine	Vertebrae	Nanoindentation	14.7-20	(Wang et al. 2006)
	Proximal Tibia	Nanoindentation	18.86	(Isaksson et al. 2010)

Table 1.3: Summary of values for cortical bone ultimate strength from the literature.

Animal	Location	Test method	σ_U (MPa)	Reference
Sheep	Tibia	3-Point Bending	110-124	(Malizos et al. 2006)
	Tibia	3-Point Bending	289	(Schorlemmer et al. 2005)
	Femur	3-Point Bending	136-201	(Wallace et al. 2013)
Human	Tibia	Compression	200	(Kemper et al. 2007)
	Femur	Tension	10.27	(Evans 1976)
	Femur	Tension Compression	50-160 160-240	(Hansen et al. 2008)
Pig	Femur	Tension	96.7-119.2	(Feng and Jasiuk 2011)
Dog	Tibia	Torsion	28.5	(Markel et al. 1990)

Table 1.4: Summary of values for trabecular bone ultimate strength from the literature.

Animal	Location	Test method	σ_U (MPa)	Reference
Sheep	Tibia	Compression	11.6-26.3	(Nafei et al. 2000)
	Femur	Compression	12-26	(Mittra et al. 2005)
Human	Vertebra	Compression	4.1	(Mosekilde et al. 1987)
	Tibia	Compression	5.3	(Linde and Hvid 1989)
	Femur	Compression	6.8	(Rohlmann et al. 1980)
Rat	Individual trabeculae	Tension	31-103	(McNamara et al. 2006)

For the case of load-bearing scaffolds in critical-sized defects, the use of an ovine animal model is advantageous due to the similarities between ovine and human body-weight, meaning that similar magnitudes of *in vivo* loading are generated. Ovine long bones also have dimensions closer in size to human bones than rabbit or rat bones (Newman et al. 1995), for example, meaning that scaffolds designed for human use can fit ovine defects. While ovine bone is macroscopically similar to human bone, differences at the microscale exist and have been reported to vary with age. Differences in bone composition also exist, with a greater trabecular bone density in the ovine femur compared to in humans (Liebschner 2004).

It is important that these macroscopic and microscopic similarities and differences between species are considered when comparing the performance of orthopaedic scaffolds *in vivo* and any differences in scaffold requirements that may occur between different animal models. It is also important to ensure that dimensions and

mechanical properties appropriate to the animal model in question are used for computational modelling of animal bones as well as *in vivo* implanted devices, including orthopaedic scaffolds. The primary purpose of scaffolds in critical-sized defects is to support *in vivo* loading, therefore scaffold requirements are specific to the defect region that is to be treated. For example, similarities between scaffold properties and cortical bone properties are required for implants that are intended to replace cortical bone, and similarities with trabecular bone are required for implants that are that intended to replace trabecular bone.

The application of interest in this thesis is the implantation of scaffolds in critical-sized bone defects in the middle of the diaphysis of long bones, as illustrated in Figure 1.5 (Lohfeld et al. 2012). The mid-diaphysis region of long bones consists of a ring of cortical bone, an external layer of periosteum and the medullary cavity which contains bone marrow, as illustrated in Figure 1.4. As the scaffold is implanted in the mid-diaphysis, each end of the scaffold is in contact with cortical bone and therefore it could be argued that the elastic modulus values of cortical bone are more relevant than those of trabecular bone, which is predominantly located in the epiphysis regions. Finite element modelling methods are used in combination with μ-CT imaging to determine the elastic modulus of ovine cortical bone, specific to the tibiae used in the *in vivo* study by (Lohfeld et al. 2012), in Chapter 6 of this thesis.

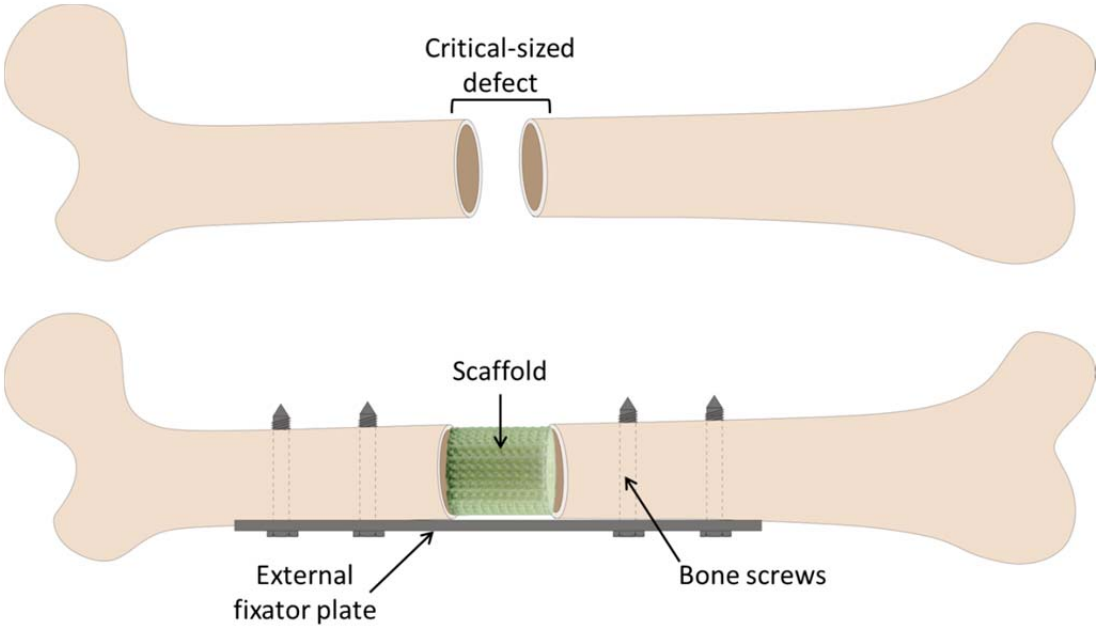

Figure 1.5: Illustration of a long bone with a critical-sized defect in the mid-diaphysis (top) and of the fixation of this type of defect with an implanted scaffold. This diagram illustrates the *in vivo* implantation of a scaffold in a critical-sized defect that is described in (Lohfeld et al. 2012).

1.5 Elastic Properties of Scaffold Materials

While some studies have found good bone formation with soft scaffolds that have stiffness similar in magnitude to the above studies (Keogh et al. 2010; Haugh et al. 2011), these values are far lower than the stiffness of native cortical bone and therefore unsuitable for use in critical-sized defects; extensive external fixation would be required in order to support loading *in vivo* and, as a result of this excessive fixation, little or no loading would be transferred through the scaffold

itself. As it is known that local strains are required to encourage new bone formation (Frost 1992; Baas et al. 2010), this situation is not desirable.

It has been suggested that scaffold stiffness should mimic that of developing bone in order to encourage osteogenic differentiation of mesenchymal stem cells (MSCs) (Breuls et al. 2008), whereas scaffold stiffness similar to mature native bone is required to encourage the infiltration of cells from the surrounding native tissue (Lo et al. 2000). Increasing scaffold stiffness is also desirable only up to a point, as a scaffold that is stiffer than the surrounding trabecular bone can cause stress concentrations in the surrounding healthy tissue resulting in bone resorption (Huiskes et al. 1992).

As stated above, the primary focus of the research in this thesis is polymer-ceramic scaffold materials; specifically PCL/β-TCP orthopaedic bone scaffolds fabricated using SLS. Fully β-TCP orthopaedic bone scaffold materials are also considered in Chapter 6 for comparison purposes. Both types of scaffold have been shown to have sufficient stiffness for *in vivo* load-bearing in critical-sized defects (Lohfeld et al. 2012). In that study, the use of an external fixator plate was required for defect stabilisation, and the full bone-scaffold-fixator assembly is illustrated in Figure 1.5. The ceramic particles (β-TCP) were incorporated in the PCL/β-TCP scaffolds for their osteoconductive properties, and an effective scaffold elastic modulus of approximately 6 MPa was evaluated for these scaffolds prior to implantation. While this value is far lower than the reported values for cortical bone, as shown in Table 1.1, the use of external fixation is intended to stabilise the defect at early stages, and

the formation of new bone within the defect is indented to increase the load-bearing abilities of the scaffold-callus construct over time.

As discussed in Section 1.2, the mechanical behaviour of materials fabricated using SLS are strongly dependent on the manufacturing process and the influence of ceramic particles on the material microstructure. The ability to predict the elastic properties of this type of material using computational modelling presents significant benefits for the design of orthopaedic scaffolds, by providing a method to evaluate the load-bearing capacity of scaffold designs, to evaluate scaffold suitability for a specific defect and to evaluate the *in vivo* mechanical performance of these scaffolds. The generation of a multi-scale methodology to predict the macro-scale stiffness of PCL/β-TCP materials with different volume fractions of ceramic is the focus of Chapters 3 and 4 of this thesis. An advantage of this method is that information about local stiffness at the level of cells seeded on a scaffold is retained through element-specific assignment of material properties. This has significance as it has been shown that local stiffness influences tissue differentiation (Engler et al. 2006) and new bone formation (Bhumiratana et al. 2011).

1.5.1 Degradation of Scaffold Materials

Bone tissue engineering scaffolds fabricated using biodegradable materials are intended to degrade slowly over time as new bone forms within the scaffold and defect. This allows for the scaffold to be replaced by new, native bone over time. From a mechanical perspective, the design requirement for tissue engineering bone scaffolds that are to be implanted in critical-sized defects is that they must be capable

of withstanding physiological loading; therefore the change in mechanical properties of bone scaffold materials over time is a critical design parameter.

PCL is a bioresorbable, biocompatible polymer with a slow degradation time of > 2 years (Gunatillake and Adhikari 2003; Middleton and Tipton 2000). It is easily processed with a melt temperature of 55 to 60°C and a glass transition temperature of -60°C (Woodruff and Hutmacher 2010), making it a popular material for scaffold fabrication using various techniques. Experimentally evaluated values for the elastic modulus of PCL range from 122 MPa (Williams et al. 2005) to 299 MPa (Eshraghi and Das 2012) for SLS fabricated samples.

β-TCP is a bioresorbable ceramic material and has a much faster degradation rate than biodegradable polymers such as PCL. The biodegradation of β-TCP occurs first with the physiochemical dissolution of the material, which starts at the necks between individual grains of β-TCP and is induced *in vivo* by low pH conditions (De Groot 1988). This is then followed by disintegration of the material into small parts rapidly on implantation, compared to hydroxyapatite, a material with similar composition, where the degradation process is predominantly physiochemical dissolution (De Groot 1988).

Degradation of biodegradable polymeric materials occurs through two main mechanisms: Surface erosion and bulk erosion. Surface erosion occurs when degradation at the surface occurs at a faster rate than bulk degradation of the material. The removal of surface material means that the molecular weight of the bulk material is not affected (Lam et al. 2008). Bulk degradation is a less predictable process, where diffusion of water through the material occurs faster than the removal

of material at the surface. This generates a build-up of acidic degradation products within the bulk material which causes an increase in the rate of degradation (internal autocatalysis), resulting in a low molecular weight core and higher molecular weight material at the outer surface (Lam et al. 2008; Vieira et al. 2011). Homogeneous bulk degradation can occur when water can diffuse through the material and degradation products can also freely diffuse into the surrounding media, thereby preventing a build-up of acidic degradation products (Lam et al. 2008).

The most accurate way to evaluate the change in mechanical properties of biodegradable materials during ageing in the body is through retrieval studies; however this is not always practically possible. *In vivo* conditions can be replicated *in vitro* by exposing materials to simulated physiological conditions by immersion in phosphate buffered saline at 37°C and pH 7.4. Methods of accelerated ageing have been developed in order to assess the degradation behaviour of materials with long degradation times, such as PCL, at reduced length scales. Examples of accelerated degradation methods include temperature elevation (Hukins et al. 2008), changes in pH (Lam et al. 2008; Lam et al. 2007) and enzymatic degradation (Wan et al. 2008; Lam et al. 2008; Castilla-Cortázar et al. 2012). Temperature-driven accelerated ageing can be achieved by assuming that the chemical reactions of the material degradation can be described by the Arrhenius reaction rate function, which states that a 10°C change in temperature doubles the reaction rate, according to ASTM F1980-02 and (Hukins et al. 2008). A major advantage of using this method of accelerated ageing is that there is a clear relationship between the increase in temperature and degradation time. This means that data from accelerated ageing studies can be related back to real-time data (degradation at 37°C).

Of particular interest in this thesis are PCL/β-TCP materials that contain relatively small volumes (10 to 50wt% or approximately 5 to 25vol%) of β-TCP. As β-TCP degrades through dissolution and disintegration, it is assumed that degradation is dominated by material removal and the material properties of the (remaining) β-TCP material remains constant. Therefore, for the purpose of this thesis, it is assumed that the degradation of these PCL/β-TCP materials is dominated by degradation of the PCL phase. The degradation behaviour, specifically the change in mechanical properties, of PCL and of PCL/β-TCP scaffold materials is the subject of study in Chapter 5 of this thesis.

1.6 Computational Modelling in Orthopaedic Applications

1.6.1 Generation of High Resolution Finite Element Meshes

The use of 3D CAD models in FE modelling of SLS orthopaedic scaffolds has been shown to over-predict scaffold stiffness by up to 147% (Cahill et al. 2009). The use of elastic modulus values that are fitted to experimental results in FE models using CAD scaffold geometries has shown improved predictions of scaffold stiffness, (Lohfeld et al. 2014), however the use of fitted mechanical properties of this type does not account for the real material microstructure. By their nature, CAD models account for only the designed scaffold macroporosity and do not account for microporosity within the scaffold structure or surface roughness that is present due to the fabrication process; the incorporation of surface roughness has been shown to improve FE model predictions (Cahill et al. 2009).

High-resolution FE meshes have been successfully generated from μ-CT scans giving accurate models of the real geometries of both bone tissue engineering scaffolds (Figure 1.6 B) (Sandino and Lacroix 2011) and native bone tissue (Figure 1.6 C) (Liebschner et al. 2005). FE meshes with tetrahedral and hexahedral elements can be generated using commercially available software such as MIMICS and 3-Matic (Materialise, Belgium) and custom codes such as the FEEBE code developed at the NCBES (NUI Galway) (Harrison et al. 2008). Mesh elements are generated from each μ-CT scan pixel to generate high resolution FE meshes that can accurately capture the real geometry of the scaffold or object in question. Thresholding of the scans allows for the use of heterogeneous, voxel-specific material properties that are dependent on the grey-value of the μ-CT scan pixels. This is has been shown to yield greater accuracy by capturing local heterogeneity in mechanical properties in FE modelling of trabecular bone (Harrison et al. 2008). This approach is employed to capture the local heterogeneity in mechanical properties in macro-scale FE models of individual PCL/β-TCP scaffold struts with different volume fractions of β-TCP in Chapters 3 and 4 of this thesis.

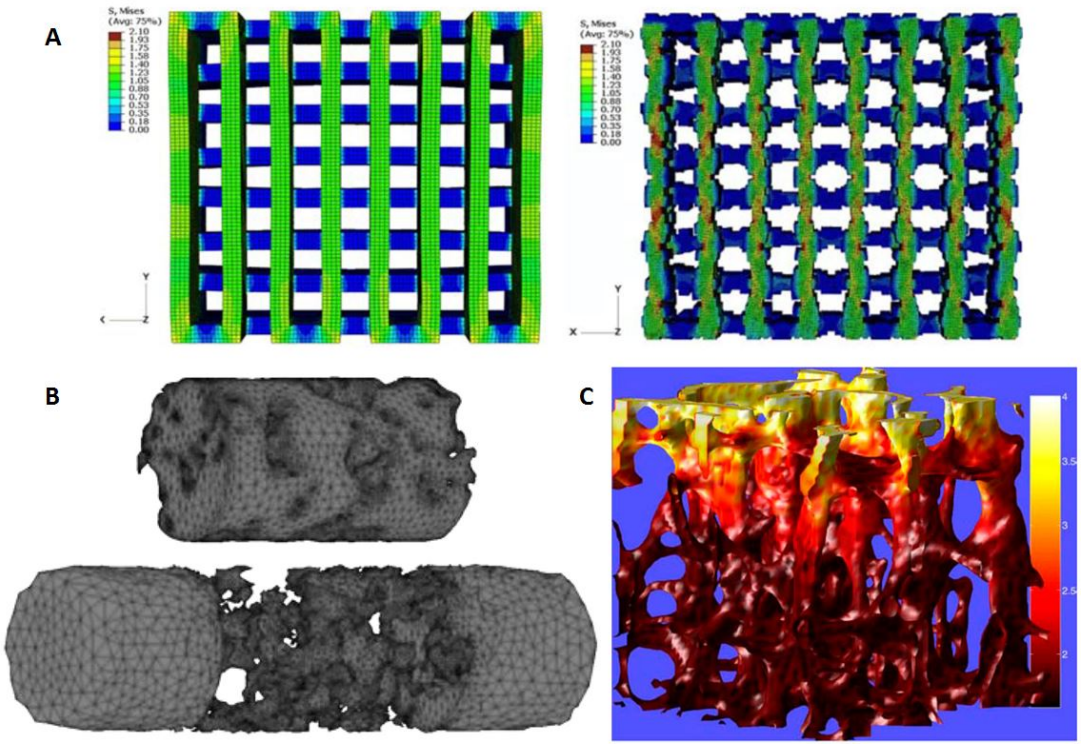

Figure 1.6: (A) CAD model (left) and CAD model with approximated surface roughness (right) showing von Mises stress (Cahill et al. 2009). (B) Tetrahedral FE mesh with complex geometry generated from µ-CT scans of a porous calcium phosphate material (Sandino et al. 2008). (C) Trabecular bone FE model geometry generated from µ-CT scans, showing strain (Liebschner et al. 2005).

1.6.2 Micromechanical Modelling of Multiphase Materials

The influence of ceramic particles on the sintering of polymer-ceramic SLS materials has been shown to be dependent on the volume of ceramic and the processing parameters used during fabrication (Lohfeld et al. 2012), as discussed in Section 1.2. That study found that increasing the volume of ceramic resulted in difficulties in sintering, resulting in a poorly sintered product with low stiffness rather than increasing the macro-scale elastic properties of the material as expected.

The resulting complex microstructures play a significant role in the macro-scale mechanical properties of this type of sintered material. A full understanding of the micromechanical behaviour of this type of SLS materials is required in order to fully understand the influence of ceramic particles on the macro-scale mechanical behaviour of these materials.

Micromechanics approaches have been developed to evaluate the mechanical properties of particle-reinforced composites (Böhm 2004). Examples of different types of volume elements that are commonly used in microstructural modelling are shown in Figure 1.7. Traditionally, idealised microstructures based on periodic particle distributions are used and volume elements are modelled under periodic boundary conditions to generate effective elastic properties (Eshraghi and Das 2012). Methods such as this require assumptions and simplifications regarding microstructural geometry, particle distribution and particle size distribution, and the microstructure of the material within the volume element must be periodic.

A Representative Volume Element (RVE) approach is also commonly used for homogenization of material microstructures. An RVE can be defined as "the smallest material volume element of the composite for which the usual spatially constant (overall modulus) macroscopic constitutive representation is a sufficiently accurate model to represent mean constitutive response" (Drugan and Willis 1996). RVE microstructures can be generated with random particle distributions with reinforcement volume fractions that are representative of the bulk material (Llorca and Segurado 2004), and particle distributions that are statistically representative of the real material microstructure (Vaughan and McCarthy 2010).

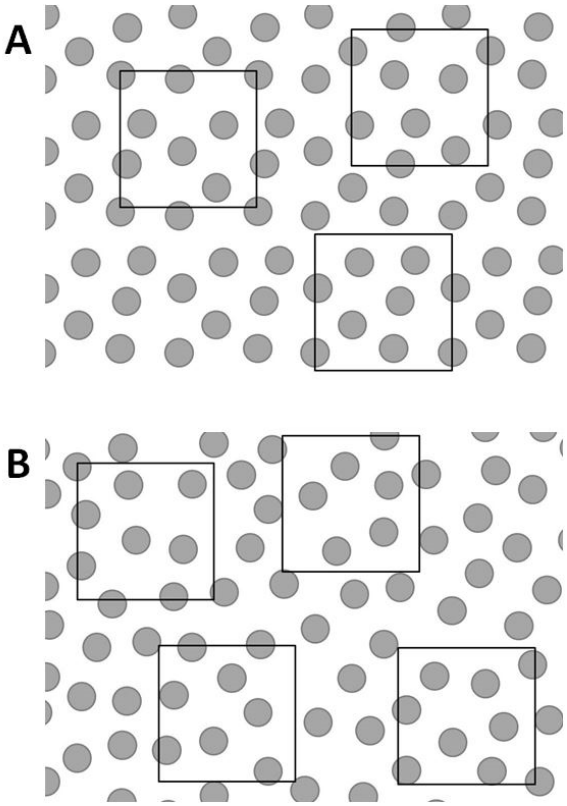

Figure 1.7: Illustration of 2D unit cell volume elements (indicated by black squares) for different matrix-inclusion microstructures. A microstructure with a periodic distribution of particles is shown in (A), where periodic boundary conditions can be applied to the unit cell. A microstructure with randomly distributed particles is shown in (B), where periodic boundary conditions are not appropriate; instead the windowing approach is commonly used.

The windowing method uses non-periodic volume elements to determine an estimate or bounds for the microscale elastic properties of a material. These volume elements are generally too small to constitute a RVE, and are extracted at random locations in the material and the results of analysis are specific to the individual samples. Upper and lower bounds of the effective properties of these volume elements can be evaluated for inhomogeneous materials using this method (Böhm 2004). This can be

achieved by using uniform boundary conditions to fulfil a surface integral version of the Hill condition (Hazanov and Amieur 1995); this is described in further detail in Chapter 3 of this thesis.

In the case where high resolution images of the real material microstructure are available, for example from high resolution μ-CT scans, the windowing method allows for the generation of microscale effective elastic properties specific to RVEs generated directly from the real material microstructure. In this way, realistic micro-scale mechanical properties are generated for real material microstructures. This is particularly advantageous in the case of particulate-reinforced materials with randomly distributed particles. Examples of applications of this modelling method include random heterogeneous materials (Kanit and Forest 2003), cancellous bone (Pahr and Zysset 2008), silicon carbide fibre reinforced composites (Chateau et al. 2010) and particle reinforced composites (Kanit et al. 2006).

The micromechanical properties of PCL/β-TCP scaffold materials are determined using the windowing technique for different volume fractions of β-TCP in Chapters 3 and 4 of this thesis. These properties provide local elastic properties for application in accurate, high-resolution macro-scale FE models discussed in Section 1.6.1.

1.6.3 Computational Modelling of Critical-Sized Defects

Traditionally, the mechanical properties of bone defects have been evaluated using mechanical testing of the bone. Mechanical testing methods, such as compression or bending testing, yield valuable information regarding the macro-scale mechanical properties of the defect, as well as the load-bearing capabilities of the bone.

Microscale testing methods such as nanoindentation can also be used to determine the local elastic properties of cortical bone (Rho et al. 2000) and trabecular bone tissues (Harrison et al. 2008). Nanoindentation has also been used to determine the elastic properties of newly forming callus tissues (Manjubala et al. 2009), giving insight into the increasing stiffness of the callus tissues over time. However, these mechanical testing methods all require sacrificing of the subject, and the mechanical testing that is carried out usually results in destruction of the samples.

FE models of bone defects with anatomically accurate geometries can be generated from μ-CT scans using the same methods described for orthopaedic scaffolds in Section 1.6.1. When appropriate mechanical properties are used, the macro-scale mechanical properties of the defect and the load-bearing capabilities of the bone can be determined using FE modelling. The use of FE modelling in a clinical setting has significant value for non-invasive evaluation of the progress of new bone formation. As this method is non-invasive, it allows for the generation of computational models for an individual sample at successive points in time to evaluate the progression of bone formation (Weis et al. 2010) (Figure 1.8).

FE modelling also allows for the stability of implanted devices, such as orthopaedic scaffolds, within a defect to be assessed non-invasively. Simulations with idealised scaffold, defect and external fixation geometries have been used to test ability of a scaffold design to withstand *in-vivo* loading (Wieding et al. 2013). In general, idealised geometries have limited value due to limitations in geometrical accuracy, with regards to both variations in patient bone geometry (Crabtree et al. 2000) and limitations of the use of idealised scaffold geometries (Cahill et al. 2009). Idealised

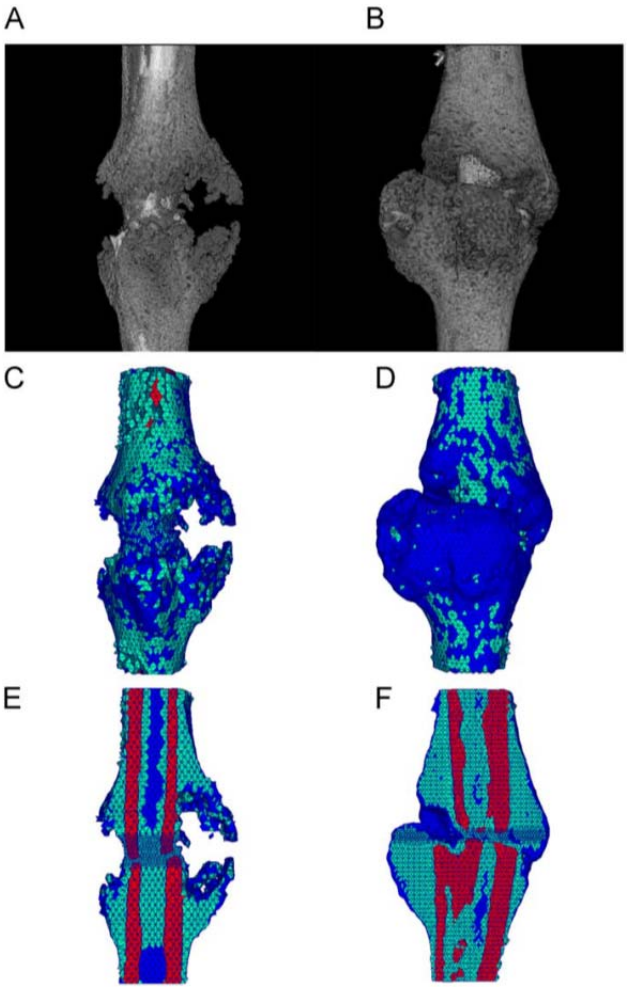

Figure 1.8: 3D reconstructions of a murine tibial fracture defect at 10 days (A) and 14 days (B) post-fracture. FE models of the defect at 10 days (C) and 14 days (D) are shown with section views of each model geometry shown in (E) and (F) respectively (Weis et al. 2010).

model geometries are not useful for the assessment of new bone formation within a scaffold or defect as the geometry of the new bone is not predictable. Accurate FE model geometries of real scaffold-bone constructs have been generated from μ-CT scans for use in uniaxial simulations to determine the mechanical properties of the scaffold-bone construct (Boerckel et al. 2012; Roshan-Ghias et al. 2011). This model geometry type has also been used to determine scaffold-defect construct radial bending stiffness (Shefelbine et al. 2005) and to assess the transmission of *in-vivo*

loading through a tibial fracture callus (Vijayakumar et al. 2006). μ-CT scan data is generated in many clinical studies in order to assess the volume, quality and distribution of bone formation within a defect (Beck et al. 2013; Freeman et al. 2009). These scans provide valuable information in addition to bone volume, such as non-invasive evaluation of mechanical properties and load distribution paths. FE models of defects, such as those discussed above, can also be generated directly from these μ-CT scans for the non-invasive evaluation of defect mechanical integrity.

Assignment of appropriate mechanical properties is critical in simulations using high resolution model geometries to generate accurate FE model predictions, as discussed in Section 1.6.1. *In-vivo* studies using nanoindentation to investigate the macro-scale mechanical properties of callus tissues have shown that the stiffness of fracture callus tissues increases over time as calcium content (mineralisation) increases, as indicated in Figure 1.9 (Manjubala et al. 2009). Increased mineralisation has also been observed in the callus tissue surrounding scaffolds implanted in critical-sized defects at 12 months compared to at 3 months (Cipitria et al. 2012), as shown in Figure 1.10. These results indicate that the mechanical properties used in FE models of callus construct must be representative of the callus stiffness at that specific stage in healing and mineralisation.

Experimentally-obtained mechanical properties of the actual tissues being modelled should be used where possible to ensure that the mechanical properties specific to each model region are used. However this is not always feasible when building models using non-invasive modelling techniques such as from μ-CT scans, specifically for the case of live subjects. In such cases, the geometry can be obtained

non-invasively but local tissue properties cannot. FE models with anatomically accurate geometries have been used to determine fracture callus tissue properties by calibrating models against experimental data (Vijayakumar et al. 2006; Steiner et al. 2012). Similarly, an iterative approach to determining callus tissue elastic properties was used by (Weis et al. 2010) to match computational modelling results to experimental data.

The *in vivo* performance of orthopaedic scaffolds in critical-sized tibial defects was assessed as part of an animal trial in a study by Lohfeld et al. (Lohfeld et al. 2012). Two types of scaffold were implanted and evaluated after 14 weeks using X-ray imaging and μ-CT scanning, as well as four-point bending after removal of the tibia. The results indicated major differences between the volumes of bone formation within each scaffold type, as shown in Figure 1.11, as well as in the bending stiffness of the scaffold-callus construct, as shown in Figure 1.12. The local tissue mechanical properties were not evaluated, and finite element modelling of the scaffold-callus construct was not attempted. It is important to understand the reasons for the relatively low bone formation and bending stiffness in defects with one type of implanted scaffold, as well as to assess the influence of this on the mechanical integrity of the scaffold-callus construct. The ability to generate anatomically-accurate FE models of this type of defect would also open doors for the use of FE modelling to assess defect mechanical integrity at incremental time-points during an animal trial such as this. This would allow for the generation of additional information regarding the progression of bone growth and mechanical properties of the construct, as well as informing clinician decisions regarding fixator removal.

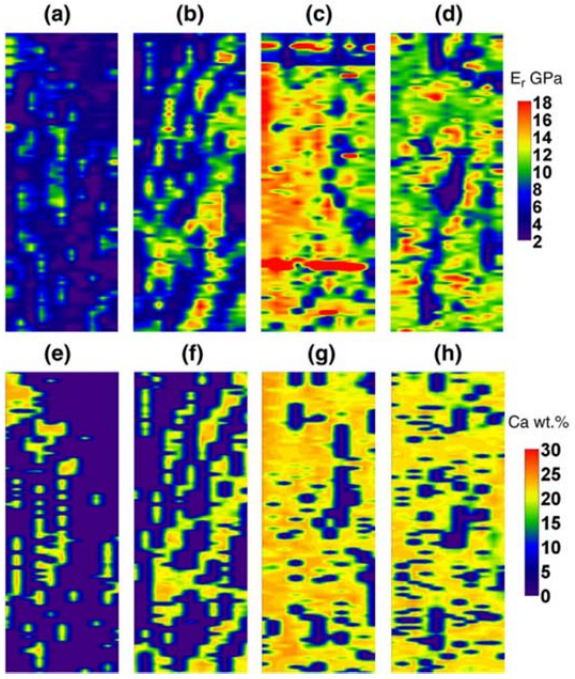

Figure 1.9: Increase in elastic modulus (E_r) and calcium content (Ca wt.%) during healing in a fracture callus at 2 weeks (a and e), 3 weeks (b and f), 6 weeks (c and g) and 9 weeks (d and h), from (Manjubala et al. 2009).

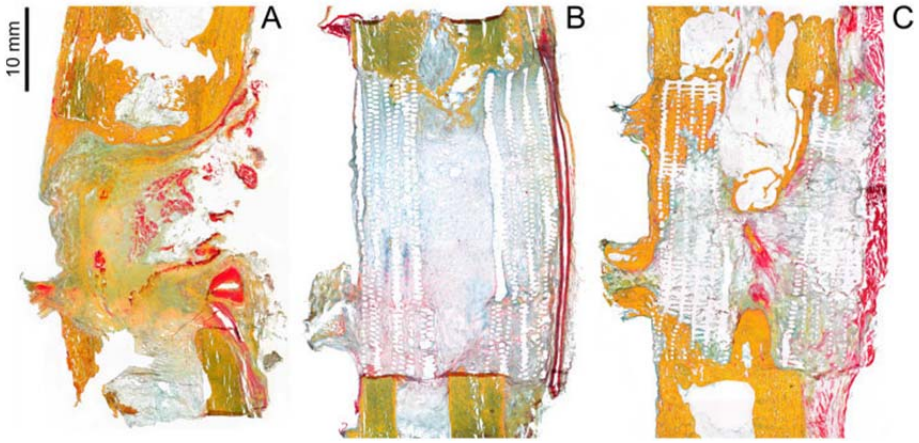

Figure 1.10: Histology sections of an empty defect (A) and a defect with an implanted PCL/β-TCP scaffold at 3 months (B) and 12 months (C) , from (Cipitria et al. 2012). Mineralised tissue and collage I fibres are stained in yellow, reticular fibres in blue, cell nuclei in black and elastin fibres in red. Increased mineralisation and tissue infiltration is evident at 12 months (C) compared to 3 months (B).

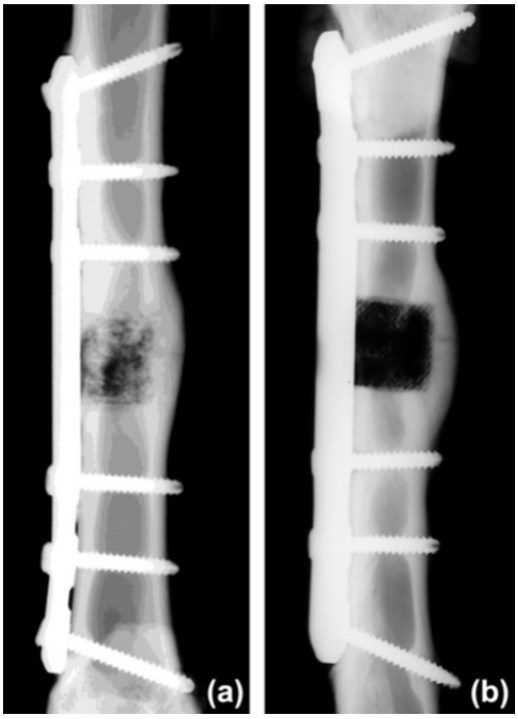

Figure 1.11: X-ray images of tibial defects with implanted β-TCP (a) and PCL/β-TCP scaffolds (a) after 14 weeks, showing greater bone formation within the defect containing the β-TCP scaffold. External fixator stabilisation of the defect is shown here where each critical-sized defect is stabilised with a fixed metal plate and screws. Note that the PCL/β-TCP scaffold is not visible in the defect (Lohfeld et al. 2012).

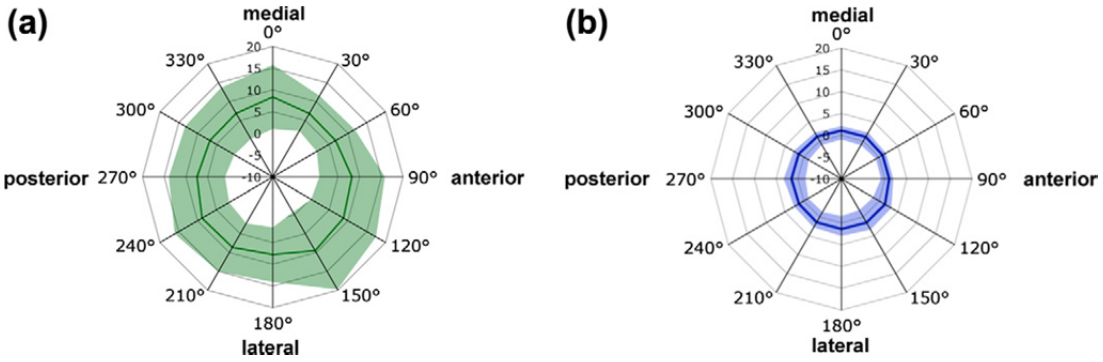

Figure 1.12: Radial bending stiffness (Nm^{-2}) of critical-sized tibial defects with implanted β-TCP (a) and PCL/β-TCP scaffolds (b) after 14 weeks, determined using four point bending (Lohfeld et al. 2012).

The main objective of Chapter 6 of this thesis is to construct anatomically accurate FE models of animal-specific tibial defects based on the available μ-CT scan data. The bending stiffness data generated as part of the original animal study (Lohfeld et al. 2012) provides experimental data for the verification of the FE models. The process by which these models are constructed is discussed in Chapter 6.

1.7 Removal of Fracture Fixation Devices

The success of the *in vivo* performance of orthopaedic scaffolds can be assessed in a number of ways. For the case of critical-sized defects, the load-bearing ability of the scaffold is of utmost importance as failure of the scaffold would result in further injury and pain for the patient. For the initial stages of healing, the scaffold, along with any external fixation devices, must support the full physiological loading through the defect. As degradation of the scaffold material occurs over time and new bone formation progresses resulting in increased volume and mineralisation of new bone tissue, the focus shifts towards the mechanical performance of the full scaffold-callus defect.

External fixation is required for stabilisation of critical-sized defects with implanted scaffolds to minimise or eliminate motion between the scaffold and the neighbouring native bone, as well as to provide additional load-bearing support during the early stages of healing. Long bones such as the tibia and femur are subjected to complex loading conditions *in-vivo*, with a combination of vertical loading due to body weight and loading applied in various directions at muscle attachment points during

movement as illustrated in Figure 1.13 (Duda et al. 1998; Taylor et al. 2006). An example of a scaffold-filled tibial defect with a metal plate external fixation device is shown in Figure 1.11. Determining when it is appropriate to remove external fixation

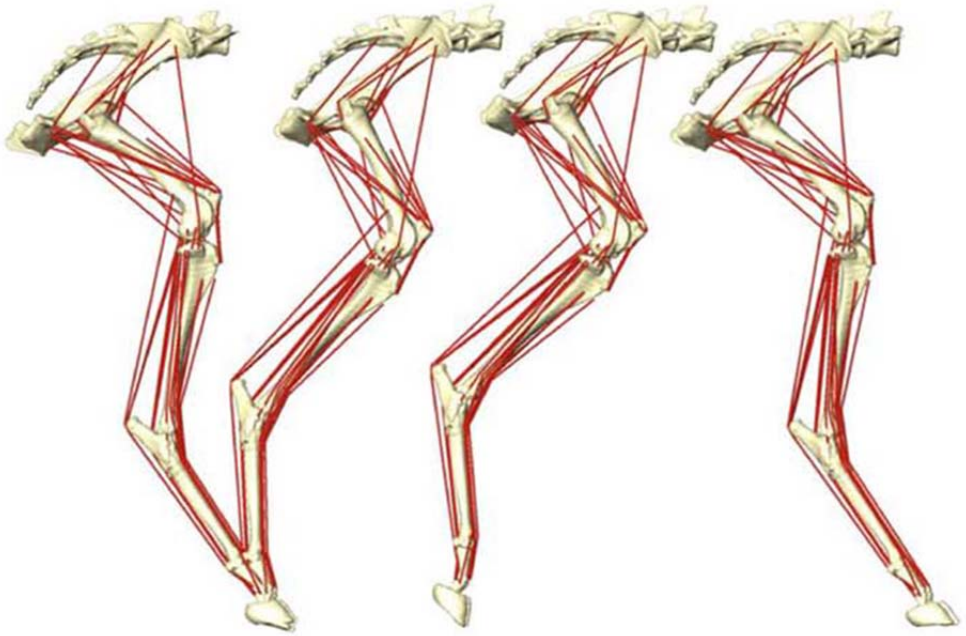

Figure 1.13: Reconstruction of the sheep lower limb during four time instances in the gait cycle, showing the lines of action of the muscles. Adapted from Taylor et al. (Taylor et al. 2006).

is important as "leaving the apparatus on for longer than necessary is as harmful as removing the fixator too early" (Ilizarov 1990). Quantifying the degree of healing, or volume of callus tissue, and mechanical integrity of the callus that is required for safe external fixation removal remains a challenge.

Mechanical testing methods have been used to determine the mechanical integrity of scaffold-tissue constructs *ex-vivo*. While uniaxial testing provides useful information regarding load-bearing in the axial direction (Roshan-Ghias et al. 2011), it does not account for other possible loading configurations. Radial four-point bending tests

have been used to evaluate callus bending stiffness giving a more robust measure of the mechanical integrity of the scaffold-tissue construct (Lohfeld et al. 2012), generating radial bending stiffness data as shown in Figure 1.12. Mechanical testing methods such as these have limited value for the evaluation of the safety of fracture fixation removal as they are destructive tests and cannot be carried out on live subjects.

Non-invasive methods to quantify bone formation within a defect site have also been developed based on imaging methods such as X-Ray and μ-CT, allowing clinicians to make informed decisions regarding fixation removal. Such methods have been developed primarily for treatment of distraction osteogenesis, a surgical technique used to lengthen long bones. A gap in the length of the bone is created and new bone forms within the gap, and the defect is stabilised with external fixation during the treatment. The type of defect that is the subject of study in Chapter 6 of this thesis is anatomically similar to a distraction osteogenesis defect, with the major difference being that the defect is filled with a bone tissue engineering scaffold.

The most common criterion for the removal of fixation is the measurement of the thickness of continuous cortices of bone bridging a defect using X-rays. A thickness of 2 mm in three bridging cortices has been reported as sufficient for removal of fixation, with reported re-fracture rates of 4% (Skaggs et al. 1999) and 3% (Fischgrund et al. 1994). This method is commonly used due to the wide availability and low cost of X-rays; however it is user-subjective and the thickness of cortices and any small defects within the bridging bone are also somewhat dependent on the angle at which the X-ray is taken. Pixel value ratio (P_r), also evaluated using X-ray

images, has been used to evaluate fracture risk. Correlation of P_r with the fracture of regenerate bone has shown the occurrence of fracture with $P_r < 0.8$ and no fracture with $P_r > 1$ (Song et al. 2005), therefore an optimal P_r value of 1 has been suggested (Zhao et al. 2009). The use of bone mineral density measurements (BMD), a one dimensional number from a DEXA scan, to evaluate fixation removal has been correlated with low refracture rates (Saran and Hamdy 2008). Good correlation between P_r and BMD has been shown (Hazra et al. 2008; Song et al. 2012).

The use of P_r and BMD as quantitative callus assessments methods are limited due to their 2D nature. 3D variations in callus density or continuous loading paths through bone are not accounted for. Measurements from μ-CT imaging have also been employed to assess fracture risk. The cross-sectional moment of inertia ($CSMI$) of a defect callus was found to have high correlation with bending breaking force determined using three-point bending (Jamsa et al. 1998). The strength–strain index (SSI), defined as the cross-sectional moment of inertia ($CSMI$) weighted by density distribution, has also been shown to correlate well with stiffness (Kokoroghiannis et al. 2009; Lind et al. 2001). Both $CSMI$ and SSI are based on 3D measurements of callus bone density, and therefore give a more complete picture of overall callus mechanical integrity than P_r or BMD.

Each of the methods above, P_r, BMD, $CSMI$ and SSI, involves some degree of averaging of properties. This means that information regarding continuous paths of load-bearing material is lost. A relatively small gap or crack in callus tissue can result in mechanical failure of a defect; however this may not be picked up by these methods. It is also worth noting that polymeric scaffolds may not be visible in the X-

ray or μ-CT images, as illustrated in Figure 1.11 for X-rays for example. The scaffold was also not visible in μ-CT images of this defect, as discussed in Chapter 6 of this thesis. When this is considered, the methods above do not account for the presence of the scaffold or its contribution to the load-bearing abilities of the scaffold-callus construct. Therefore these methods are unlikely to be able to predict mechanical stability of defects with implanted scaffolds.

As discussed in Section 1.6.3 above, FE models of the defect geometry can be constructed from μ-CT images and are often generated along with X-rays in a clinical setting for analysis of the patient defect. The ability of FE modelling to predict the success of fracture fixation device removal is assessed in Chapter 6 of this thesis. P_r and $CSMI$ are chosen as representative 2D and 3D methods of predicting the safety of fracture fixation removal, and comparisons are made between these imaging-based measures and the capabilities of FE modelling to predict safe fixation removal.

1.8 Thesis Objectives

The overall objective of this work is to develop a computational modelling framework to accurately predict the mechanical properties of orthopaedic scaffold materials. This research is specifically focused on selective laser sintered PCL/β-TCP scaffolds which are known to have a complex microstructure due to the incorporation of ceramic particles. The aim of Chapters 3, 4 and 5 of this thesis is to assess the influence of these particles on the microstructure, mechanical properties

and degradation the material, through the use of microscale and macro-scale FE modelling, and mechanical testing.

Following on from this, macro-scale FE models of four critical-sized ovine tibial defects with implanted scaffolds are constructed in Chapter 6, that use the mechanical properties of PCL/β-TCP scaffolds determined in the earlier chapters. Additionally, careful attention is paid to the use of correct material properties for each of the tissue types present. The aim of this chapter is to gain an insight into the mechanical performance of the scaffold and regenerated tissue construct in an *in vivo* setting using non-invasive methods.

The specific objectives of this thesis, as introduced in this chapter, are as follows:

- Develop a microstructure-based methodology to accurately predict the elastic properties of a 50/50wt% PCL/β-TCP SLS scaffold material using a combination of mechanical testing, micromechanical simulations and macro-scale simulations of individual scaffold struts.
- Determine if the relationship between the material elastic properties and average grey-value on the microscale is the same for SLS materials with different volumes of β-TCP particles. This is explored specifically by considering a 90/10wt% PCL/β-TCP SLS scaffold material.
- Test the ability of the microstructure-based methodology developed here to predict the macro-scale effective elastic properties of SLS materials with different volumes of β-TCP particles.

- Assess the effect of increasing the ceramic content of the scaffold materials on material microstructure and on the resulting material elastic properties through mechanical testing and imaging methods.
- Determine the effect of material composition on the changes in mechanical properties and material microstructure during simulated physiological degradation.
- Construct macro-scale FE models of *in-vivo* critical-sized ovine tibial defects with two types of implanted scaffold (PCL/β-TCP and β-TCP) from μ-CT scan data of the real defects that can accurately predict the experimentally-determined bending stiffness.
- Assess the stability and load-bearing abilities of each defect. Evaluate the load-bearing abilities of each individual defect using stress distribution analysis of both callus tissues and scaffold materials under simulated bending loading and *in vivo* compressive loading.
- Evaluate clinically-used callus-evaluation parameters to predict the safety of removing the external fixator device for individual scaffold-callus defects and assess suitability of the use of these parameters by comparing with the results of bending and compressive loading simulations.

1.9 Thesis Outline

The theoretical framework for the computational analyses presented in this thesis (Chapters 3, 4 and 6) are presented in **Chapter 2**. Definitions for stress and strain measures are given, and the constitutive laws describing elasticity are also outlined. A description of the FE method is presented to demonstrate the numerical problem solution procedures that are employed in this thesis.

A method to accurately model the realistic mechanical behaviour of a 50/50wt% PCL/β-TCP sintered scaffold material is developed in **Chapter 3**. High-resolution finite element macro-scale and microscale models of material samples are generated from μ-CT scans. A range of methods is then explored to determine the most appropriate and most practical way to assign the elastic constants in the high resolution models. A multi-scale, microstructure-based modelling methodology is developed whereby effective elastic constants are calculated from FE microscale models of real segments of the material and the relationship between the material elastic modulus and average grey-value is evaluated. Heterogeneous assignment of material properties in the macro-scale models is shown to give the best prediction of the macro-scale material elastic properties. The microstructure-based modelling methodology developed in this chapter is also used in Chapter 4, and results of strut mechanical testing are included as baseline (undegraded) material properties in Chapter 5.

The relationship between the material elastic modulus and average grey-value on the microscale is evaluated for a 90/10wt% PCL/β-TCP SLS material in **Chapter 4** to determine whether this relationship is the same for SLS materials with different

volumes of β-TCP particles. The ability of the microstructure-based modelling methodology developed in Chapter 3 to predict the macro-scale elastic properties of this material is evaluated and is assessed in comparison with experimentally evaluated elastic properties. The results of this study show that this methodology can predict the macro-scale stiffness of both the 90/10wt% and the 50/50wt% materials. The relationship between elastic modulus and grey-value is found to be specific to each material. As before, results of strut mechanical testing are included as baseline (undegraded) material properties in Chapter 5.

The impact of increasing the volume of ceramic in scaffold materials fabricated using selective laser sintering on the material microstructure and material elastic properties is evaluated in **Chapter 5**. SLS scaffold materials are fabricated from PCL and from two volume fractions of β-TCP. The changes in mechanical properties and material microstructure of these materials during simulated physiological degradation are evaluated. Differences in the microstructure of materials with increasing ceramic content were observed in both undegraded and degraded states, as were resulting differences in material elastic properties.

Computational model geometries of tibial defects that include implanted scaffold and bone callus geometries are carefully constructed from μ-CT scan images in **Chapter 6**. The accuracy of these models is assessed by comparing the predicted bending stiffness from bending testing simulations of each defect with experimentally-evaluated data that was generated in a previous study using these scaffolds. Stress distribution analysis is used to evaluate the load-bearing abilities of each individual scaffold-callus construct under simulated bending and compressive loading.

Clinically-used image-based parameters to predict the safety of removing external fixation are calculated for each defect and comparisons are made with the results of computational simulations of bending and compressive loading to make conclusions on the suitability of the use of these callus-evaluation parameters.

Chapter 7 summarises the key findings of this thesis. The implications of these findings, for the analysis of SLS scaffold materials as well as for computational modelling of these scaffolds in realistic defects, are discussed. Some indications for possible future experimental and computational work are provided.

1.10 References

Baas, E., Kuiper, J.H., Yang, Y., Wood, M. a and El Haj, A.J. 2010. In vitro bone growth responds to local mechanical strain in three-dimensional polymer scaffolds. *Journal of Biomechanics* 43(4), pp. 733–9.

Bayraktar, H.H., Morgan, E.F., Niebur, G.L., Morris, G.E., Wong, E.K. and Keaveny, T.M. 2004. Comparison of the elastic and yield properties of human femoral trabecular and cortical bone tissue. *Journal of Biomechanics* 37(1), pp. 27–35.

Beck, A., Woods, S., Lansdowne, J.L. and Arens, D. 2013. The effects of multiple high-resolution peripheral quantitative computed tomography scans on bone healing in a rabbit radial bone defect model. *Bone* 56(2), pp. 312–9.

Bhumiratana, S., Grayson, W.L., Castaneda, A., Rockwood, D.N., Gil, E.S., Kaplan, D.L. and Vunjak-Novakovic, G. 2011. Nucleation and growth of mineralized bone matrix on silk-hydroxyapatite composite scaffolds. *Biomaterials* 32(11), pp. 2812–20.

Boerckel, J., Kolambkar, Y., Stevens, H., Lin, A., Dupont, K. and Guldberg, R. 2012. Effects of in vivo mechanical loading on large bone defect regeneration. *Journal of Orthopaedic Research* 30(7), pp. 1067–1075.

Böhm, H.J. 2004. A Short Introduction to Continuum Micromechanics. In: Bohm, H. J. ed. *Mechanics of Microstructured Materials*. 464th ed. Vienna: CISM Courses and Lectures, Springer-Verlag, pp. 1–40.

Breuls, R.G.M., Jiya, T.U. and Smit, T.H. 2008. Scaffold stiffness influences cell behavior: opportunities for skeletal tissue engineering. *The Open Orthopaedics Journal* 2, pp. 103–9.

Burr, D.B., Milgrom, C., Fyhrie, D., Forwood, M., Nyska, M., Finestone, a, Hoshaw, S., Saiag, E. and Simkin, a 1996. In vivo measurement of human tibial strains during vigorous activity. *Bone* 18(5), pp. 405–10.

Cahill, S., Lohfeld, S. and McHugh, P.E. 2009. Finite element predictions compared to experimental results for the effective modulus of bone tissue engineering scaffolds fabricated by selective laser sintering. *Journal of Materials Science. Materials in Medicine* 20(6), pp. 1255–62.

Carnelli, D., Lucchini, R., Ponzoni, M., Contro, R. and Vena, P. 2011. Nanoindentation testing and finite element simulations of cortical bone allowing for anisotropic elastic and inelastic mechanical response. *Journal of Biomechanics* 44(10), pp. 1852–8.

Castilla-Cortázar, I., Más-Estellés, J., Meseguer-Dueñas, J.M., Escobar Ivirico, J.L., Marí, B. and Vidaurre, A. 2012. Hydrolytic and enzymatic degradation of a poly(ε-caprolactone) network. *Polymer Degradation and Stability* 97(8), pp. 1241–1248.

Caulfield, B., McHugh, P.E. and Lohfeld, S. 2007. Dependence of mechanical properties of polyamide components on build parameters in the SLS process. *Journal of Materials Processing Technology* 182(1-3), pp. 477–488.

Chateau, C., Gélébart, L., Bornert, M., Crépin, J. and Caldemaison, D. 2010. Multiscale approach of mechanical behaviour of SiC / SiC composites : elastic behaviour at the scale of the tow. *Technische Mechanik* 30, pp. 45–55.

Chatterjee, K., Sun, L., Chow, L.C., Young, M.F. and Simon, C.G. 2010. Combinatorial screening of osteoblast response to 3D calcium phosphate/poly(ε-caprolactone) scaffolds using gradients and arrays. *Biomaterials* 32(5), pp. 1361–1369.

Cheal, E.J., Mansmann, K. a, DiGioia, a M., Hayes, W.C. and Perren, S.M. 1991. Role of interfragmentary strain in fracture healing: ovine model of a healing osteotomy. *Journal of Orthopaedic Research* 9(1), pp. 131–42.

Chen, C.S. and Ingber, D.E. 1999. Tensegrity and mechanoregulation: from skeleton to cytoskeleton. *Osteoarthritis and Cartilage* 7(1), pp. 81–94.

Chevalier, Y., Pahr, D., Allmer, H., Charlebois, M. and Zysset, P. 2007. Validation of a voxel-based FE method for prediction of the uniaxial apparent modulus of human trabecular bone using macroscopic mechanical tests and nanoindentation. *Journal of Biomechanics* 40(15), pp. 3333–40.

Cipitria, A., Lange, C., Schell, H., Wagermaier, W., Reichert, J.C., Hutmacher, D.W., Fratzl, P. and Duda, G.N. 2012. Porous scaffold architecture guides tissue formation. *Journal of Bone and Mineral Research* 27(6), pp. 1275–88.

Crabtree, N., Lunt, M., Holt, G., Kröger, H., Burger, H., Grazio, S., Khaw, K.T., Lorenc, R.S., Nijs, J., Stepan, J., Falch, J. a, Miazgowski, T., Raptou, P., Pols, H. a, Dequeker, J., Havelka, S., Hoszowski, K., Jajic, I., Czekalski, S., Lyritis, G., Silman, a J. and Reeve, J. 2000. Hip geometry, bone mineral distribution, and bone strength in European men and women: the EPOS study. *Bone* 27(1), pp. 151–9.

Von Doernberg, M.-C., von Rechenberg, B., Bohner, M., Grünenfelder, S., van Lenthe, G.H., Müller, R., Gasser, B., Mathys, R., Baroud, G. and Auer, J. 2006. In vivo behavior of calcium phosphate scaffolds with four different pore sizes. *Biomaterials* 27(30), pp. 5186–98.

Dong, J., Uemura, T., Shirasaki, Y. and Tateishi, T. 2002. Promotion of bone formation using highly pure porous beta-TCP combined with bone marrow-derived osteoprogenitor cells. *Biomaterials* 23(23), pp. 4493–502.

Drugan, W.J. and Willis, J.R. 1996. A micromechanics-based nonlocal constitutive equation and estimates of representative volume element size for elastic composites. *Journal of the Mechanics and Physics of Solids* 44(4), pp. 497 – 524.

Duda, G.N., Heller, M., Albinger, J., Schulz, O., Schneider, E. and Claes, L. 1998. Influence of muscle forces on femoral strain distribution. *Journal of Biomechanics* 31(9), pp. 841–6.

Engler, A.J., Sen, S., Sweeney, H.L. and Discher, D.E. 2006. Matrix elasticity directs stem cell lineage specification. *Cell* 126(4), pp. 677–89.

Eshraghi, S. and Das, S. 2012. Micromechanical finite-element modeling and experimental characterization of the compressive mechanical properties of polycaprolactone-hydroxyapatite composite scaffolds prepared by selective laser sintering for bone tissue engineering. *Acta Biomaterialia* 8(8), pp. 3138–43.

Evans, F.G. 1976. Mechanical properties and histology of cortical bone from younger and older men. *The Anatomical Record* 185(1), pp. 1–11.

Fan, Z., Swadener, J.G., Rho, J.Y., Roy, M.E. and Pharr, G.M. 2002. Anisotropic properties of human tibial cortical bone as measured by nanoindentation. *Journal of Orthopaedic Research* 20(4), pp. 806–10.

Feng, L., Chittenden, M., Schirer, J., Dickinson, M. and Jasiuk, I. 2012. Mechanical properties of porcine femoral cortical bone measured by nanoindentation. *Journal of Biomechanics* 45(10), pp. 1775–82.

Feng, L. and Jasiuk, I. 2011. Multi-scale characterization of swine femoral cortical bone. *Journal of Biomechanics* 44(2), pp. 313–320.

Fischgrund, J., Paley, D. and Suter, C. 1994. Variables affecting time to bone healing during limb lengthening. *Clinical Orthopaedics and Related Research* 301, pp. 31–37.

Franco, A., Lanzetta, M. and Romoli, L. 2010. Experimental analysis of selective laser sintering of polyamide powders: an energy perspective. *Journal of Cleaner Production* 18(16-17), pp. 1722–1730.

Freeman, T. a, Patel, P., Parvizi, J., Antoci, V. and Shapiro, I.M. 2009. Micro-CT analysis with multiple thresholds allows detection of bone formation and resorption during ultrasound-treated fracture healing. *Journal of Orthopaedic Research* 27(5), pp. 673–9.

Frost, H.M. 1992. Perspectives: bone's mechanical usage windows. *Bone and Mineral* 19(3), pp. 257–271.

Gabriel, M., van Nieuw Amerongen, G.P., Van Hinsbergh, V.W.M., Amerongen, A.V.V.N. and Zentner, A. 2006. Direct grafting of RGD-motif-containing peptide on the surface of polycaprolactone films. *Journal of Biomaterials Science. Polymer Edition* 17(5), pp. 567–77.

Gardner, T.N., Stoll, T., Marks, L., Mishra, S. and Knothe Tate, M. 2000. The influence of mechanical stimulus on the pattern of tissue differentiation in a long bone fracture--an FEM study. *Journal of Biomechanics* 33(4), pp. 415–25.

Grant, C. a, Wilson, L.J., Langton, C. and Epari, D. 2014. Comparison of mechanical and ultrasound elastic modulus of ovine tibial cortical bone. *Medical Engineering & Physics* 36(7), pp. 869–74.

De Groot, K. 1988. Effect of porosity and physicochemical properties on the stability, resorption, and strength of calcium phosphate ceramics. *Annals of the New York Academy of Sciences* 523, pp. 227–33.

Gunatillake, P. a and Adhikari, R. 2003. Biodegradable synthetic polymers for tissue engineering. *European Cells & Materials* 5, pp. 1–16.

Hansen, U., Zioupos, P., Simpson, R., Currey, J.D. and Hynd, D. 2008. The effect of strain rate on the mechanical properties of human cortical bone. *Journal of Biomechanical Engineering* 130(1), p. 011011.

Harrison, N.M., McDonnell, P.F., O'Mahoney, D.C., Kennedy, O.D., O'Brien, F.J. and McHugh, P.E. 2008. Heterogeneous linear elastic trabecular bone modelling using micro-CT attenuation data and experimentally measured heterogeneous tissue properties. *Journal of Biomechanics* 41(11), pp. 2589–96.

Haugh, M.G., D, P., Murphy, C.M., Sc, B., Mckiernan, R.C., Altenbuchner, C. and Brien, F.J.O. 2011. Cell Attachment , Proliferation, and Migration Within Collagen Glycosaminoglycan Scaffolds. *Tissue Engineering. Part A* 17(9-10), pp. 1201–8.

Hazanov, S. and Amieur, M. 1995. On Overall Properties of Elastic Heterogeneous Bodies Smaller than the Representative Volume. *International Journal of Engineering Science* 33(9), pp. 1289–1301.

Hazra, S., Song, H.-R., Biswal, S., Lee, S.-H., Lee, S.H., Jang, K.-M. and Modi, H.N. 2008. Quantitative assessment of mineralization in distraction osteogenesis. *Skeletal Radiology* 37(9), pp. 843–7.

Hengsberger, S., Kulik, A. and Zysset, P. 2002. Nanoindentation Discriminates the Elastic Properties of Individual Human Bone Lamellae Under Dry and Pysiological Conditions. *Bone* 30(1), pp. 178–184.

Hollister, S.J. 2005. Porous scaffold design for tissue engineering. *Nature Materials* 4(7), pp. 518–24.

Hollister, S.J. 2009. Scaffold design and manufacturing: from concept to clinic. *Advanced Materials* 21(32-33), pp. 3330–42.

Huiskes, R., Weinans, H. and van Rietbergen, B. 1992. The relationship between stress shielding and bone resorption around total hip stems and the effects of flexible materials. *Clinical Orthopaedics and Related Research* (274), pp. 124–34.

Hukins, D.W.L., Mahomed, A. and Kukureka, S.N. 2008. Accelerated aging for testing polymeric biomaterials and medical devices. *Medical Engineering & Physics* 30(10), pp. 1270–4.

Ilizarov, G. 1990. Clinical application of the tension-stress effect for limb lengthening. *Clinical Orthopaedics and Related Research* 250, pp. 8–26.

Isaksson, H., Nagao, S., Małkiewicz, M., Julkunen, P., Nowak, R. and Jurvelin, J.S. 2010. Precision of nanoindentation protocols for measurement of viscoelasticity in cortical and trabecular bone. *Journal of Biomechanics* 43(12), pp. 2410–7.

Jamsa, T., Jalovaara, P., Peng, Z., Ams, T.J. and Tuukkanen, J. 1998. Comparison of Three-Point Bending Test and Peripheral. *Bone* 23(2), pp. 155–161.

Jones, A.C., Arns, C.H., Hutmacher, D.W., Milthorpe, B.K., Sheppard, A.P. and Knackstedt, M. a 2009. The correlation of pore morphology, interconnectivity and physical properties of 3D ceramic scaffolds with bone ingrowth. *Biomaterials* 30(7), pp. 1440–51.

Kang, Y., Scully, A., Young, D. a, Kim, S., Tsao, H., Sen, M. and Yang, Y. 2011. Enhanced mechanical performance and biological evaluation of a PLGA coated β-TCP composite scaffold for load-bearing applications. *European Polymer Journal* 47(8), pp. 1569–1577.

Kanit, T. and Forest, S. 2003. Determination of the size of the representative volume element for random composites : statistical and numerical approach. *International Journal of Solids and Structures* 40, pp. 3647–3679.

Kanit, T., N'Guyen, F., Forest, S., Jeulin, D., Reed, M. and Singleton, S. 2006. Apparent and effective physical properties of heterogeneous materials: Representativity of samples of two materials from food industry. *Computer Methods in Applied Mechanics and Engineering* 195, pp. 3960–3982.

Keaveny, T.M., Morgan, E.F., Niebur, G.L. and Yeh, O.C. 2001. Bomechanics of trabecular bone. *Annual review of biomedical engineering* 3, pp. 307–333.

Kemper, A., Mcnally, C., Kennedy, E., Manoogian, S., Tech, V., Forest, W. and Biomechanics, I. 2007. The material properties of human tibia cortical bone in tension and compression: implications for the tibia index. In: *Proceedings of the 20th Enhanced Safety of Vehicles Conference*.

Keogh, M.B., O'Brien, F.J. and Daly, J.S. 2010. Substrate stiffness and contractile behaviour modulate the functional maturation of osteoblasts on a collagen-GAG scaffold. *Acta Bomaterialia* 6(11), pp. 4305–13.

Koike, M., Shimokawa, H., Kanno, Z., Ohya, K. and Soma, K. 2005. Effects of mechanical strain on proliferation and differentiation of bone marrow stromal cell line ST2. *Journal of Bone and Mineral Metabolism* 23(3), pp. 219–25.

Kokoroghiannis, C., Charopoulos, I., Lyritis, G., Raptou, P., Karachalios, T. and Papaioannou, N. 2009. Correlation of pQCT bone strength index with mechanical testing in distraction osteogenesis. *Bone* 45(3), pp. 512–6.

Lam, C.X.F., Savalani, M.M., Teoh, S.-H. and Hutmacher, D.W. 2008. Dynamics of in vitro polymer degradation of polycaprolactone-based scaffolds: accelerated versus simulated physiological conditions. *Biomedical Materials* 3(3), p. 034108.

Lam, C.X.F., Teoh, S.H. and Hutmacher, D.W. 2007. Comparison of the degradation of polycaprolactone and polycaprolactone-(β-tricalcium phosphate) scaffolds in alkaline medium. *Polymer International* 56(October 2006), pp. 718–728.

Lee, H. and Kim, G. 2011. Three-dimensional plotted PCL/β-TCP scaffolds coated with a collagen layer: preparation, physical properties and in vitro evaluation for bone tissue regeneration. *Journal of Materials Chemistry* 21(17), p. 6305.

Leong, P.L. and Morgan, E.F. 2009. Correlations between indentation modulus and mineral density in bone-fracture calluses. *Integrative and Comparative Biology* 49(1), pp. 59–68.

Liebschner, M. a K., Müller, R., Wimalawansa, S.J., Rajapakse, C.S. and Gunaratne, G.H. 2005. Testing two predictions for fracture load using computer models of trabecular bone. *Biophysical Journal* 89(2), pp. 759–67.

Liebschner, M. a. K. 2004. Biomechanical considerations of animal models used in tissue engineering of bone. *Biomaterials* 25(9), pp. 1697–1714.

Lind, P.M., Lind, L., Larsson, S. and Orberg, J. 2001. Torsional testing and peripheral quantitative computed tomography in rat humerus. *Bone* 29(3), pp. 265–70.

Linde, F. and Hvid, I. 1989. The effect of constraint on the mechanical behaviour of trabecular bone specimens. *Journal of Biomechanics* 22(5), pp. 485–490.

Liu, G., Zhao, L., Cui, L., Liu, W. and Cao, Y. 2007. Tissue-engineered bone formation using human bone marrow stromal cells and novel beta-tricalcium phosphate. *Biomedical Materials* 2(2), pp. 78–86.

Llorca, J. and Segurado, J. 2004. Three-dimensional multiparticle cell simulations of deformation and damage in sphere-reinforced composites. *Materials Science and Engineering: A* 365, pp. 267–274.

Lo, C.M., Wang, H.B., Dembo, M. and Wang, Y.L. 2000. Cell movement is guided by the rigidity of the substrate. *Biophysical Journal* 79(1), pp. 144–52.

Lohfeld, S., Cahill, S., Barron, V., McHugh, P., Dürselen, L., Kreja, L., Bausewein, C. and Ignatius, A. 2012. Fabrication, mechanical and in vivo performance of polycaprolactone/tricalciumphosphate composite scaffolds. *Acta Biomaterialia* 8(9), pp. 3446–3456.

Lohfeld, S., Cahill, S., Doyle, H. and McHugh, P. 2014. Improving the Finite Element Model Accuracy of Tissue Engineering Scaffolds Produced by Selective Laser Sintering. *Journal of Materials Science. Materials in Medicine* In Press.

Lohfeld, S., Tyndyk, M.A., Cahill, S., Flaherty, N., Barron, V. and McHugh, P.E. 2010. A method to fabricate small features on scaffolds for tissue engineering via selective laser sintering. *Journal of Biomedical Science and Engineering* 3, pp. 138–147.

Lu, Z. and Zreiqat, H. 2010. Beta-tricalcium phosphate exerts osteoconductivity through alpha2beta1 integrin and down-stream MAPK/ERK signaling pathway. *Biochemical and Biophysical Research Communications* 394(2), pp. 323–9.

Malizos, K.N., Papachristos, A. a, Protopappas, V.C. and Fotiadis, D.I. 2006. Transosseous application of low-intensity ultrasound for the enhancement and monitoring of fracture healing process in a sheep osteotomy model. *Bone* 38(4), pp. 530–9.

Manjubala, I., Liu, Y., Epari, D.R., Roschger, P., Schell, H., Fratzl, P. and Duda, G.N. 2009. Spatial and temporal variations of mechanical properties and mineral content of the external callus during bone healing. *Bone* 45(2), pp. 185–192.

Markel, M.D., Wikenheiser, M. a and Chao, E.Y. 1990. A study of fracture callus material properties: relationship to the torsional strength of bone. *Journal of Orthopaedic Research* 8(6), pp. 843–50.

McDonnell, P., Harrison, N. and McHugh, P.E. 2010. Investigation of the failure behaviour of vertebral trabecular architectures under uni-axial compression and wedge action loading conditions. *Medical Engineering & Physics* 32(6), pp. 569–76.

McNamara, L.M., Ederveen, a G.H., Lyons, C.G., Price, C., Schaffler, M.B., Weinans, H. and Prendergast, P.J. 2006. Strength of cancellous bone trabecular tissue from normal, ovariectomized and drug-treated rats over the course of ageing. *Bone* 39(2), pp. 392–400.

Middleton, J.C. and Tipton, a J. 2000. Synthetic biodegradable polymers as orthopedic devices. *Biomaterials* 21(23), pp. 2335–46.

Mittra, E., Rubin, C. and Qin, Y.-X. 2005. Interrelationship of trabecular mechanical and microstructural properties in sheep trabecular bone. *Journal of biomechanics* 38(6), pp. 1229–37.

Mosekilde, L., Mosekilde, L. and Danielsen, C.C. 1987. Biomechanical competence of vertebral trabecular bone in relation to ash density and age in normal individuals. *Bone* 8(2), pp. 79–85.

Nafei, a., Danielsen, C.C., Linde, F. and Hvid, I. 2000. Properties of growing trabecular ovine bone: Part I. *The Journal of Bone and Joint Surgery* 82(6), pp. 910–920.

Nakamoto, T., Shirakawa, N., Miyata, Y. and Inui, H. 2009. Selective laser sintering of high carbon steel powders studied as a function of carbon content. *Journal of Materials Processing Technology* 209(15-16), pp. 5653–5660.

Newman, E., Turner, a S. and Wark, J.D. 1995. The potential of sheep for the study of osteopenia: current status and comparison with other animal models. *Bone* 16(4 Suppl), p. 277S–284S.

Pahr, D.H. and Zysset, P.K. 2008. Influence of boundary conditions on computed apparent elastic properties of cancellous bone. *Biomechanics and Modeling in Mechanobiology* 7, pp. 463–476.

Rai, B., Lin, J.L., Lim, Z.X.H., Guldberg, R.E., Hutmacher, D.W. and Cool, S.M. 2010. Differences between in vitro viability and differentiation and in vivo bone-forming efficacy of human mesenchymal stem cells cultured on PCL-TCP scaffolds. *Biomaterials* 31(31), pp. 7960–70.

Rho, J.Y., Roy, M. and Pharr, G.M. 2000. Elastic modulus and hardness of cortical and trabecular bone lamellae measured by nanoindentation in the human femur. *Journal of Biomechanics* 33(10), pp. 1335–7.

Rho, J.Y., Tsui, T.Y. and Pharr, G.M. 1997. Elastic properties of human cortical and trabecular lamellar bone measured by nanoindentation. *Biomaterials* 18(20), pp. 1325–30.

Rodriguez-Florez, N., Oyen, M.L. and Shefelbine, S.J. 2013. Insight into differences in nanoindentation properties of bone. *Journal of the Mechanical Behavior of Bomedical Materials* 18, pp. 90–9.

Rohlmann, A., Zilch, H., Bergmann, G. and Kölbel, R. 1980. Material properties of femoral cancellous bone in axial loading. Part I: Time independent properties. *Archives of orthopaedic and trauma surgery* 97(2), pp. 95–102.

Roshan-Ghias, A., Lambers, F.M., Gholam-Rezaee, M., Müller, R. and Pioletti, D.P. 2011. In vivo loading increases mechanical properties of scaffold by affecting bone formation and bone resorption rates. *Bone* 49(6), pp. 1357–64.

Sandino, C. and Lacroix, D. 2011. A dynamical study of the mechanical stimuli and tissue differentiation within a CaP scaffold based on micro-CT finite element models. *Biomechanics and Modeling in Mechanobiology* 10(4), pp. 565–576.

Sandino, C., Planell, J. a and Lacroix, D. 2008. A finite element study of mechanical stimuli in scaffolds for bone tissue engineering. *Journal of Biomechanics* 41(5), pp. 1005–14.

Saran, N. and Hamdy, R.C. 2008. DEXA as a predictor of fixator removal in distraction osteogenesis. *Clinical Orthopaedics and Related Research* 466(12), pp. 2955–61.

Schorlemmer, S., Ignatius, A., Claes, L. and Augat, P. 2005. Inhibition of cortical and cancellous bone formation in glucocorticoid-treated OVX sheep. *Bone* 37(4), pp. 491–6.

Shefelbine, S.J., Simon, U., Claes, L., Gold, A., Gabet, Y., Bab, I., Müller, R. and Augat, P. 2005. Prediction of fracture callus mechanical properties using micro-CT images and voxel-based finite element analysis. *Bone* 36(3), pp. 480–8.

Shepherd, T.N., Zhang, J., Ovaert, T.C., Roeder, R.K. and Niebur, G.L. 2011. Direct comparison of nanoindentation and macroscopic measurements of bone viscoelasticity. *Journal of the Mechanical Behavior of Biomedical Materials* 4(8), pp. 2055–2062.

Silva, M.J., Brodt, M.D., Fan, Z. and Rho, J.-Y. 2004. Nanoindentation and whole-bone bending estimates of material properties in bones from the senescence accelerated mouse SAMP6. *Journal of Biomechanics* 37(11), pp. 1639–46.

Skaggs, D., Leet, A., Money, M., Shaw, B., Hale, J. and Tolo, V. 1999. Secondary fractures associated with external fixation in pediatric femur fractures. *Journal of Pediatric Orthopedics.* 19(5), pp. 582–6.

Song, H., Oh, C., Mattoo, R., Park, B., Kim, S., Park, I., Jeon, I. and Ihn, J. 2005. Femoral lengthening over an intramedullary nail using the external fixator: risk of infection and knee problems in 22 patients with a follow-up of 2 years or more. *Acta Orthopaedica* 76(2), pp. 245–252.

Song, S.-H., Agashe, M., Kim, T.-Y., Sinha, S., Park, Y.-E., Kim, S.-J., Hong, J.-H., Song, S.-Y. and Song, H.-R. 2012. Serial bone mineral density ratio measurement for fixator removal in tibia distraction osteogenesis and need of a supportive method using the pixel value ratio. *Journal of Pediatric Orthopedics. Part B* 21(2), pp. 137–45.

Steiner, M., Claes, L., Simon, U., Ignatius, A. and Wehner, T. 2012. A computational method for determining tissue material properties in ovine fracture calluses using electronic speckle pattern interferometry and finite element analysis. *Medical Engineering and Physics* 34(10), pp. 1521–1525.

Tan, K.H., Chua, C.K., Leong, K.F., Cheah, C.M., Cheang, P., Abu Bakar, M.S. and Cha, S.W. 2003. Scaffold development using selective laser sintering of polyetheretherketone–hydroxyapatite biocomposite blends. *Biomaterials* 24(18), pp. 3115–3123.

Taylor, W.R., Ehrig, R.M., Heller, M.O., Schell, H., Seebeck, P. and Duda, G.N. 2006. Tibio-femoral joint contact forces in sheep. *Journal of Biomechanics* 39(5), pp. 791–8.

Tsuruga, E., Takita, H., Itoh, H., Wakisaka, Y. and Kuboki, Y. 1997. Pore size of porous hydroxyapatite as the cell-substratum controls BMP-induced osteogenesis. *Journal of Biochemistry* 121(2), pp. 317–24.

Vaughan, T.J. and McCarthy, C.T. 2010. A combined experimental–numerical approach for generating statistically equivalent fibre distributions for high strength laminated composite materials. *Composites Science and Technology* 70(2), pp. 291–297.

Vayron, R., Barthel, E., Mathieu, V., Soffer, E., Anagnostou, F. and Haiat, G. 2012. Nanoindentation measurements of biomechanical properties in mature and newly formed bone tissue surrounding an implant. *Journal of Biomechanical Engineering* 134(2), p. 021007.

Vieira, a C., Vieira, J.C., Ferra, J.M., Magalhães, F.D., Guedes, R.M. and Marques, a T. 2011. Mechanical study of PLA-PCL fibers during in vitro degradation. *Journal of the Mechanical Behavior of Biomedical Materials* 4(3), pp. 451–60.

Vijayakumar, V., Marks, L., Bremmer-Smith, A., Hardy, J. and Gardner, T. 2006. Load transmission through a healing tibial fracture. *Clinical Biomechanics* 21(1), pp. 49–53.

Wallace, R.J., Pankaj, P. and Simpson, a H.R.W. 2013. The effect of strain rate on the failure stress and toughness of bone of different mineral densities. *Journal of Biomechanics* 46(13), pp. 2283–7.

Wan, Y., Wu, H., Cao, X. and Dalai, S. 2008. Compressive mechanical properties and biodegradability of porous poly(caprolactone)/chitosan scaffolds. *Polymer Degradation and Stability* 93(10), pp. 1736–1741.

Wang, N., Butler, J.P. and Ingber, D.E. 1993. Mechanotransduction across the cell surface and through the cytoskeleton. *Science* 260(5111), pp. 1124–1127.

Wang, X.J., Chen, X.B., Hodgson, P.D. and Wen, C.E. 2006. Elastic modulus and hardness of cortical and trabecular bovine bone measured by nanoindentation. *Transactions of Nonferrous Metals Society of China* 16, pp. 744–748.

Weis, J. a, Miga, M.I., Granero-Moltó, F. and Spagnoli, A. 2010. A finite element inverse analysis to assess functional improvement during the fracture healing process. *Journal of Biomechanics* 43(3), pp. 557–62.

Wieding, J., Souffrant, R., Mittelmeier, W. and Bader, R. 2013. Finite element analysis on the biomechanical stability of open porous titanium scaffolds for large segmental bone defects under physiological load conditions. *Medical Engineering and Physics* 35(4), pp. 422–32.

Williams, J.M., Adewunmi, A., Schek, R.M., Flanagan, C.L., Krebsbach, P.H., Feinberg, S.E., Hollister, S.J. and Das, S. 2005. Bone tissue engineering using polycaprolactone scaffolds fabricated via selective laser sintering. *Biomaterials* 26(23), pp. 4817–27.

Wolfram, U., Wilke, H.-J. and Zysset, P.K. 2010. Valid micro finite element models of vertebral trabecular bone can be obtained using tissue properties measured with nanoindentation under wet conditions. *Journal of Biomechanics* 43(9), pp. 1731–7.

Wongwitwichot, P., Kaewsrichan, J., Chua, K.H. and Ruszymah, B.H.I. 2010. Comparison of TCP and TCP/HA Hybrid Scaffolds for Osteoconductive Activity. *The Open Biomedical Engineering Journal* 4, pp. 279–85.

Woodruff, M.A. and Hutmacher, D.W. 2010. The return of a forgotten polymer—Polycaprolactone in the 21st century. *Progress in Polymer Science* 35(10), pp. 1217–1256.

Zhao, L., Fan, Q., Venkatesh, K.P., Park, M.S. and Song, H.R. 2009. Objective guidelines for removing an external fixator after tibial lengthening using pixel

value ratio: a pilot study. *Clinical Orthopaedics and Related Research* 467(12), pp. 3321–6.

2 Theory

2.1 Chapter Summary

The simulations in Chapters 3, 4 and 6 in this thesis involve solving continuum mechanics problems using Abaqus, a commercial finite element (FE) solver (DS SIMULIA, USA). The theoretical framework, finite deformation kinematics, governing equations and material constitutive theories used to solve these problems are introduced in Section 2.2. Further detail on the theoretical framework used here can be found in Malvern (Malvern 1969) and in Belytschko et al. (Belytschko et al. 2000). The finite element method (FEM) is introduced in Section 2.3. In the presentation of the theory reference is made to the Abaqus implementation, as appropriate.

2.2 Continuum Mechanics

2.2.1 Notation

This section outlines the notation that is used in this chapter. Capital letters indicate tensors and matrices while lower-case letters are used for vectors. Regular italic type face denotes scalars and bold type face is used for vectors, tensors and matrices. A

Cartesian coordinate system is used with unit vectors in the three coordinate directions described as $\boldsymbol{e}_1$ = (1, 0, 0), $\boldsymbol{e}_2$ = (0, 1, 0) and $\boldsymbol{e}_3$ = (0, 0, 1), respectively. Indicial notation can be demonstrated using the dot product (summation of the component parts) of two vectors $\boldsymbol{u}$ and $\boldsymbol{v}$ as follows:

$$\mathbf{u} \cdot \mathbf{v} = u_i v_i = u_1 v_1 + u_2 v_2 + u_3 v_3 \tag{2.1}$$

A 3D second order tensor, e.g. $\boldsymbol{A}$, can be written in component form as A_{ij}, where the subscripts i and j are used to identify the matrix components. The tensor product of two vectors $\boldsymbol{u}$ and $\boldsymbol{v}$ can be written as $\boldsymbol{uv}$, where ($\boldsymbol{uv}$) = $u_i v_j$. A fourth order tensor is the linear tensor function of a second order tensor; for example, the second order stress tensor $\boldsymbol{\sigma}$ is related to the strain tensor $\boldsymbol{\varepsilon}$ by a fourth order elastic modulus tensor $\boldsymbol{K}$ as described by Equation (2.2).

$$\boldsymbol{\sigma} = \boldsymbol{K} : \boldsymbol{\varepsilon} \text{ or } \sigma_{ij} = K_{ijk}\varepsilon_{kl} \tag{2.2}$$

2.2.2 Deformation and Stress

The reference configuration, $\boldsymbol{B}_r$, of an arbitrary body $\boldsymbol{B}$ at an initial time and the deformed configuration at time t, $\boldsymbol{B}_t$, is shown in Figure 2-1**:**. Any particle P of the body $\boldsymbol{B}$ can be described by the position vector $\boldsymbol{X}$ relative to an origin O. The position of P at a time t is described by the position vector $\boldsymbol{x}$. The deformation of the body from $\boldsymbol{B}_r$ to $\boldsymbol{B}_t$ is described by the mapping χ as per Equation (2.3).

$$\boldsymbol{x} = \chi(\boldsymbol{X}, t) \tag{2.3}$$

The displacement $\boldsymbol{u}$ between reference and deformed configurations is described by Equation (2.4). The line vector $d\boldsymbol{X}$ describes the infinitesimal line element between the points P and Q in the reference configuration. This vector is transformed to the infinitesimal line element $d\boldsymbol{x}$ in the deformed configuration at time t through the deformation gradient $\boldsymbol{F}$, described by Equation (2.5).

$$\boldsymbol{u} = \boldsymbol{x} - \boldsymbol{X} \tag{2.4}$$

$$\boldsymbol{F} = \frac{\partial \boldsymbol{x}}{\partial \boldsymbol{X}} \text{ or } F_{ij} = \frac{\partial x_i}{\partial X_j} \tag{2.5}$$

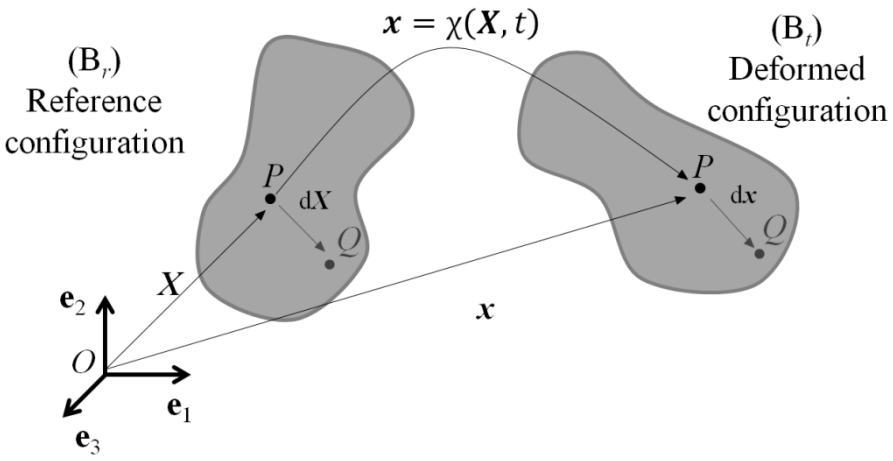

Figure 2-1: Schematic diagram of the transformation of a body $\boldsymbol{B}$ from a reference to a deformed configuration with position vectors $\boldsymbol{X}$ and $\boldsymbol{x}$ at point P.

Volume changes in the body $\boldsymbol{B}$ are quantified by the Jacobian, J, which is expressed in terms of the deformation gradient, $\boldsymbol{F}$, in Equation (2.6), where V_o is the volume of the body $\boldsymbol{B}_r$ in the reference configuration and V is the volume in the deformed configuration $\boldsymbol{B}_t$.

$$J = \det(\boldsymbol{F}) = \frac{d\mathrm{V}}{dV_o} \tag{2.6}$$

The Green-Lagrange strain, $\boldsymbol{E}$, is given by Equation (2.7) where $\boldsymbol{I}$ is the identity tensor with the property $\boldsymbol{F} \cdot \boldsymbol{I} = \boldsymbol{F}$.

$$\boldsymbol{E} = \frac{1}{2}(\boldsymbol{F}^T \cdot \boldsymbol{F} - \boldsymbol{I}) \text{ or } E_{ij} = \frac{1}{2}\left(\frac{\partial u_i}{\partial X_j} + \frac{\partial u_j}{\partial X_i} + \frac{\partial u_k}{\partial X_i}\frac{\partial u_k}{\partial X_j}\right) \tag{2.7}$$

The infinitesimal strain $\boldsymbol{\varepsilon}$ is found by assuming that the product of the infinitesimals in Equation (2.7) is negligible, giving Equation (2.8).

$$\varepsilon_{ij} = \frac{1}{2}\left(\frac{\partial u_i}{\partial X_j} + \frac{\partial u_j}{\partial X_i}\right) \tag{2.8}$$

According to the polar decomposition theorem, the deformation gradient ($\boldsymbol{F}$) can be uniquely decomposed into an orthogonal rotation tensor $\boldsymbol{R}$, symmetric spatial tensor $\boldsymbol{V}$ and material stretch tensor $\boldsymbol{U}$, according to:

$$\boldsymbol{F} = \boldsymbol{R} \cdot \boldsymbol{U} = \boldsymbol{V} \cdot \boldsymbol{R} \tag{2.9}$$

The logarithmic (true) strain, $\boldsymbol{\epsilon}$, is calculated using Equation (2.10) and the eigenvalues of $\boldsymbol{\epsilon}$ are the principal logarithmic strains. Abaqus uses the logarithmic strain for elasticity simulations when the nonlinear geometry option in Abaqus is used.

$$\boldsymbol{\epsilon} = \ln \boldsymbol{V} \tag{2.10}$$

The velocity $\boldsymbol{v}$ of material point *P* is:

$$\boldsymbol{v} = \frac{\partial \boldsymbol{x}}{\partial t} \tag{2.11}$$

where the partial derivative with respect to time means the rate of change of $\boldsymbol{x}$ for fixed $\boldsymbol{X}$. The spatial velocity gradient $\boldsymbol{L}$ is calculated as:

$$\boldsymbol{L} = \frac{\partial \boldsymbol{v}}{\partial \boldsymbol{x}} = \frac{\partial \boldsymbol{v}}{\partial \boldsymbol{X}} \cdot \frac{\partial \boldsymbol{X}}{\partial \boldsymbol{x}} = \frac{\partial \boldsymbol{F}}{\partial t} \cdot \boldsymbol{F}^{-1} = \dot{\boldsymbol{F}} \cdot \boldsymbol{F}^{-1} \tag{2.12}$$

The spatial velocity gradient can be decomposed into the symmetric rate of deformation tensor $\boldsymbol{D}$, Equation (2.13), and the antisymmetric spin tensor $\boldsymbol{W}$, Equation (2.14).

$$\boldsymbol{D} = \frac{\mathbf{1}}{\mathbf{2}}(\boldsymbol{L} + \boldsymbol{L}^T) \tag{2.13}$$

$$\boldsymbol{W} = \frac{\mathbf{1}}{\mathbf{2}}(\boldsymbol{L} - \boldsymbol{L}^T) \tag{2.14}$$

The Cauchy or true stress, $\boldsymbol{\sigma}$, describes the force per unit area on the current configuration. It is a symmetric tensor that can be expressed as a function of the traction, $\boldsymbol{t}$, on a surface in the current configuration and a unit normal vector to the surface, $\boldsymbol{n}$, as depicted in Figure 2-2**:**:

$$\boldsymbol{t} = \boldsymbol{\sigma} \cdot \boldsymbol{n} \tag{2.15}$$

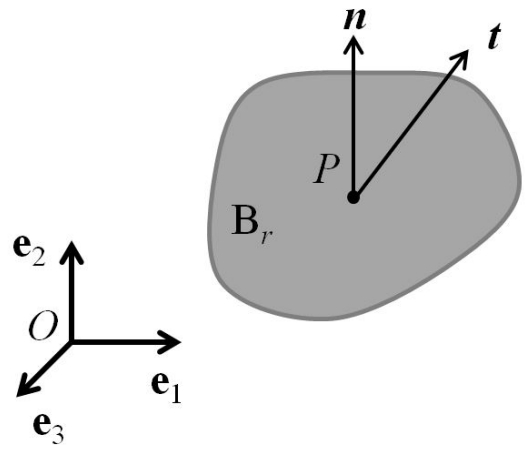

Figure 2-2: Traction vector $\boldsymbol{t}$ at point P on a body $\boldsymbol{B}_r$ in the reference configuration with unit normal $\boldsymbol{n}$.

Cauchy stress can also be expressed as a function of deviatoric stress, $\boldsymbol{S}$, and hydrostatic pressure stress, p, according to Equations (2.16) and (2.17):

$$p = \frac{-\mathrm{Tr}(\boldsymbol{\sigma})}{3} \tag{2.16}$$

$$\boldsymbol{\sigma} = \boldsymbol{S} - p\boldsymbol{I} \tag{2.17}$$

Where $\mathrm{Tr}(\boldsymbol{\sigma}) = \sigma_{ii}$. The von Mises equivalent stress, σ_{VM}, is defined as per Equation (2.18) and can be written in expanded form as per Equation (2.19):

$$\sigma_{\mathrm{VM}} = \sqrt{\frac{2}{3} S_{ij} S_{ij}} \tag{2.18}$$

$$\sigma_{\mathrm{VM}} = \sqrt{\frac{1}{2}[(\sigma_{11} - \sigma_{22})^2 + (\sigma_{22} - \sigma_{33})^2 + (\sigma_{33} - \sigma_{11})^2] + 3(\tau_{12}^2 + \tau_{23}^2 + \tau_{31}^2)} \tag{2.19}$$

The eigenvalues of the Cauchy stress tensor are the principal stresses. Finally, the nominal stress, $\tilde{\boldsymbol{\sigma}}$, is defined as:

$$\tilde{\boldsymbol{\sigma}} = J\boldsymbol{F}^{-1}\boldsymbol{\sigma} \tag{2.20}$$

2.2.3 Material Constitutive Behaviour

Isotropic linear elasticity is assumed for a number for the FE simulations presented in this thesis. In isotropic linear elasticity the nominal stress, $\tilde{\boldsymbol{\sigma}}$, is related to the infinitesimal strain $\boldsymbol{\varepsilon}$ through:

$$\tilde{\sigma}_{ij} = \lambda \varepsilon_{kk} \delta_{ij} + 2\mu \varepsilon_{ij} \tag{2.21}$$

where λ and μ are the Lamé constants and δ_{ij} is the Kronecker delta, with the property:

$$\delta_{ij} = \begin{cases} 1 & i = j \\ 0 & i \neq j \end{cases} \tag{2.22}$$

Under the assumptions of infinitesimal deformation kinematics, stress measures become equal giving $\boldsymbol{\sigma} = \tilde{\boldsymbol{\sigma}}$, yielding:

$$\sigma_{ij} = \lambda \varepsilon_{kk} \delta_{ij} + 2\mu \varepsilon_{ij} \tag{2.23}$$

The Lamé constants can be derived from Young's Modulus, E, and Poisson's Ratio, v, through:

$$\mu = \frac{E}{2(1+\nu)} \text{ and } \lambda = \frac{\nu E}{(1+\nu)(1-2\nu)} \tag{2.24}$$

A fourth order tensor of elastic modulus, $\boldsymbol{K}$, is defined such that:

$$\boldsymbol{\sigma} = \boldsymbol{K} : \boldsymbol{\varepsilon} \text{ or } \sigma_{ij} = K_{ijk} \varepsilon_{kl} \tag{2.25}$$

The stress, $\boldsymbol{\sigma}$, and strain, $\boldsymbol{\varepsilon}$, can each be written in matrix/vector form using Equation (2.26), where the engineering shear strains, γ_{ij}, are defined as per Equation (2.27).

$$\boldsymbol{\sigma} = \begin{bmatrix} \sigma_{11} \\ \sigma_{22} \\ \sigma_{33} \\ \sigma_{12} \\ \sigma_{23} \\ \sigma_{31} \end{bmatrix}; \boldsymbol{\varepsilon} = \begin{bmatrix} \varepsilon_{11} \\ \varepsilon_{22} \\ \varepsilon_{33} \\ \gamma_{12} \\ \gamma_{23} \\ \gamma_{31} \end{bmatrix} \tag{2.26}$$

$$\gamma_{ij} = \varepsilon_{ij} + \varepsilon_{ji} \tag{2.27}$$

Using matrix/vector notation and applying the Kronecker delta function, the relationship linking stress and strain in an isotropic linear elastic material can be written as a function of E and v giving Equation (2.28), or equivalently as Equation (2.29) where $\widetilde{\boldsymbol{D}}$ is the material stiffness matrix (Equation (2.30)).

$$\begin{bmatrix}\sigma_{11}\\ \sigma_{22}\\ \sigma_{33}\\ \sigma_{12}\\ \sigma_{23}\\ \sigma_{31}\end{bmatrix} = \frac{E}{(1+v)(1-2v)}\begin{bmatrix}1-v & v & v & 0 & 0 & 0\\ v & 1-v & v & 0 & 0 & 0\\ v & v & 1-v & 0 & 0 & 0\\ 0 & 0 & 0 & \frac{1-v}{2} & 0 & 0\\ 0 & 0 & 0 & 0 & \frac{1-2v}{2} & 0\\ 0 & 0 & 0 & 0 & 0 & \frac{1-2v}{2}\end{bmatrix}\begin{bmatrix}\varepsilon_{11}\\ \varepsilon_{22}\\ \varepsilon_{33}\\ \gamma_{12}\\ \gamma_{23}\\ \gamma_{31}\end{bmatrix} \tag{2.28}$$

$$\boldsymbol{\sigma} = \widetilde{\boldsymbol{D}}\boldsymbol{\varepsilon} \tag{2.29}$$

$$\widetilde{\boldsymbol{D}} = \frac{E}{(1+v)(1-2v)}\begin{bmatrix}1-v & v & v & 0 & 0 & 0\\ v & 1-v & v & 0 & 0 & 0\\ v & v & 1-v & 0 & 0 & 0\\ 0 & 0 & 0 & \frac{1-v}{2} & 0 & 0\\ 0 & 0 & 0 & 0 & \frac{1-2v}{2} & 0\\ 0 & 0 & 0 & 0 & 0 & \frac{1-2v}{2}\end{bmatrix} \tag{2.30}$$

In general, the strain energy density potential, U, can be related to the Cauchy stress, $\boldsymbol{\sigma}$, as follows:

$$\boldsymbol{\sigma} = \frac{1}{J}\boldsymbol{F}.\frac{\partial U(\boldsymbol{F})}{\partial \boldsymbol{F}} \tag{2.31}$$

The total strain energy for linear elastic materials can be developed from Equation (2.31), and can be integrated over a volume, V, to give Equation (2.32).

$$U = \frac{1}{2}\int_V \boldsymbol{\sigma}^T \boldsymbol{\varepsilon}\, dV \tag{2.32}$$

and in expanded form as Equation (2.33).

$$U = \frac{1}{2}\int_V \{\sigma_{11}\varepsilon_{11} + \sigma_{22}\varepsilon_{22} + \sigma_{33}\varepsilon_{33} + \sigma_{12}\gamma_{12} + \sigma_{23}\gamma_{23} + \sigma_{31}\gamma_{31}\}\, dV \tag{2.33}$$

The incremental strain energy, dU, for a cuboidal element with volume dV can then be written as:

$$dU = \frac{1}{2}\{\sigma_{11}\varepsilon_{11} + \sigma_{22}\varepsilon_{22} + \sigma_{33}\varepsilon_{33} + \sigma_{12}\gamma_{12} + \sigma_{23}\gamma_{23} + \sigma_{31}\gamma_{31}\}dV \tag{2.34}$$

This form of strain energy is employed for the calculation of effective isotropic linear elastic constants from the results of the micromechanical modelling of segments of material in Chapters 3 and 4.

In some of the FE simulations in this thesis isotropic elasticity theory is implemented in a finite deformation kinematic framework by using Cauchy stress, $\boldsymbol{\sigma}$, and logarithmic strain, $\boldsymbol{\epsilon}$, in place of the infinitesimal measures used in Equation (2.21), as defined in the Abaqus Theory Manual (DS SIMULIA, USA). This is done to allow for the more accurate accounting of large strains, should they occur locally in models of inhomogeneous multiphase material microstructures, as are of interest in

this work. This is the approach taken in the modelling in Chapters 3 and 4. While formally the more correct assumption for capturing local strain effects, given the low macroscopically applied strains (1%) in these simulations, the differences between the use of the finite deformation assumption and the simpler infinitesimal deformation assumption are found to be negligible for the cases considered in this thesis.

2.2.4 Estimating the Elastic Modulus of Multi-Phase Materials

The material of specific interest in this thesis is essentially a poro-elastic composite material. Under the assumption of infinitesimal deformation kinematics is it useful to generate estimates of the overall effective elastic modulus of the material. This can be done on a straightforward basis using the rule of mixtures and considering a number of different phase arrangements as follows.

In the first case, the material is assumed to consist of two phases, with Young's moduli E_1 and E_2, respectively, where the phases are arranged parallel to the direction of loading as shown in Figure 2-3(A). The volume fraction of phase 2 is v_f. In this case the overall elastic modulus in the loading direction, under the assumption of uniform strain, can be expressed as:

$$E_{eff} = \left(1 - v_f\right)E_1 + v_f E_2 \tag{2.35}$$

As a development of this, porosity with a volume fraction of $v_p$can be assumed, corresponding to the confuguration shown in Figure 2-3(B). In this case, one as the following:

$$E_{eff} = \left(1 - v_f - v_p\right)E_1 + v_f E_2 + v_p E_{pore} \tag{2.36}$$

As $E_{pore} = 0$, this gives:

$$E_{eff} = \left(1 - v_f - v_p\right)E_1 + v_f E_2 \tag{2.37}$$

Alterntively, the phases can be arranged perpendicular to the loading direction as shown in Figure 2-3(C) for the two-phase case under niform stress loading. One can establish that:

$$E_{eff} = \frac{E_1 E_2}{\left(1 - v_f\right)E_1 + v_f E_2} \tag{2.38}$$

Finally, in this extreme case, if the porosity is introduced in the loading direction (Figure 2-3(D)) an overall effective modulus of zero is generated. As this is not necessarily representative of a realistic scenario, an alternative material configuration is shown in Figure 2-4.

Here, $\overline{E_2}$ can be described by Equation (2.47), and by Equation (2.48) as $E_{pore} = 0$.

$$\overline{E_2} = \left(1 - v_p\right)E_2 + v_p E_{pore} \tag{2.39}$$

$$\overline{E_2} = \left(1 - v_p\right)E_2 \tag{2.40}$$

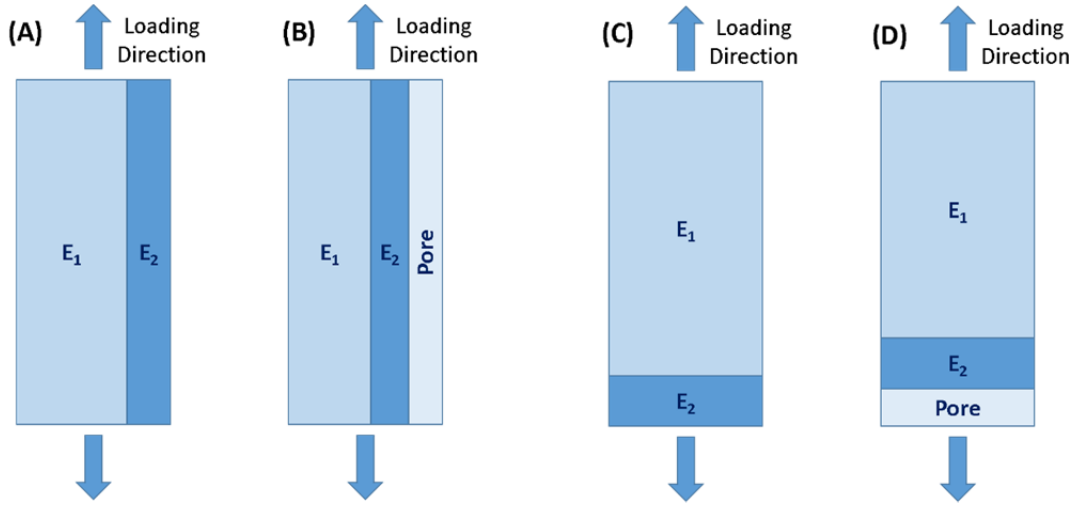

Figure 2-3: Four possible material configuration arrangements for idealised multiphase materials as considered in Section 2.2.4.

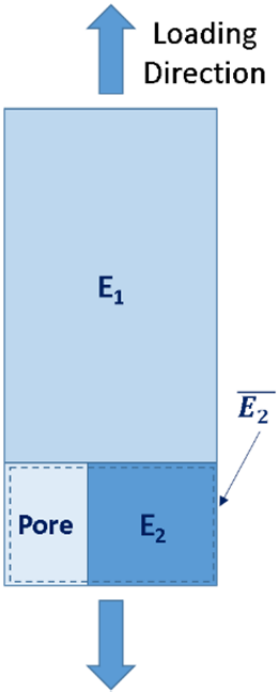

Figure 2-4: Alternative material configuration for the case of porosity perpendicular to the loading direction (i.e. Figure 2-3(D)) for idealised multiphase materials as considered in Section 2.2.4. Here, $\overline{E_2}$ is the effective elastic modulus of the region indicated by a dotted line.

Following this, the value of E_{eff} for this material configuration can be described by Equation(2.49), and following this as Equation (2.50).

$$E_{eff} = \frac{E_1 \overline{E_2}}{(1 - v_f - v_p)E_1 + (v_f + v_p)\overline{E_2}} \tag{2.41}$$

$$E_{eff} = \frac{E_1(1 - v_p)E_2}{(1 - v_f - v_p)E_1 + (v_f + v_p)(1 - v_p)E_2} \tag{2.42}$$

These estimates are invoked in Chapters 3 and 4 of this work.

2.3 Numerical Implementation for the Deformation of Solids

2.3.1 Equilibrium Equations and Principle of Virtual Work

The balance of linear momentum for a deformable body can be expressed as:

$$\frac{\partial \sigma_{ij}}{\partial x_i} = \rho \frac{\partial v_i}{\partial t} = \rho \dot{v}_i = \rho \ddot{u}_i \tag{2.43}$$

where ρ_0 is the density in the reference configuration, $\rho = J^{-1}\rho_0$, and $\ddot{u}$ is the acceleration. As $\boldsymbol{\sigma}$ is symmetric, Equation (2.43) can be written in tensor notation as:

$$\nabla \cdot \boldsymbol{\sigma} = \rho \frac{\partial \boldsymbol{v}}{\partial t} = \rho \dot{\boldsymbol{v}} = \rho \ddot{\boldsymbol{u}} \tag{2.44}$$

These equations can be solved through the application of appropriate boundary conditions and initial conditions. These equations are solved using FEM by expressing them through the principle of virtual work which can be expressed in rate form as:

$$\delta W = \int_V (\nabla \cdot \boldsymbol{\sigma} - \rho \ddot{\boldsymbol{u}}) \cdot \delta \boldsymbol{v} \, dV = 0 \tag{2.45}$$

where δW is the virtual work rate per unit volume, $\delta \boldsymbol{v}$ is a virtual velocity field which satisfies the kinematic boundary conditions of the problem and V is the volume of the body $\boldsymbol{B}$. This can also be expressed as shown in Equation (2.46)

$$\int_V \boldsymbol{\sigma} : \delta \boldsymbol{D} \delta V = \int_{\partial V} \boldsymbol{t} \cdot \delta \boldsymbol{v} \, d\partial V - \int_V \rho \ddot{\boldsymbol{u}} \cdot \delta \boldsymbol{v} \, dV \tag{2.46}$$

where $\boldsymbol{\sigma} : \delta \boldsymbol{D} = \sigma_{ij} : \delta D_{ij}$ and ∂V is the surface bounding the volume V. This equation is approximated and solved using the FEM as discussed below in Section 2.3.2.

2.3.2 The Finite Element Method

In the finite element method, a solid body $\boldsymbol{B}$ is divided into subsections called elements which are connected together at nodes (i.e. a finite element mesh), as per Figure 2-5, in order to solve boundary value problems (BVP). The governing constitutive equations, which are calculated for each discrete element, assemble to form a system equation to describe the behaviour in the material body as a whole. By applying boundary conditions to the system of equations, the stress and strain can be calculated for each element.

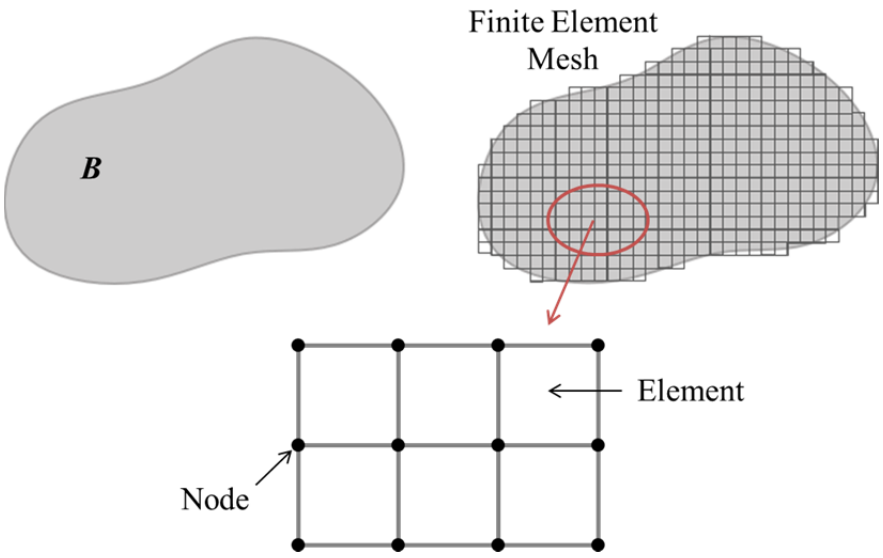

Figure 2-5: Discretization of a region ***B*** into a number of finite elements.

For FE purposes it is useful to rewrite the principal of virtual work (Equation (2.46)) in matrix/vector notation as follows:

$$\int_V \delta \boldsymbol{D}^T \boldsymbol{\sigma} dV = \int_{\partial V} \delta \boldsymbol{v}^T \boldsymbol{t}\, d\partial V - \int_V \delta \boldsymbol{v}^T \rho \ddot{\boldsymbol{u}}\, dV \tag{2.47}$$

For the present application, quasi-static deformation is all that is of interest, hence the dynamic term can be dropped yielding:

$$\int_V \delta \boldsymbol{D}^T \boldsymbol{\sigma} dV = \int_{\partial V} \delta \boldsymbol{v}^T \boldsymbol{t}\, d\partial V \tag{2.48}$$

For each element, e, in the finite element mesh the following interpolation holds true:

$$\delta \boldsymbol{D} = \boldsymbol{B}_{(e)} \delta \boldsymbol{v}_{(e)} \tag{2.49}$$

$$\delta \boldsymbol{v} = \boldsymbol{N}_{(e)} \delta \boldsymbol{v}_{(e)} \tag{2.50}$$

where $\delta \boldsymbol{v}_{(e)}$ is a column vector of element nodal virtual velocities, $\boldsymbol{N}_{(e)}$ is the element shape function matrix and $\boldsymbol{B}_{(e)}$ is the element shape function gradient matrix. The FE approximation of the principle of virtual work can then be assembled as follows:

$$\sum_e \int_{V_{(e)}} \delta \boldsymbol{v}_{(e)}^T \boldsymbol{B}_{(e)}^T \boldsymbol{\sigma} dV = \sum_e \int_{\partial V_{(e)}} \delta \boldsymbol{v}_{(e)}^T \boldsymbol{N}_{(e)}^T \boldsymbol{t} \, d\partial V \tag{2.51}$$

where the summation is over all elements e in the finite element mesh. The summation (assembling element quantities into global quantities) is performed to yield the following global expression:

$$\int_V \boldsymbol{B}^T \boldsymbol{\sigma} dV = \int_{\partial V} \boldsymbol{N}^T \boldsymbol{t} \, d\partial V \tag{2.52}$$

In general for the solution of BVPs (both linear and nonlinear) the out of balance force vector, $\boldsymbol{G}$, can be expressed as follows:

$$\boldsymbol{G}(\boldsymbol{u}) = \int_V \boldsymbol{B}^T(\boldsymbol{u}) \boldsymbol{\sigma}(\boldsymbol{u}) dV - \int_{\partial V} \boldsymbol{N}^T(\boldsymbol{u}) \boldsymbol{t} \, d\partial V \tag{2.53}$$

where $\boldsymbol{u}$ is now the global nodal displacement vector for the mesh. To solve the BVP it is necessary to determine $\boldsymbol{u}$ such that Equation (2.54) is true at any point in time t.

$$\boldsymbol{G}(\boldsymbol{u}) = 0 \tag{2.54}$$

Dropping the $\boldsymbol{u}$ dependence for convenience, one can say:

$$\boldsymbol{G} = \int_V \boldsymbol{B}^T \boldsymbol{\sigma} dV - \int_{\partial V} \boldsymbol{N}^T \boldsymbol{t}\, d\partial V = 0 \tag{2.55}$$

The Abaqus/Standard implicit solver takes an incremental approach to the solution of quasi-static problems, and uses the Newton-Raphson iterative method to ensure that Equation (2.55) is solved at the end of each time increment Δt. Specifically, if t is the time at the start of the current increment, then the Newton-Raphson formula for iteration states that:

$$\boldsymbol{u}_{n+1}^{t+\Delta t} = \boldsymbol{u}_n^{t+\Delta t} - \left[\frac{\partial \boldsymbol{G}(\boldsymbol{u}_n^{t+\Delta t})}{\partial \boldsymbol{u}}\right]^{-1} \cdot \boldsymbol{G}(\boldsymbol{u}_n^{t+\Delta t}) \tag{2.56}$$

where $\boldsymbol{u}_n^{t+\Delta t}$ is the current estimate of the nodal displacement vector at time $t+\Delta t$ and $\boldsymbol{u}_{n+1}^{t+\Delta t}$ is the improved estimate after the n^{th} iteration. Iterations proceed until convergence in the incremental solution is achieved. This method requires the determination and inversion of the Jacobian matrix, $\frac{\partial \boldsymbol{G}(\boldsymbol{u}_n^{t+\Delta t})}{\partial \boldsymbol{u}}$, to obtain each approximation. This incremental and iterative approach over the course of the deformation history provides equilibrium at the end of each time step.

2.4 References

Belytschko, T., Liu, W. and Moran, B. 2000. *Nonlinear Finite Elements for Continua and Structures.* Chichester New York: Wiley.

Malvern, L. 1969. *Introduction to the Mechanics of a Continuous Medium.* Englewood Cliffs, N.J.: Prentice- Hall.

3 Predicting the Elastic Properties of Selective Laser Sintered PCL/β-TCP Materials.

3.1 Chapter Summary

The aim of this chapter is to assess the ability of FE models to capture the mechanical behaviour of individual 50/50wt% poly-ε-caprolactone (PCL)/β-tricalcium phosphate (β-TCP) struts fabricated using selective laser sintering (SLS). The tensile elastic modulus of single struts is determined experimentally. Tensile loading simulations using high resolution meshes generated from μ-CT scans are carried out with three material assignment methods: (1) homogeneous PCL elastic constants, (2) composite PCL/β-TCP elastic constants based on rule of mixtures, and (3) heterogeneous distribution of micromechanically-determined elastic constants. The ability of each model to capture the experimentally evaluated strut modulus is evaluated. The results presented in this chapter indicate that the multi-scale approach of linking micromechanical modelling of the sintered scaffold material with macro-scale modelling gives an accurate prediction of the mechanical behaviour of the sintered structure.

3.2 Introduction

The purpose of bone tissue engineering scaffolds is to fill defects and support mechanical loading while providing a template on which new bone will form. The remodelling of native bone in response to mechanical loading occurs when cells convert mechanical stimuli to chemical signals to direct the formation of new tissue or resorption through mechanotransduction (Di Palma et al. 2005; Liedert et al. 2006). The mechanical stimuli that influence bone formation *in vivo* are a combination of both fluid shear over the cells (Vance et al. 2005; Melchels et al. 2011) and mechanical loading of the cells (Guldberg et al. 1997; Koike et al. 2005; Willie et al. 2010), therefore it is important to be able to accurately predict the mechanical behaviour of bone tissue engineering scaffolds.

In this study, the focus is on bone scaffold material fabricated from PCL and β-TCP using SLS. While there is debate over whether soft or stiff scaffolds are more suitable for bone formation *in vivo*, here the case of relatively stiff scaffolds is considered, for application in bridging critical sized defects in large bones (Lohfeld et al. 2010) that require the scaffold to support high levels of mechanical loading. The accurate knowledge and prediction of the overall mechanical properties, in particular the overall elastic modulus of the scaffold, is of considerable importance to the scaffold developer, and is the primary focus of the present work.

Similar PCL/β-TCP scaffolds for bone tissue engineering applications have been fabricated with varying volume fractions (Lohfeld et al. 2012). An advantage of SLS is the high degree of repeatability and conformity of the scaffold to the original 3D CAD design on the macro-scale compared to the relatively random distribution of

pores in scaffolds fabricated using, for example, salt leaching (Wu et al. 2012; Chatterjee et al. 2010; Sabir et al. 2009; Lee et al. 2006). However, this type of scaffold material is inhomogeneous at the micro-scale level with the inclusion of micropores and β-TCP particles (Lohfeld et al. 2012). Previous studies using simple 3D CAD geometries have been insufficient to capture the mechanical behaviour of this type of SLS-fabricated scaffolds using finite element modelling (Williams et al. 2005; Cahill et al. 2009). The use of elastic modulus values that are fitted to experimental results in CAD-generated FE modelling of scaffolds has shown improved predictions of scaffold stiffness, (Lohfeld et al. 2014), however the fitting method that was used results in FE models that are not representative of the real material microstructures. By their nature, CAD models account for only the designed scaffold macroporosity and do not account for microporosity within the scaffold structure or surface roughness that are present due to the fabrication process. High resolution finite element meshes have been successfully generated from μ-CT scans in order to avoid the over-simplifications required with CAD model geometries giving accurate model geometries of real bone tissue engineering scaffold geometries (Sandino and Lacroix 2011) and native bone tissue (Liebschner et al. 2005).

Micromechanics approaches to evaluate the mechanical properties of particle-reinforced composites traditionally use idealised microstructures based on the particle distribution and are often modelled under periodic boundary conditions (Chan et al. 2010). This approach has been used to determine the bulk mechanical properties of a PCL/hydroxyapatite (HA) SLS scaffold (Eshraghi and Das 2012). Methods such as this require assumptions and simplifications regarding microstructural geometry, particle distribution and particle size distribution. In the

case where high resolution images of the real material microstructure are available, effective properties for the material microstructure can be evaluated using uniform boundary conditions (Hazanov 1998) which are implemented by imposing either uniform stress or strain conditions on the surfaces of a microstructural unit segment. This approach has been applied to a range of applications including random heterogeneous materials (Kanit and Forest 2003), cancellous bone (Pahr and Zysset 2008) and silicon carbide fibre reinforced composites (Chateau et al. 2010). The effective properties of particle reinforced composites have also been explored (Galli et al. 2008; Kanit et al. 2006); however the mechanical properties of the particular sintered material of interest here have not yet been explored using this method.

The primary aim of this study is to develop a method to accurately model the realistic mechanical behaviour of a sintered PCL/β-TCP scaffold material. To achieve this, high-resolution finite element modelling of the material samples is used. A range of methods is then explored to determine the most appropriate and most practical way to assign the mechanical properties in the high resolution models, specifically the elastic constants. In particular, micromechanical modelling approaches are employed to determine appropriate elastic constants. Comparisons are made with the predictions of simpler approaches and recommendations are made on how best to determine elastic properties for such complex materials.

3.3 Methods

3.3.1 Materials and Fabrication

Materials

PCL powder (CAPA6506, Solvay, UK) with an average molecular weight (Mn) of 60,000 Da and a particle size of 600 μm was cryogenically ground to a maximum particle size of 50 μm. β-TCP (Fluka) with a molecular weight of 310.18 g/mol and a particle size of 3-5 μm was mixed with the PCL powder in a 50/50 wt% ratio (approximately 25 vol% β-TCP) using a hand mixer for five minutes until well blended.

Pure PCL Tensile Samples

Rectangular bars of pure PCL with rectangular cross section were fabricated using vacuum moulding for characterisation of the mechanical properties of PCL, with a specimen design based on type V of ASTM D638. A rectangular bar geometry was used as machining the material to a dog bone shape would have run the risk of exceeding the melt temperature of PCL. Stainless steel moulds with well dimensions 50 x 10 x 15 mm were filled with 3 g of PCL powder. The filled moulds were placed in an oven at 120°C under a vacuum for 5 hours to remove any air bubbles and allowed to cool. The solid samples were then removed from the moulds and cut to 3 mm thickness to give a uniform cross-section of 3 x 10 mm.

Single Scaffold Struts

Single bone tissue engineering scaffold struts were fabricated in ladders of 10 struts from the mixed PCL and β-TCP powders by SLS with the Sinterstation 2500^{plus} system (DTM, USA). These struts were designed to have the same dimensions as the individual scaffold struts in the PCL/β-TCP scaffolds used in Lohfeld et al. (Lohfeld et al. 2010) and were manufactured using the same laser scan process as for struts in the scaffold. The dimensions of each individual strut are approximately 13 mm length with an approximately rectangular cross section of 0.77 mm x 0.55 mm. In order to achieve this relatively small strut thickness in a scaffold with relatively small overall dimensions, the "outline scan" fabrication method was employed (Lohfeld et al. 2010). A laser power of 7 W was used, and the part bed heater was held at 49°C during fabrication. The build was paused for two minutes during heating up to 49°C to allow the powder to reach a uniform temperature prior to sintering. The nitrogen supply to the chamber was turned off, as it is not required for the materials being sintered. The powder layer thickness was set to 0.11 mm. A total of 16 strut ladders were fabricated in a single fabrication run. An example of a strut ladder is shown in Figure 3.1(a). Following the build, the parts were left to cool in the machine part bed overnight and excess powder was removed using pressurised air.

3.3.2 Structural and Morphological Characterisation

Prior to mechanical testing, high resolution scans of 40 single scaffold struts were obtained using a μ-CT scanner (SkyScan-1072 High-resolution desk-top μ-CT system, University of Aberdeen, UK) at a resolution of approximately 14.4 μm.

Higher resolution images of a small segment of a scaffold strut (approximate dimensions 0.77 mm x 0.1 mm x 0.1 mm) were obtained using X-ray microtomography (XMT) (phoenix nanotom®, GE, at SEAM, Waterford Institute of Technology, Ireland) with a scan resolution of 1.2 μm. Scaffolds were cut into 3 mm thick sections using a backed blade, mounted on a coupon and gold-coated before imaging using a Hitachi S-4700 scanning electron microscope (SEM) (Hitachi, UK) at a power of 15 kV. SEM images of the material microstructure are shown in Figure 3.1(b) and (c). The presence of both partially sintered and fully sintered regions of material are visible in Figure 3.1(b), where partial sintering results in regions of porous material that will influence the overall mechanical behaviour of the scaffold material. The smaller β-TCP particles can be seen on the larger PCL particles in Figure 3.1(c).

The macro-scale porosity of each full strut sample was calculated from the μ-CT scans using MIMICS (Materialise, Belgium). A rectangular segment with dimensions 10 x 0.7 x 0.5 mm was selected within the centre of each strut, in order to select the most solid region of the strut and to exclude the effects of surface roughness. An example of the region selected for porosity analysis is shown in Figure 3.2. Porosity (%) was calculated as pore volume / total segment volume x 100.

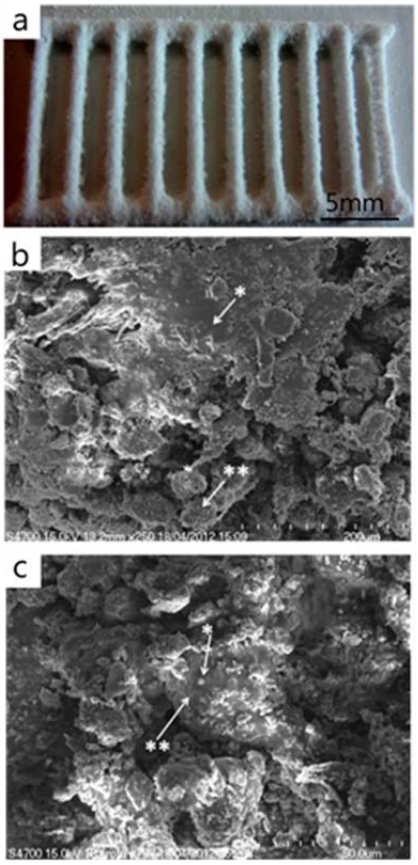

Figure 3.1: Selective laser sintered strut ladder (a).SEM images of the PCL/β-TCP scaffolds showing areas of fully sintered material (*) and partially sintered material (**) (b). A higher magnification image (c) shows β-TCP (*) and PCL (**).

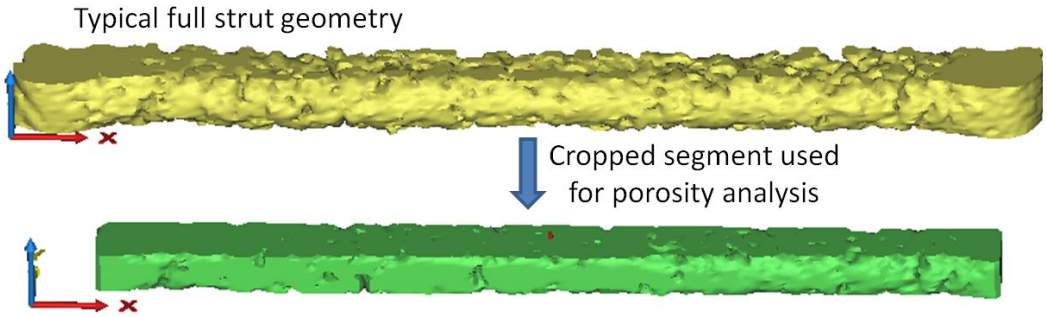

Figure 3.2: A typical full strut geometry is shown in yellow (above). The region selected for porosity analysis is shown in green below.

3.3.3 Mechanical Characterisation

Pure PCL Samples

Tensile tests were carried out on the pure PCL samples at room temperature using an Instron Series IX 4467 screw-driven testing system as per ISO 527-1 (ISO 2012), at a strain rate of 1% of the gauge length per minute. The initial gauge length was set to 20 mm, with 15 mm at each end held in the grips. The width (w) and thickness (t) of each sample were measured using a vernier callipers prior to testing and the original cross sectional area (CSA) was calculated as $CSA = w*t$. The force (F) and change in gauge length were recorded. Uniaxial tensile engineering stress was calculated as per Equation (3.1) where A is the original CSA. The elastic modulus (E_{PCL}) was calculated as per Equation (3.2), where σ_a is the stress at ε_a and σ_b is the stress at ε_b, where ε is the tensile engineering strain and both ε_a and ε_b are taken in the initial linear region of the tensile curves for the material, in accordance with ISO 527-1.

$$\sigma = \frac{F}{A} \tag{3.1}$$

$$E_{\mathrm{PCL}} = \frac{\sigma}{\varepsilon} = \frac{\sigma_{\mathrm{b}} - \sigma_{\mathrm{a}}}{\varepsilon_{\mathrm{b}} - \varepsilon_{\mathrm{a}}} \tag{3.2}$$

Single Strut Tensile Samples

The mechanical properties of the individual scaffold struts were characterised through tensile testing. Compression testing would not have been practical due to a tendency towards buckling (as verified by some initial trials), a consequence of the

sample geometry selected. Tensile test specimens were cut from the SLS PCL/β-TCP strut ladders (Figure 3.1(a)) using a blade. As the struts are porous and delicate with a relatively low stiffness, they could not be held directly in machine grips for tensile testing without permanently damaging the test sample when tightening the grips. In order to overcome this problem, they were glued to a stiffer material for testing using the process illustrated in Figure 3.3. Small plastic tubes with an outer diameter of 2.5 mm and wall thickness of 0.4 mm and a length of 10 mm were used for this purpose. A cyanoacrylate adhesive (Loctite® Power Easy™) was then injected inside the tube using a syringe to fill the cavity (Figure 3.3). Conventional superglues are soaked up by the struts due to their porous nature whereas this glue has a higher viscosity which prevents this and also allows for easier manipulation of the samples. Each end of the strut was then carefully positioned with approximately 2 mm of the strut length in contact with the glue inside the tube. This assembly was allowed to set for 3 hours before repeating to position a tube on the remaining end of the strut. As alignment of the samples with the tensile axis during testing is critical, a plastic alignment guide consisting of a piece of thin plastic folded at an angle was used to align the tubes and the struts during the bonding process as shown in Figure 3.3. The full assembly was allowed to set overnight prior to mechanical testing. Uniaxial tensile tests were carried out at room temperature on a Zwick biaxial testing machine as per ISO 527-1, at a strain rate of 1% of the gauge length per minute. Strain was measured using a calibrated video extensometer camera. The average gauge length for samples tested was 6.994 mm ± 0.766 mm and dimensions were measured prior to testing using the video extensometer camera. Nominal strain and tensile elastic modulus were calculated as per ISO 527-1, as outlined above.

3.3.4 Finite Element Analysis of Full Struts

High resolution FE models of the full scaffold struts were generated from μ-CT scans with a resolution of approximately 14.4 μm. These images were manipulated to reduce the spatial resolution to an element length of 28.8 μm to reduce the computational cost of running the models. The mesh module in MIMICS was used to convert the μ-CT scan images to a high resolution FE mesh with 8-noded hexahedral voxel elements. Reduced integration was used for each strut model with the nonlinear geometry option selected. Meshes were generated for four individual struts and tensile tests of each scaffold strut were simulated to replicate the experimental test set-up, as illustrated in Figure 3.4.

A total of four strut geometries were used for these full strut simulations in order to maintain consistency; all struts were fabricated in the same batch and within the same powder layers within the part bed, and μ-CT scanning of these four struts was carried out in one scan. The FE mesh of each strut used in these simulations is shown in Figure 3.5 (A), with mesh size ranging from 196,541 to 216,103 elements. A cross-sectional view of a typical strut is shown in Figure 3.5 (B), where heterogeneous elastic property assignment (for the case described in Section 3.3.4.3 only) and the porous strut microstructure can be seen. The same four mesh geometries are used for each set of simulations, the only difference between each set of simulations is the material properties that are assigned to each element in the full strut model. For the first two cases (see Section 3.3.4.1 and Section 3.3.4.2) homogeneous elastic properties are assigned, while in the third case (see Section 3.3.4.3) heterogeneous elastic properties are assigned. The external nodes of the

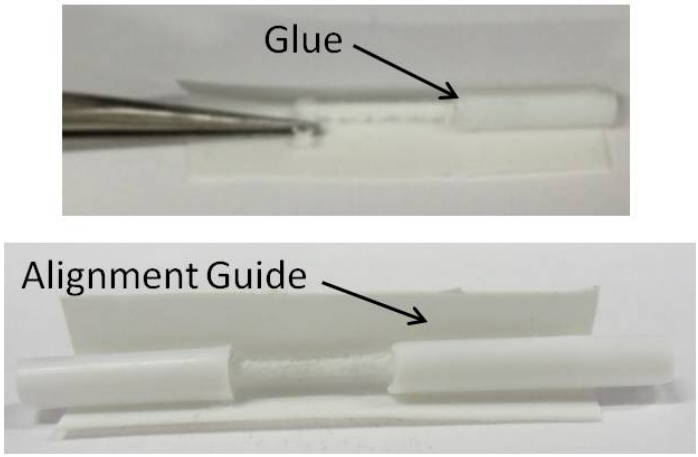

Figure 3.3: Preparation of tensile test specimens from single struts.

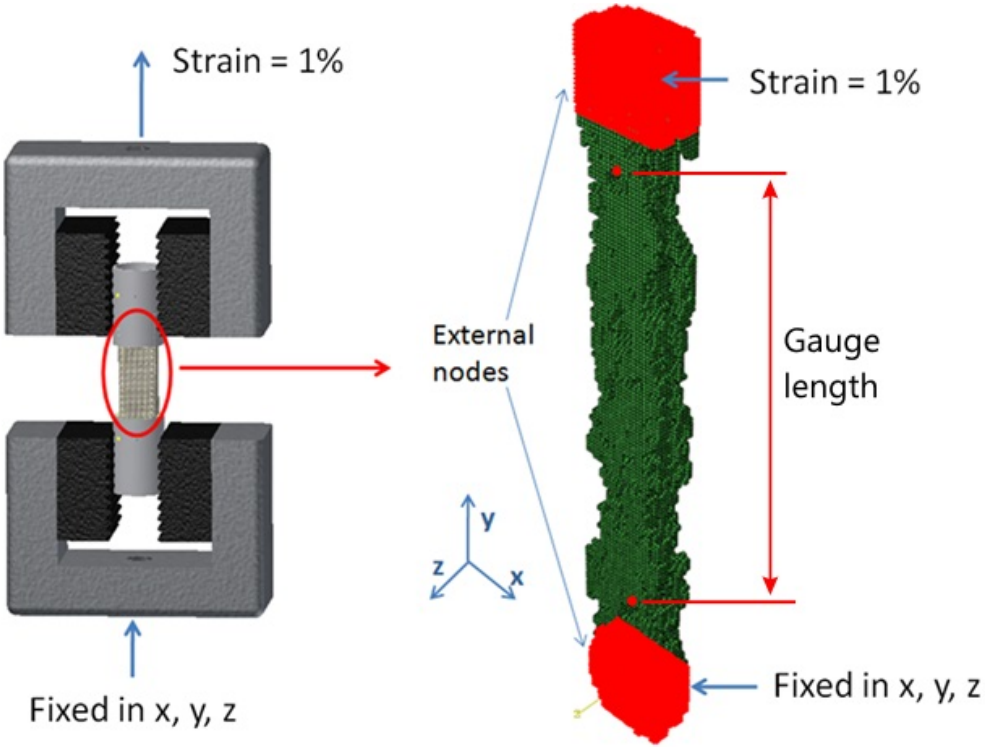

Figure 3.4: Schematic diagram of tensile test set-up for single strut testing (left) and finite element model set-up for strut tensile test simulation (right).

lower 2 mm of the strut were fixed in the 1-, 2- and 3-directions while an equation constraint was applied to the external nodes of the upper 2 mm of the strut to constrain their movement in all directions to a controlling node. A tensile

displacement of 1% of the gauge length was then applied to the controlling node. In order to calculate strain in the gauge length in a comparable method to that used by the video extensometer software in the actual tensile tests, two nodes were selected at the same distance apart as the initial gauge length used by the video extensometer. Nominal strain was then measured by calculating the change in distance between these two nodes during the simulation and dividing by the original gauge length. Stress was calculated as the reaction force at the controlling node divided by the average cross-section area, and the effective strut modulus was calculated as per Section 3.3.3.

In all cases isotropic linear elastic constants were used. Three different methods for determining the elastic modulus were employed as described below. Abaqus/Standard V6.10 (DS SIMULIA, USA) was used for the FE simulations with the NLGEOM option selected to account for large deformations should they occur locally in the material. Mesh sizes ranged between 196,541 and 216,103 elements.

3.3.4.1 PCL Models

It was anticipated that the material properties of the PCL component would dominate the mechanical behaviour of the material as the SEM images indicated that it acts as a matrix to bind the materials together, as sintering is carried out above the melt temperature of PCL but below the melt temperature of β-TCP. Therefore, the first type of material assignment used was *homogeneous assignment* of isotropic linear elastic properties of PCL: v = 0.3 (Eshraghi and Das 2010), and E_{PCL} determined from pure PCL tensile testing. It should be noted that this method is not representative of the real material and is only intended as a comparison.

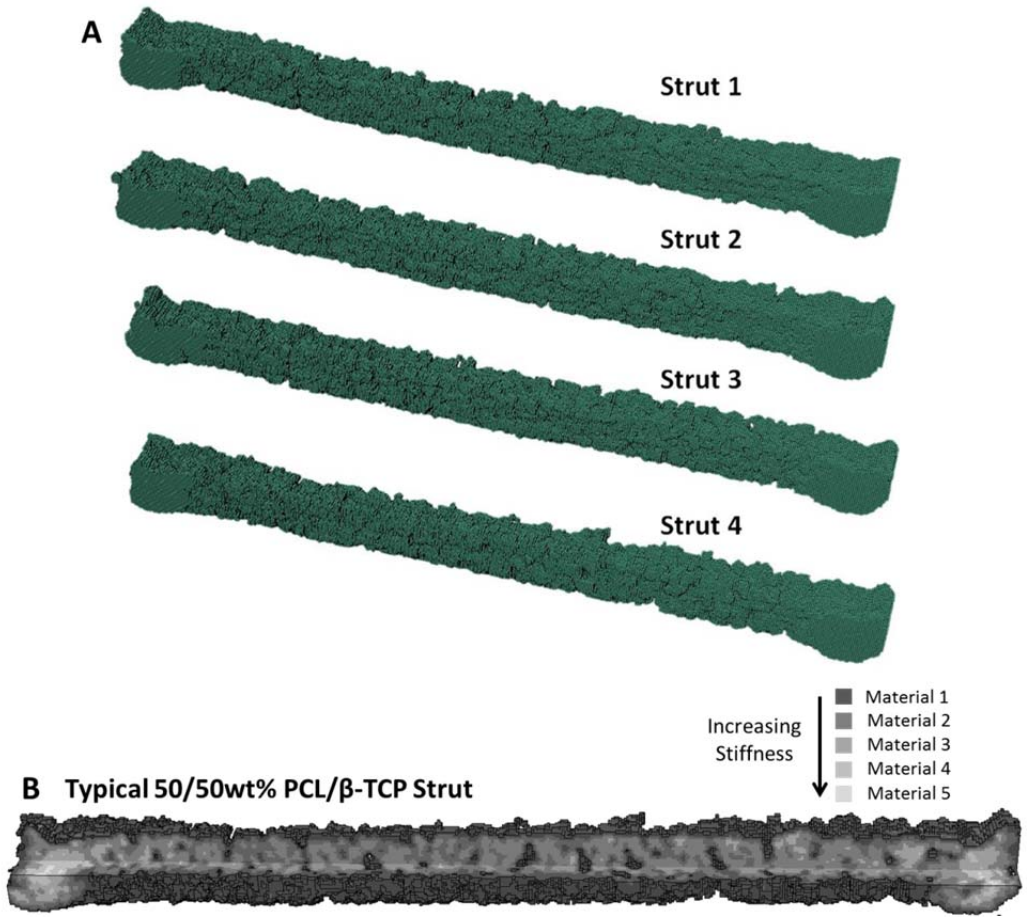

Figure 3.5: (A) FE meshes of each of the four scaffold struts used in full strut simulations. Mesh sizes range from 196,541 to 216,103 elements. (B) Section view of FE strut mesh showing material property assignment (lighter elements have higher stiffness than darker elements) and the presence of pores along the strut length.

3.3.4.2 RoM Models

In order to account for the presence of β-TCP in the sintered material the rule of mixtures (RoM) was used to calculate an effective modulus for the material as per Equation (3.3), where E_x is the elastic modulus of material phase x, E_{RoM} is the modulus calculated using the rule of mixtures and vf_x is the volume fraction of each material phase, x.

$$E_{\mathrm{RoM}} = E_{PCL} vf_{pcl} + E_{TCP} vf_{TCP} \tag{3.3}$$

It should be noted that this corresponds to the rule of mixtures case (A) considered in Section 2.2.3. The elastic modulus of β-TCP was taken from Wang et al. (Wang et al. 2004) where the elastic modulus of sintered β-TCP was evaluated at different sintering temperatures. The average modulus at the lowest sintering temperature was chosen for this study, with a value of 24.6 GPa. This gives an elastic composite modulus E_{RoM} = 277 x 0.75 + 24.6x10^3 x 0.25 = 6.36 GPa; this was then assigned homogeneously to the strut geometries, with v = 0.3 as before. The rule of mixtures applies specifically for the case of aligned fibre-reinforced composite, which is clearly different to the material configuration that is presented here. However, as it is a well-known, straightforward method for determining the elastic moduli of composites it is used here for basic comparison purposes. Given that the rule of mixtures assumed configuration is of continuous fibres aligned in the loading direction, it is to be expected that it would over-predict the elastic modulus for the material presented here.

3.3.4.3 Microstructure-Based Models

In order to capture the local inhomogeneity of the sintered material and the contribution of the β-TCP particles to its mechanical performance, the effective elastic constants of segments of material equal in size to one element in the full strut models were determined from micromechanical modelling (described below in Section 3.4.3). Here, the μ-CT scan grey-value of each element in the full scaffold strut mesh (see Figure 3.5) is used to identify the appropriate values of effective

isotropic elastic modulus (E_{eff}) and Poisson's ratio (v_{eff}) to assign to this element using the relationship generated in the micromechanical analysis described in Section 3.4.3. This approach is illustrated in Figure 3.6. In order to implement this approach, the "material expressions method" in the MIMICS FEA module's material assignment tool was used to assign density, Young's modulus and Poisson's ratio using Equations (3.4), (3.5) and (3.6) respectively, where a_1, a_2, a_3, b_1, b_2 and b_3 are

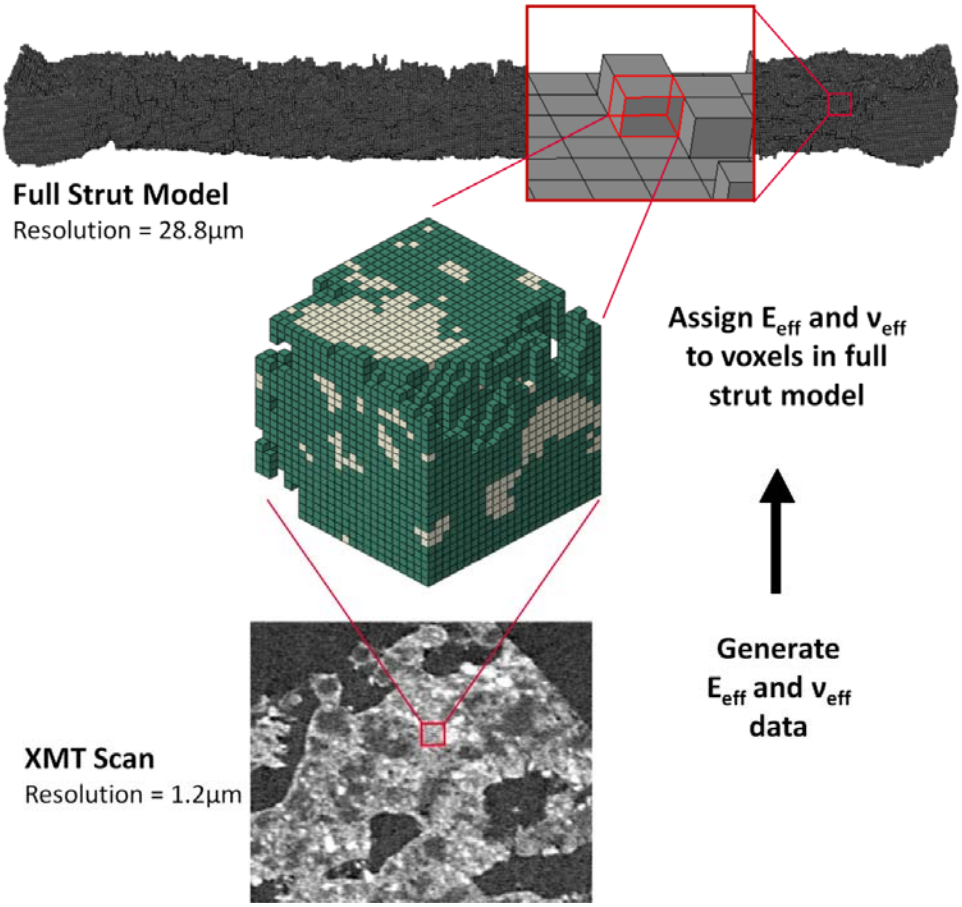

Figure 3.6: Micromechanical models, which are generated from the real material microstructure, are used to generate E_{eff} and v_{eff} data, which is then used to assign individual finite element mechanical properties to elements in the full strut mesh, based on average element grey-value.

user-defined constants, GV is grey-value and ρ is density. The constants a_1 and b_1 were set to one and zero, respectively, to make E and υ directly proportional to GV, under the assumption of a linear relationship between E and GV, and between and υ and GV.

$$\rho = a_1 \times GV + b_1 \tag{3.4}$$

$$E = a_2 \times \rho + b_2 \tag{3.5}$$

$$\nu = a_3 \times \rho + b_3 \tag{3.6}$$

3.3.5 Micromechanical Finite Element Analysis

Due to the mixing of the powders prior to sintering and the difference in sizes of the PCL and β-TCP particles, there is an inhomogeneous distribution of materials in the resulting sintered material. In order to capture this inhomogeneity and to account for it in the generation of effective elastic constants for the material, FE models of cuboidal segments of material representing varying average grey-values were generated from the 1.2 μm XMT scan using MIMICS, as illustrated in Figure 3.6. Each segment has dimensions equal to one element in the full strut models (edge length 28.8 μm). The thresholding and dynamic region growing tools in MIMICS were used to isolate the PCL and β-TCP phases in the 1.2 μm XMT scan of the block of material. The average grey-value (GV_{ave}) was identified for each segment of material with 28.8 μm edge length extracted from the XMT scan. A FE mesh with 8-

noded hexahedral voxel elements with reduced integration was generated for each segment. The PCL and β-TCP phases were represented as separate sections in one meshed part and the appropriate linear elastic material properties were assigned to each phase. The experimentally evaluated elastic modulus for PCL (E_{PCL}) of 277 MPa, as per Section 3.4.1 below, was used for PCL phases and the elastic modulus of β-TCP was taken as 24.6 GPa, as per Section 3.3.4. A Poisson's ratio of 0.3 was assumed for both phases in all simulations and Abaqus/Standard V6.10 was used with NLGEOM selected.

Given that, in this particular implementation, material segment size has been fixed for the micromechanical model by the full strut model element size (edge length of 28.8 μm), the "windowing approach" is used to generate the effective elastic constants (and specifically in this case an effective isotropic elastic modulus (E_{eff}) and Poisson's ratio (v_{eff})), as described for example in references (Nemat-Nasser and Hori 1993; Hazanov 1998; Böhm 2004). Consistent with the windowing approach, three different sets of uniform boundary conditions were applied to the models as follows:

1. Kinematic uniform boundary conditions (KUBC): A macroscopically homogeneous strain tensor $\boldsymbol{\varepsilon}$ is imposed on all boundaries with radius vector $\boldsymbol{x}$, giving a displacement vector $\boldsymbol{\xi}$ as per Equation (3.7), where $\langle\boldsymbol{\varepsilon}\rangle$ is the volume averaged strain:

$$\boldsymbol{\xi} = \langle\boldsymbol{\varepsilon}\rangle \cdot \boldsymbol{x} \tag{3.7}$$

2. Static uniform boundary conditions (SUBC): A macroscopically homogeneous stress tensor $\boldsymbol{\sigma}$ is imposed on all boundaries with exterior unit normal $\boldsymbol{n}$, giving a traction vector density $\boldsymbol{P}$ as per Equation (3.8), where $\langle\boldsymbol{\sigma}\rangle$ is the volume averaged stress:

$$\boldsymbol{P} = \langle\boldsymbol{\sigma}\rangle \cdot \boldsymbol{n} \tag{3.8}$$

3. Mixed uniform boundary conditions (MUBC): These are a combination of the KUBC and SUBC as detailed in Section 3.3.5.1.

For the first phase of model development, FE analyses of each segment under six modes of deformation were carried out under kinematic, static and mixed uniform boundary conditions in order to identify the effective isotropic elastic constants. Three tensile simulations in 1-, 2- and 3-directions were simulated as well as three shear simulations in the 1-2, 2-3 and 3-1 planes. Details of the implementation of the three types of boundary conditions are outlined in Section 3.3.5.1. The effective elastic constants (E_{eff} and v_{eff}) were determined for each individual segment using strain energy density equivalence, as detailed in Section 3.3.5.2. Segments with significant porosity were excluded due to the complications of assigning KUBC and SUBC to these segments. From consideration of the full data set of one hundred 28 μm cube segments generated from the XMT scan, the use of seven grey-value categories was judged to be sufficient to give a reasonable representation of the full data set. Seven levels of average grey-value were chosen within a range of 93.8 to 150.1 and meshes were generated to represent each level of grey-value, giving a total of seven segments. The seven meshed segments are shown in Figure 3.7.

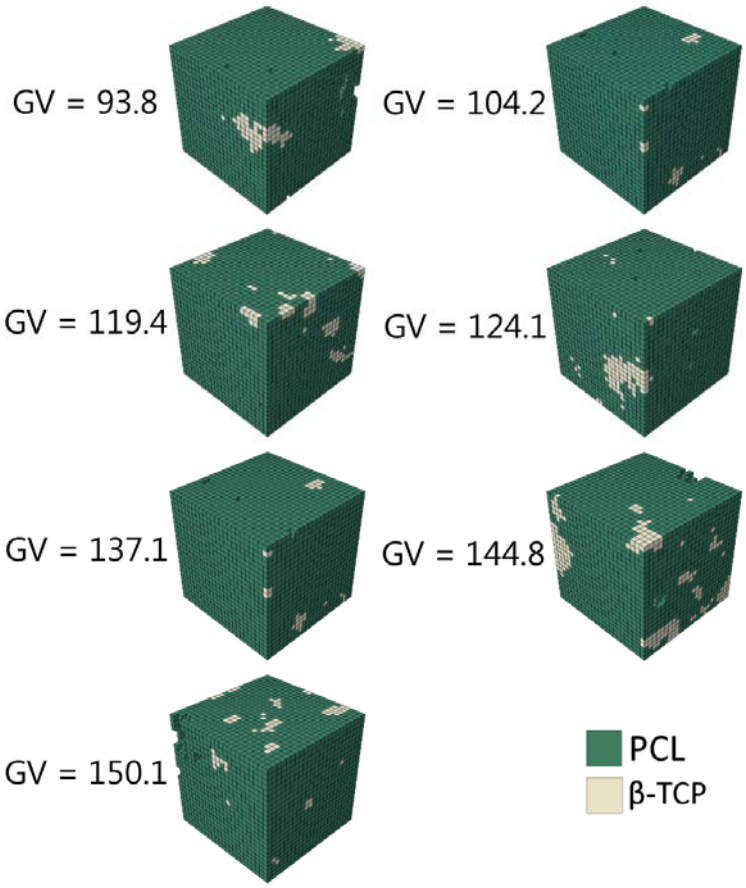

Figure 3.7: FE mesh of each individual segment used in the first phase of the micromechanical analysis, with average grey-values ranging from 93.8 to 150.1. Elements with PCL elastic properties are shown in green and elements with β-TCP elastic properties are shown in ivory.

Results for the first phase of model development are given in Figure 3.8, where E_{eff}, is plotted against grey-value for multiple segments, with no porosity, for each boundary condition case. The effective isotropic elastic modulus E_{eff} is plotted with respect to average grey-value for the seven segment models covering a range of grey-values, representative of the spread of grey-values observed in the scans as indicated above. From the results it can be noted that $E_{\text{eff}}^{\text{KUBC}} > E_{\text{eff}}^{\text{MUBC}} > E_{\text{eff}}^{\text{SUBC}}$, consistent with the expectations of the windowing approach on the effects of the different boundary condition types and the generation of upper and lower bounds to

effective elastic modulus, as described by Nemat-Nasser and Hori, Hazanov and Böhm (Nemat-Nasser and Hori 1993; Hazanov 1998; Böhm 2004). However it is observed that overall the differences between $E_{\text{eff}}^{\text{KUBC}}$ and $E_{\text{eff}}^{\text{SUBC}}$ are not that significant and indeed in one case $E_{\text{eff}}^{\text{KUBC}} \approx E_{\text{eff}}^{\text{MUBC}} \approx E_{\text{eff}}^{\text{SUBC}}$ indicating that a Representative Volume Element (RVE) has been identified (Böhm 2004).

The effective Poisson's ratio (υ_{eff}) results, as a function of GV_{ave}, are shown in Figure 3.9. From these results it is evident that the differences in υ_{eff} are also not that large, consistent with the observation for E_{eff}; in fact, in all cases υ_{eff} was found to be very close to 0.3 with a mean value of 0.299 ± 0.17.

It is important to note that it would have been possible to generate effective anisotropic or orthotropic elastic constants for the material segments using the described modelling framework; however the implementation of these material properties in the full strut models is impractical. This is because there is no directional dependence data available for the full strut models as they are generated from scan data and each element is described by only one number – its grey-value. Hence, an effective isotropic representation is the only practical option.

Based on the above, a second phase of model development was performed to generate the final set of effective isotropic elastic constants for the full strut model analyses. For these simulations, models of material segments that incorporate the presence of porosity were included to account for the possible presence of some micropores in the material that may not be captured in the full strut scan due to insufficient scan resolution. Neglecting the presence of these micropores could result in the models overestimating element stiffness.

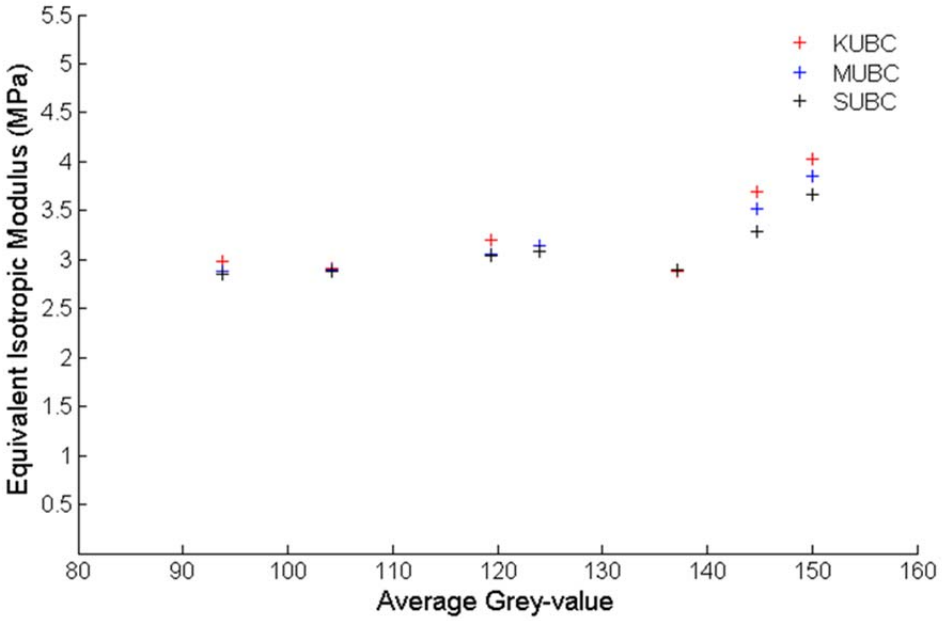

Figure 3.8: E_{eff} plotted against average segment grey-value for segments in the first phase of model development.

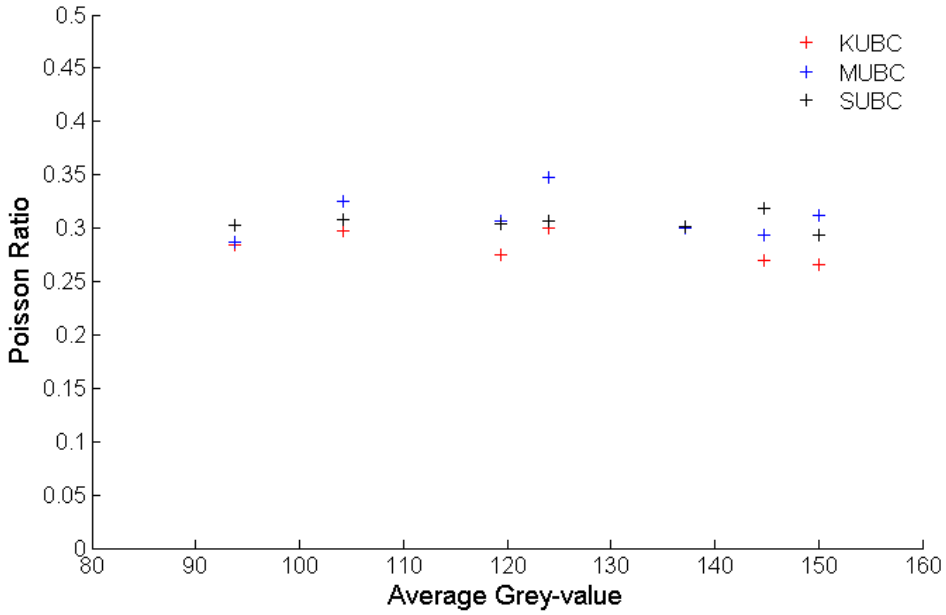

Figure 3.9: Poisson's ratio υ_{eff} plotted against average segment grey-value (GV_{ave}) for segments in the first phase of model development.

Only MUBCs were applied to segments during this phase of modelling given the closeness of the $E_{\text{eff}}^{\text{KUBC}}$ and $E_{\text{eff}}^{\text{SUBC}}$ results from Figure 3.8 and the fact that the $E_{\text{eff}}^{\text{MUBC}}$ results lie between these upper and lower bounds respectively. The MUBCs are also the simplest to assign to segments that include porosity. Again, seven levels of average grey-value were chosen within a range of 93.8 to 150.7, representative of the overall spread of grey-values observed in the material, and meshes were generated for three separate segments for each level to represent possible variations in material composition within each level of grey-value. A nominal value of GV_{ave} for each level was calculated as the average of the GV_{ave} value range for that level. Only two segments were successfully generated for the lowest range of grey-values as these segments typically had high levels of surface porosity making it difficult to assign boundary conditions, giving a total of 20 segments. The percentage of elements within each segment representing PCL, β-TCP and pores, as well as element average segment grey-value, are shown in Figure 3.10. The 20 meshed segments are shown in Figure 3.11. This plot shows that multiple different configurations of material composition can exist with the same GV_{ave}. This can result in variation in E_{eff} and v_{eff} for one GV_{ave}, for example as represented by the data at GV_{ave} of 147 in Figure 3.17(a) and Figure 3.18 (a) (see Section 3.4 Results below for more detailed discussion on these figures).

Each segment was modelled under the six modes of uniaxial and shear deformation with MUBC applied as described in Section 3.3.5.1. The equivalent isotropic elastic constants E_{eff} and v_{eff} were evaluated for each segment as per Section 3.3.5.2. The average E_{eff} and v_{eff} for each grey-value level was calculated and these values are shown in Figure 3.17(b) and Figure 3.18(b) respectively (as will be described in

greater detail below); the line fit for each E_{eff} and v_{eff} was used to assign appropriate elastic constants to the individual elements in the full strut models, as described in Section 3.3.4.

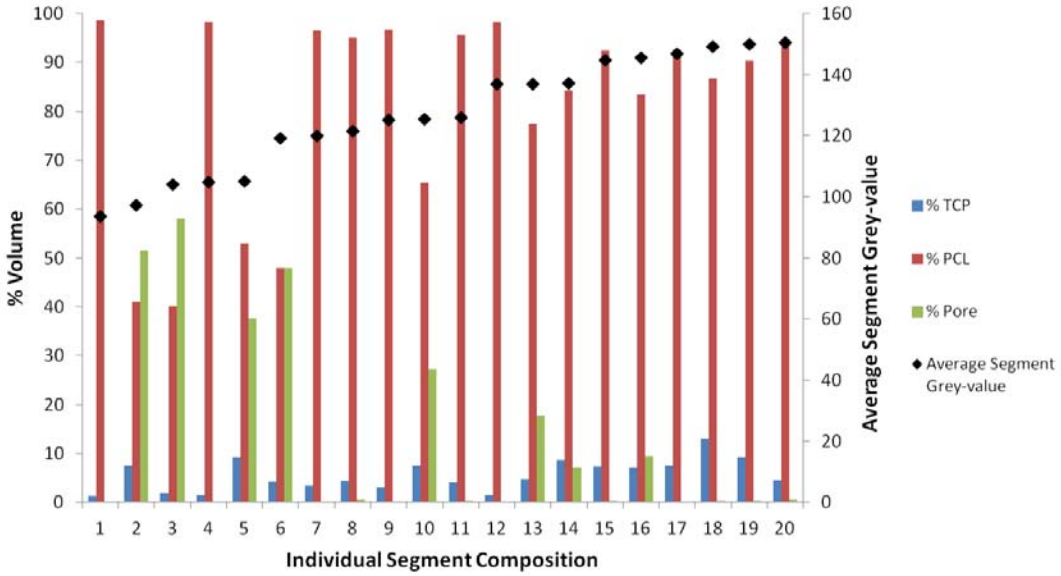

Figure 3.10: Segment material composition and average segment grey-value (GV_{ave}) for segments in the second phase of model development.

3.3.5.1 Implementation of Boundary Conditions

This section outlines the implementation of the three types of boundary conditions used in the simulation of the microstructure segment models. The notation used to describe the faces of a segment cube for this section is specified in Figure 3.12. Full details of the prescribed boundary conditions are given in Table 3.1(a), (b) and (c).

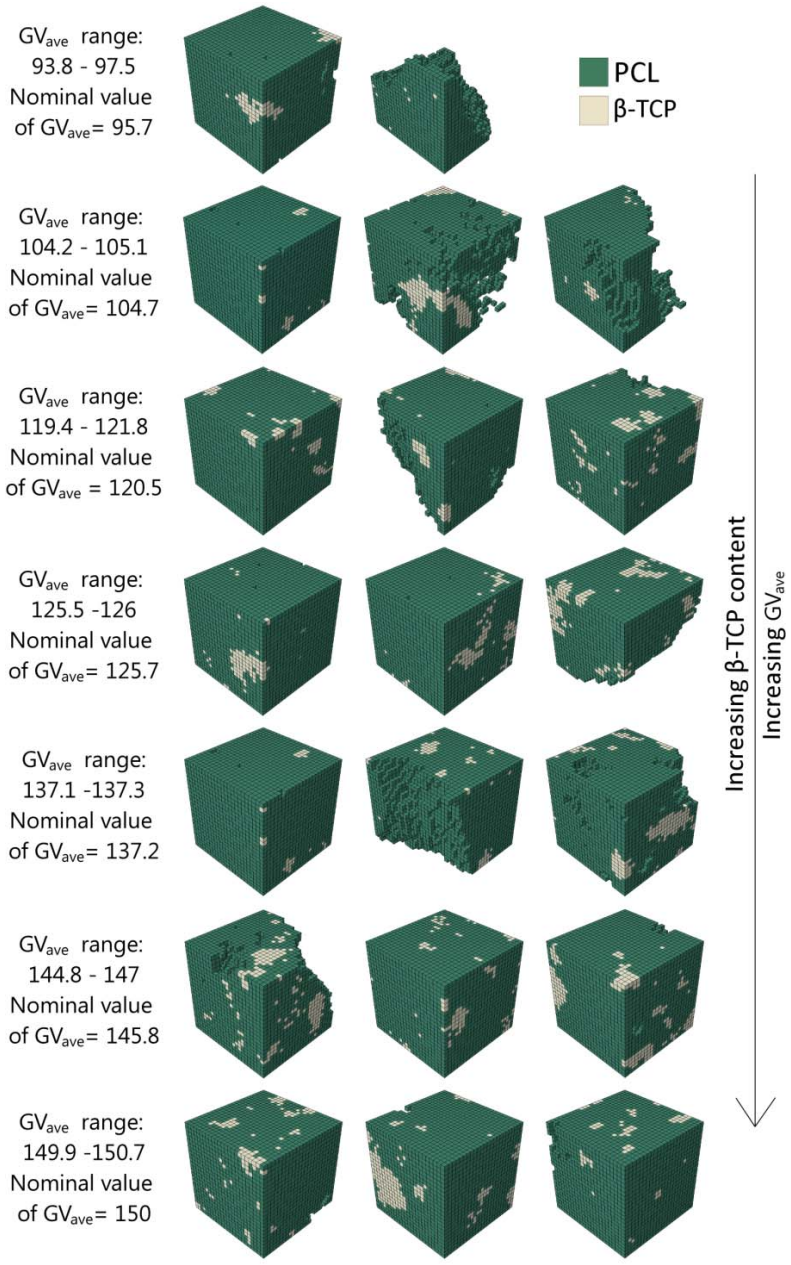

Figure 3.11: FE mesh of each individual segment used in the second phase of the micromechanical analysis, with average segment grey-values (GV_{ave}) ranging from 93.8 to 150.7. These were divided into seven grey-value levels with a GV_{ave} range for each level, as shown. A nominal value of GV_{ave} for each level was calculated as the average of the GV_{ave} value range for that level. Elements with PCL elastic properties are shown in green and elements with β-TCP elastic properties are shown in ivory.

Kinematic Uniform Boundary Conditions

KUBC are implemented by assigning boundary conditions such that the average strains in all directions other than the loading direction must be equal to zero. With reference to Figure 3.12, for the case of uniaxial strain in the 1-direction, a strain (nodal displacement) is applied on the front (positive) 1-face (A_{1f}) and the displacement on all other faces is constrained perpendicular to the plane of each face, meaning that the normal strains on these faces are equal to zero while the stresses are not necessarily equal to zero. Specifically, in this case, the applied displacement for a node on the A_{1f} face is $u_1{}^{node} = u_1{}^{CN}$ where $u_1{}^{node}$ is the nodal displacement and $u_1{}^{CN}$ is the displacement of a control node (CN) in the 1-direction. In each loading case, the corners of the cube are constrained such that rotations about the 1-, 2- and 3-axes were prevented.

For the case of simple shear with KUBC, certain faces of the segment need to reorient while remaining straight/flat. For this, *EQUATION constraints were used within Abaqus to keep the faces straight by specifying the displacement of each node on the face. For the case of simple shear in the 1-2 direction, for example, the equation for the displacement of a node on face A_{1f} is as per Equation (3.9):

$$u_1^{node} = u_1^{CN}\left(\frac{x_2^{node}}{x_2^{CN}}\right) \tag{3.9}$$

where $x_2{}^{node}$ is the nodal position of the node and $x_2{}^{CN}$ is the length of the cube segment in the 2-direction.

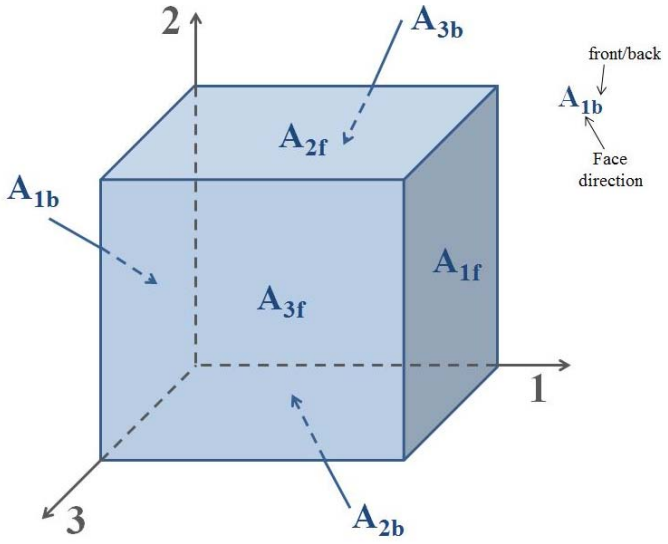

Figure 3.12: Notation used to describe the faces of a cube segment for the application of uniform boundary conditions discussed in Section 3.3.5.1. For example, A_{1f} is the front (positive) face in the 1-direction, and A_{1b} is the back (negative) face in the 1-direction.

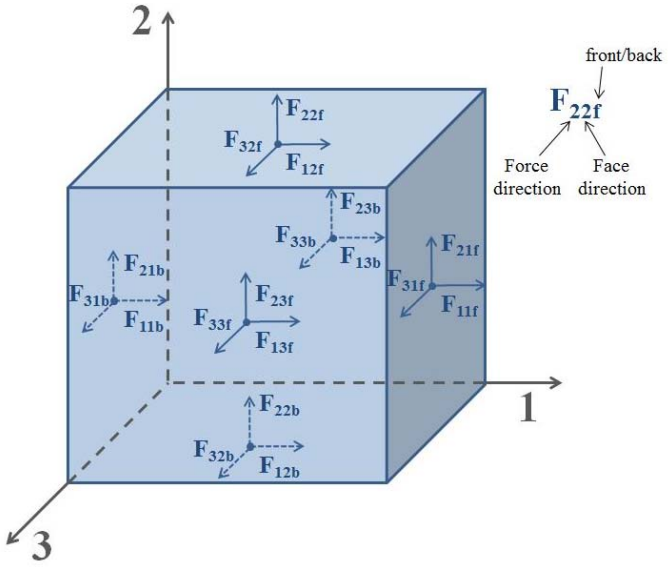

Figure 3.13: Notation used to describe the forces on the faces of a cube segment for the application of static uniform boundary conditions (SUBC) discussed in Section 3.3.5.1. For example, F_{11f} is a force in the 1-direction on the front (positive) face in the 1-direction, and F_{32b} is a force in the 3-direction on the back (negative) face in the 2-direction.

Mixed Uniform Boundary Conditions

MUBC are applied in a similar manner to KUBC, where a displacement is assigned to the faces of the segment. However, in this case boundary conditions are applied to the faces perpendicular to the loading directions for uniaxial deformation and the stresses on the remaining faces are set equal to zero while the strains are not necessarily equal to zero. For the case of shear deformation in the 1-2 direction, for example, the equation for the displacement of nodes on the face A_{2f} is $u_1{}^{node} = u_1{}^{CN}$ and the displacement of nodes on the face A_{2b} is $u_1{}^{node} = 0$. In each loading case, the corners of the cube were constrained to prevent rotation of the segment under loading.

Static Uniform Boundary Conditions

SUBC are assigned by imposing opposing stresses (total forces on faces) on the faces perpendicular to the loading directions, while nodal deformations on the faces are not constrained. For the case of uniaxial loading in the 1-direction, for example, a force F is applied to the face A_{1f} and an opposing force $-F$ is applied to the opposing face, A_{1b}, where F is the magnitude of the force applied to a cube segment face where the cube face forces are defined in Figure 3.13. For the case of shear loading in the 1-2 direction for example, a force F is applied to the faces A_{1f} and A_{2f}, and opposing forces $-F$ are applied to the opposing faces, A_{1b} and A_{2b}. Each face is allowed to freely deform, meaning that the stresses on non-loaded faces are equal to zero while the strains are not necessarily equal to zero. In each loading case, the corners of the cube were constrained such that rotations about the axes were prevented.

Table 3.1: The boundary conditions used for the assignment of uniform boundary conditions in micromechanical models in this study are described in this table. The boundary conditions required for kinematic uniform boundary conditions (KUBC) are described in section (a) of this table, for mixed uniform boundary conditions (MUBC) in section (b) of this table, and for static uniform boundary conditions (SUBC) in section (c) of this table. The cube segment faces are defined in Figure 3.12. For the KUBC and MUBC cases, i is the direction (1, 2 or 3), u_i^{CN} is the i-direction displacement of the controlling node (CN), u_i^{node} is the i-direction displacement of each node on a cube segment face, x_1^{CN} is the i-direction controlling node position, and x_1^{node} is the i-direction position of each node on the cube segment face. For the SUBC case, F is the magnitude of the force applied to a cube segment face where the cube face forces are defined in Figure 3.13. For simulations using KUBC and MUBC, all displacements are controlled by the CN; for simulations using SUBC, all stresses are induced by the applied forces. Sections (a) to (c) of this table are shown on the following pages.

Table 3.1 (a): KUBC

	KUBC					
	Uniaxial strain			Simple Shear		
Loading direction → / Face ↓	1	2	3	1-2	2-3	3-1
A_{1b}	$u_1^{node} = 0$	$u_1^{node} = 0$	$u_1^{node} = 0$	$u_1^{node} = u_1^{CN}\left(\frac{x_2^{node}}{x_2^{CN}}\right)$	$u_1^{node} = 0$	$u_1^{node} = 0$ $u_3^{node} = 0$
A_{1f}	$u_1^{node} = u_1^{CN}$	$u_1^{node} = 0$	$u_1^{node} = 0$	$u_1^{node} = u_1^{CN}\left(\frac{x_2^{node}}{x_2^{CN}}\right)$	$u_1^{node} = 0$	$u_1^{node} = 0$ $u_3^{node} = 0$
A_{2b}	$u_2^{node} = 0$	$u_2^{node} = 0$	$u_1^{node} = 0$	$u_1^{node} = 0$ $u_2^{node} = 0$	$u_2^{node} = u_2^{CN}\left(\frac{x_3^{node}}{x_3^{CN}}\right)$	$u_1^{node} = 0$
A_{2f}	$u_2^{node} = 0$	$u_2^{node} = u_2^{CN}$	$u_2^{node} = 0$	$u_1^{node} = 0$ $u_2^{node} = 0$	$u_2^{node} = u_2^{CN}\left(\frac{x_3^{node}}{x_3^{CN}}\right)$	$u_2^{node} = 0$
A_{3b}	$u_3^{node} = 0$	$u_3^{node} = 0$	$u_3^{node} = 0$	$u_3^{node} = 0$	$u_2^{node} = 0$ $u_3^{node} = 0$	$u_3^{node} = u_3^{CN}\left(\frac{x_1^{node}}{x_1^{CN}}\right)$
A_{3f}	$u_3^{node} = 0$	$u_3^{node} = 0$	$u_3^{node} = u_3^{CN}$	$u_3^{node} = 0$	$u_2^{node} = 0$ $u_3^{node} = 0$	$u_3^{node} = u_3^{CN}\left(\frac{x_1^{node}}{x_1^{CN}}\right)$

Table 3.1 (b): MUBC

MUBC							
		Uniaxial strain			Simple Shear		
Loading direction → / Face ↓		1	2	3	1-2	2-3	3-1
A_{1b}		$u_1^{node} = 0$	-	-	-	-	$u_3^{node} = 0$
A_{1f}		$u_1^{node} = u_1^{CN}$	-	-	-	-	$u_3^{node} = u_3^{CN}$
A_{2b}		-	$u_2^{node} = 0$	-	$u_1^{node} = 0$	-	-
A_{2f}		-	$u_2^{node} = u_2^{CN}$	-	$u_1^{node} = u_1^{CN}$	-	-
A_{3b}		-	-	$u_3^{node} = 0$	-	$u_2^{node} = 0$	-
A_{3f}		-	-	$u_3^{node} = u_3^{CN}$	-	$u_2^{node} = u_2^{CN}$	-

Table 3.1 (c): SUBC

	SUBC						
	Uniaxial strain			Simple Shear			
Loading direction → / **Face ↓**	**1**	**2**	**3**	**1-2**	**2-3**	**3-1**
A_{1b}	$F_{11b} = -F$	-	-	$F_{21b} = -F$	-	$F_{31b} = -F$
A_{1f}	$F_{11f} = F$	-	-	$F_{21f} = F$	-	$F_{31f} = F$
A_{2b}	-	$F_{22b} = -F$	-	$F_{12b} = -F$	$F_{32b} = -F$	-
A_{2f}	-	$F_{22f} = F$	-	$F_{12f} = F$	$F_{32f} = F$	-
A_{3b}	-	-	$F_{33b} = -F$	-	$F_{23b} = -F$	$F_{13b} = -F$
A_{3f}	-	-	$F_{33f} = F$	-	$F_{23f} = F$	$F_{13f} = F$

3.3.5.2 Calculation of Effective Isotropic Constants Using Strain Energy Density Equivalence

In order to generate effective isotropic elastic constants (E_{eff} and υ_{eff}) for each micromechanical segment model, the strain energy density (U) for each deformed configuration was calculated using Equation 2.34, repeated here for convenience:

$$U = \frac{1}{2}\{\sigma_{11}\varepsilon_{11} + \sigma_{22}\varepsilon_{22} + \sigma_{33}\varepsilon_{33} + \sigma_{12}\gamma_{12} + \sigma_{23}\gamma_{23} + \sigma_{31}\gamma_{31}\} \tag{3.10}$$

In Equation (3.10) σ_{11} is the volume average stress in the 1-direction, σ_{12} is the volume average shear stress in the 1-2-plane, ε_{11} is the volume average strain in the 1-direction and γ_{12} is the volume average shear strain in the 1-2 plane with γ_{12}=2 ε_{12}. This can then be related to the constitutive equations for a linear elastic material for an applied strain (Case 1) or an applied stress (Case 2) as per Bower et al. (Bower 2008).

Case 1:

The constitutive equations for a linear elastic material for the case of an applied strain, where the volume averaged stress $\langle\boldsymbol{\sigma}\rangle$ can be calculated as a function of volume averaged strain $\langle\boldsymbol{\varepsilon}\rangle$, E_{eff} and υ_{eff}, are described by Equation (3.11).

$$\begin{bmatrix}\sigma_{11}\\ \sigma_{22}\\ \sigma_{33}\\ \sigma_{12}\\ \sigma_{23}\\ \sigma_{31}\end{bmatrix} = \frac{E_{\text{eff}}}{(1+v_{\text{eff}})(1-2v_{\text{eff}})}\begin{bmatrix} 1-v_{\text{eff}} & v_{\text{eff}} & v_{\text{eff}} & 0 & 0 & 0 \\ v_{\text{eff}} & 1-v_{\text{eff}} & v_{\text{eff}} & 0 & 0 & 0 \\ v_{\text{eff}} & v_{\text{eff}} & 1-v_{\text{eff}} & 0 & 0 & 0 \\ 0 & 0 & 0 & \frac{1-2v_{\text{eff}}}{2} & 0 & 0 \\ 0 & 0 & 0 & 0 & \frac{1-2v_{\text{eff}}}{2} & 0 \\ 0 & 0 & 0 & 0 & 0 & \frac{1-2v_{\text{eff}}}{2} \end{bmatrix}\begin{bmatrix}\varepsilon_{11}\\ \varepsilon_{22}\\ \varepsilon_{33}\\ \gamma_{12}\\ \gamma_{23}\\ \gamma_{31}\end{bmatrix} \quad (3.11)$$

This is an application of Equation (2.28), presented in Chapter 2, where the stress components (σ_{ij}) and strain components (ε_{ij}) are identified as volume averaged quantities. By rearranging Equation (3.10) and equating to the Equation (3.11) for the specific loading case, E_{eff} can be re-written as a function of strain energy density, v_{eff} and strain, giving Equation (3.12) for the case of uniaxial tension and Equation (3.13) for simple shear. Directional variations in mechanical properties of the material, if present, are accounted for in the effective isotropic modulus E_{eff} and Poisson's ratio v_{eff} by averaging strain energy density and strain over a number of loading modes and directions. Specifically, U_{uniax} is the average of U_{11}, U_{22} and U_{33} where U_{11} is the strain energy density for uniaxial tensile loading in the 1-direction, U_{22} for uniaxial tensile loading in the 2-direction, etc., and U_{shear} is the average of U_{12}, U_{23} and U_{31} where U_{12} is the strain energy density for shear loading in the 1-2 plane, U_{23} for shear loading in the 2-3 plane, etc. Similarly, $\varepsilon_{\text{uniax}}$ is the average of ε_{11}, ε_{22} and ε_{33} and γ_{shear} is the average of γ_{12}, γ_{23} and γ_{31}. Equations (3.12) and (3.13) below can be equated to solve for v_{eff}, giving Equation (3.14). Once evaluated, v_{eff} can then be substituted back into Equation (3.12) or (3.13) to solve for E_{eff}.

$$E_{\text{eff}} = \frac{2U_{\text{uniax}}}{\varepsilon_{\text{uniax}}{}^2}\frac{(1+v_{\text{eff}})(1-2v_{\text{eff}})}{(1-v_{\text{eff}})} \tag{3.12}$$

$$E_{\text{eff}} = \frac{4U_{\text{shear}}}{\gamma_{\text{shear}}{}^2}(1+v_{\text{eff}}) \tag{3.13}$$

$$v_{\text{eff}} = \frac{\left(\frac{2U_{\text{shear}}}{\gamma_{\text{shear}}{}^2} - \frac{U_{\text{uniax}}}{\varepsilon_{\text{uniax}}{}^2}\right)}{\left(\frac{2U_{\text{shear}}}{\gamma_{\text{shear}}{}^2} - \frac{2U_{\text{uniax}}}{\varepsilon_{\text{uniax}}{}^2}\right)} \tag{3.14}$$

Case 2:

The constitutive equations for a linear elastic material for the case of an applied stress, where $\langle \boldsymbol{\varepsilon} \rangle$ can be calculated as a function of $\langle \boldsymbol{\sigma} \rangle$, E_{eff} and v_{eff}, are described by Equation (3.15), the inverse of Equation (3.11).

$$\begin{bmatrix}\varepsilon_{11}\\ \varepsilon_{22}\\ \varepsilon_{33}\\ \gamma_{12}\\ \gamma_{23}\\ \gamma_{31}\end{bmatrix} = \frac{1}{E_{\text{eff}}}\begin{bmatrix}1 & -v_{\text{eff}} & -v_{\text{eff}} & 0 & 0 & 0\\ -v_{\text{eff}} & 1 & -v_{\text{eff}} & 0 & 0 & 0\\ -v_{\text{eff}} & -v_{\text{eff}} & 1 & 0 & 0 & 0\\ 0 & 0 & 0 & 2(1+v_{\text{eff}}) & 0 & 0\\ 0 & 0 & 0 & 0 & 2(1+v_{\text{eff}}) & 0\\ 0 & 0 & 0 & 0 & 0 & 2(1+v_{\text{eff}})\end{bmatrix}\begin{bmatrix}\sigma_{11}\\ \sigma_{22}\\ \sigma_{33}\\ \sigma_{12}\\ \sigma_{23}\\ \sigma_{31}\end{bmatrix} \tag{3.15}$$

Again, by rearranging Equation (3.10) and setting it equal to Equation (3.15) for the relevant loading case, E_{eff} can be re-written as a function of strain energy density, v_{eff} and strain, as demonstrated for the cases of uniaxial tension using Equation (3.16) and simple shear using Equation (3.17) below. U_{uniax} and U_{shear} are as per Case 1, and σ_{uniax} is the average of σ_{11}, σ_{22} and σ_{33} and σ_{shear} is the average of σ_{12}, σ_{23} and σ_{31}. Equations (3.16) and (3.17) can be equated to solve for v_{eff}, giving Equation (3.18).

As for Case 1, once evaluated, υ_{eff} can then be substituted back into Equation (3.16) or (3.17) to solve for E_{eff}.

$$E_{\text{eff}} = \frac{\sigma_{\text{uniax}}^2}{U_{\text{uniax}}}(1 + \upsilon_{\text{eff}}) \tag{3.16}$$

$$E_{\text{eff}} = \frac{\sigma_{\text{shear}}^2}{2U_{\text{shear}}} \tag{3.17}$$

$$E_{\text{eff}} = \frac{\sigma_{\text{shear}}^2}{2U_{\text{shear}}} \tag{3.18}$$

3.4 Results

3.4.1 Structural and Morphological Characterisation

The macro-scale porosity of the four strut geometries used in this study were calculated form the μ-CT scan images of the struts as per Section 3.3.2. The calculated values for strut porosity and the average value of strut porosity are shown in Table 3.2. Images showing pore morphology in a cross-section of a strut, taken perpendicular to the long axis of the strut, are shown in Figure 3.14. Typical pore dimensions are also indicated, pore widths range from 45.18 to 137.18 μm.

Table 3.2: Summary of values for strut porosity (%).

Strut	Porosity (%)
1	4.535112
2	9.218038
3	11.71967
4	12.80762
Average	9.570111

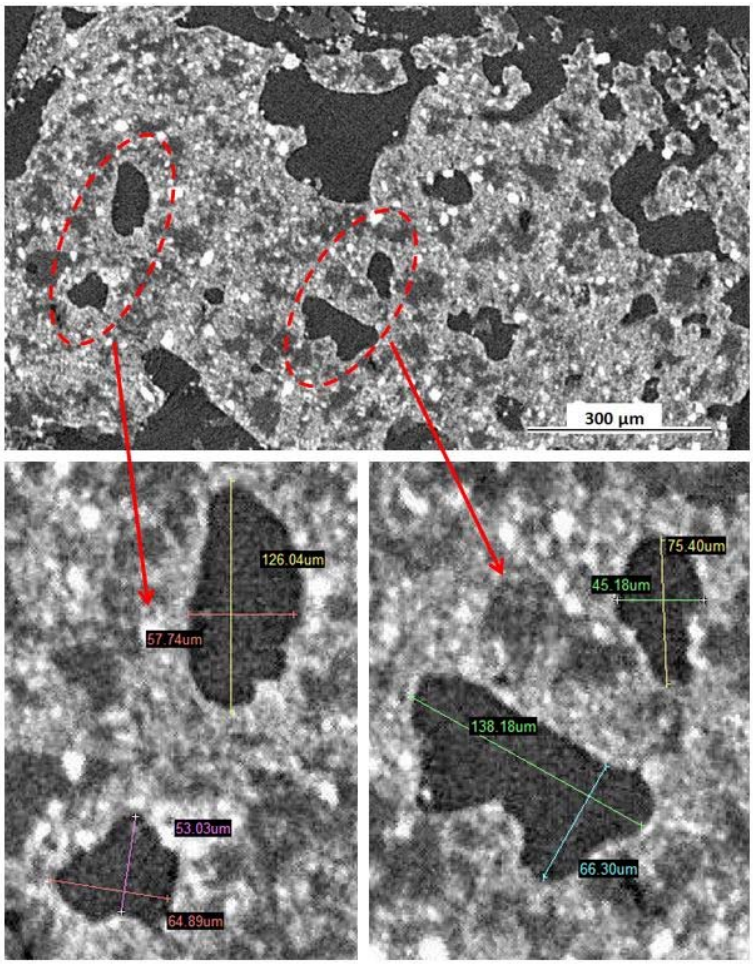

Figure 3.14: Typical pore morphology in a cross-section of a full strut (top), perpendicular to the long axis of the strut, as seen in the XMT scan of a strut segment showing typical pore dimensions (below).

3.4.2 Mechanical Characterisation

Pure PCL Samples

Tensile stress-strain curves for the pure PCL sample tests are shown in Figure 3.15. For the purposes of input into the finite element models, the elastic modulus is evaluated in the linear portion of the curve, i.e. up to a strain of 0.02. The linear elastic modulus of PCL was evaluated as 277.06 ± 27.66 MPa (n = 7), which is comparable to values observed in the literature listed in Table 3.3. This experimental value was used as input in the micromechanical simulations.

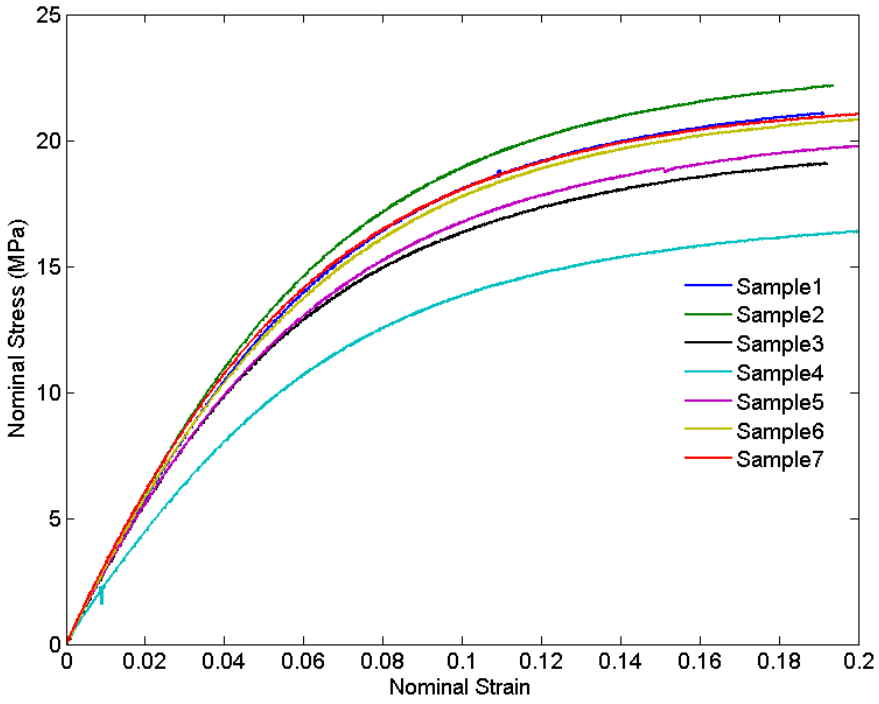

Figure 3.15: Tensile curves for pure PCL samples tested to 0.2 strain.

Table 3.3: Summary of values for PCL elastic modulus (E) from the literature.

Material Source	Mw (Da)	E (MPa)	Fabrication Method	Reference
CAPA 6501, Solvay	50000	122	SLS	(Williams et al. 2005)
	50000	297.8	SLS	(Eshraghi and Das 2010)
	50000	299	SLS	(Eshraghi and Das 2012)
	50000	120	Material Datasheet	(Williams et al. 2005)
	50000	645.88	Vacuum melting	(Roosa et al. 2010)
	50000	320	Extrusion	(Little et al. 2009)
Sigma-Aldrich	65000	250	Drop-on-demand printer	(Mondrinos et al. 2006)
	80000	373	Solvent casting, film pressing	(Ng et al. 2000)
	80000	400	Melt blending & pressing	(Chen et al. 2005)

Single Sintered Struts

Single struts of composite sintered PCL and β-TCP were tested to failure in tension. Tensile stress-strain curves are shown in Figure 3.16(a). The brittleness of the material relative to the pure PCL material, for example, should be noted. For comparison with the predictions of the full strut finite element models the experimental effective strut elastic modulus was determined from the initial linear elastic region (Figure 3.16(b)), giving 98.87 ± 22.59 MPa (n = 7).

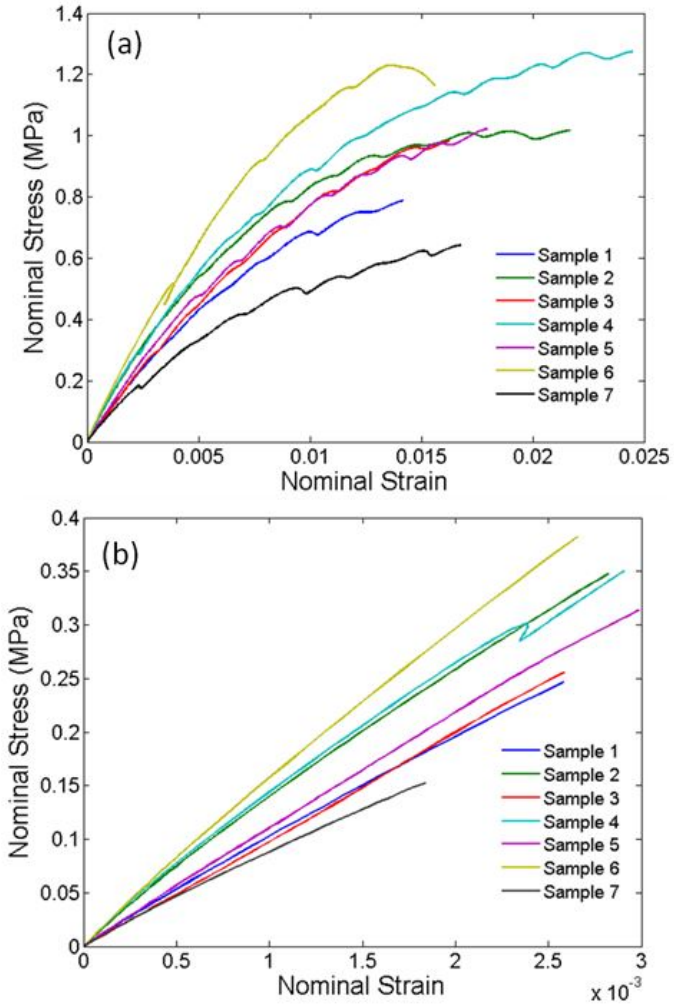

Figure 3.16: Tensile curves for sintered struts tested to failure, with n = 7 (a). An expanded view of the linear region of tensile curves for evaluation of elastic modulus is shown in (b).

3.4.3 Micromechanical Finite Element Analysis

The results for the second phase of micromechanical modelling are shown in Figure 3.17 and Figure 3.18. As noted above, models for seven GV_{ave} values, with up to three segments per GV_{ave}, were used giving a total of 20 models as shown in Figure 3.11. The full set of predicted values of E_{eff} and υ_{eff} are presented as a function of GV_{ave} in Figure 3.17(a) and Figure 3.18(a), respectively. The average E_{eff} and υ_{eff} for

each for GV_{ave} range was calculated and a linear relationship was determined as shown in Figure 3.17(b) and Figure 3.18(b), respectively, giving the following equations:

$$E_{\text{eff}} = m_E * GV_{ave} + c_E \tag{3.19}$$

$$\nu_{\text{eff}} = m_\nu * GV_{ave} + c_\nu \tag{3.20}$$

where m_x and c_x are the slope and constant of the line describing the linear relationship, calculated using least squares method, between the elastic constant x and the nominal average segment grey-value for the corresponding grey-value level, see Figure 3.17. The values of m_x and c_x are also given in Figure 3.17(b) and Figure 3.18(b). Overall it was observed that E_{eff} ranged from 277.43 MPa to 374.45 MPa with a mean value of 324.69 MPa, and υ_{eff} varied from 0.2393 to 0.3517 with a mean value of 0.289. The relationships described by Equations (3.19) and (3.20) above were used to assign element specific effective elastic constants (E_{eff} and υ_{eff}) in the full strut models as a function of average segment grey-value.

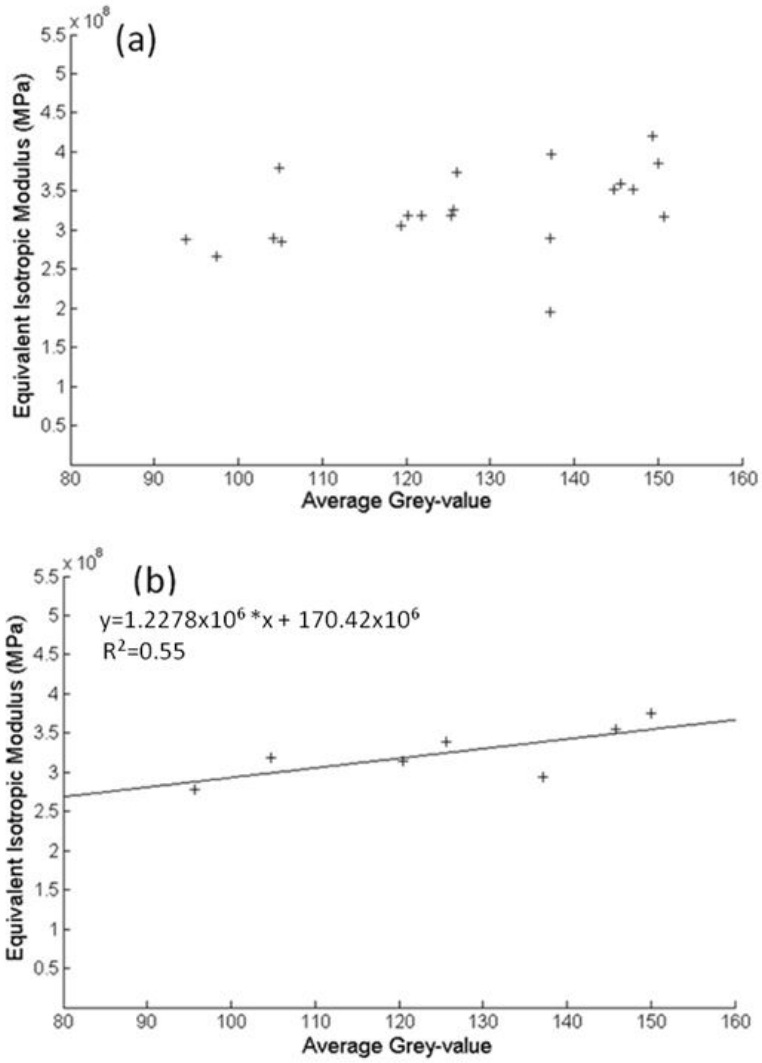

Figure 3.17: Variation of effective elastic modulus (E_{eff}) with average grey-value (GV_{ave}), for the full set of cube segment models, for the second phase of model development (a). The average value of E_{eff} for each grey-value level (typically an average of three values) is shown with respect to the corresponding nominal GV_{ave} value for that level is shown in (b). The linear fit is also shown in (b).

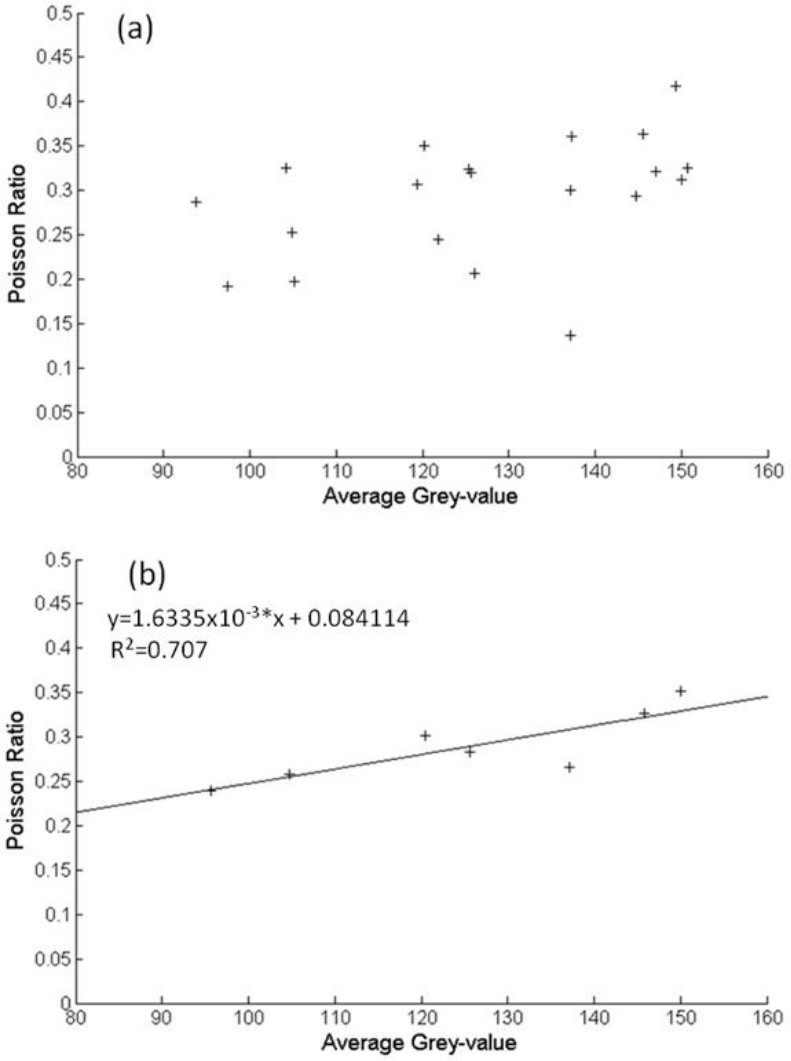

Figure 3.18: Variation of Poisson's ratio (υ_{eff}) with average grey-value (GV_{ave}), for the full set of cube segment models, for the second phase of model development (a). The average value of υ_{eff} for each grey-value level (typically an average of three values) is shown with respect to the corresponding nominal GV_{ave} value for that level is shown in (b). The linear fit is also shown in (b).

3.4.4 Macro-Scale Analysis of Struts

The effective strut modulus was determined from the full strut models for each material assignment case described in Section 3.3.4: PCL, RoM and Microstructure-based. These values are shown in comparison with the experimentally evaluated strut modulus in Figure 3.19. Strut models utilising E_{PCL} (n = 4) gave an effective strut modulus with no statistical difference from the experimentally observed strut modulus (n = 7) when compared using a Mann-Whitney test (p-value = 0.0726). A non-parametric test was used due to low sample numbers. Models using E_{RoM} (n = 4) aim to account for the contribution of the β-TCP particles present in the material to the overall strut mechanical performance by using the rule of mixtures to calculate a composite modulus including both PCL and β-TCP phase, but this method actually overestimates the experimentally observed strut stiffness by a factor of 27, as can be seen in Figure 3.19.

Analysis of the results show no statistical difference between the experimental strut modulus (n = 7) and the effective strut modulus (n = 4) evaluated using E_{eff} and υ_{eff} when compared using a Mann-Whitney test (p-value = 0.0726). Again, a non-parametric test was used due to low sample numbers. This indicates that using E_{eff} and υ_{eff} gives a better approximation of the mechanical behaviour of the sintered PCL/β-TCP struts than other material assignment methods that account for the presence of both PCL and β-TCP.

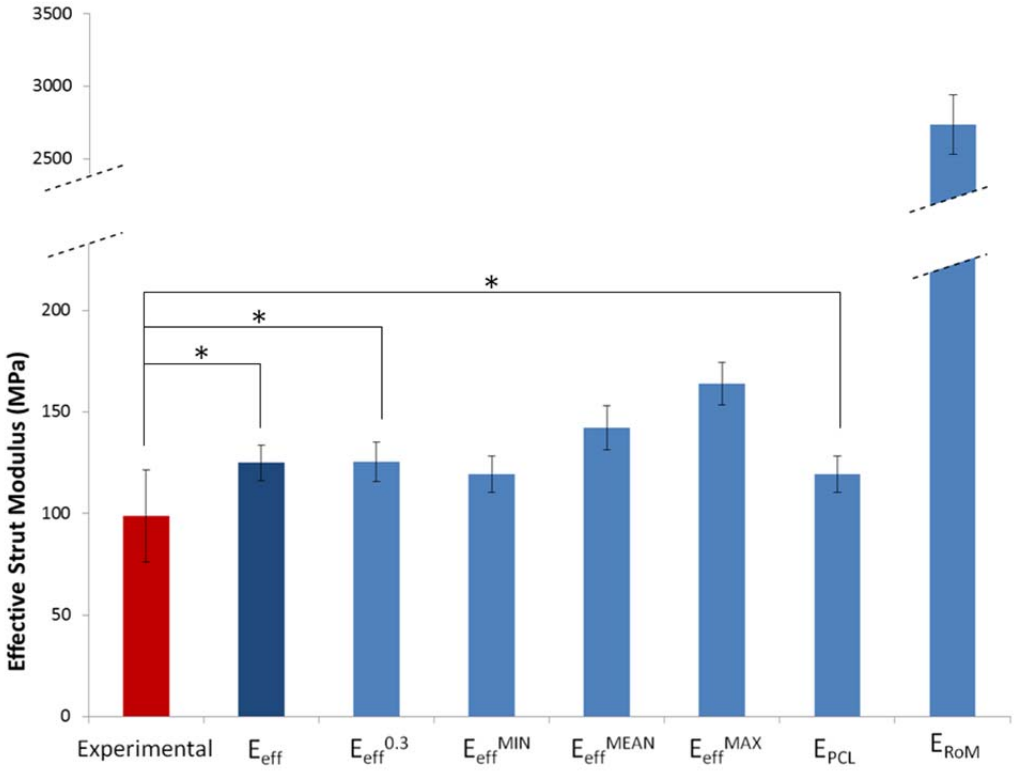

Figure 3.19: Comparison of experimental (red, n = 7) and computationally evaluated (blue, n = 4) strut effective moduli for different methods of material assignment, with input material property type indicated on the x-axis. Mean values for each data set are shown and error bars represent standard deviation. E_{eff} uses heterogeneous assignment of E_{eff} and v_{eff}, while $E_{\text{eff}}^{0.3}$ uses heterogeneous assignment of E_{eff} and a constant Poisson's ratio of 0.3. $E_{\text{eff}}^{\text{MIN}}$, $E_{\text{eff}}^{\text{MEAN}}$ and $E_{\text{eff}}^{\text{MAX}}$ use homogeneous assignment of the minimum, mean and maximum values of E_{eff} respectively, each with a constant Poisson's ratio of 0.3. E_{PCL} and E_{RoM} use homogeneous assignment of the elastic modulus of PCL and a composite modulus calculated using the RoM respectively, with a constant Poisson's ratio of 0.3. Note that the plot is shown with a broken y-axis in order to show the RoM result on the same plot as the experimental results. *p > 0.05.

In addition, other versions of the microstructure-based models were formulated for comparison purposes, and results for these models are compared and included in Figure 3.19, namely:

- Element-specific assignment of elastic modulus using E_{eff} as per Section 3.3.4.3, but using a constant Poisson's ratio of 0.3, labelled as $E_{\text{eff}}^{0.3}$ in Figure 3.19.
- Homogeneous assignment of elastic constants, using the minimum value of grey-value averaged E_{eff} of 277.43 MPa and a constant Poisson's ratio of 0.3, labelled as $E_{\text{eff}}^{\text{MIN}}$ in Figure 3.19.
- Homogeneous assignment of elastic constants, using the mean value of grey-value averaged E_{eff} of 324.69 MPa and a constant Poisson's ratio of 0.3, labelled as $E_{\text{eff}}^{\text{MEAN}}$ in Figure 3.19.
- Homogeneous assignment of elastic constants, using the maximum value of grey-value averaged E_{eff} of 374.45 MPa and a constant Poisson's ratio of 0.3, labelled as $E_{\text{eff}}^{\text{MAX}}$ in Figure 3.19.

As it is evident from Figure 3.19, keeping the Poisson's ratio constant at 0.3 ($E_{\text{eff}}^{0.3}$ case) has a negligible effect on overall modulus prediction, whereas using a homogeneous minimum or maximum value for elastic modulus does have a noticeable effect, for example if one compares the $E_{\text{eff}}^{\text{MIN}}$ and $E_{\text{eff}}^{\text{MAX}}$ cases.

3.5 Discussion

The linear elastic properties of solid PCL tensile samples fabricated by vacuum melting were evaluated giving an elastic modulus of 277.06 ± 27.66 MPa. This falls within the expected range when compared to the literature in Table 3.3. The linear elastic properties of single sintered PCL/β-TCP struts fabricated by SLS were evaluated giving an average elastic modulus of 98.87 ± 22.59 MPa. Comparison of elastic moduli of the pure PCL samples and sintered struts reveals that the pure PCL samples were approximately three times stiffer than the sintered struts, despite the inclusion of β-TCP particles that are 88.8 times stiffer than PCL. The reason for this difference is the presence of pores in the sintered struts, whereas the pure PCL samples have effectively no porosity. Other studies where PCL-based composites were fabricated with the inclusion of particles such as β-TCP (Lam et al. 2008), phosphate glass (Shah et al. 2010) and titanium oxide (Gupta et al. 2012) have shown an initial increase in stiffness, however in these cases there was no increase in porosity as a result of the addition of the particles. These studies also found that the rate of degradation was affected by the addition of the particles, which should be taken into consideration in studies involving the change in material properties over time, but was not the focus of the study in the present chapter.

In the SEM images of the scaffold struts, fully sintered areas are visible as smooth surfaces in Figure 3.1(b), and partially-sintered areas are also visible. These images indicate that the material has a porous microstructure, resulting in lower mechanical properties than the solid PCL samples. Examination of the XMT scans indicates that the β-TCP particles are embedded in a PCL matrix (Figure 3.1(b)); therefore the

mechanical behaviour of the sintered material may be dominated by the stiffness of the PCL phase. This was approximated in full strut models using E_{PCL}, where homogeneous PCL properties were assigned. These models were found to give a good estimate of strut effective modulus when compared to the experimental results, however they are not sufficiently representative of the real material as it does not account for both PCL and β-TCP phases. The primary purpose of the addition of ß-TCP particles to this material is to promote osteogenesis, i.e. the formation of new bone, and not necessarily to change mechanical properties. FE models with homogeneous PCL properties assigned to PCL/β-TCP strut geometries were included here for comparison purposes only.

Full strut models using E_{RoM} aim to account for the influence of β-TCP particles on strut stiffness using a homogeneous elastic modulus calculated based on the volume fractions of PCL and β-TCP in the material. The strut elastic moduli for simulations using E_{RoM} overestimated the experimentally observed strut stiffness by a factor of 27 indicating that this method of material assignment is overly simplistic when dealing with a material with a complex microstructure such as this. As discussed in Section 3.3.4.2, it is to be expected that it would over-predict the elastic modulus of this material as the rule of mixtures assumed configuration is of continuous fibres aligned in the loading direction.

The effective material elastic modulus of a full strut was also approximated using the rule of mixtures for other possible material configurations which are discussed in Section 2.2.4 in Chapter 2 of this thesis. Here, the strut is assumed to be a solid rectangular bar with no surface roughness. The average value of strut porosity was

assumed (9.57%, Table 3.2), and the effective strut elastic modulus approximated for each material configuration is shown below. It is clear from the values shown in Table 3.4 that the these idealised methods for approximating strut elastic modulus consistently significantly over predict strut elastic modulus when compared to the experimentally-evaluated value of 98.87 MPa.

Table 3.4: Summary of values for strut porosity (%).

Material Configuration	E_{eff} (GPa)
Parallel to loading direction, no porosity	6.36
Parallel to loading direction, with porosity	5.75
Perpendicular to loading direction, no porosity	1.07
Perpendicular to loading direction, with porosity	0.84

It should be noted that the porosity measured relates to the reference volume of the strut chosen for the calculation. As stated above, the reference volume was chosen such that the influence of surface roughness was excluded. Should a larger volume have been chosen to include surface roughness then the porosity value would more than likely have been larger. This approach was not adopted here due to the high degree of variation in surface roughness across the sample population, and the related difficulty in choosing a standard volume representative of this population.

The XMT scans reveal that strut microstructure is inhomogeneous by nature and may play a role in the mechanical behaviour of the sintered material. Micromechanical modelling methods were successfully employed to calculate effective isotropic constants E_{eff} and v_{eff} for material segments. It can be approximated that E_{eff} increases linearly with increasing grey-value, which is expected as the grey-value of

the stiffer β-TCP particles is greater than the grey-value of the softer PCL regions. This means that increasing grey-value indicates increasing β-TCP content, resulting in increased stiffness. Consideration of Figure 3.17(b) and Figure 3.18(b) would appear to indicate that E_{eff} and υ_{eff} are not hugely sensitive to changes in average grey-value over the range considered. E_{eff} has an increase of only 97.02 MPa (35%) over an increase of 54.38 (57%) in grey-value, while υ_{eff} increases from 0.2393 to 0.3517 over a 57% increase in grey-value. For example the maximum value of E_{eff} is still far lower than that estimated by the rule of mixtures (E_{RoM}).

The relationships between the elastic constants and average grey-value were then used to assign element-specific effective elastic properties to the full strut meshes to determine strut effective stiffness. The use of E_{eff} and υ_{eff} was found to be the most accurate method of assigning elastic constants explored here with no statistical difference between the experimental strut modulus and the computational strut modulus. This microstructure-based method of using micromechanical models to inform the appropriate local mechanical properties in the full strut model gives improved accuracy in modelling this type of SLS fabricated scaffold material in comparison to other methods explored here as these were either not representative of the real sintered material or significantly overestimated the strut stiffness. Using E_{eff} and υ_{eff} gives a method of incorporating the β-TCP phase in the material while giving an accurate representation of the real mechanical behaviour of the sintered material.

The results of the simulations using E_{eff} and υ_{eff} were compared to those of simulations using homogeneous assignment of $E_{\text{eff}}^{\text{MIN}}$, $E_{\text{eff}}^{\text{MAX}}$ and $E_{\text{eff}}^{\text{MEAN}}$ and $\upsilon =$

0.3 in Figure 3.19. The closest estimate of the experimentally observed strut effective modulus is given by $E_{\text{eff}}^{\text{MIN}}$ while both $E_{\text{eff}}^{\text{MEAN}}$ and $E_{\text{eff}}^{\text{MAX}}$ give less accurate estimations of strut stiffness with higher values than strut stiffness evaluated using E_{eff} and υ_{eff}. If grey-value throughout the strut was uniform and equal to the mean value of the grey-value range considered here (mean of range 93 to 150), it would be safe to assume that the best approximation of the experimental modulus would be given by $E_{\text{eff}}^{\text{MEAN}}$. This is not the case here and the strut modulus generated using E_{eff} is in fact closest in value to that generated using a homogenous assignment of $E_{\text{eff}}^{\text{MIN}}$, indicating that the majority of elements in the strut have a grey-value at the lower end of the range of grey-values. The situation might be quite different if for example the distribution of grey-values in the strut models was predominantly towards the higher end of the range; in this case a homogeneous assignment of $E_{\text{eff}}^{\text{MAX}}$ might be closest to E_{eff} in terms of strut modulus prediction. The implication is that it would not be sufficiently accurate to take a simple approach and assume that one can use a homogeneous $E_{\text{eff}}^{\text{MEAN}}$ to accurately predict strut modulus, even though as observed above the dependence of E_{eff} on GV_{ave} does not appear to be particularly strong. On the contrary, the indications are that an element-specific elastic property (E_{eff} and υ_{eff}) assignment by average grey-value is required for accuracy.

To explore this further, simulations were also carried out using a constant Poisson's ratio of 0.3 and an element-specific E_{eff}, $E_{\text{eff}}^{0.3}$, see Figure 3.19, giving an almost identical strut effective modulus to that of E_{eff} and υ_{eff} when compared using an unpaired T-test (P = 0.9479, n = 4) with no statistical difference from the experimentally observed modulus (P = 0.0555). This means that for the prediction of

strut stiffness the variation of elastic modulus with grey-value is more significant than the variation of Poisson's ratio with grey-value. In fact, this result may indicate that it is acceptable to assume a homogeneous Poisson's ratio in this type of analysis, however this may just be the case for this material and the validity of using a constant Poisson's ratio should be determined for the specific material being studied. In relation to the potential acceptability of using a homogeneous Poisson's ratio, the same cannot be said for elastic modulus; even though the dependence of E_{eff} on GV_{ave} may not be that strong (Figure 3.17(b)), the variation is sufficient to generate a noticeable effect at the macro-scale (full strut model stiffness), as represented by the ${E_{\text{eff}}}^{\text{MIN}}$, ${E_{\text{eff}}}^{\text{MAX}}$ and ${E_{\text{eff}}}^{\text{MEAN}}$ cases in Figure 3.19.

The microstructure-based modelling implementation reported here is specific to the constituent material properties and the ratio of powder blend used. In order to be accurate for different powder blends, micromechanical analysis of the specific sintered material is required to identify the relationship between grey-value and elastic constants specific to that material. The direction of sintering may also influence the accuracy of this method, as previous studies have shown that the density and overall mechanical properties of solid sintered parts can vary with orientation of the sintered part in the part bed, i.e. whether the part oriented is parallel or perpendicular to the laser path (Eshraghi and Das 2010). However, this variation is presumably due to variations in local densities in the directions parallel or perpendicular to the laser path and density is directly related to grey-value. As E_{eff} and υ_{eff} are controlled by grey-value, it is expected that this method would be sensitive enough to capture these differences provided that sufficient mesh resolution is obtained to capture local variations in density.

As discussed above, the resulting geometries of selective laser sintered products, as used in this study, are not the same as the idealised CAD geometries from which they were designed. Idealised microstructures were used in FE modelling of idealised sintered PCL/HA scaffold geometries to predict the effect of varying percentages of HA on scaffold stiffness by Eshraghi et al (Eshraghi and Das 2012). The lack of realistic geometries and microstructures in their study may account for some of the discrepancies between computational and experimental results. The present study is based on similar principles, but includes high resolution FE meshes to account for the real geometry of the sintered materials and incorporates micromechanical models developed using real as opposed to idealised microstructure geometries to capture the real geometries on both the macro- and micro-scale as accurately as possible. Harrison et al. included the influence of locally-varying mechanical properties on macro-scale mechanical behaviour of trabecular bone by using voxel-specific mechanical properties determined using nanoindentation (Harrison et al. 2008). In a similar approach, Scheiner et al. used the Mori-Tanaka scheme to generate and assign homogenised voxel-specific properties based on grey-value to include the influence of material microstructure on the mechanical performance of glass-ceramic scaffolds and found good correlation between computational results and ultrasonic measurements (Scheiner et al. 2009). Here, voxel- or element-specific assignment of material properties has also been incorporated in order to account for variations in local mechanical properties due to variations in material distributions. However, effective material properties have been generated from microstructural models that are specific to the real geometry of the material microstructure to account for the highly heterogeneous and complex nature

of the microstructure of this sintered material. By including both real micro- and macro-scale geometries and locally-varying mechanical properties, a method has been developed that is capable of accounting for the influence of both the influence of microstructural geometries and stiffness on the macro-scale behaviour of these sintered PCL/β-TCP scaffold materials. An advantage of the microstructure-based method that has been developed here is that information about local stiffness at the level of cells seeded on a scaffold is retained through element-specific assignment of material properties. This has significance as it has been shown that local stiffness influences tissue differentiation (Engler et al. 2006); in particular, regions of high material stiffness can act as nucleation sites for mineralisation and new bone formation (Bhumiratana et al. 2011). Using the methods presented here, information about local stiffness could, in theory, be used to direct tissue differentiation in studies looking at tissue formation in a scaffold-filled defect.

The strength of the bonding between the PCL and β-TCP particles in this material was not considered in this study. As the β-TCP particles do not undergo sintering during fabrication, it is unlikely that a strong adhesive bond is formed between the two materials; therefore delamination between PCL and β-TCP particles in the material may occur in the material under tensile loading. This effect was not accounted for in the models presented here; however, as the macro-scale tensile strain that is imposed is only 1%, it is not expected that particle delamination would have a significant effect on the results of this chapter. Incorporating the possibility of delamination occurring in FE models of this material at the micro-scale may contribute to a better understanding of the overall mechanical performance of this type of composite SLS material.

In this study, the modelling methods presented here have been demonstrated to accurately predict the macro-scale mechanical behaviour of SLS scaffold material when compared with the results of tensile tests on the actual material. This has been achieved by attempting to accurately capture the micro-scale architecture and composition of the material in microstructure-based models. Given that these models have now been generated and have been validated by their accurate prediction of experimentally measured (macro-scale) mechanical behaviour, the use of these models for other purposes relevant to tissue engineering scaffold mechanics could be considered. Chief among these is the characterisation and quantification of the micro-scale strain and stress state in the material and at the pore surfaces, to get a direct understanding of the micro-biomechanical stimuli that cells will experience when seeded in the scaffold. This has significant implications for scaffold design.

3.6 Conclusions

A novel method to improve the ability of FE models to capture the real mechanical behaviour of selective laser sintered materials is presented in this chapter. The elastic moduli of PCL and 50/50wt% PCL/β-TCP struts were determined using uniaxial tensile testing. Micromechanical segment models of the material equal in size to one element in the full strut models were generated from XMT scans, capturing the real material microstructure including porosity and β-TCP particles. Micromechanical modelling methods were used to determine a relationship between grey-value and effective isotropic elastic constants these segment.

Tensile simulations of four macro-scale strut models, generated from μ-CT scans, were carried out with three different material assignment methods. The traditional rule of mixtures method for modelling composite materials was shown to be inaccurate for this type of material as it significantly overestimated the strut modulus. The use of solid PCL properties gave a good estimate of strut modulus; however it is not representative of the real material as it does not account for the presence of the β-TCP phase in the material. There was no statistical difference between the experimentally evaluated strut modulus and a computationally evaluated modulus from simulations using element-specific elastic constants assigned based on grey-value. These results indicate that the microstructure-based approach of incorporating micro-scale mechanical analysis of the sintered scaffold material in macro-scale FE modelling of sintered structures gives an accurate prediction the mechanical behaviour of these sintered structures.

The microstructure-based methodology presented in this chapter is utilised in Chapter 4 where a multi-scale analysis of 90/10wt% PCL/β-TCP SLS struts is carried out. While the aim of this chapter was to develop a methodology to accurately predict the stiffness of 50/50wt% PCL/β-TCP struts, the objectives of Chapter 4 are to determine if the relationship between E_{eff} and GV_{ave} is the same for both materials and if the multi-scale, microstructure-based methodology presented in this chapter can be used to accurately predict the stiffness of 90/10wt% struts.

3.7 References

Bhumiratana, S., Grayson, W.L., Castaneda, A., Rockwood, D.N., Gil, E.S., Kaplan, D.L. and Vunjak-Novakovic, G. 2011. Nucleation and growth of mineralized bone matrix on silk-hydroxyapatite composite scaffolds. *Biomaterials* 32(11), pp. 2812–20.

Böhm, H.J. 2004. A Short Introduction to Continuum Micromechanics. In: Bohm, H. J. ed. *Mechanics of Microstructured Materials*. 464th ed. Vienna: CISM Courses and Lectures, Springer-Verlag, pp. 1–40.

Bower, A.F. 2008. Applied Mechanics of Solids [Online]. Available at: http://solidmechanics.org/text/Chapter3_2/Chapter3_2.htm [Accessed: 21 March 2013].

Cahill, S., Lohfeld, S. and McHugh, P.E. 2009. Finite element predictions compared to experimental results for the effective modulus of bone tissue engineering scaffolds fabricated by selective laser sintering. *Journal of Materials Science. Materials in Medicine* 20(6), pp. 1255–62.

Chan, K.S., Liang, W., Francis, W.L. and Nicolella, D.P. 2010. A multiscale modeling approach to scaffold design and property prediction. *Journal of the Mechanical Behavior of Biomedical Materials* 3(8), pp. 584–93.

Chateau, C., Gélébart, L., Bornert, M., Crépin, J. and Caldemaison, D. 2010. Multiscale approach of mechanical behaviour of SiC / SiC composites : elastic behaviour at the scale of the tow. *Technische Mechanik* 30, pp. 45–55.

Chatterjee, K., Sun, L., Chow, L.C., Young, M.F. and Simon, C.G. 2010. Combinatorial screening of osteoblast response to 3D calcium phosphate/poly(ε-caprolactone) scaffolds using gradients and arrays. *Biomaterials* 32(5), pp. 1361–1369.

Chen, B., Sun, K. and Ren, T. 2005. Mechanical and viscoelastic properties of chitin fiber reinforced poly(ε-caprolactone). *European Polymer Journal* 41(3), pp. 453–457.

Engler, A.J., Sen, S., Sweeney, H.L. and Discher, D.E. 2006. Matrix elasticity directs stem cell lineage specification. *Cell* 126(4), pp. 677–89.

Eshraghi, S. and Das, S. 2010. Mechanical and microstructural properties of polycaprolactone scaffolds with one-dimensional, two-dimensional, and three-dimensional orthogonally oriented porous architectures produced by selective laser sintering. *Acta Biomaterialia* 6(7), pp. 2467–76.

Eshraghi, S. and Das, S. 2012. Micromechanical finite-element modeling and experimental characterization of the compressive mechanical properties of

polycaprolactone-hydroxyapatite composite scaffolds prepared by selective laser sintering for bone tissue engineering. *Acta Biomaterialia* 8(8), pp. 3138–43.

Galli, M., Botsis, J. and Janczak-Rusch, J. 2008. An Elastoplastic Three Dimensional Homogenization Model for Particle Reinforced Composites. *Computational Materials Science* 41(March 2007), pp. 312–321.

Guldberg, R.E., Caldwell, N.J., Guo, X.E., Goulet, R.W., Hollister, S.J. and Goldstein, S. a 1997. Mechanical stimulation of tissue repair in the hydraulic bone chamber. *Journal of Bone and Mineral Research* 12(8), pp. 1295–302.

Gupta, K.K., Kundan, A., Mishra, P.K., Sirvastava, P., Mohanty, S., Singh, N.K., Mishra, A. and Maiti, P. 2012. Polycaprolactone composites with TiO 2 for potential nanobiomaterials: tunable properties using different phases. *Physical Chemistry Chemical Physics* 14(37), pp. 12844–12853.

Harrison, N.M., McDonnell, P.F., O'Mahoney, D.C., Kennedy, O.D., O'Brien, F.J. and McHugh, P.E. 2008. Heterogeneous linear elastic trabecular bone modelling using micro-CT attenuation data and experimentally measured heterogeneous tissue properties. *Journal of Biomechanics* 41(11), pp. 2589–96.

Hazanov, S. 1998. Hill condition and overall properties of composites. *Archive of Applied Mechanics* 68, pp. 385–394.

ISO 2012. Plastics - Determination of tensile properties - Part 1: General principles. *ISO 27-1*.

Kanit, T. and Forest, S. 2003. Determination of the size of the representative volume element for random composites : statistical and numerical approach. *International Journal of Solids and Structures* 40, pp. 3647–3679.

Kanit, T., N'Guyen, F., Forest, S., Jeulin, D., Reed, M. and Singleton, S. 2006. Apparent and effective physical properties of heterogeneous materials: Representativity of samples of two materials from food industry. *Computer Methods in Applied Mechanics and Engineering* 195, pp. 3960–3982.

Koike, M., Shimokawa, H., Kanno, Z., Ohya, K. and Soma, K. 2005. Effects of mechanical strain on proliferation and differentiation of bone marrow stromal cell line ST2. *Journal of Bone and Mineral Metabolism* 23(3), pp. 219–25.

Lam, C.X.F., Savalani, M.M., Teoh, S.-H. and Hutmacher, D.W. 2008. Dynamics of in vitro polymer degradation of polycaprolactone-based scaffolds: accelerated versus simulated physiological conditions. *Biomedical Materials* 3(3), p. 034108.

Lee, S.J., Lim, G.J., Lee, J.-W., Atala, A. and Yoo, J.J. 2006. In vitro evaluation of a poly(lactide-co-glycolide)-collagen composite scaffold for bone regeneration. *Biomaterials* 27(18), pp. 3466–72.

Liebschner, M. a K., Müller, R., Wimalawansa, S.J., Rajapakse, C.S. and Gunaratne, G.H. 2005. Testing two predictions for fracture load using computer models of trabecular bone. *Biophysical Journal* 89(2), pp. 759–67.

Liedert, A., Kaspar, D., Blakytny, R., Claes, L. and Ignatius, A. 2006. Signal transduction pathways involved in mechanotransduction in bone cells. *Biochemical and Biophysical Research Communications* 349, pp. 1–5.

Little, U., Buchanan, F., Harkin-Jones, E., McCaigue, M., Farrar, D. and Dickson, G. 2009. Accelerated degradation behaviour of poly(ε-caprolactone) via melt blending with poly(aspartic acid-co-lactide) (PAL). *Polymer Degradation and Stability* 94(2), pp. 213–220.

Lohfeld, S., Cahill, S., Barron, V., McHugh, P., Dürselen, L., Kreja, L., Bausewein, C. and Ignatius, A. 2012. Fabrication, mechanical and in vivo performance of polycaprolactone/tricalciumphosphate composite scaffolds. *Acta Biomaterialia* 8(9), pp. 3446–3456.

Lohfeld, S., Cahill, S., Doyle, H. and McHugh, P. 2014. Improving the Finite Element Model Accuracy of Tissue Engineering Scaffolds Produced by Selective Laser Sintering. *Journal of Materials Science. Materials in Medicine* In Press.

Lohfeld, S., Tyndyk, M.A., Cahill, S., Flaherty, N., Barron, V. and McHugh, P.E. 2010. A method to fabricate small features on scaffolds for tissue engineering via selective laser sintering. *Journal of Biomedical Science and Engineering* 3, pp. 138–147.

Melchels, F.P.W., Tonnarelli, B., Olivares, A.L., Martin, I., Lacroix, D., Feijen, J., Wendt, D.J. and Grijpma, D.W. 2011. The influence of the scaffold design on the distribution of adhering cells after perfusion cell seeding. *Biomaterials* 32(11), pp. 2878–2884.

Mondrinos, M.J., Dembzynski, R., Lu, L., Byrapogu, V.K.C., Wootton, D.M., Lelkes, P.I. and Zhou, J. 2006. Porogen-based solid freeform fabrication of polycaprolactone – calcium phosphate scaffolds for tissue engineering. *Biomaterials* 27, pp. 4399–4408.

Nemat-Nasser, S. and Hori, M. 1993. *Micromechanics: Overall Properties of Heterogeneous Materials*. North Holland.

Ng, C.S., Teoh, S.H., Chung, T.S. and Hutmacher, D.W. 2000. Simultaneous biaxial drawing of poly (e-caprolactone) films. *Polymer* 41, pp. 5855–5864.

Pahr, D.H. and Zysset, P.K. 2008. Influence of boundary conditions on computed apparent elastic properties of cancellous bone. *Biomechanics and Modeling in Mechanobiology* 7, pp. 463–476.

Di Palma, F., Guignandon, A., Chamson, A., Lafage-Proust, M.-H., Laroche, N., Peyroche, S., Vico, L. and Rattner, A. 2005. Modulation of the responses of human osteoblast-like cells to physiologic mechanical strains by biomaterial surfaces. *Biomaterials* 26(20), pp. 4249–57.

Roosa, S.M.M., Kemppainen, J.M., Moffitt, E.N., Krebsbach, P.H. and Hollister, S.J. 2010. The pore size of polycaprolactone scaffolds has limited influence on bone regeneration in an in vivo model. *Journal of Biomedical Materials Research. Part A* 92(1), pp. 359–68.

Sabir, M.I., Xu, X. and Li, L. 2009. A review on biodegradable polymeric materials for bone tissue engineering applications. *Journal of Materials Science* 44(21), pp. 5713–5724.

Sandino, C. and Lacroix, D. 2011. A dynamical study of the mechanical stimuli and tissue differentiation within a CaP scaffold based on micro-CT finite element models. *Biomechanics and Modeling in Mechanobiology* 10(4), pp. 565–576.

Scheiner, S., Sinibaldi, R., Pichler, B., Komlev, V., Renghini, C., Vitale-Brovarone, C., Rustichelli, F. and Hellmich, C. 2009. Micromechanics of bone tissue-engineering scaffolds, based on resolution error-cleared computer tomography. *Biomaterials* 30(12), pp. 2411–9.

Shah, M., Ahmed, I., Marelli, B., Rudd, C., Bureau, M.N. and Nazhat, S.N. 2010. Acta Biomaterialia Modulation of polycaprolactone composite properties through incorporation of mixed phosphate glass formulations. *Acta Biomaterialia* 6(8), pp. 3157–3168.

Vance, J., Galley, S., Liu, D.F. and Donahue, S.W. 2005. Mechanical stimulation of MC3T3 osteoblastic cells in a bone tissue-engineering bioreactor enhances prostaglandin E2 release. *Tissue Engineering* 11(11-12), pp. 1832–9.

Wang, C., Zhou, X. and Wang, M. 2004. Influence of sintering temperatures on hardness and Young's modulus of tricalcium phosphate bioceramic by nanoindentation technique. *Materials Characterization* 52(4-5), pp. 301–307.

Williams, J.M., Adewunmi, A., Schek, R.M., Flanagan, C.L., Krebsbach, P.H., Feinberg, S.E., Hollister, S.J. and Das, S. 2005. Bone tissue engineering using polycaprolactone scaffolds fabricated via selective laser sintering. *Biomaterials* 26(23), pp. 4817–27.

Willie, B.M., Ph, D., Yang, X., Kelly, N.H., Han, J., Nair, T., Wright, T.M., Meulen, M.C.H. Van Der and Bostrom, M.P.G. 2010. Cancellous Bone Osseointegration Is Enhanced by In Vivo Loading. *Bone* 16(6).

Wu, F., Liu, C., O'Neill, B., Wei, J. and Ngothai, Y. 2012. Fabrication and properties of porous scaffold of magnesium phosphate/polycaprolactone biocomposite for bone tissue engineering. *Applied Surface Science* 258(19), pp. 7589–7595.

4 Evaluation of a Microstructure-Based Modelling Methodology for PCL/β-TCP SLS Scaffold Materials.

4.1 Chapter Summary

The objectives of this chapter are to determine if the relationship between the material elastic modulus and average grey-value on the micro-scale is the same for poly-ε-caprolactone (PCL)/β-tricalcium phosphate (β-TCP) SLS materials with different volumes of β-TCP particles and to assess the ability of the microstructure-based methodology developed in Chapter 3 to predict the macro-scale effective modulus of SLS struts with different volumes of β-TCP particles. The results of this chapter indicate that the relationship between E_{eff} and GV_{ave} is material-specific and that one definition cannot be used to describe all materials. These results also show that this multi-scale, microstructure-based modelling methodology accurately predicts the effective elastic modulus of SLS struts with different material configurations when a material-specific definition of the relationship between E_{eff} and GV_{ave} is used.

4.2 Introduction

As discussed in previous chapters, the advantages of the SLS fabrication method are that it produces a high degree of repeatability and conformity to the original component design, the flexibility of design possibilities and the range of materials that can be used, including polymers (Yeong et al. 2010; Partee et al. 2006; Goodridge et al. 2012; Franco et al. 2010; Vitor et al. 2007), polymer-ceramic composites (Lohfeld et al. 2012; Zhang et al. 2008; Tan et al. 2003; Eosoly et al. 2012; Das 2008; Eosoly et al. 2010) and metals (Tolochko et al. 2003; Nakamoto et al. 2009). The fabrication of ceramic composite materials using SLS can result in complex material microstructures that are influenced by many factors including particle size, laser power and ceramic content (Caulfield et al. 2007; Lohfeld et al. 2012; Goodridge et al. 2012; Zhang et al. 2008; Das 2008).

As discussed before, the purpose of the incorporation of ceramic particles in polymer-based matrix is to improve material properties by reinforcing the polymer phase, in particular to increase the material elastic modulus (Borbély et al. 2006; Chawla et al. 2006). However, in the case of SLS-fabricated composite materials, the ceramic phase has been shown to act as a barrier to sintering, requiring increased laser power for sintering (Lohfeld et al. 2012). This is due to the difference in sintering temperatures of the polymer and ceramic phases. Sintering of this type of composite material is carried out at temperatures above the melt temperature of the polymer phase but below the melt temperature of the ceramic phase. Therefore the ceramic particles do not get sintered, and act as a physical barrier to the flow and consolidation of the polymer melt. β-TCP particles are commonly included in

orthopaedic scaffolding materials as they have good biocompatibility and osteoconductivity, both on their own and in combination with polymers (Dong et al. 2002; Kang et al. 2011; Wongwitwichot et al. 2010; Rai et al. 2010; Liu et al. 2007; Lu and Zreiqat 2010). While the inclusion of large volumes of β-TCP in polymeric scaffolds is desirable to promote osteoconductivity, the effect of this on the resulting scaffold material properties must be considered.

FE models using 3D CAD geometries have proven to be unable to capture the mechanical behaviour of this type of SLS-fabricated scaffold (Williams et al. 2005; Cahill et al. 2009; Lohfeld et al. 2014) due to the fact that CAD models can only account for the intended scaffold macroporosity but cannot account for any scaffold microporosity or surface roughness that occur as a result of the fabrication process. High resolution FE meshes generated from μ-CT scans of bone tissue engineering scaffolds can overcome this by accurately capturing real scaffold geometries on the macro-scale and micro-scale (Saey and Hutmacher 2005; Van Cleynenbreugel et al. 2006; Sandino and Lacroix 2011; Scheiner et al. 2009; Milan et al. 2010; Williams et al. 2005; Charles-Harris et al. 2007). A methodology to generate effective elastic properties on the micro-scale of 50/50wt% PCL/β-TCP SLS materials using microstructural modelling methods was established in Chapter 3. Heterogeneous material property assignment based on element grey-value was applied in high resolution full strut FE models (macro-scale) generated from μ-CT scans, resulting in an accurate prediction of the experimentally obtained strut elastic modulus.

The overall goals of the study in this chapter are to test the capabilities of the previously developed microstructure-based modelling methodology by applying it to

a similar material with a different polymer-ceramic ratio. Specifically, the first objective of this study is to establish whether the relationship between the material elastic modulus and average grey-value on the micro-scale is the same for SLS materials with different volumes of β-TCP particles. The second objective of this study is to test the ability of this microstructure-based methodology to predict the macro-scale strut effective modulus of the materials. The validity of these models is assessed by comparing the predicted macro-scale strut effective modulus of 90/10wt% PCL/β-TCP struts with the experimentally evaluated strut modulus.

4.3 Materials and Methods

4.3.1 Materials, Fabrication and Tensile Testing

Single bone tissue engineering scaffold struts were fabricated in ladders of struts as described in Chapter 3. Briefly, PCL powder (CAPA6506, Solvay, UK) with a particle size of 50-100 μm and β-TCP (Fluka) with a particle size of 3-5 μm were mixed in a 90/10wt% ratio (approximately 5 vol% β-TCP) using a hand mixer for five minutes until well blended to give a 90/10wt% PCL/β-TCP powder mix. This PCL particle size is the same as used in the fabrication of full 90/10wt% scaffolds by Lohfeld et al. (Lohfeld et al. 2010). Individual struts with a rectangular cross section of 0.77 mm x 0.55 mm and length of 13 mm were fabricated in ladders of struts using SLS with the Sinterstation 2500^{plus} system (DTM, USA) with a powder layer thickness of 0.11 mm.

The elastic modulus of the 90/10wt% PCL/β-TCP struts was evaluated using uniaxial tensile testing on a Zwick biaxial testing machine at a strain rate of 1% of the gauge length per minute. Tensile samples were prepared by gluing each strut end

inside small diameter stiff plastic tubes, which were then gripped directly to prevent damage to the strut at the grips as previously described in Chapter 3. Strain was measured using a calibrated video extensometer camera and dimensions were measured prior to testing using the calibrated video extensometer camera. Tensile tests were carried out as per ISO 527-1 (ISO 2012).

4.3.2 Structural and Morphological Characterization

High resolution scans of the 90/10wt% single scaffold struts (macro-scale scan) were obtained using a μ-CT scanner (SkyScan-1072 High-resolution desk-top μ-CT system, University of Aberdeen, UK) with a voxel size of 14.65 μm. In addition a higher resolution CT scan of the 90/10wt% material (micro-scale scan) was obtained from a small segment of a 90/10wt% strut (approximate dimensions 0.77 mm x 0.1 mm x 0.1 mm) using X-ray micro-computed tomography (XMT) (phoenix nanotom®, GE, at SEAM, Waterford Institute of Technology, Ireland) with a voxel size of 0.83 μm. All scanning was carried out on struts that had not been tensile tested but that were fabricated in the same batch as the tensile specimens in Section 4.3.1.

4.3.3 Micromechanical Modelling Analysis

A micromechanical modelling study was conducted to determine the relationship between material modulus (E_{eff}) and average grey-value (GV_{ave}) on the micro-scale, according to the methods developed in Chapter 3. FE models of cuboidal material segments were generated from the micro-scale scan (voxel size 0.83 μm) using MIMICS software (Materialise, Belgium) with segment dimensions approximately

equal to one element in the full strut models described in Section 4.3.4 (edge length 29.05 μm). The PCL and β-TCP phases were represented as separate materials in one meshed part and the average μ-CT scan grey-value was calculated for each segment. A FE mesh with 8-noded hexahedral voxel elements with reduced integration was generated for each segment. Linear elastic material properties and a Poisson's ratio of 0.3 were assumed for both phases. The elastic modulus of cast PCL determined in Chapter 3 (E_{PCL} = 277MPa) and a β-TCP elastic modulus ($E_{\text{β-TCP}}$) of 24.6 GPa were assumed (Wang et al. 2004). Abaqus/Standard V6.10 (DS SIMULIA, USA) was used for the FE simulations with the NLGEOM option selected to account for large deformations should they occur locally in the material. A total of 21 segment models were generated, with average segment grey-values ranging from 100 to 141. The 21 meshed segments are shown in Figure 4.1. Following the approach used in Chapter 3, these were divided into seven levels based on GV_{ave}, with three segments per level in order to represent possible variations in material composition.

The "windowing approach" described in Chapter 3 was used to generate the effective elastic modulus (Nemat-Nasser and Hori 1993; Hazanov 1998; Böhm 2004). The windowing approach involves the application of three types of uniform boundary conditions: kinematic, static and mixed uniform boundary conditions. As described in Chapter 3, for kinematic uniform boundary conditions (KUBC) a macroscopically homogeneous strain tensor, $\boldsymbol{\varepsilon}$, is imposed on all boundaries, whereas for static uniform boundary conditions (SUBC) a macroscopically homogeneous stress tensor, $\boldsymbol{\sigma}$, is imposed on all boundaries. Mixed uniform boundary conditions (MUBC) are a

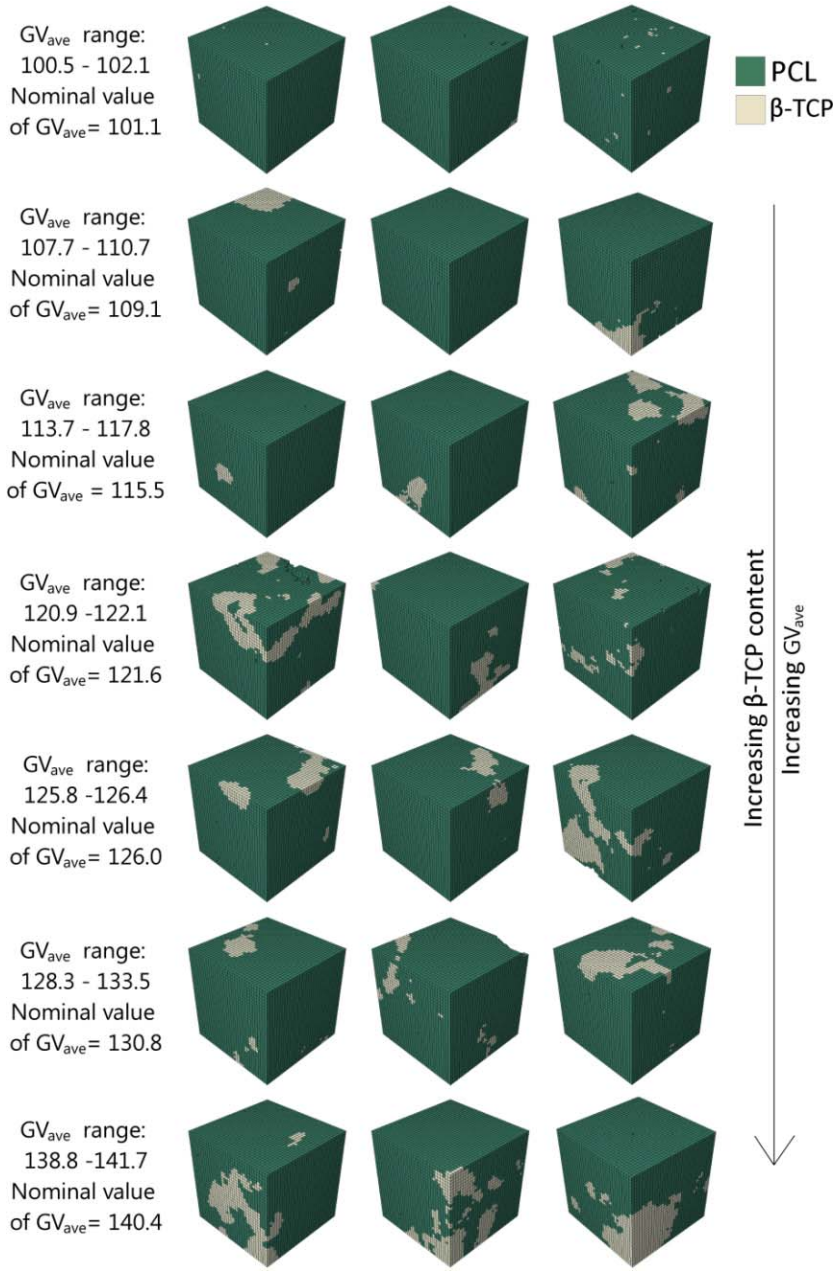

Figure 4.1: FE mesh of each individual segment used in the micromechanical analysis of the 90/10wt% material, with average segment grey-values (GV_{ave}) ranging from 100.5 to 141.7. These were divided into seven grey-value levels with a GV_{ave} range for each level, as shown. A nominal value of GV_{ave} for each level was calculated as the average of the GV_{ave} value range for that level. Note that β-TCP is not visible on the surface of some segments due to the low volume of β-TCP in the segment.

combination of KUBC and SUBC. In this case, boundary conditions are only assigned to the faces perpendicular to the loading direction allowing the other four faces to freely deform, resulting in zero stresses and non-zero strains on non-loaded faces. It was established in Chapter 3 that E_{eff} evaluated using MUBC falls between E_{eff} evaluated using KUBC and SUBC, and that it can be used to predict the macro-scale elastic properties of sintered struts. For this reason, MUBC are used to evaluate E_{eff} in this study.

MUBC were applied to each segment, and tensile simulations in 1, 2 and 3 directions as well as shear simulations in the 1-2, 2-3 and 3-1 planes were carried out for each segment. The effective isotropic elastic modulus, E_{eff}, was evaluated for each segment using strain energy density equivalence as described in Chapter 3.

4.3.4 Computational Modelling of Full Strut Geometries

High resolution FE models of the 90/10wt% full scaffold struts with a voxel size of 29.3 μm were generated from μ-CT scans using MIMICS software; the voxel size was increased from 14.65 μm to reduce the computational cost of running the models. Reduced integration 8-noded hexahedral voxel elements were used for each strut model. Meshes were generated for four individual struts, and tensile tests of each scaffold strut were simulated to replicate the experimental test set-up as described in Section 4.3.1, as per Chapter 3. Strain in the strut gauge length was calculated from the displacement of two nodes at a distance of 8 mm apart, representative of the measurement of nominal strain in experimental tensile tests of the 90/10wt% struts (Section 4.3.1). Nominal strain (ε) was calculated as the change in distance between these two nodes during the simulation and dividing by the

original distance between these nodes. Stress (σ) was calculated as the total reaction force divided by the average cross-section area, and the strut effective modulus E was calculated as $E = \sigma/\varepsilon$.

The elastic modulus for each individual element of each strut model was assigned based on the grey-value of that element and the E_{eff} - GV_{ave} relationship generated using the micromechanical models, as described in Section 4.3.3 (see Figure 4.2, which will be discussed in more detail below in Section 4.5 Results). This is the microstructure-based property assignment approach introduced in Chapter 3. The element-specific modulus values were assigned to the full strut models based on GV_{ave} using MIMICS software. For comparison, simulations of all four strut geometries were carried out where the elastic modulus value of cast PCL (E_{PCL} = 277 MPa, Chapter 3) was uniformly assigned to the individual elements in each strut. It should be noted that this method is not representative of the real material as it does not account for the β-TCP phase. However, as PCL constitutes approximately 95% of the volume of this material it is anticipated that that the material properties of the PCL component would dominate the overall strut mechanical behaviour, therefore E_{PCL} is included for comparison purposes. In all cases isotropic linear elastic constants were used with a Poisson's ratio υ = 0.3 (Eshraghi and Das 2010).

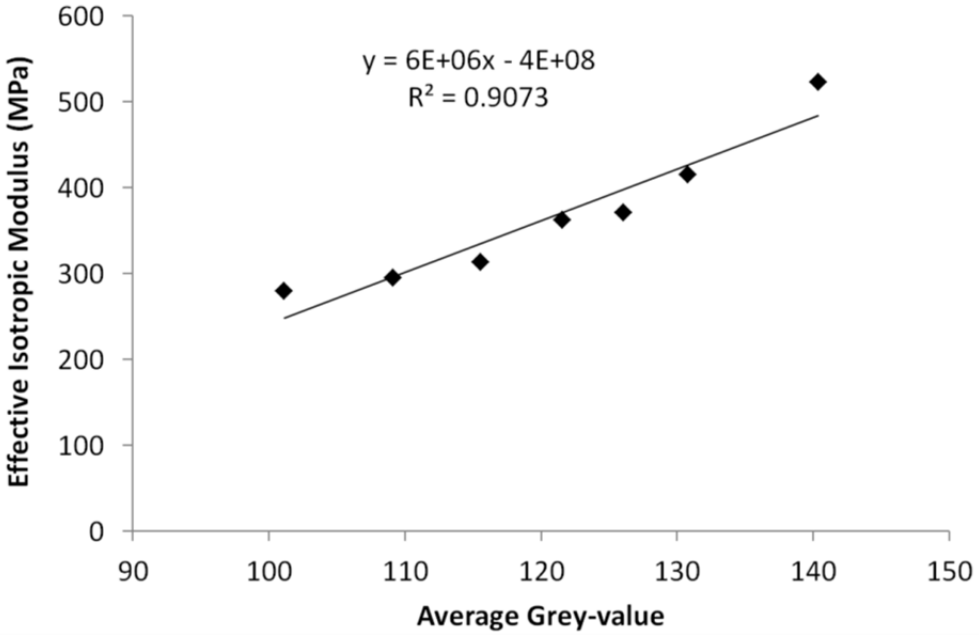

Figure 4.2: Average effective isotropic elastic modulus (E_{eff}) versus nominal average segment grey-value (GV_{ave}) for each of the seven average grey-value levels, for 90/10wt% PCL/β-TCP, showing the linear relationship between E_{eff} and GV_{ave}.

4.4 Degree of Anisotropy

Isotropic elastic properties are assumed in all macro-scale full strut models (Section 4.3.4) as the voxel grey-value is the only information available, i.e. no directional information is available. In order to validate assumption of isotropy, the degree of anisotropy (A) of the micro-scale segment models was calculated using the method outlined by Kanit et al. (Kanit et al. 2006) where anisotropy is calculated as a function of the 3D material stiffness matrix $\widetilde{\boldsymbol{D}}$, as opposed to calculating anisotropy in a given plane as is common elsewhere (Sone and Zoback 2013; Baron et al. 2007; Gassan et al. 2001; Ni and Chiang 2007). Simulations of seven micromechanical

segments of the 90/10wt% material, one segment from each average grey-value level, were carried out using KUBC (Kanit et al. 2006). The values of A for segments of the 50/50wt% material used in Chapter 3 were also evaluated for comparison purposes. The anisotropy value is calculated from Equation (4.2), where Y_{11}, Y_{12} and Y_{44} are calculated from $\widetilde{\boldsymbol{D}}$ (Equation (4.1)) using Equations (4.3) - (4.5), where A =1 for an isotropic material. $\widetilde{\boldsymbol{D}}$ was introduced in its simplest isotropic form in Chapter 2, but here it is used in its more general anisotropic form.

$$\begin{bmatrix}\sigma_{11}\\ \sigma_{22}\\ \sigma_{33}\\ \sigma_{12}\\ \sigma_{23}\\ \sigma_{31}\end{bmatrix} = \begin{bmatrix}\widetilde{D}_{11} & \widetilde{D}_{12} & \widetilde{D}_{13} & \widetilde{D}_{14} & \widetilde{D}_{15} & \widetilde{D}_{16}\\ & \widetilde{D}_{22} & \widetilde{D}_{23} & \widetilde{D}_{24} & \widetilde{D}_{25} & \widetilde{D}_{26}\\ & & \widetilde{D}_{33} & \widetilde{D}_{34} & \widetilde{D}_{35} & \widetilde{D}_{36}\\ & & & \widetilde{D}_{44} & \widetilde{D}_{45} & \widetilde{D}_{46}\\ & & & & \widetilde{D}_{55} & \widetilde{D}_{56}\\ & & & & & \widetilde{D}_{66}\end{bmatrix}\begin{bmatrix}\varepsilon_{11}\\ \varepsilon_{22}\\ \varepsilon_{33}\\ \gamma_{12}\\ \gamma_{23}\\ \gamma_{31}\end{bmatrix} \tag{4.1}$$

$$A = \frac{2Y_{44}}{Y_{11} - Y_{12}} \tag{4.2}$$

$$Y_{11} = \frac{\widetilde{D}_{11} + \widetilde{D}_{22} + \widetilde{D}_{33}}{3} \tag{4.3}$$

$$Y_{11} = \frac{\widetilde{D}_{11} + \widetilde{D}_{22} + \widetilde{D}_{33}}{3} \tag{4.4}$$

$$Y_{44} = \frac{\widetilde{D}_{44} + \widetilde{D}_{55} + \widetilde{D}_{66}}{3} \tag{4.5}$$

4.5 Results

4.5.1 Materials, Fabrication and Tensile Testing

Single bone tissue engineering scaffold struts were successfully fabricated from a 90/10wt% PCL/β-TCP powder mixture using SLS. The experimentally determined

elastic modulus of the 90/10wt% struts was found to be 123.51 ± 30.20 MPa (n=16). The experimentally determined elastic modulus of 50/50wt% struts was evaluated in Chapter 3 of this thesis, giving 98.87 ± 22.59 MPa (n = 7).

4.5.2 Structural and Morphological Characterization

High resolution micro-scale scan images of the 90/10wt% material are shown in comparison with micro-scale scan images for the 50/50wt% material, generated in Chapter 3, in Figure 4.3, showing inhomogeneous microstructures for both 90/10wt% and 50/50wt% SLS materials. The β-TCP content and particle sizes in the 90/10wt% struts are the same as those used to fabricate full 90/10wt% PCL/β-TCP scaffolds for the *in vivo* study of Lohfeld et al. (Lohfeld et al. 2010), discussed previously, whereas a reduced PCL particle size was required for the fabrication of 50/50wt% PCL/β-TCP struts in Chapter 3 in order to achieve sintering with increased β-TCP content. A smaller volume of individual β-TCP particles is visible in the scan image of the 90/10wt% material, as expected from the lower % composition in this material. Small agglomerations of β-TCP are visible as bright regions and porous regions are visible as darker regions in both scan images. The small β-TCP particles in the 90/10wt% material are located along the outside of the larger PCL particles and in 'seams' along the interface between sintered PCL particles in fully-sintered regions. In contrast, the small β-TCP particles in the 50/50wt% material are more interspersed throughout the material, likely as a result of the smaller PCL particles.

4.5.3 Micromechanical Modelling Results

Micromechanical modelling results for the 90/10wt% material, carried out for the twenty one segments using MUBC, are presented in terms of the seven grey-value levels in Figure 4.2. As for Chapter 3, the average E_{eff} and nominal GV_{ave} for each grey-value level was calculated and the line fit in Figure 4.2 gives a linear relationship between E_{eff} and GV_{ave}. This established relationship between E_{eff} and GV_{ave} for the 90/10wt% material is shown in Figure 4.4 in comparison to the equivalent relationship for the 50/50wt% material established in Chapter 3. The slope is greater for the 90/10wt% material, indicating that the change in E_{eff} with increasing GV_{ave} is greater for the 90/10wt% material than the 50/50wt% material.

4.5.4 Full Strut Modelling

Full strut FE models were successfully generated for the 90/10wt% full scaffold struts using MIMICS software. Section view images of the strut FE model geometry of a 90/10wt% strut and a 50/50wt% strut are shown in Figure 4.5, with regions of stiff material highlighted by a lighter grey and regions of softer materials marked by darker greys. A greater amount of porosity along the loading axis is visible in the 50/50wt% strut than the 90/10wt% strut. The volume percentage of elements within each grey-value level for each strut model type is shown in Figure 4.6. A similar distribution of elements is observed for each material however the greatest percentage of elements in the 90/10wt% struts are at a grey-value of approximately 100, whereas the greatest percentage of elements in the 50/50wt% struts have a lower grey-value of approximately 70.

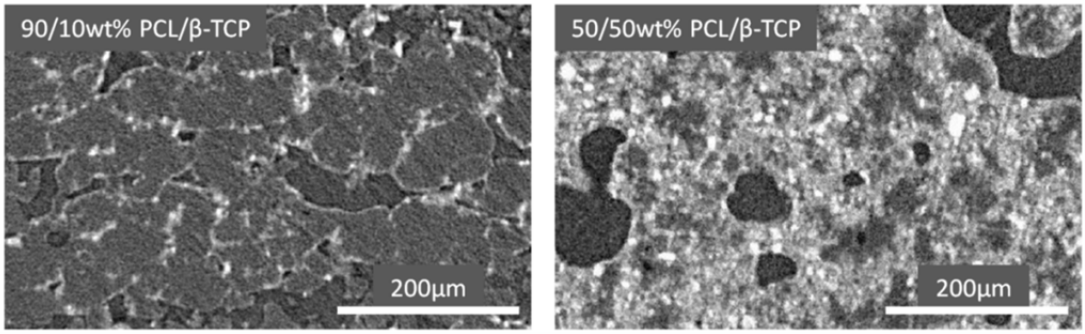

Figure 4.3: High resolution micro-scale scans of the 90/10wt% PCL/β-TCP material (left) and the 50/50wt% PCL/β-TCP from Chapter 3 (right). β-TCP particles are visible as bright regions in the scans, with PCL material visible as grey regions and pores as dark regions in the scans.

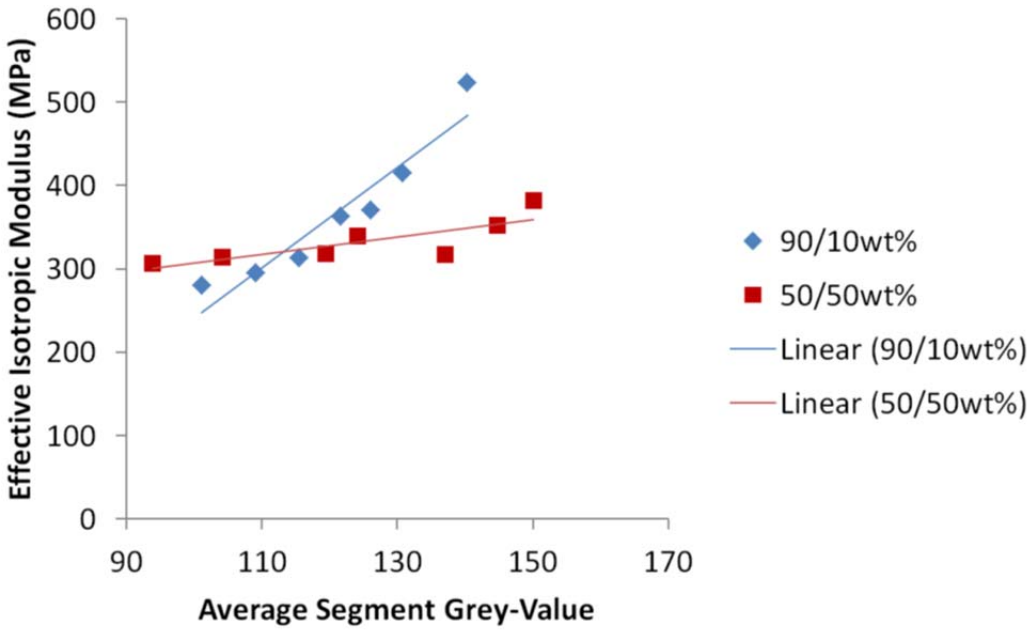

Figure 4.4: Average effective isotropic elastic modulus (E_{eff}) versus nominal average segment grey-value (GV_{ave}) for each of the seven average grey-value levels for the 90/10wt% material and the 50/50wt% material (Chapter 3), showing the linear relationship between E_{eff} and GV_{ave}. The dependence of segment E_{eff} on GV_{ave} is greater for the 90/10wt% material than for the 50/50wt% material.

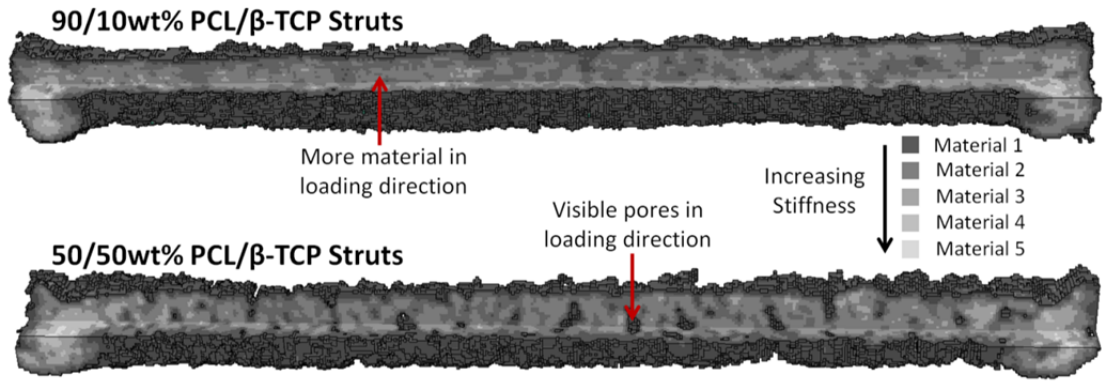

Figure 4.5: Section view of 90/10wt% struts (top) and 50/50wt% struts (bottom) showing material property assignment. Differences in strut geometry are visible, with a greater amount of material along the strut length for the 90/10wt% struts and visible pores along the strut length in the 50/50wt% struts.

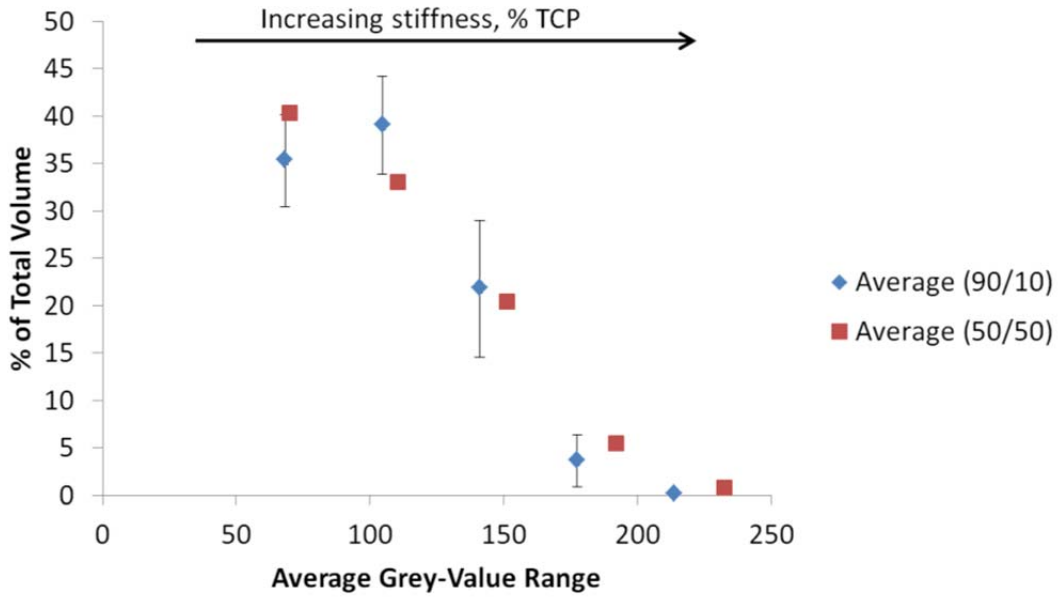

Figure 4.6: Element grey-value distribution in full strut FE models for both the 90/10wt% and 50/50wt% struts (average over four struts for each strut type). Mean values for each data set are shown and error bars represent standard deviation.

The experimentally evaluated elastic modulus of the 90/10wt% struts was evaluated as 123.51 ± 30.20 MPa (n = 16); the elastic modulus of 50/50wt% struts was measured as 98.87 ± 22.59 MPa (n = 7) in Chapter 3 of this thesis. The strut effective modulus calculated from tensile simulations of the 90/10wt% struts with a range of input mechanical properties are shown in comparison with the experimental strut modulus in Figure 4.7. Computational strut models using the microstructure-based methodology accurately predict strut stiffness for both the 90/10wt% and the 50/50wt% struts. However, the use of homogeneous PCL elastic properties in the same strut FE mesh geometries does happen to predict strut stiffness for the 50/50wt% struts, strut stiffness is over-predicted for the 90/10wt% struts. Analysis of the results show no statistical difference between the experimental strut modulus and the effective strut modulus of the 90/10wt% struts (n = 4) evaluated using the microstructure-based method when compared using a Mann-Whitney test (p-value = 0.1190). A non-parametric test was used due to low sample numbers. The computational and experimental strut effective modulus values of the 50/50wt% struts, generated in Chapter 3, are included for comparison purposes. Results for the 50/50wt% struts show no statistical difference between the experimental strut modulus and the effective strut modulus (n = 4) evaluated using the microstructure-based method when compared using a Mann-Whitney test (p-value = 0.0726). It is clear from the figure that the heterogeneously assigned material properties generated from micromechanical modelling give the most accurate prediction of strut elastic modulus.

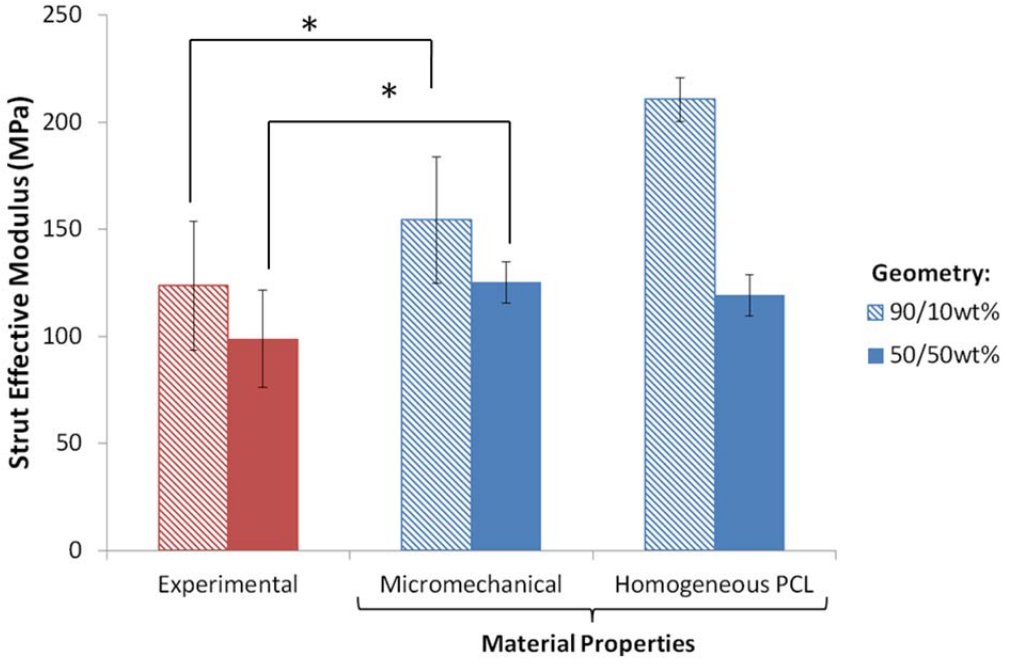

Figure 4.7: Full strut computational model results for 90/10wt% and 50/50wt% PCL/β-TCP struts (n = 4 for all computational models). For experimentally evaluated strut modulus values, n = 16 (90/10wt% struts) and n = 7 (50/50wt% struts). Mean values for each data set are shown and error bars represent standard deviation. Models using the microstructure-based material properties best approximate of the experimental result (shown in red) for both strut types. *p > 0.05.

4.5.5 Degree of Anisotropy

The degree of anisotropy was calculated for micromechanical segments of both the 90/10wt% material used in this study and the 50/50wt% material presented in Chapter 3. The results for both materials are shown in Figure 4.8 with respect to GV_{ave} (Figure 4.8 (A)) and volume % of β-TCP (Figure 4.8 (B)). These results indicate that the segment models for both materials are generally close to isotropy (A = 1), with an average of A = 1.11 for the 90/10wt% material and A = 1.02 for the

50/50wt% material, with the 50/50wt% material being slightly less isotropic. Representative segment model geometries for segments containing small and larger quantities of β-TCP are presented in Figure 4.9 for each material with the internal β-TCP structure highlighted, showing the values of *A* for each segment.

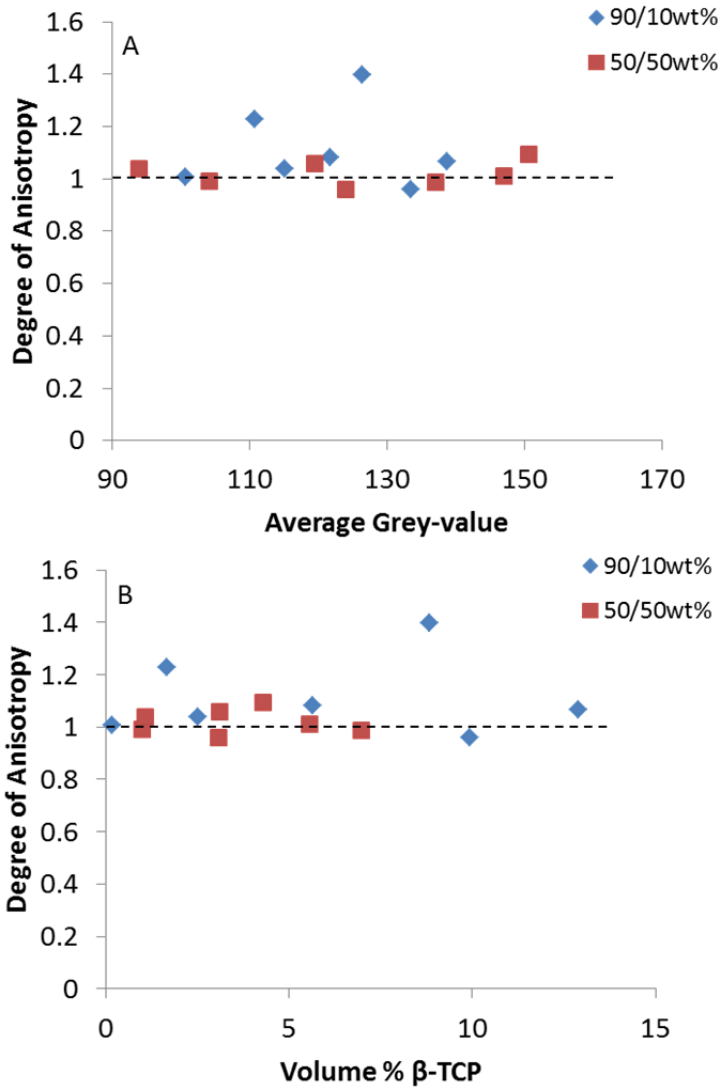

Figure 4.8: Degree of anisotropy (*A*) versus average segment grey-value (A) and volume % β-TCP (B).

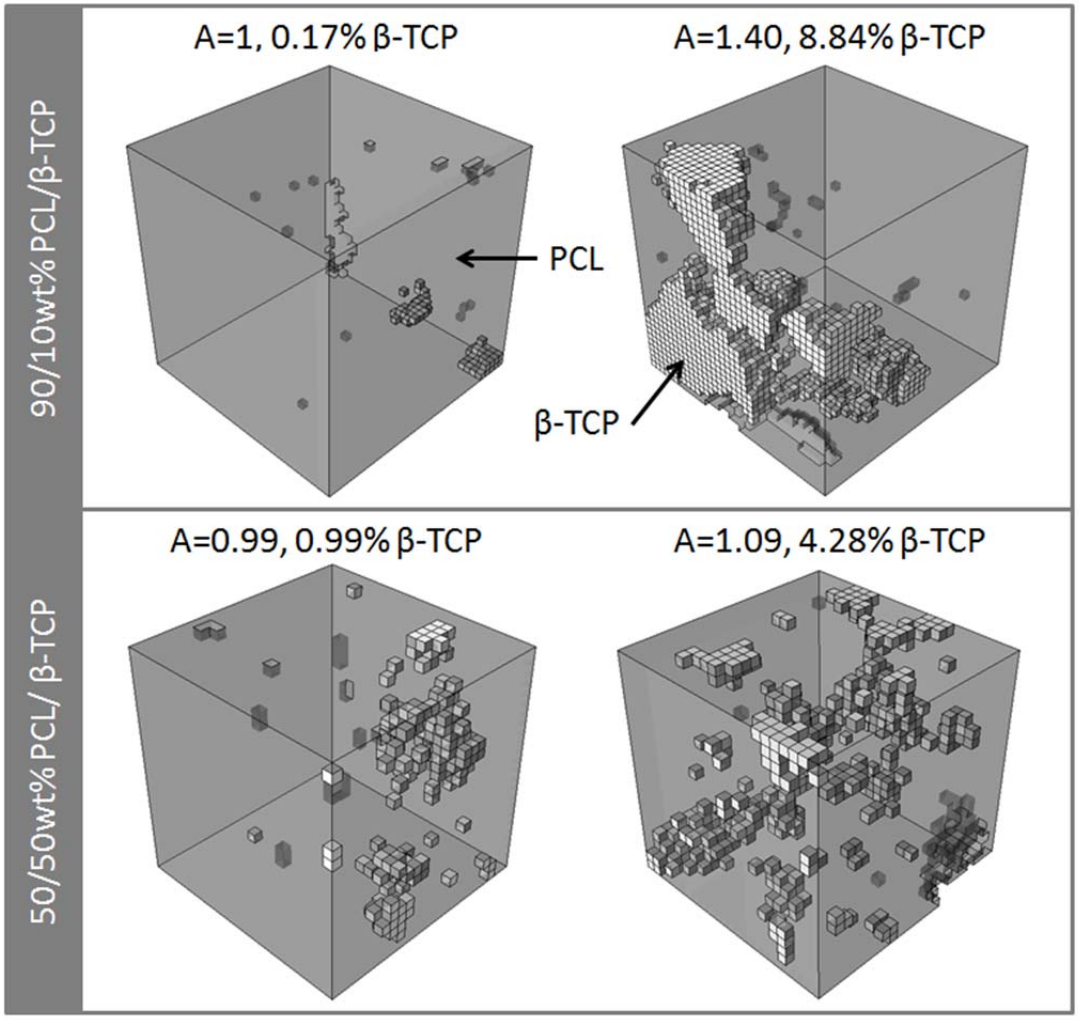

Figure 4.9: Representative micromechanical segment models for 90/10wt% PCL/β-TCP (top) and 50/50wt% PCL/β-TCP (bottom). Highlighted voxel elements represent β-TCP particles and the surrounding shaded grey regions represent PCL. Segments with low volumes of β-TCP (left) are close to being isotropic whereas segments with higher volumes of β-TCP are less isotropic.

4.6 Discussion

The first objective of this study was to determine whether the relationship between E_{eff} and GV_{ave} is the same for SLS materials with different volumes of β-TCP. It is clear from Figure 4.4 that this is not the case. The increase in E_{eff} with increasing grey-value is greater for the 90/10wt% material than for the 50/50wt% material and therefore the E_{eff} - GV_{ave} relationship is specific to each material. This is likely due to the influence of the different material compositions on sintering conditions and on the resulting material microstructures (Figure 4.3). It is clear from Figure 4.4 that the difference in E_{eff} between low and high values of GV_{ave} is greater for the 90/10wt% material than for the 50/50wt% material. This is due to the difference in the distribution of β-TCP particles in the two materials, as seen in Figure 4.3 and in Figure 4.9: β-TCP particles are relatively evenly dispersed throughout the PCL matrix in the 50/50wt% material, whereas β-TCP particles are present in concentrations or 'seams' of material along the edges of PCL particles in the 90/10wt% material. This affects the values of E_{eff} in each material, with a greater dependence of E_{eff} on GV_{ave} for the 90/10wt% material than for the 50/50wt% material, as well as introducing anisotropy in the 90/10wt% material segments, as shown in Figure 4.9.

The R^2 value for the 50/50wt% material (0.55) is significantly lower than for the 90/10wt% material (0.9). It is not clear from the results of this study why this is the case, however this may be caused by differences in material distribution at the micro-scale, as discussed above. This may also be due in part to the specific segments of material that were used for each material type. For this study segments

were selected at random in each case and then grouped into ranges of average grey-value, and it is possible that if different segments were selected the resulting R^2 value would differ from those presented here.

The degree of anisotropy (A) (Kanit et al. 2006) of the micromechanical segments was calculated to evaluate if the use of isotropic elastic moduli is appropriate. The segment models for both materials are generally close to isotropy (A = 1), with average values of $A_{90/10wt\%}$ = 1.11 and $A_{50/50wt\%}$ = 1.02. This verifies the assumption of isotropy for full strut FE models where anisotropy cannot be applied for the simple reason that the only element information available is grey-value and that no directional information is available. Segments generated from the 90/10wt% material are slightly less isotropic than segments generated from the 50/50wt% material (see Figure 4.8). This is seen to be due to the presence of 'seams' of β-TCP along one direction in the 90/10wt% material, for example along the front-facing side of the segment in the top right of Figure 4.9.

The second objective of this study was to determine the ability of this multi-scale modelling methodology to predict the macro-scale strut effective modulus of the SLS materials. The microstructure-based approach to elastic modulus assignment in the full strut simulations gives a more accurate estimate of strut modulus compared to the use of uniform homogeneous elastic modulus values, as shown by comparisons with E_{PCL} in Figure 4.7.

In full strut simulations with homogeneous PCL elastic modulus (Figure 4.7) the effect of macropores and surface roughness are accounted for by the high resolution strut mesh but micro-scale features are not. Using the modulus values presented in

Figure 4.7, the ratio of the 90/10wt% strut modulus to the 50/50wt% strut modulus is 1.77 when homogeneous PCL elastic properties are used, indicating the large effect that the increased number of macropores in the 50/50wt% struts (Figure 4.5) has on reducing the overall strut modulus. However, the value for the 90/10wt% strut modulus is much higher than the experimentally determined value due to the fact that strut microporosity is not accounted for in these models, i.e. the modulus for solid, cast PCL is assigned uniformly to all elements.

In full strut simulations where the microstructure-based elastic moduli are applied (Figure 4.7) the effect of the macropores and the micro-scale features are accounted for, giving a much better representation of the overall material behaviour. The micro-scale features that are captured include the microporosity of the sintered material, which has the effect of reducing the strut modulus compared to the homogeneous PCL properties, and also the reinforcing effect of the β-TCP particles. For these strut models, the ratio of the 90/10wt% strut modulus to the 50/50wt% strut modulus is 1.23, which is close to the value of 1.25 for the experimental results and considerably less than that of the homogeneous PCL models (1.77).

In relation to the micro-scale features, for the 90/10wt% struts, the microporosity of the sintered material has the effect of reducing the overall strut modulus while reinforcing effect of the 10wt% β-TCP is relatively small. For the 50/50wt% struts, again the microporosity of the sintered material has the effect of reducing the strut modulus but the reinforcing effect of the 50wt% β-TCP is much greater than for the 90/10wt% material. For the 50/50wt% struts, it is the reinforcing effect which

dominates, causing a slight increase in the overall strut modulus for the micromechanical model compared to the homogeneous model.

Although the modulus ratio between the 90/10wt% and 50/50wt% struts for the microstructure-based models agrees quite well with the experimental results, the absolute values of the strut modulus are approximately 25% higher in both cases. This may be due to the value of the PCL modulus that was chosen for the micromechanical modelling (E_{PCL} = 277 MPa, Chapter 3) which was based on tensile testing of cast PCL material. It is possible that the modulus of cast PCL is higher than that of PCL which is processed by laser sintering, which would have the effect of increasing the strut elastic modulus in the model results presented in Figure 4.7. The exact processing conditions of PCL during sintering (temperature, duration of exposure, etc.) are not known. However, it should be noted that in order to replicate the conditions as closely as possible, the same PCL powder was used to create the PCL tensile samples and the sintered struts, and a vacuum melt temperature of 120°C was used as per a study by Roosa et al. in which solid PCL samples were fabricated using vacuum moulding (Roosa et al. 2010).

The intention of the methodology presented in this chapter and in Chapter 3 of this thesis is to bridge the size scale difference between element size in the full strut models (element length 28 μm) and β-TCP particles (diameter 3-5 μm) which are visible in the micro-scale models (element length 0.83 - 1.2 μm) but not in the full strut models. For the purpose of this methodology, it was assumed that the grey-value of a pixel (corresponding to one element) in the full strut scan is equal to the average of the grey-values of the materials contained within that element/pixel.

Equivalently, it was assumed that the average grey-value of one micro-scale model segment is equal to the average grey-value of each element within the segment and is proportional to the amount of each constituent material within the segment. It can then be assumed that the grey-value of the micro-scale segments corresponds directly to the grey-value of each element within the full strut models, and allows us to relate the micro-scale-derived material elastic properties to element-specific elastic properties in the full strut models. In theory, it would be possible to verify this assumption by taking CT scan images of a two-phase material at two length scales, micro and macro, such that the region in the micro-scale scan corresponds directly to a known region in the macro-scale scan. The average grey-value in a segment of material in the micro-scale scan that corresponds to one element/pixel in the macro-scale scan can then be calculated. The above assumption is then valid if the average micro-scale segment grey-value is equal to the grey-value of the corresponding element in the macro-scale scan. Variation in grey-value can occur between two scans of the same material when different scanning equipment is used, or even when the same scanner is used due to the use of different scan parameters or an ageing x-ray tube. Therefore, the use of a phantom, i.e. a standard material with known density and geometry, during scanning of materials is recommended to ensure consistency between scans.

It is worth noting that while the two composite SLS materials considered here are referred to by their weight percentage, i.e. 90/10wt% and 50/50wt% PCL/β-TCP, they are not actually as different in volume fraction as these numbers would suggest. A 10wt% of β-TCP corresponds to approximately 5% by volume, and 50wt% of β-TCP corresponds to approximately 25% by volume. These numbers refer to the

weighted amounts of each material prior to mixing or fabrication. The actual volume fractions in the material as measured from the XMT scans are actually lower, as shown for the 50/50wt% case in Fig. 3.9. From this, it can be concluded that there is a lot of variation in the actual volume fraction of β-TCP that is present in the materials. This could be due a number of possible factors in the fabrication process, including inhomogeneous mixing of the powders, settling of the smaller β-TCP particles during sintering, operation of the SLS machine or different amounts of β-TCP particles being picked up by the roller.

As a result of the above, it is difficult to be categorical on the denominations of 50/50wt% or 90/10wt% and these values are very approximate. As you can't assume face value regarding the volume fraction of materials in each SLS material, you have to test each sample down to the level of fine detail, as demonstrated by the multiscale modelling methodology presented here. The two materials considered here may not actually be as different in terms of volume fraction as the labels would suggest. The actual differences in volume fraction may be more related to the material microstructure and the fabrication method, as a result of particle size, particle bonding and clustering, than the actual 50/50wt% and 90/10wt% denominations.

The results of this study have established that the relationship between E_{eff} and average segment grey-value of composite SLS materials is specific to each material configuration and that a 'one size fits all' definition does not apply. The methodology established in Chapter 3 has been used to generate a material-specific definition of the relationship between E_{eff} and average segment grey-value for the 90/10wt% PCL/β-TCP material. This relationship has been shown to successfully

predict the stiffness of 90/10wt% PCL/β-TCP struts by using grey-value specific assignment of elastic properties in full strut simulations. The μ-CT approach to full SLS strut modelling captures variations due to macro-scale features, i.e. macropores and surface roughness, through the use of μ-CT derived high resolution macro-scale FE meshes. Micro-scale features such as microporosity and the presence of β-TCP particles are accounted for in models where the μ-CT derived micromechanical elastic modulus is applied. This would not be possible with CAD based FE modelling, as neither macro-scale nor micro-scale features would be accounted for.

For repetition of the methodology presented here, the following recommendations are advised. A phantom of known density should be included in scans of material microstructure for accuracy. Scan settings, specifically for the highest resolution scans, should be optimised to reduce noise between the relatively low density polymeric material and the surrounding air to streamline model generation. If possible, the micro-scale scan should be taken of a specific region corresponding directly to a known region in the macro-scale scan to allow for comparisons between grey-values at the two length scales.

4.7 Conclusions

The results presented in this chapter indicate that the relationship between elastic modulus and grey-value, as evaluated using micromechanical modelling, is material-specific and that one definition cannot be used to describe the 90/10wt% and the 50/50wt% PCL/β-TCP materials studied in this chapter and in Chapter 3 of this

thesis, respectively. The results of this chapter do however show that the multi-scale modelling framework that has been developed can accurately capture the effective elastic modulus of SLS struts of different materials, when a material-specific definition of the relationship between micro-scale stiffness and grey-value is employed.

4.8 References

Baron, C., Talmant, M. and Laugier, P. 2007. Effect of porosity on effective diagonal stiffness coefficients (cii) and elastic anisotropy of cortical bone at 1 MHz: A finite-difference time domain study. *The Journal of the Acoustical Society of America* 122(3), p. 1810.

Böhm, H.J. 2004. A Short Introduction to Continuum Micromechanics. In: Bohm, H. J. ed. *Mechanics of Microstructured Materials*. 464th ed. Vienna: CISM Courses and Lectures, Springer-Verlag, pp. 1–40.

Borbély, A., Kenesei, P. and Biermann, H. 2006. Estimation of the effective properties of particle-reinforced metal – matrix composites from microtomographic reconstructions. *Acta Materialia* 54, pp. 2735–2744.

Cahill, S., Lohfeld, S. and McHugh, P.E. 2009. Finite element predictions compared to experimental results for the effective modulus of bone tissue engineering scaffolds fabricated by selective laser sintering. *Journal of Materials Science. Materials in Medicine* 20(6), pp. 1255–62.

Caulfield, B., McHugh, P.E. and Lohfeld, S. 2007. Dependence of mechanical properties of polyamide components on build parameters in the SLS process. *Journal of Materials Processing Technology* 182(1-3), pp. 477–488.

Charles-Harris, M., del Valle, S., Hentges, E., Bleuet, P., Lacroix, D. and Planell, J. a 2007. Mechanical and structural characterisation of completely degradable polylactic acid/calcium phosphate glass scaffolds. *Biomaterials* 28(30), pp. 4429–38.

Chawla, N., Sidhu, R.S. and Ganesh, V. V 2006. Three-dimensional visualization and microstructure-based modeling of deformation in particle-reinforced composites. *Acta Materialia* 54, pp. 1541–1548.

Van Cleynenbreugel, T., Schrooten, J., Van Oosterwyck, H. and Vander Sloten, J. 2006. Micro-CT-based screening of biomechanical and structural properties of bone tissue engineering scaffolds. *Medical & Biological Engineering & Computing* 44(7), pp. 517–25.

Das, S. 2008. Selective Laser Sintering of Polymers and Polymer-Ceramic Composites. In: *Virtual Prototyping & Bio Manufacturing in Medical Applications*. pp. 226–260.

Dong, J., Uemura, T., Shirasaki, Y. and Tateishi, T. 2002. Promotion of bone formation using highly pure porous beta-TCP combined with bone marrow-derived osteoprogenitor cells. *Biomaterials* 23(23), pp. 4493–502.

Eosoly, S., Brabazon, D., Lohfeld, S. and Looney, L. 2010. Selective laser sintering of hydroxyapatite/poly-epsilon-caprolactone scaffolds. *Acta Biomaterialia* 6(7), pp. 2511–7.

Eosoly, S., Vrana, N.E., Lohfeld, S., Hindie, M. and Looney, L. 2012. Interaction of cell culture with composition effects on the mechanical properties of polycaprolactone-hydroxyapatite scaffolds fabricated via selective laser sintering (SLS). *Materials Science and Engineering: C* 32(8), pp. 2250–2257.

Eshraghi, S. and Das, S. 2010. Mechanical and microstructural properties of polycaprolactone scaffolds with one-dimensional, two-dimensional, and three-dimensional orthogonally oriented porous architectures produced by selective laser sintering. *Acta Biomaterialia* 6(7), pp. 2467–76.

Franco, A., Lanzetta, M. and Romoli, L. 2010. Experimental analysis of selective laser sintering of polyamide powders: an energy perspective. *Journal of Cleaner Production* 18(16-17), pp. 1722–1730.

Gassan, J., Chate, A. and Bledzki, A.K. 2001. Calculation of elastic properties of natural fibers. *Journal of Materials Science* 6, pp. 3715–3720.

Goodridge, R.D., Tuck, C.J. and Hague, R.J.M. 2012. Laser sintering of polyamides and other polymers. *Progress in Materials Science* 57(2), pp. 229–267.

Hazanov, S. 1998. Hill condition and overall properties of composites. *Archive of Applied Mechanics* 68, pp. 385–394.

ISO 2012. Plastics - Determination of tensile properties - Part 1: General principles. *ISO 27-1*.

Kang, Y., Scully, A., Young, D. a, Kim, S., Tsao, H., Sen, M. and Yang, Y. 2011. Enhanced mechanical performance and biological evaluation of a PLGA coated β-TCP composite scaffold for load-bearing applications. *European Polymer Journal* 47(8), pp. 1569–1577.

Kanit, T., N'Guyen, F., Forest, S., Jeulin, D., Reed, M. and Singleton, S. 2006. Apparent and effective physical properties of heterogeneous materials: Representativity of samples of two materials from food industry. *Computer Methods in Applied Mechanics and Engineering* 195, pp. 3960–3982.

Liu, G., Zhao, L., Cui, L., Liu, W. and Cao, Y. 2007. Tissue-engineered bone formation using human bone marrow stromal cells and novel beta-tricalcium phosphate. *Biomedical Materials* 2(2), pp. 78–86.

Lohfeld, S., Cahill, S., Barron, V., McHugh, P., Dürselen, L., Kreja, L., Bausewein, C. and Ignatius, A. 2012. Fabrication, mechanical and in vivo performance of polycaprolactone/tricalciumphosphate composite scaffolds. *Acta Biomaterialia* 8(9), pp. 3446–3456.

Lohfeld, S., Cahill, S., Doyle, H. and McHugh, P. 2014. Improving the Finite Element Model Accuracy of Tissue Engineering Scaffolds Produced by Selective Laser Sintering. *Journal of Materials Science. Materials in Medicine* In Press.

Lohfeld, S., Tyndyk, M.A., Cahill, S., Flaherty, N., Barron, V. and McHugh, P.E. 2010. A method to fabricate small features on scaffolds for tissue engineering via selective laser sintering. *Journal of Biomedical Science and Engineering* 3, pp. 138–147.

Lu, Z. and Zreiqat, H. 2010. Beta-tricalcium phosphate exerts osteoconductivity through alpha2beta1 integrin and down-stream MAPK/ERK signaling pathway. *Biochemical and Biophysical Research Communications* 394(2), pp. 323–9.

Milan, J.-L., Planell, J.A. and Lacroix, D. 2010. Simulation of bone tissue formation within a porous scaffold under dynamic compression. *Biomechanics and Modeling in Mechanobiology* 9(5), pp. 583–96.

Nakamoto, T., Shirakawa, N., Miyata, Y. and Inui, H. 2009. Selective laser sintering of high carbon steel powders studied as a function of carbon content. *Journal of Materials Processing Technology* 209(15-16), pp. 5653–5660.

Nemat-Nasser, S. and Hori, M. 1993. *Micromechanics: Overall Properties of Heterogeneous Materials*. North Holland.

Ni, Y. and Chiang, M.Y.M. 2007. Prediction of elastic properties of heterogeneous materials with complex microstructures. *Journal of the Mechanics and Physics of Solids* 55(3), pp. 517–532.

Partee, B., Hollister, S.J. and Das, S. 2006. Selective Laser Sintering Process Optimization for Layered Manufacturing of CAPA® 6501 Polycaprolactone Bone Tissue Engineering Scaffolds. *Journal of Manufacturing Science and Engineering* 128(2), p. 531.

Rai, B., Lin, J.L., Lim, Z.X.H., Guldberg, R.E., Hutmacher, D.W. and Cool, S.M. 2010. Differences between in vitro viability and differentiation and in vivo bone-forming efficacy of human mesenchymal stem cells cultured on PCL-TCP scaffolds. *Biomaterials* 31(31), pp. 7960–70.

Roosa, S.M.M., Kemppainen, J.M., Moffitt, E.N., Krebsbach, P.H. and Hollister, S.J. 2010. The pore size of polycaprolactone scaffolds has limited influence on bone regeneration in an in vivo model. *Journal of Biomedical Materials Research. Part A* 92(1), pp. 359–68.

Saey, H. and Hutmacher, D.W. 2005. Application of micro CT and computation modeling in bone tissue engineering. *Computer-Aided Design* 37(11), pp. 1151–1161.

Sandino, C. and Lacroix, D. 2011. A dynamical study of the mechanical stimuli and tissue differentiation within a CaP scaffold based on micro-CT finite element models. *Biomechanics and Modeling in Mechanobiology* 10(4), pp. 565–576.

Scheiner, S., Sinibaldi, R., Pichler, B., Komlev, V., Renghini, C., Vitale-Brovarone, C., Rustichelli, F. and Hellmich, C. 2009. Micromechanics of bone tissue-engineering scaffolds, based on resolution error-cleared computer tomography. *Biomaterials* 30(12), pp. 2411–9.

Sone, H. and Zoback, M.D. 2013. Mechanical properties of shale-gas reservoir rocks — Part 1: Static and dynamic elastic properties and anisotropy. *Geophysics* 78(5), pp. D381–D392.

Tan, K.H., Chua, C.K., Leong, K.F., Cheah, C.M., Cheang, P., Abu Bakar, M.S. and Cha, S.W. 2003. Scaffold development using selective laser sintering of polyetheretherketone–hydroxyapatite biocomposite blends. *Biomaterials* 24(18), pp. 3115–3123.

Tolochko, N.K., Arshinov, M.K., Gusarov, A. V., Titov, V.I., Laoui, T. and Froyen, L. 2003. Mechanisms of selective laser sintering and heat transfer in Ti powder. *Rapid Prototyping Journal* 9(5), pp. 314–326.

Vitor, G., Henrique, C. and Klauss, P. 2007. Rapid Manufacturing of Polyethylene Parts With Controlled Pore Size Gradients Using Selective Laser Sintering. *Materials Research* 10(2), pp. 211–214.

Wang, C., Zhou, X. and Wang, M. 2004. Influence of sintering temperatures on hardness and Young's modulus of tricalcium phosphate bioceramic by nanoindentation technique. *Materials Characterization* 52(4-5), pp. 301–307.

Williams, J.M., Adewunmi, A., Schek, R.M., Flanagan, C.L., Krebsbach, P.H., Feinberg, S.E., Hollister, S.J. and Das, S. 2005. Bone tissue engineering using polycaprolactone scaffolds fabricated via selective laser sintering. *Biomaterials* 26(23), pp. 4817–27.

Wongwitwichot, P., Kaewsrichan, J., Chua, K.H. and Ruszymah, B.H.I. 2010. Comparison of TCP and TCP/HA Hybrid Scaffolds for Osteoconductive Activity. *The Open Biomedical Engineering Journal* 4, pp. 279–85.

Yeong, W.Y., Sudarmadji, N., Yu, H.Y., Chua, C.K., Leong, K.F., Venkatraman, S.S., Boey, Y.C.F. and Tan, L.P. 2010. Porous polycaprolactone scaffold for cardiac tissue engineering fabricated by selective laser sintering. *Acta Biomaterialia* 6(6), pp. 2028–34.

Zhang, Y., Hao, L., Savalani, M.M., Harris, R. a and Tanner, K.E. 2008. Characterization and dynamic mechanical analysis of selective laser sintered hydroxyapatite-filled polymeric composites. *Journal of Biomedical Materials Research. Part A* 86(3), pp. 607–16.

5 Evaluating the Influence of Ceramic Content on the Degradation of PCL/β-TCP SLS Materials.

5.1 Chapter Summary

The first objective of this chapter is to compare the effect of varying the ceramic content in the scaffold materials on material microstructure and the resulting elastic properties through mechanical testing and imaging methods. The second objective of this chapter is to determine the effect of material composition on the changes in mechanical properties and material microstructure during simulated physiological degradation. The mechanical properties and degradation behaviour of three types of selective laser sintered materials are determined: poly-ε-caprolactone (PCL), 90/10wt% PCL/β-tricalcium phosphate (β-TCP) and 50/50wt% PCL/β-TCP. The results of this study show that, while incorporating ceramic particles has a slight stiffening effect, PCL/β-TCP materials have lower strength and strain at maximum stress compared to PCL struts. The reduction in strut stiffness and strength due to degradation was greater for struts containing β-TCP than for PCL struts. The results of this study highlight the influence of ceramic content on the mechanical properties and degradation behaviour of PCL/β-TCP SLS materials, and indicate that these changes must be considered in the design of scaffolds for critical-sized defects.

5.2 Introduction

Biodegradable materials are of significant interest in the field of bone tissue engineering scaffolds as the nature of their biodegradability allows the body to produce new bone in place of the scaffold as it degrades. Such scaffolds, in the cases of large bone defects, provide structural support during the initial stages of healing, and degrade over time allowing the body to replace the scaffold with new, native bone tissue. This is advantageous in comparison to non-degradable materials as in the long-term the defect is effectively filled with bone produced naturally by the body as opposed to the undesirable permanent presence of synthetic material in the body. Synthetic calcium phosphates such as hydroxyapatite and β-TCP are biodegradable materials that have a similar composition to the mineral component of natural bone (Vallet-Regi and Gonzalez-Calbet 2004) and are commonly used in orthopaedic applications (Eosoly et al. 2010; Bhumiratana et al. 2011; Cunningham et al. 2010; Daphalapurkar et al. 2010; Cahill et al. 2009; Sohier et al. 2010; Yang et al. 1996; Yanoso-Scholl et al. 2010; Lohfeld et al. 2012). Incorporating particles of ceramics such as these in polymer-based orthopaedic scaffold materials has been shown to have significant osteogenic benefits and to encourage the formation of new bone on scaffold surfaces (Bhumiratana et al. 2011; Lu and Zreiqat 2010; Wang et al. 2007). As discussed in previous chapters, SLS can be used to fabricate bone scaffolds from biodegradable materials such as PCL and β-TCP in virtually any imaginable geometry, making the fabrication of scaffolds to fit patient-specific defects a reality (Williams et al. 2005).

For orthopaedic scaffolds designed to be placed in critical-sized defects where a large portion of the body-weight is to be supported by the scaffold, the stiffness of the scaffold material to be implanted is a critical design factor. Given the relatively high stiffness of ceramic materials in general, it is expected that increasing the ceramic content of a polymer-ceramic composite scaffold will result in an increase in stiffness. Incorporation of ceramic particles has been found to have a stiffening effect in polymer-ceramic composite materials where a homogeneous cross-section can be achieved, for example using fabrication methods such as extrusion (Azevedo et al. 2003; Cui et al. 2012; Okada and Usuki 1995), fused deposition moulding (Hutmacher et al. 2001) and melt compounding (Kotek et al. 2011). However, the stiffening effect of ceramic particles in polymer-ceramic SLS materials has been shown to be less than for fully-solid materials (i.e. no porosity) with the same polymer-ceramic ratio (Eshraghi and Das 2012), which is consistent with the results already presented in Chapters 3 and 4, and which is a significant concern for the design of materials for load-bearing applications. As discussed in previous chapters, difficulties in sintering have been found with increasing volumes of ceramic in polymer-ceramic SLS materials due to settling of ceramic particles on the surface of the polymer particles, impeding sintering (Lohfeld et al. 2012). It is important to fully understand the effects of increasing ceramic content on the sintering of scaffold materials and on their resulting mechanical properties in order to allow for effective material and scaffold design and to ensure successful scaffold performance *in vivo*.

The change in mechanical properties of biodegradable scaffold materials during degradation is another critical design factor. Therefore, it is important that the influence of the *in vivo* environment on the mechanical properties of scaffold

materials is fully understood, in particular for scaffolds intended for load-bearing applications. Little has been reported on the degradation behaviour of PCL/β-TCP materials fabricated using SLS; however, it is known that the ceramic content of composite materials (Lam et al. 2007) and surface area (Vidaurre et al. 2008) both influence the rate of material degradation *in vivo*.

The most accurate way to evaluate the performance of biodegradable materials during ageing in the body is through retrieval studies; however this is not always practically possible. Laboratory testing of these materials carried out at room temperature and dry conditions is generally acceptable for the evaluation of material mechanical properties, but does not necessarily give an accurate evaluation of material performance in the intended use in the body. *In vivo* conditions can be replicated *in vitro* by exposing materials to simulated physiological conditions by immersion in phosphate buffered saline at 37°C and pH 7.4. PCL has a long degradation time, ranging between 2 and 4 years *in vivo* (Sun et al. 2006; Gunatillake and Adhikari 2003; Middleton and Tipton 2000); long degradation times such as this can be prohibitive for the timely development of new medical implants and devices. Accelerated ageing methods have been developed to increase the rate of the degradation reactions so that material degradation can be assessed at reduced length scales by controlling the rate of polymer degradation using temperature (Hukins et al. 2008), pH (Lam et al. 2008; Lam et al. 2007) and the addition of enzymes to degradation media (Wan et al. 2008; Lam et al. 2008; Castilla-Cortázar et al. 2012). Accelerated ageing can be characterised by assuming that the chemical reactions of the material degradation can be described by the Arrhenius reaction rate function, which predicts that a 10°C change in temperature doubles the reaction rate,

according to ASTM F1980-02 (ASTM 2002) and Hukins et al. (Hukins et al. 2008). A major advantage of using this approach is that there is a clear relationship between the increase and temperature and degradation time, and data from accelerated ageing studies can related back to real-time (degradation at 37°C) data.

The objective of this study is to evaluate the impact of increasing the volume of ceramic particles in polymer-ceramic SLS-produced materials on the structure and mechanical properties of these materials and their suitability for orthopaedic scaffold material applications. SLS scaffold materials are fabricated from PCL and from PCL with two volume fractions of β-TCP (10wt% and 50wt% as considered in Chapters 3 and 4). Firstly, the effect of increasing the ceramic content on material microstructure and elastic properties is assessed through mechanical testing and imaging methods. This first objective is achieved in part by comparing experimental data generated here with experimental data presented in previous two chapters (Chapters 3 and 4). Secondly, the degradation of these materials is achieved using accelerated ageing under simulated physiological conditions in order to replicate the *in vivo* degradation of the scaffold materials at 14 weeks. The changes in mechanical properties and material microstructure during simulated physiological degradation are evaluated. The implications of the results for the performance and suitability of the material for the intended application are then discussed.

5.3 Materials and Methods

5.3.1 Materials and Fabrication

PCL powder (CAPA6506, Solvay, UK) (average molecular weight (Mn) = 60,000 Da, particle size = 600μm) was cryogenically ground to produce particle sizes in two ranges: < 50 μm and 50 - 110 μm. β-TCP (Fluka) (molecular weight = 310.18 g/mol, particle size = 3 - 5 μm) was mixed with the PCL powder using a hand mixer for five minutes until well blended to produce PCL/β-TCP powder blends for sintering with ratios of 90/10wt% (approximately 3 vol% β-TCP) and 50:50wt% (approximately 25 vol% β-TCP).

Individual scaffold struts were fabricated using SLS, as described in Chapter 3 of this thesis, in three ratios of powder blends: 100% PCL, 90/10wt% PCL/β-TCP and 50/50wt% PCL/β-TCP. The 100% PCL and 90/10wt% PCL/β-TCP struts were fabricated using the larger PCL particle size to replicate the material composition of PCL/β-TCP scaffolds that were implanted *in vivo* in ovine tibiae by Lohfeld et al. (Lohfeld et al. 2012). The 50/50wt% PCL/β-TCP struts were fabricated using the smaller PCL particle size as the inclusion of large quantities of β-TCP particles were found to inhibit sintering (Lohfeld et al. 2012). In short, the outline scan method (Lohfeld et al. 2010) was used to achieve a small strut cross section with a laser power of 7 W, laser spot diameter of 410 μm, part bed temperature of 49°C and powder layer thickness of 0.11 mm with the Sinterstation 2500^{plus} system (DTM, USA). The intended dimensions of each strut are 13 mm in length with a cross section of 0.55 mm x 0.55 mm.

Strut tensile samples were prepared by gluing each strut end inside plastic tubes (inner diameter 1.6 mm) with a cyanoacrylate adhesive (Loctite® Power Easy™) for gripping during tensile testing, as per Chapter 3. The mass of each sample (m_0) was measured and recorded. An example of a strut ladder and a tensile sample assembly are shown in Figure 5.1.

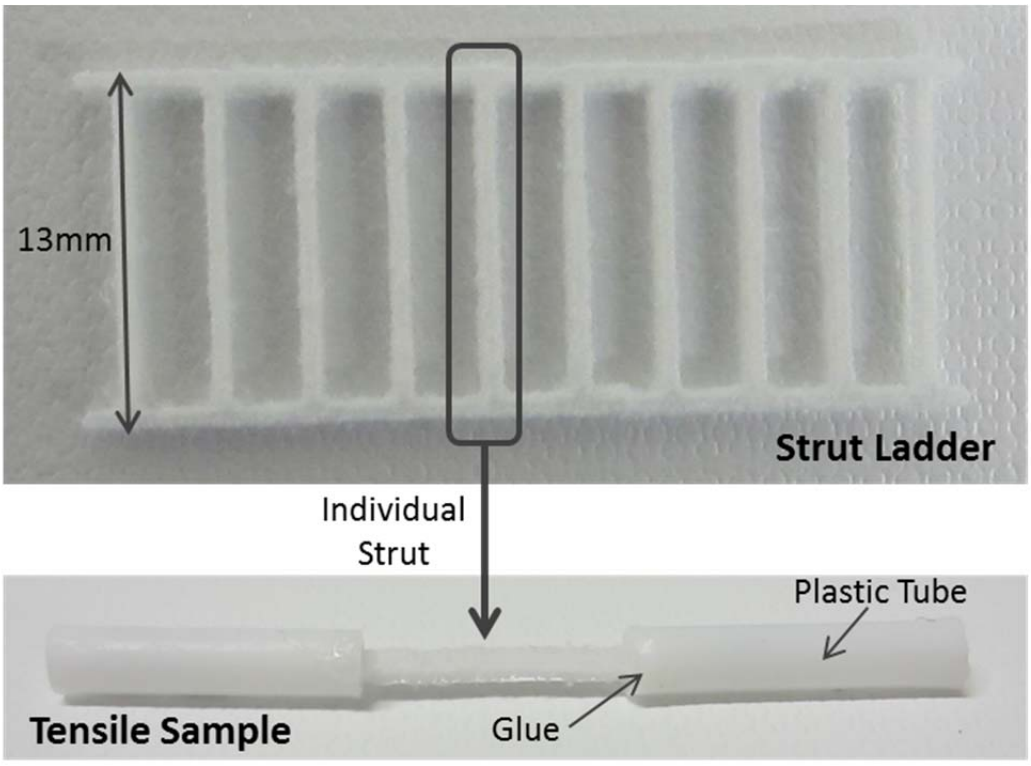

Figure 5.1: Example of a PCL SLS strut ladder, top, and tensile sample assembly, bottom.

Successful fixation of the strut tensile sample assemblies was found to be significantly more challenging for the PCL struts in comparison with the struts containing β-TCP, and strut pull-out during tensile testing was observed in a substantial number of cases as a result of incomplete glue bonding. Note that all samples in which pull-out was observed were discarded and are not included in data

presented here. Further to extensive efforts to address fixation (including assessment of different types of glue as well as tubes of different materials and with different diameters), improved results were found for smaller diameter plastic tubes (inner diameter 1.3 mm). This smaller diameter reduces the bond gap between the strut and the inside of the tubes; it is known that the bond gap is an important factor in the bond strength of cyanoacrylate glues (Loctite® 2007). These fixation issues resulted in a variation in successful tensile test sample numbers (n) at each time point. PCL test sample sizes were n = 4, 3 and 5, for tests at weeks 1, 4 and 7, respectively. 90/10wt% test sample sizes were n = 4, 8 and 9, for tests at weeks 1, 4 and 7, respectively. 50/50wt% test sample sizes were n = 7, 8 and 10, for tests at weeks 1, 4 and 7, respectively. Samples were also removed for testing after 1 day of accelerated ageing for the 90/10wt% material (n = 8) and for the 50/50wt% material (n = 7).

5.3.2 Accelerated Degradation

Accelerated degradation of hydrolytically degradable polymers can be achieved using heat. The Arrhenius reaction rate function predicts that a 10°C change in temperature correlates to a change of a factor of two in the rate of the degradation chemical reaction, as outlined in ASTM F1980-02 and Hukins et al. (Hukins et al. 2008). Consequently, a degradation temperature of 47°C was chosen for this study in order to double the reaction rate relative to an assumed body temperature of 37°C. A real-time degradation time of 14 weeks was chosen in order to compare with the *in vivo* performance of 90/10wt% PCL/β-TCP scaffolds reported in Lohfeld et al. (Lohfeld et al. 2012), giving a corresponding accelerated test time of 7 weeks. It should be noted that the '10 degree rule' is intended for use below the polymer glass

transition temperature (T_g). This method of accelerating degradation is most commonly used with poly(l-lactide), which has a T_g of between 60 and 65°C (Woodruff and Hutmacher 2010). PCL, however, has a T_g of -60°C and a melt temperature (T_m) of 60°C (Woodruff and Hutmacher 2010). While this means that the degradation conditions presented here are above the T_g of PCL, so too are physiologically representative degradation conditions at 37°C. This method of accelerating degradation has been used successfully for PCL with increased temperatures of 45-50°C (McDonald et al. 2009; Chung et al. 2012).

To simulate *in vivo* degradation conditions, tensile samples of each material were placed in phosphate-buffered saline solution (PBS) with pH 7.4. Separate sterilized containers were used for each material with sealed lids to prevent evaporation of the fluid. All samples were fully submerged during the degradation study. The containers were placed in an oven at an elevated temperature of 47°C and both temperature and pH were maintained constant and monitored throughout the course of the study.

5.3.3 Mechanical Testing

The primary tensile testing reported in this chapter is for degraded PCL, 90/10wt% and 50/50wt% struts. This was carried out at 1, 4 and 7 weeks under accelerated degradation conditions corresponding to 2, 8 and 14 weeks real-time degradation. Degraded tensile samples were removed from the PBS and blotted with paper towels prior to tensile testing at each time point.

Tensile testing of undegraded PCL struts was also carried out as part of this study. Additionally, results previously presented in Chapters 3 and 4 for tensile testing of

undegraded 50/50wt% struts and 90/10wt% are included here for comparison purposes.

All tensile testing of struts was carried out on a Zwick biaxial testing machine as per ISO 527-1 (ISO 2012), at a strain rate of 1% of the gauge length per minute, to generate tensile data for each sample. Strain and sample cross-sectional area (CSA) were measured using a calibrated video extensometer camera. The overall strut elastic modulus (E) was calculated from the linear portion of the tensile curve up to a strain of 0.005. The tensile strength (σ_s) was calculated as the maximum stress in the tensile curve and the corresponding strain at this value (ε_s) was recorded. Following tensile testing, each sample was dried to a constant weight in an oven at 47°C and the mass following degradation (m_d) was recorded. Percentage mass loss ($\%m$) was calculated for each sample using the following formula: $m = (m_0 - m_d) / m_0 \times 100$.

5.3.4 Structural and Morphological Characterisation

Scanning electron microscopy (SEM) was carried out on undegraded and degraded (seven weeks) dried samples of each materialpost tensile testing to evaluate changes in surface morphology during degradation. Strut segments were gold-coated before imaging at magnifications of x100 and x1000 using a Hitachi S-4700 SEM (Hitachi, UK) at a power of 10kV. Energy-dispersive X-ray analysis (EDX) was used to identify regions of PCL and β-TCP at the highest magnification. High resolution images of a small segment of each scaffold strut (approximate dimensions 0.1 mm x 0.1 mm x 0.1 mm) were obtained post tensile testing, undegraded and degraded (seven weeks), using μ-CT scanning with a voxel size of 3 μm (MicroCT 100,

Scanco Medical, Switzerland). The degree of sintering was assessed visually using MIMICS (Materialise, Belgium).

5.4 Results

5.4.1 Mechanical Testing

Individual scaffold struts were successfully fabricated using SLS from PCL and from 90/10wt% and 50/50wt% PCL/β-TCP powder blends as per Section 5.3.1 (Figure 5.1). Average tensile curves for undegraded materials, with standard error presented for each material as a shaded region, are presented for full curves and the linear portion of curves in Figure 5.2(A) and (B). A trend of decreasing σs and εs with increasing ceramic content is visible in Figure 5.2(A). Data for E, σs, εs and CSA for each strut type (undegraded) are presented in Figure 5.3. There is negligible difference in the elastic moduli of the 90/10wt% and 50/50wt% struts but PCL struts have a lower stiffness (Figure 5.3(A)). A trend of decreasing σs and εs with increasing ceramic content is visible in Figure 5.2(A) and in Figure 5.3(B) and (C). No difference in CSA was observed for the PCL and 90/10wt% struts ($P > 0.05$) while the CSA of the 50/50wt% struts was much higher than the PCL struts ($P < 0.001$) when compared using a one-way ANOVA test (Figure 5.3(D)).

Mean tensile curves with standard error, generated from the full set of tensile curves at each time point, for undegraded and degraded (week seven) are shown in Figure 5.4 for each material for comparison purposes and to illustrate the scatter observed in test data. The full set of mean tensile curves are shown for PCL (Figure 5.5(A)),

90/10wt% (Figure 5.5(C)) and 50/50wt% struts (Figure 5.5(E)), with undegraded tensile curves included for reference. Standard deviation is not shown in these plots for visual purposes. Linear portions of the tensile curves are shown in Figure 5.5(B), (D) and (F). Variation in sample sizes (n) as indicated on the above figures is due to the strut pull-out issue described in Section 5.3.1. Note that no increase in test data scatter was observed at week seven in comparison to the undegraded test data (Figure 5.4).

The change in elastic modulus E during degradation is shown in Figure 5.6(A). No reduction in E was observed at seven weeks for the PCL struts, however a 63% and 54% drop in E was observed for the 90/10wt% and 50/50wt% struts respectively at seven weeks. The largest reduction in E occurred in the first week of degradation for the 90/10wt% material (57%) and in the first four weeks for the 50/50wt% material (52%). A reduction of 29.5% in E compared to undegraded material after one day accelerated ageing was observed for the 90/10wt% material (n = 8), while an increase of 3% was observed for the 50/50wt% material (n = 7).

A reduction in σ_s was observed at week seven for all materials, with reductions of 22% for PCL, 32% for 90/10wt% and 34% for 50/50wt% strut, with the largest decrease in σ_s occurring in the first week (Figure 5.6(B)). A reduction of 7.4% (90/10wt%) and an increase of 1.8% (50/50wt%) in σ_s was observed compared to undegraded material after one day accelerated ageing. A similar increase in ε_s was observed for the 90/10wt% and 50/50wt% struts (95% and 94% respectively), however an 18% decrease in ε_s was observed for the PCL struts (Figure 5.6(C)). No change in CSA was observed during degradation for PCL struts (P = 0.5308),

90/10wt% struts (P = 0.9527) or for 50/50wt% struts (P = 0.0820) when compared using a two-tailed unpaired T-test, indicating that no swelling due to water update or reduction in CSA due to degradation of the materials occurred. Similar mass loss

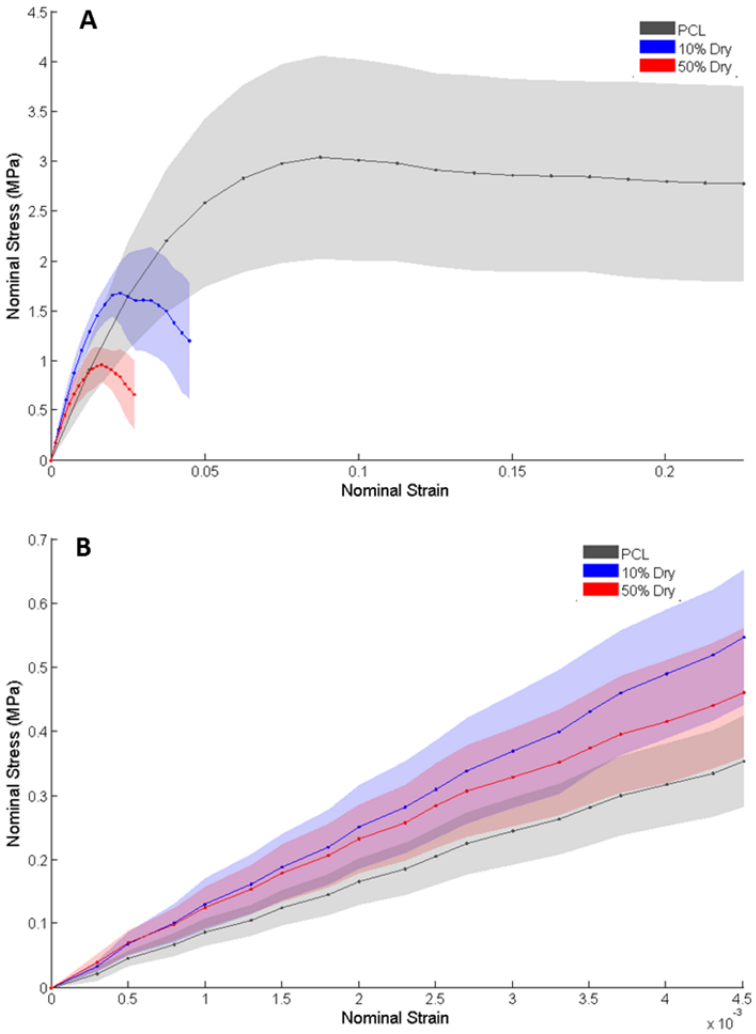

Figure 5.2: Average tensile stress-strain curves of PCL struts (grey, n = 19), 90/10wt% (blue, n = 16) and 50/50wt% (red, n = 7) PCL/β-TCP struts with standard error presented as shaded areas (A). The linear portion of each curve used for the calculation of the material elastic modulus is presented in (B). Tensile curves for 50/50wt% struts to maximum stress have been presented in Chapter 3 and an average curve is presented here for comparison purposes.

was observed at seven weeks for all materials with a loss of 5.82% for PCL struts, 4.99% for 90/10wt% struts and 5.08% for 50/50wt% struts. This mass loss was not significant when compared to dried, undegraded control samples for PCL (P = 0.1790), 90/10wt% struts (0.7044) or for 50/50wt% struts (0.8437) when compared using a two-tailed unpaired T-test.

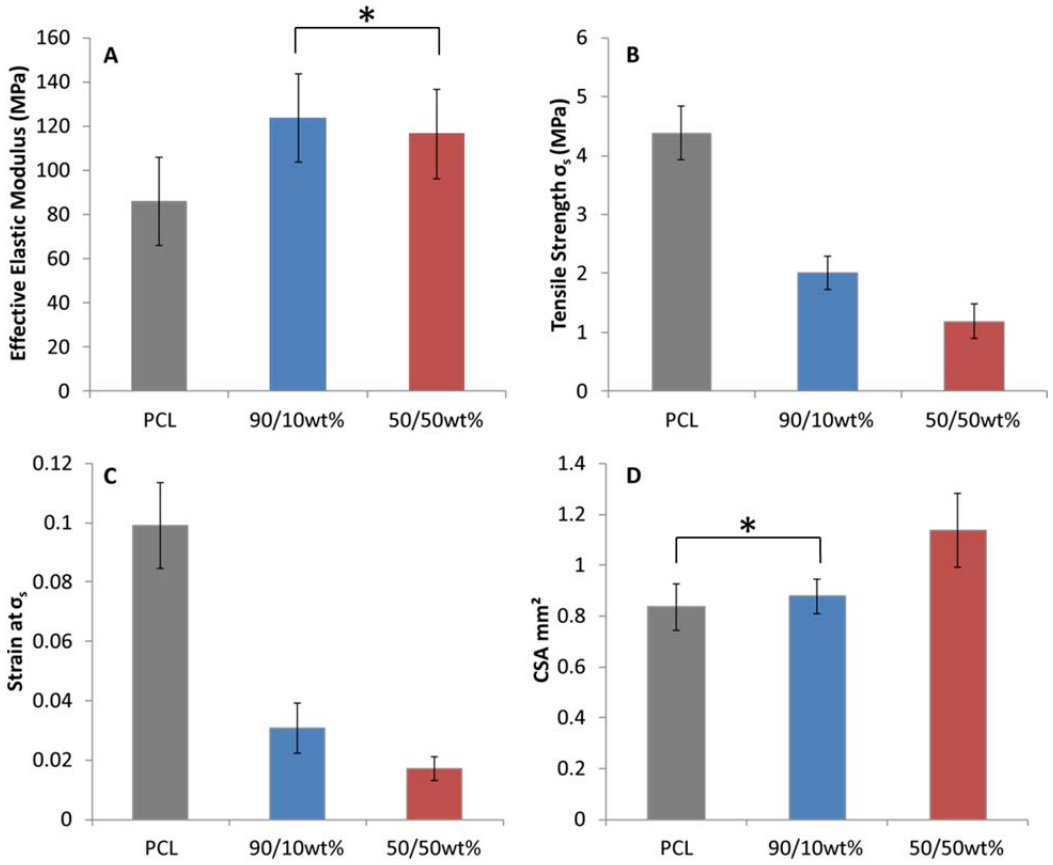

Figure 5.3: Comparison of elastic modulus (A), tensile strength σ_s (B), strain at σ_s (C) and average cross-sectional area (D) for undegraded PCL, 90/10wt% and 50/50wt% PCL/β-TCP struts. Mean values for each data set are shown and error bars represent standard deviation. The elastic modulus of 90/10wt% and 50/50wt% struts presented elsewhere in this thesis (Chapters 4 and 3, respectively) have been included in (A) for comparison purposes. *p > 0.05.

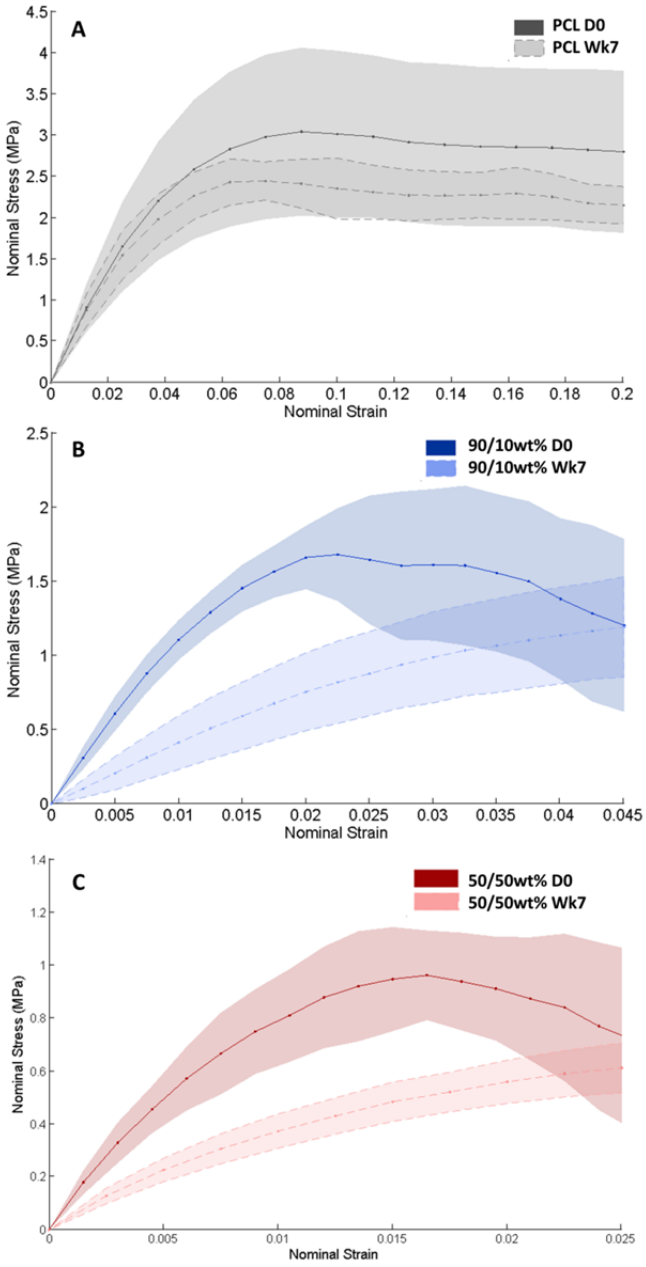

Figure 5.4: Average tensile curves for (A) PCL, (B) 90/10wt% struts and (C) 50/50wt% struts before (D0, solid lines) and after seven weeks of degradation (dashed lines). The shaded region in each plot represents the standard deviation of the full set of tensile curves. Tensile data for 50/50wt% struts at D0 has been presented in Chapter 3 and an average curve is included here for comparison purposes.

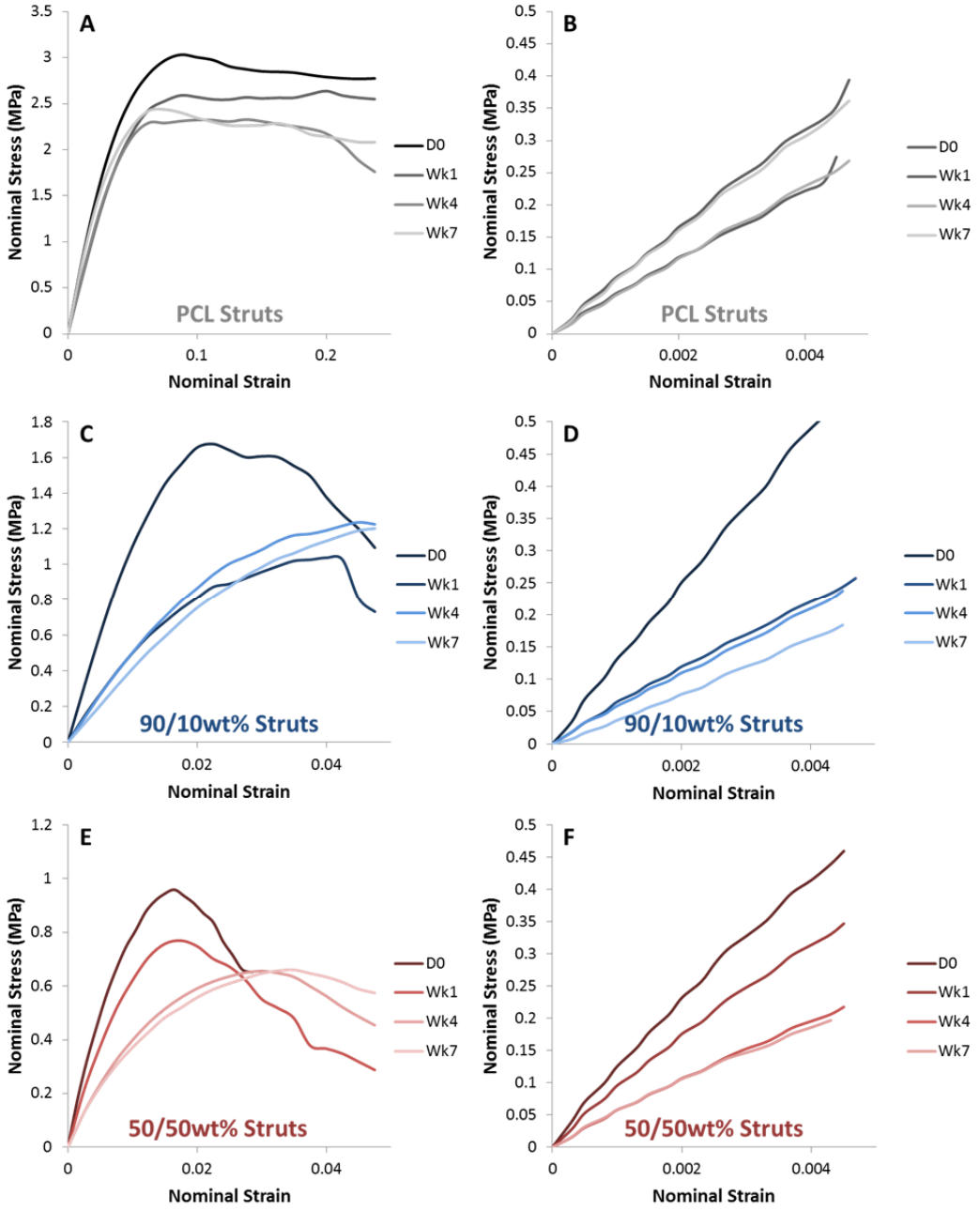

Figure 5.5: Mean tensile curves for PCL struts (A, B), 90/10wt% struts (C, D) and 50/50wt% struts (E, F) after 0 days (D0) and one, four and seven weeks degradation. Full curves are shown in (A) and (B); linear portions of the tensile curves are shown in (C) and (D). Tensile data for 50/50wt% struts at D0 has been presented in Chapter 3 and an average curve is included here for comparison purposes.

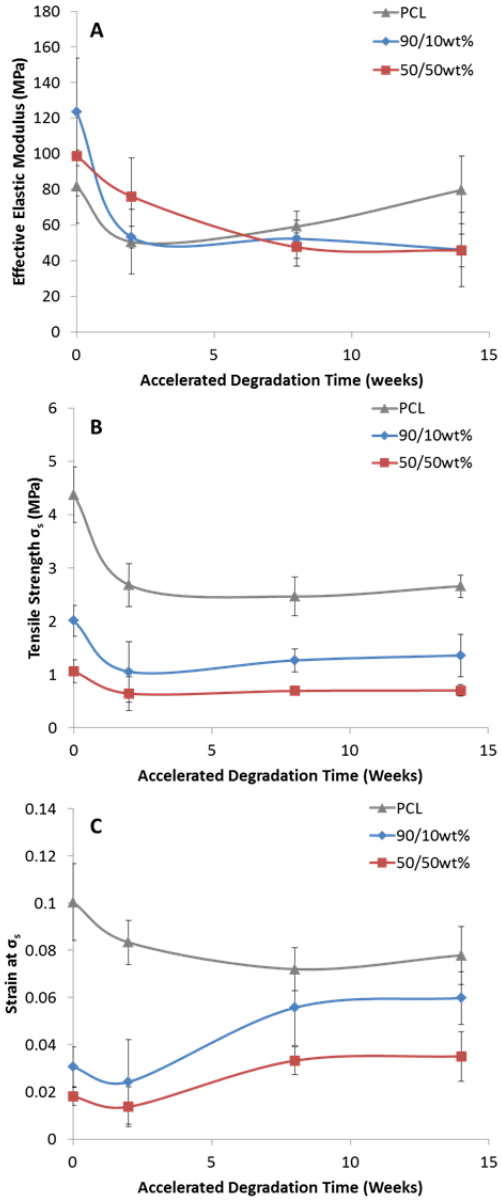

Figure 5.6: Summary of degradation study mechanical testing data for PCL (grey), 90/10wt% (blue) and 50/50wt% struts (red). Mean values for each data set are shown and error bars represent standard deviation. The change in elastic modulus for each material is shown in (A), the change in tensile strength is shown in (B) and the change in strain at the tensile strength is shown in (C). Elastic modulus data for undegraded 90/10wt% PCL/β-TCP struts and 50/50wt% struts are evaluated elsewhere in this thesis (Chapters 4 and 3 respectively) and are included here for comparison purposes.

5.4.2 Structural and Morphological Characterisation

SEM images of each material under magnification of x100 are shown in Figure 5.7 and under x1000 in Figure 5.8. In both cases, undegraded materials are shown in the top row and degraded materials are shown in the bottom row. β-TCP particles are visible as small bright regions, indicated by arrows in Figure 5.8, whereas the larger PCL particles have smoother surfaces. 50/50wt% struts have a finer particulate nature on the macro-scale compared to the PCL and the 90/10wt% struts due to differences in PCL particle size and indicating that a greater degree of partial sintering occurred at the surface in the PCL and 90/10wt% struts than in the 50/50wt% struts (Figure 5.7). β-TCP particles (diameter 1-3 μm) are visible on the surfaces of the PCL particles in Figure 5.8, verified by EDX, with similar amounts of β-TCP visible before and after degradation. Less individual PCL particles are visible attached at the surface of each strut post-degradation (Figure 5.7), indicating some removal of surface particles.

The microstructure of the strut materials is visible in the μ-CT scan images of each strut type shown in Figure 5.9. Regions of β-TCP are visible as bright pixels on the scans and regions of PCL consist of less bright pixels. Images of the strut materials pre-degradation are shown along the top and images of the strut materials post-degradation are shown along the bottom. Larger regions of fully sintered PCL material are visible in the PCL struts than the struts containing β-TCP, and more continuous material is visible in the 90/10wt% struts than the 50/50wt% struts, in which larger pores are visible. An increase in porosity in all three materials is visible in the μ-CT scan images at seven weeks compared to the μ-CT scan images of the

undegraded materials. Regions of β-TCP are present at the outer edges of PCL particles in the 90/10wt% struts, both for individual partially sintered particles and through the cross-section of fully sintered regions of material indicating the original boundaries between particles.

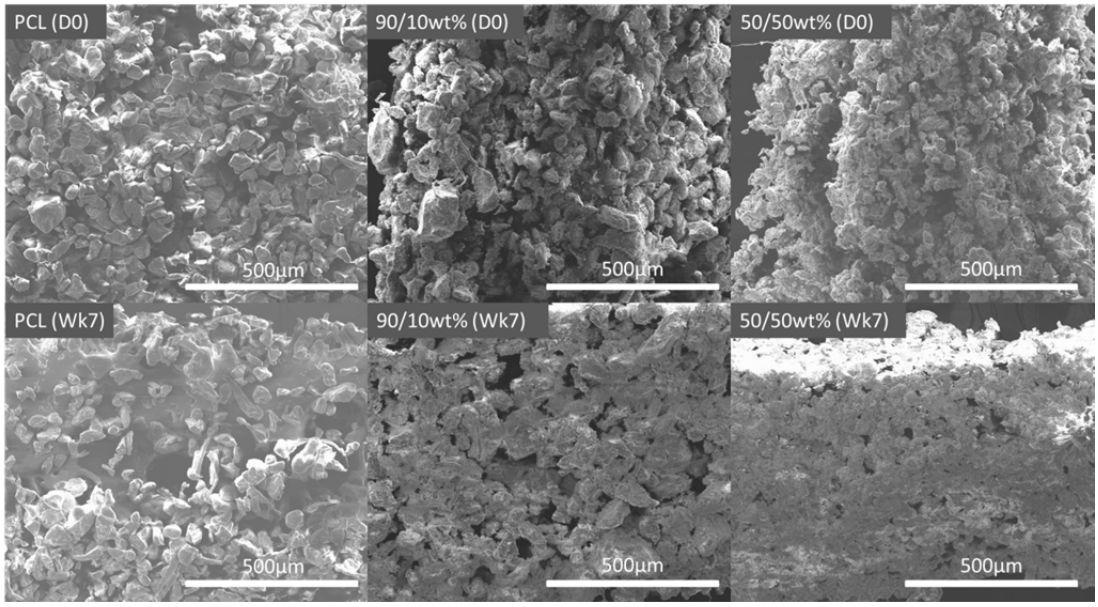

Figure 5.7: SEM images of PCL, 90/10wt% and 50/50wt% PCL/β-TCP struts under magnification of x100 with zero degradation (D0) and after seven weeks degradation (Wk7).

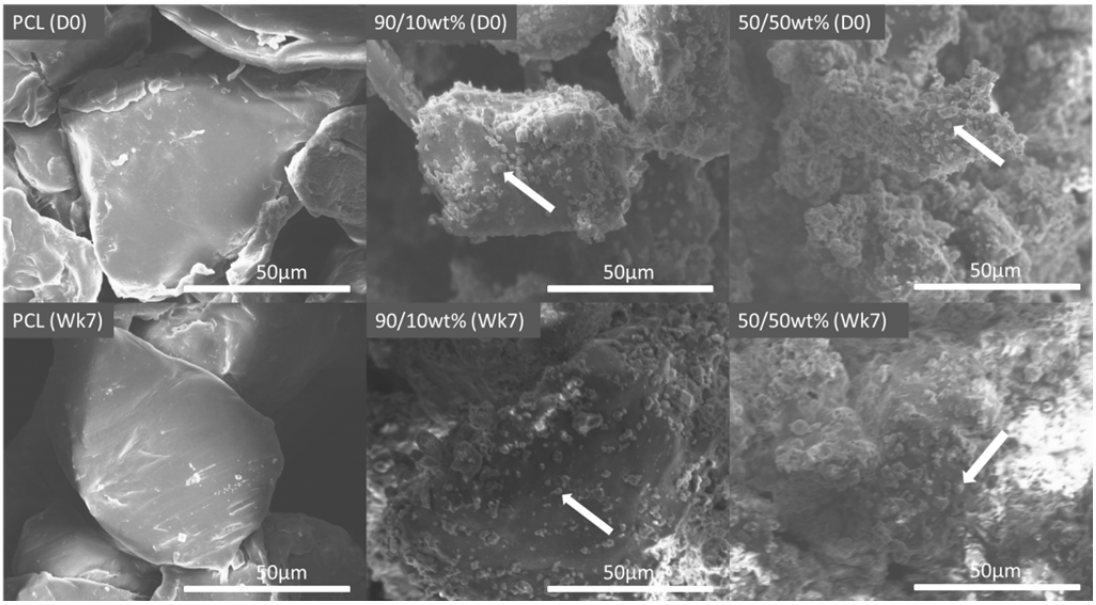

Figure 5.8: SEM images of PCL, 90/10wt% and 50/50wt% PCL/β-TCP struts under magnification of x1000 with zero degradation (D0) and after seven weeks degradation (Wk7). Arrows point to β-TCP particles in 90/10wt% and 50/50wt% struts.

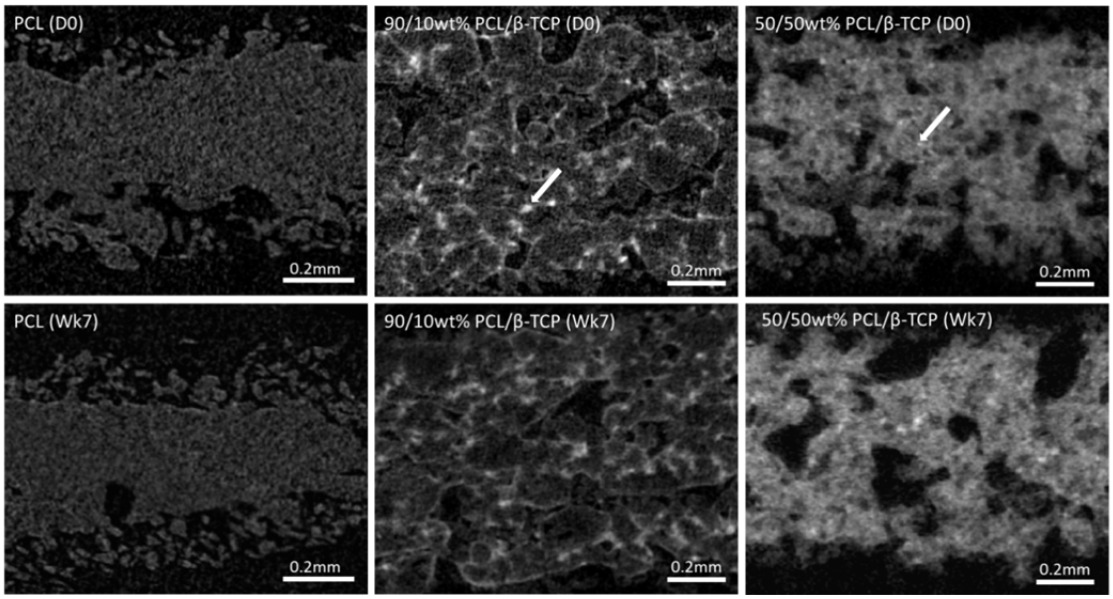

Figure 5.9: µ-CT scan images of PCL, 90/10wt% and 50/50wt% PCL/β-TCP struts (left to right) with zero degradation (top) and after seven weeks degradation (bottom). White arrows point to β-TCP particles.

5.5 Discussion

Single scaffold struts were successfully fabricated from PCL and from 90/10wt% and 50/50wt% PCL/β-TCP powder blends using SLS. Each type of sintered struts exhibit both fully and partially sintered regions with a highly porous microstructure (Figure 5.7 and Figure 5.9). Increased porosity in struts containing β-TCP compared to PCL struts (Figure 5.9) is a result of partial sintering which occurs when the sintering energy is below a minimal threshold required for full sintering. When this occurs, only partial sintering of the outer regions of the particle is achieved, creating a highly porous structure with particles connected at contact points by 'necks' between particles (Figure 5.10(A)).

The volume of ceramic in each sintered material affects the microstructure of the resulting material as illustrated in Figure 5.10(B). The smaller β-TCP particles can be seen coating the outside of the PCL particles in the SEM images (Figure 5.7) and μ-CT scan images (Figure 5.9). In a two-phase polymer-ceramic composite, sintering is carried out above the T_m of the polymer phase but below the temperatures that would be required for sintering of the ceramic phase. Therefore the ceramic particles do not get sintered and act to inhibit the flow and consolidation of the polymer melt. As a result greater porosity is visible in the 90/10wt% struts than the PCL struts (Figure 5.9). Increasing the volume of β-TCP particles in the material accentuates this effect resulting in a lower degree of sintering, and as a result greater porosity is visible in the 50/50wt% struts than the 90/10wt% struts (Figure 5.9).

PCL particles with diameter 50 to 110 μm were used for the fabrication of PCL and 90/10wt% struts; however a reduced PCL particle size of < 50 μm was required for

the fabrication of 50/50wt% struts due to the increased volume of β-TCP and the resulting difficulties in sintering this type of material (Lohfeld et al. 2012). The CSA of the PCL and 90/10wt% struts were the same, but the 50/50wt% struts had a greater CSA suggesting that CSA is controlled by the PCL particle size used. In general, this can be related to the ratio of PCL particle size ($Ø_{PCL}$) to laser spot diameter ($Ø_s$) used during fabrication, as illustrated in Figure 5.10(C). When $Ø_{PCL}$ is less than $Ø_s$, multiple particles are sintered directly by the laser (Case A), whereas when $Ø_{PCL}$ is greater than $Ø_s$, only single particles in the laser path are directly sintered (Case B). Heat energy is transferred through contact points between particles forming partially sintered regions of material connected by a 'neck' of sintered material. For Case A, a large number of particles are directly sintered and a large number of neighbouring particles are partially sintered. In this case a larger number of particles, in a larger volume of space, are sintered this results in a greater CSA, but also in increased porosity.

The results of mechanical testing presented here indicate that the inclusion of β-TCP particles have a stiffening effect compared to PCL struts, with increases of 52.6% and 22.2% with β-TCP inclusions of 10wt% and 50wt% respectively (Figure 5.3). However, the increase in β-TCP particles in the 50/50wt% struts did not result in a significant increase in the measured elastic modulus compared to the 90/10wt% struts ($P = 0.6254$, two-tailed unpaired T-test). For the 50/50wt% struts, the reinforcing effect of the greater volume of the β-TCP particles is offset by the greater degree of microporosity (Figure 5.9), resulting in a similar overall strut elastic modulus to the 90/10wt% struts.

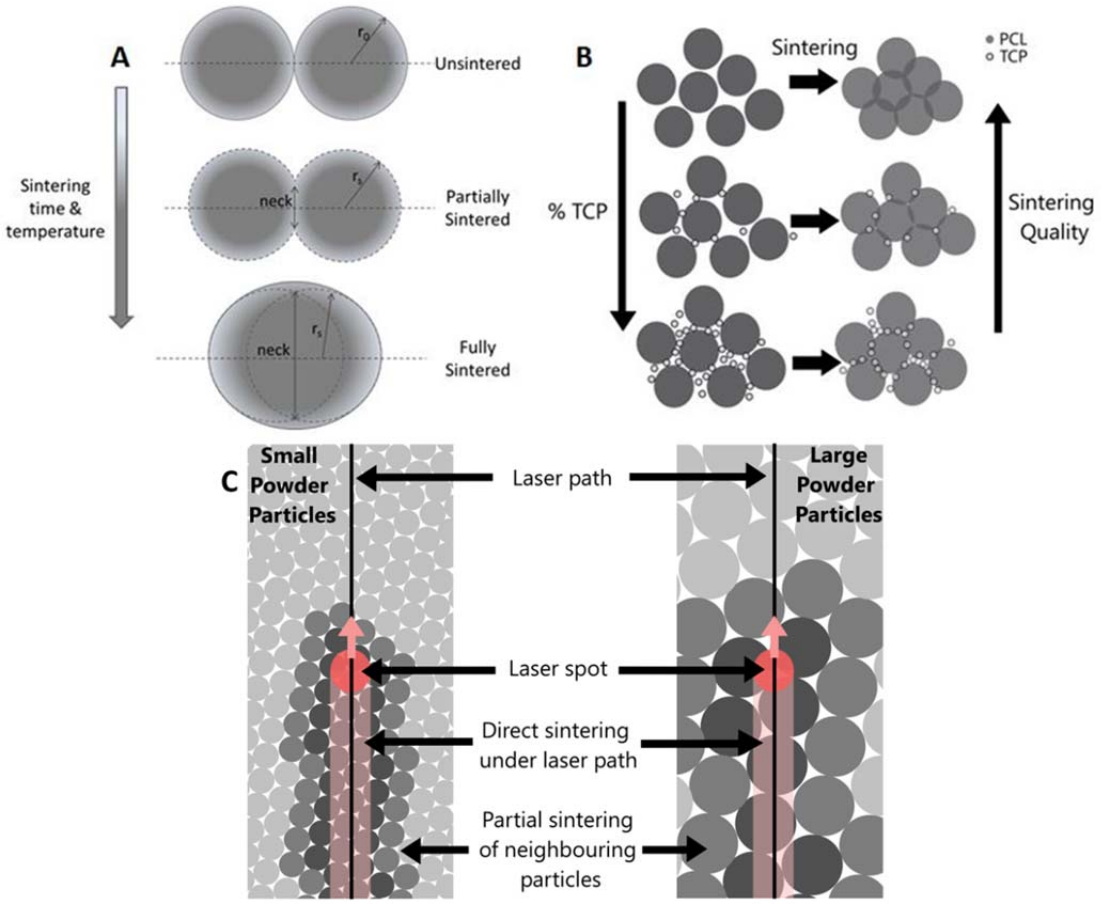

Figure 5.10: (A) Sintering of individual polymer particles to form partially sintered and fully sintered material with time and temperature. (B) Illustration of the effect of increasing β-TCP content on the sintering of PCL/β-TCP composite materials. A lower degree of sintering is achieved with increasing β-TCP content. (C) Schematic of sintering of powder particles with different particle sizes. Regions directly under the laser path are fully sintered, and heat is transferred to surrounding particles through contact points to form partially sintered regions. Full sintering occurs in a greater number of particles when the particle size is less than the laser spot diameter ($Ø_s$) than when particles are larger than $Ø_s$. Greater partial sintering and lower porosity occurs with particle sizes less than $Ø_s$.

The inclusion of β-TCP particles has a more significant effect on σ_s ($P < 0.001$) and ε_s ($P < 0.0001$) than on the values of strut elastic modulus, with reductions of 41.2% and 68.9% in σ_s and reductions of 67.9% and 81.0% in ε_s for 90/10wt% and 50/50wt% struts, respectively, compared to PCL struts (Figure 5.2, Figure 5.3). The PCL struts exhibit a more ductile behaviour than struts containing β-TCP with failure strains 5.3 times greater than ε_s, compared to 179% and 216% for 90/10wt% and 50/50wt% struts respectively (Figure 5.2A). This is due to the greater number of pores and the lower amount of fully sintered material in the loading direction in struts containing β-TCP compared to the PCL struts. Increasing ceramic content has the effect of further reducing σ_s and ε_s due to the further increase in porosity (Figure 5.2, Figure 5.3). When the sintered struts are loaded in tension, forces are transferred through the bonds or necks between individual sintered particles. Failure of these individual bonds is visible as reductions in stress at high strains (Figure 5.2). The failure behaviour of these sintered materials is therefore dictated by the degree of sintering between particles, which in turn is reduced by increasing ceramic content. Similar results were observed by Eshragi et al. (Eshraghi and Das 2012), where the strength and yield strain of polymer-ceramic SLS scaffolds were not seen to improve with increasing ceramic content.

The elastic modulus of the PCL struts remained unchanged after seven weeks degradation, as expected from the long degradation times reported for PCL in the literature ranging from 2 to 4 years *in vivo* (Sun et al. 2006; Gunatillake and Adhikari 2003; Middleton and Tipton 2000). Reductions of 63% and 54% in E were observed for the 90/10wt% and 50/50wt% struts respectively at seven weeks, i.e. the inclusion of β-TCP particles in these struts result a larger reduction in elastic

modulus. This could potentially be attributed to the shorter degradation time of β-TCP (Wang et al. 2012; Artzi et al. 2004; Draenert et al. 2013; Wiltfang and Merten 2002; Galois and Mainard 2004) compared to PCL. However no increase in mass loss was observed for struts containing β-TCP and *E* was not found to decrease with increasing ceramic content at seven weeks. Struts containing β-TCP do have greater porosity than the PCL struts (Figure 5.9) and as a result a greater surface area is exposed to the degradation medium. As surface area has been shown to influence degradation (Vidaurre et al. 2008), struts containing β-TCP have a greater decrease *E* than the PCL struts as a result of greater porosity within the struts. No conclusive results regarding the influence of ceramic particles on the change in mechanical properties of the struts after one day accelerated ageing can be inferred from the results of strut mechanical testing as an increase in stiffness and strength were observed for the 90/10wt% material (followed by a sharp drop in each measure following this time point) and slight decreases in stiffness and strength were observed for the 50/50wt% material.

Reductions in σ_s were observed for all materials at seven weeks. The decrease in σ_s for the PCL struts was 10% greater than for struts containing β-TCP particles are still visible in μ-CT scans of the PCL/β-TCP materials at seven weeks, indicating that these particles are still present embedded in the PCL matrix. While degradation of the PCL matrix is likely occurring (as evidenced by the reduction in σ_s for the PCL struts, Figure 5.6) the β-TCP particles still provide reinforcement. Similar trends of increasing ε_s were observed for the 90/10wt% and 50/50wt% struts, however a decrease of 18% was observed for the PCL struts. The trend of reduced ε_s with increasing ceramic content is visible after seven weeks of degradation. Note that it is

difficult to make conclusions regarding the effect of increasing ceramic content on the mechanical properties or degradation behaviour of the materials due to differences in PCL particle sizes between the 90/10wt% and 50/50wt% materials.

UTS is a nominal stress measure as per ISO standards (ISO 2012). However, due to the complexity of the material structure and the large overall strains experienced by the material at the UTS point the local stress at UTS could be quite different. It is quite difficult to determine what these local stresses would be experimentally again due to material complexity and inhomogeneity of cross-sectional area along the sample. However, assuming the standard formula for true stress calculated as $\sigma_{true} = \sigma(1 + \varepsilon)$ one would obtain $\sigma_{UTS,true}$ values such as 3.75 MPa, 2.07 MPa and 1.21 MPa for PCL, 90/10wt% and 50/50wt% struts (undegraded), respectively; these values represent an increase of 3.74%, 3.06% and 1.71% relative to the measured values for σ presented in Figure 5.3. However, it has to be said that the application of this formula in this case is questionable since it is based on the incompressibility of plastic deformation, which is certainly of questionable relevance in this case.

It is possible that some degree of specimen misalignment may have occurred during the assembly of tensile samples and during tensile testing of the tensile samples in this study despite efforts to prevent this due to the very small size of the tensile samples and the associated difficulty in handling the samples. The possible effects of misalignment on the results presented here can be approximated based on the angle of misalignment (θ), i.e. the angle between the direction of the tensile force applied and the strut longitudinal axis. A typical value for the maximum possible angle of

misalignment is 1°, as measured from video stills taken during tensile testing of selected samples in this study. If misalignment occurs during tensile testing, the real elastic modulus (E_{real}) can be approximated from the measured value of elastic modulus (E_{meas}) as $E_{\text{real}} = \text{Cos}\theta\ E_{\text{meas}}$, giving a possible error of only 0.0123%.

The changes in mechanical properties of the SLS scaffold materials observed in this degradation study are important considerations for the design and performance of orthopaedic scaffolds fabricated from these materials. The reduction of material properties during degradation must be taken into account for scaffold design to ensure that loads are supported even after a period of degradation, in particular for critical sized defects. Degradation of the scaffold itself is desirable to allow for new, native bone to replace the scaffold and to fill the defect space over time and eventually replace the scaffold. New bone forming around scaffolds *in vivo* (Lohfeld et al. 2012) would contribute to the overall stiffness of the scaffold and defect which, depending on volume and quality, would offset the resulting reduction in stiffness.

Changes in scaffold material properties and the resulting changes in the local environment of tissues surrounding the scaffold will influence the healing response of native tissue and the formation of new bone in the defect. It is known that the stiffness of scaffold materials influences the differentiation of MSCs (Engler et al. 2006) and mechanical strain has been shown to influence the regeneration of bone tissue (Baas et al. 2010; Di Palma et al. 2003), therefore the change in E and ε_s in each of these scaffold materials will play a role in the adaptation of native bone tissue in the defect site. The change in material properties during degradation was found to be dependent on the materials from which the struts were fabricated.

Changes in material properties were similar for struts containing β-TCP but differences between PCL/β-TCP struts and PCL struts were observed. In all cases, both undegraded and degraded, increasing the amount of β-TCP was found to decrease the strength of the sintered materials and struts with β-TCP were found to be less stiff than the PCL struts.

The *in vivo* performance of an orthopaedic scaffold with the same material composition as the 90/10wt% struts presented here has been demonstrated in a previous study (Lohfeld et al. 2012). While both the/10wt% PCL/β-TCP and 100% β-TCP scaffolds showed good *in vivo* performance and load-bearing capacity, a greater volume of bone formation was seen in defects containing 100% β-TCP scaffolds as a result of the osteoconductive properties of β-TCP (Bhumiratana et al. 2011; Lu and Zreiqat 2010; Wang et al. 2007). As presented here, the incorporation of a 50wt% volume of β-TCP particles in this type of scaffold material resulted in only a slight reduction in the mechanical properties of the material, and resulted in only a slight increase in the amount of degradation observed, compared to the 90/10wt% material. As the purpose of the increased β-TCP content in the 50/50wt% strut materials is to improve scaffold osseointegration, the results here suggest that the small reduction in mechanical properties with increased ceramic content is more than compensated for by the increase in bone formation that would be expected with a larger ceramic content (Lohfeld et al. 2012; Bhumiratana et al. 2011; Lu and Zreiqat 2010; Wang et al. 2007). On this basis, it is recommended that the *in vivo* performance of this type of scaffold material should be further investigated.

5.6 Conclusions

Composite orthopaedic scaffold materials were successfully fabricated from 100% PCL and from 90/10wt% and 50/50wt% PCL/β-TCP powder blends using SLS. The wt% of β-TCP and the PCL particle sizes used were found to influence the material microstructure and the material properties. The inclusion of ceramic particles resulted in a slight increase in stiffness compared to PCL struts, however increasing the amount of ceramic from 10wt% to 50wt% did not result in a further increase in stiffness. Struts containing ceramic particles had significantly reduced strength and strain at maximum stress than PCL struts, with increasing ceramic content causing a further significant reduction in both strength and strain. The incorporation of β-TCP was found to influence the change in material properties during degradation. The reduction in stiffness due to degradation was greater for struts containing β-TCP than for PCL struts, however lower reductions in strength due to degradation were observed in struts containing β-TCP than for PCL struts. Materials containing β-TCP became more ductile due to degradation, whereas the PCL struts became less ductile.

The results presented in this chapter illustrate the complexity of the microstructure of polymer-ceramic SLS materials, and the influence of the material composition on the mechanical properties of these materials. The resulting mechanical properties, and their changes during degradation, must be considered for the design of orthopaedic scaffolds for critical-sized defects.

5.8 References

Artzi, Z., Weinreb, M., Givol, N., Rohrer, M., Nemcovsky, C., Prasad, H. and Tal, H. 2004. Biomaterial Resorption Rate and Healing Site Morphology of Inorganic Bovine Bone and ß-Tricalcium Phosphate in the Canine : A 24-month Longitudinal Histologic Study and Morphometric Analysis. *International Journal of Oral and Maxillofacial Implants* 19, pp. 357–368.

ASTM 2002. Standard Guide for Accelerated Aging of Sterile Medical Device Packages 1. *ASTM F1980-02*.

Azevedo, M.C., Reis, R.L., Claase, M.B., Grijpma, D.W. and Feijen, J. 2003. Development and properties of polycaprolactone/hydroxyapatite composite biomaterials. *Journal of Materials Science. Materials in Medicine* 14(2), pp. 103–7.

Baas, E., Kuiper, J.H., Yang, Y., Wood, M. a and El Haj, A.J. 2010. In vitro bone growth responds to local mechanical strain in three-dimensional polymer scaffolds. *Journal of Biomechanics* 43(4), pp. 733–9.

Bhumiratana, S., Grayson, W.L., Castaneda, A., Rockwood, D.N., Gil, E.S., Kaplan, D.L. and Vunjak-Novakovic, G. 2011. Nucleation and growth of mineralized bone matrix on silk-hydroxyapatite composite scaffolds. *Biomaterials* 32(11), pp. 2812–20.

Cahill, S., Lohfeld, S. and McHugh, P.E. 2009. Finite element predictions compared to experimental results for the effective modulus of bone tissue engineering scaffolds fabricated by selective laser sintering. *Journal of Materials Science. Materials in Medicine* 20(6), pp. 1255–62.

Castilla-Cortázar, I., Más-Estellés, J., Meseguer-Dueñas, J.M., Escobar Ivirico, J.L., Marí, B. and Vidaurre, A. 2012. Hydrolytic and enzymatic degradation of a poly(ε-caprolactone) network. *Polymer Degradation and Stability* 97(8), pp. 1241–1248.

Chung, A.S., Hwang, H.S., Das, D., Zuk, P., McAllister, D.R. and Wu, B.M. 2012. Lamellar stack formation and degradative behaviors of hydrolytically degraded poly(ε-caprolactone) and poly(glycolide-ε-caprolactone) blended fibers. *Journal of Bomedical Materials Research. Part B, Applied Biomaterials* 100(1), pp. 274–84.

Cui, Z., Nelson, B., Peng, Y., Li, K., Pilla, S., Li, W.-J., Turng, L.-S. and Shen, C. 2012. Fabrication and characterization of injection molded poly (ε-caprolactone) and poly (ε-caprolactone)/hydroxyapatite scaffolds for tissue engineering. *Materials Science & Engineering. C, Materials for Biological Applications* 32(6), pp. 1674–81.

Cunningham, E., Dunne, N., Walker, G., Maggs, C., Wilcox, R. and Buchanan, F. 2010. Hydroxyapatite bone substitutes developed via replication of natural marine sponges. *Journal of Materials Science. Materials in Medicine* 21(8), pp. 2255–61.

Daphalapurkar, N.P., Wang, F., Fu, B., Lu, H. and Komanduri, R. 2010. Determination of Mechanical Properties of Sand Grains by Nanoindentation. *Experimental Mechanics* 51(5), pp. 719–728.

Draenert, M., Draenert, A. and Draenert, K. 2013. Osseointegration of hydroxyapatite and remodeling-resorption of tricalciumphosphate ceramics. *Microscopy Research and Technique* 76(4), pp. 370–80.

Engler, A.J., Sen, S., Sweeney, H.L. and Discher, D.E. 2006. Matrix elasticity directs stem cell lineage specification. *Cell* 126(4), pp. 677–89.

Eosoly, S., Brabazon, D., Lohfeld, S. and Looney, L. 2010. Selective laser sintering of hydroxyapatite/poly-epsilon-caprolactone scaffolds. *Acta Biomaterialia* 6(7), pp. 2511–7.

Eshraghi, S. and Das, S. 2012. Micromechanical finite-element modeling and experimental characterization of the compressive mechanical properties of polycaprolactone-hydroxyapatite composite scaffolds prepared by selective laser sintering for bone tissue engineering. *Acta Biomaterialia* 8(8), pp. 3138–43.

Galois, L. and Mainard, D. 2004. Bone ingrowth into two porous ceramics with different pore sizes: an experimental study. *Acta Orthopaedica Belgica* 70(6), pp. 598–603.

Gunatillake, P. a and Adhikari, R. 2003. Biodegradable synthetic polymers for tissue engineering. *European Cells & Materials* 5, pp. 1–16.

Hukins, D.W.L., Mahomed, A. and Kukureka, S.N. 2008. Accelerated aging for testing polymeric biomaterials and medical devices. *Medical Engineering & Physics* 30(10), pp. 1270–4.

Hutmacher, D.W., Schantz, T., Zein, I., Ng, K.W., Teoh, S.H. and Tan, K.C. 2001. Mechanical properties and cell cultural response of polycaprolactone scaffolds designed and fabricated via fused deposition modeling. *Journal of Biomedical Materials Research* 55(2), pp. 203–16.

ISO 2012. Plastics - Determination of tensile properties - Part 1: General principles. *ISO 27-1*.

Kotek, J., Kubies, D., Baldrian, J. and Kovářová, J. 2011. Biodegradable polyester nanocomposites: The effect of structure on mechanical and degradation behavior. *European Polymer Journal* 47(12), pp. 2197–2207.

Lam, C.X.F., Savalani, M.M., Teoh, S.-H. and Hutmacher, D.W. 2008. Dynamics of in vitro polymer degradation of polycaprolactone-based scaffolds: accelerated versus simulated physiological conditions. *Biomedical Materials* 3(3), p. 034108.

Lam, C.X.F., Teoh, S.H. and Hutmacher, D.W. 2007. Comparison of the degradation of polycaprolactone and polycaprolactone-(β-tricalcium phosphate) scaffolds in alkaline medium. *Polymer International* 56(October 2006), pp. 718–728.

Loctite® 2007. *Loctite® 454™ Technical Data Sheet*.

Lohfeld, S., Cahill, S., Barron, V., McHugh, P., Dürselen, L., Kreja, L., Bausewein, C. and Ignatius, A. 2012. Fabrication, mechanical and in vivo performance of polycaprolactone/tricalciumphosphate composite scaffolds. *Acta Biomaterialia* 8(9), pp. 3446–3456.

Lohfeld, S., Tyndyk, M.A., Cahill, S., Flaherty, N., Barron, V. and McHugh, P.E. 2010. A method to fabricate small features on scaffolds for tissue engineering via selective laser sintering. *Journal of Biomedical Science and Engineering* 03, pp. 138–147.

Lu, Z. and Zreiqat, H. 2010. Beta-tricalcium phosphate exerts osteoconductivity through alpha2beta1 integrin and down-stream MAPK/ERK signaling pathway. *Biochemical and Biophysical Research Communications* 394(2), pp. 323–9.

McDonald, P.F., Lyons, J.G., Geever, L.M. and Higginbotham, C.L. 2009. In vitro degradation and drug release from polymer blends based on poly(dl-lactide), poly(l-lactide-glycolide) and poly(ε-caprolactone). *Journal of Materials Science* 45(5), pp. 1284–1292.

Middleton, J.C. and Tipton, a J. 2000. Synthetic biodegradable polymers as orthopedic devices. *Biomaterials* 21(23), pp. 2335–46.

Okada, A. and Usuki, A. 1995. The chemistry of polymer-clay hybrids. *Materials Science and Engineering: C* 3(2), pp. 109–115.

Di Palma, F., Douet, M., Boachon, C., Guignandon, a., Peyroche, S., Forest, B., Alexandre, C., Chamson, a. and Rattner, a. 2003. Physiological strains induce differentiation in human osteoblasts cultured on orthopaedic biomaterial. *Biomaterials* 24(18), pp. 3139–3151.

Sohier, J., Daculsi, G., Sourice, S., de Groot, K. and Layrolle, P. 2010. Porous beta tricalcium phosphate scaffolds used as a BMP-2 delivery system for bone tissue engineering. *Journal of Bomedical Materials Research. Part A* 92(3), pp. 1105–14.

Sun, H., Mei, L., Song, C., Cui, X. and Wang, P. 2006. The in vivo degradation, absorption and excretion of PCL-based implant. *Biomaterials* 27(9), pp. 1735–40.

Vallet-Regi, M. and Gonzalez-Calbet, J.M. 2004. Calcium phosphates as substitution of bone tissues. *Progress in Solid State Chemistry* 32(1-2), pp. 1–31.

Vidaurre, A., Dueñas, J.M.M., Estellés, J.M. and Cortázar, I.C. 2008. Influence of Enzymatic Degradation on Physical Properties of Poly(ε -caprolactone) Films and Sponges. *Macromolecular Symposia* 269(1), pp. 38–46.

Wan, Y., Wu, H., Cao, X. and Dalai, S. 2008. Compressive mechanical properties and biodegradability of porous poly(caprolactone)/chitosan scaffolds. *Polymer Degradation and Stability* 93(10), pp. 1736–1741.

Wang, C., Xue, Y., Lin, K., Lu, J., Chang, J. and Sun, J. 2012. The enhancement of bone regeneration by a combination of osteoconductivity and osteostimulation using β-CaSiO3/β-Ca3(PO4)2 composite bioceramics. *Acta Biomaterialia* 8(1), pp. 350–60.

Wang, H., Li, Y., Zuo, Y., Li, J., Ma, S. and Cheng, L. 2007. Biocompatibility and osteogenesis of biomimetic nano-hydroxyapatite/polyamide composite scaffolds for bone tissue engineering. *Biomaterials* 28(22), pp. 3338–48.

Williams, J.M., Adewunmi, A., Schek, R.M., Flanagan, C.L., Krebsbach, P.H., Feinberg, S.E., Hollister, S.J. and Das, S. 2005. Bone tissue engineering using polycaprolactone scaffolds fabricated via selective laser sintering. *Biomaterials* 26(23), pp. 4817–27.

Wiltfang, J. and Merten, H. 2002. Degradation characteristics of α and β tricalcium phosphate (TCP) in minipigs. *Journal of Materials Research* 63(2), pp. 115–121.

Woodruff, M.A. and Hutmacher, D.W. 2010. The return of a forgotten polymer—Polycaprolactone in the 21st century. *Progress in Polymer Science* 35(10), pp. 1217–1256.

Yang, Z., Yuan, H., Tong, W., Zou, P., Chen, W. and Zhang, X. 1996. Osteogenesis in extraskeletally implanted porous calcium phosphate ceramics: variability among different kinds of animals. *Biomaterials* 17(22), pp. 2131–7.

Yanoso-Scholl, L., Jacobson, J. a, Bradica, G., Lerner, A.L., O'Keefe, R.J., Schwarz, E.M., Zuscik, M.J. and Awad, H. a 2010. Evaluation of dense polylactic acid/beta-tricalcium phosphate scaffolds for bone tissue engineering. *Journal of Biomedical Materials Research. Part A* 95(3), pp. 717–26.

6 Computational Modelling of Ovine Critical-Sized Tibial Defects.

6.1 Chapter Summary

Computational model geometries of tibial defects with two types of implanted tissue engineering scaffolds, β-tricalcium phosphate (β-TCP) and poly-ε-caprolactone (PCL)/β-TCP, are constructed from μ-CT scan images of the real *in vivo* defects. Simulations of each defect under four-point bending and under compressive loading that is representative of *in vivo* axial loading are performed. Model accuracy is assessed by comparing the predicted bending stiffness of each defect with experimentally-evaluated bending stiffness data that was generated as part of a previous animal trial. The mechanical integrity of each defect is analysed using stress distribution analysis. The results of these analyses highlight the influence of callus volume, and both scaffold volume and stiffness, on the load-bearing abilities of these defects. Clinically-used image-based methods to predict the safety of removing external fixation are evaluated for each defect. Conclusions are drawn on the predictions of defect stability using these methods and the results of computational and stress distribution analyses.

6.2 Introduction

Stabilisation of critical-sized defects in long bones is a major challenge in bone tissue engineering. A critical-sized defect is a large defect in a bone that will not heal on its own without intervention. It is widely understood that while often effective, donor site morbidity is an issue with the use of autografts (i.e. implanting bone from another site from the same patient) in treating this type of defect due to the volume of tissue required. Bone tissue engineering scaffolds have been developed from a wide range of materials to address this challenge (Bhumiratana et al. 2011; Lee et al. 2006; Yao et al. 2006; Rai et al. 2010; Schlichting et al. 2008; Lohfeld et al. 2012). Healing of a bone callus generally begins with the formation of a soft granulation tissue callus, with tissue differentiating towards forming fibrous tissue, cartilage and bone over time (Geris et al. 2006; Vetter et al. 2010; Vetter et al. 2011). Fracture callus stiffness increases over time as healing progresses (Gardner et al. 1998), with increasing local callus tissue stiffness as mineralisation increases (Vayron et al. 2012; Manjubala et al. 2009). External fixation of the bone is generally required for stabilisation of critical-sized defects during the early stages of healing until sufficient mechanical integrity has been achieved. Quantifying the degree of healing and mechanical integrity required for fixation removal is a challenge.

When developing FE models of anatomical objects such as a fracture callus or a scaffold implanted in a large bone defect, several factors are of critical importance to ensure the accuracy of the models. Firstly, the model geometry must be representative of the actual anatomy of the region that is being modelled. The real geometry of bone formation within such defects can be captured *in-vivo* and non-

invasively using μ-CT scanning. μ-CT scanning has been used to monitor the progression of new bone formation over time and to quantify parameters such as bone mineral density, degree of infiltration, bone formation and resorption rates (Roshan-Ghias et al. 2011; Jones et al. 2009; Jones et al. 2004; Schulte et al. 2011; van Lenthe et al. 2007; Cancedda et al. 2007; Freeman et al. 2009). Generating model geometries from μ-CT scans is an excellent way to ensure anatomical accuracy, and care must be taken to ensure that the resolution is appropriate for each modelling case.

While accurate model geometry is of critical importance, it is equally essential that the correct mechanical properties and constitutive laws are assigned in the FE models. When appropriate, experimentally-obtained mechanical properties of the actual tissues being modelled should be used; however, when building models using non-invasive techniques this is not always feasible. In some cases, data from relevant literature can be sufficient when care is taken to interpret experimental results. It can be difficult to obtain data for the specific case being modelled, in particular when there is desire to analyse a defect over time as healing progresses. As mentioned above, *in-vivo* studies using nanoindentation have shown that fracture callus stiffens over time as mineralisation increases (Vayron et al. 2012; Manjubala et al. 2009), therefore the chosen mechanical properties must be representative of the callus stiffness at the appropriate stage in healing and mineralisation. FE models constructed from μ-CT scans have been used to determine fracture callus tissue properties by calibrating material properties against experimental data (Vijayakumar et al. 2006; Steiner et al. 2012). This approach has been described as "self-validating", (Vijayakumar et al. 2006), as the model is required to conform to the

actual anatomical geometry and the callus material properties are calibrated so that the overall observed tensile mechanical behaviour is reproduced. This method of model calibration is very useful when the geometry can be obtained non-invasively but local tissue properties cannot.

FE modelling of fracture callus defects using anatomically accurate models generated from μ-CT scans has been used to assess the influence of new bone tissue formation within the defect on the mechanical properties of the scaffold-callus construct as a whole. Fracture callus mechanical integrity has been investigated using simulations of uniaxial loading (Boerckel et al. 2012; Mehta et al. 2012; Gao et al. 2013), bending loading (Shefelbine et al. 2005) and analysis of the transmission of *in-vivo* loading through a tibial fracture callus (Vijayakumar et al. 2006). Similar methods were employed by (Roshan-Ghias et al. 2011) to generate FE models of a scaffold-callus construct for uniaxial loading simulations.

It is worth noting that long bones such as the tibia and femur are subjected to complex loading conditions *in-vivo*, with a combination of vertical loading due to body weight and loading applied in various directions at muscle attachment points during normal gait (Taylor et al. 2006). As a result, it is possible that the use of uniaxial loading alone would be insufficient to make a decision on whether or not sufficient healing has occurred to allow for the removal of external fixator devices, which are used to support the fracture or defect during healing, as the bone could be stiff in compression or tension but weak in bending, in which case removal of fixation would result in fracture. The use of four-point bending tests can give a more complete picture of the mechanical integrity of the fracture callus or scaffold-callus

construct (Shefelbine et al. 2005; Lohfeld et al. 2012). The information that can be generated using FE modelling of uniaxial and bending testing has significant clinical value as it provides a non-invasive method to evaluate the progress of new bone formation and defect stability, and to inform decisions regarding the appropriate time to remove external fixation. This type of modelling has enormous potential to aid the design of scaffolds and to assess the load-bearing abilities of a scaffold-callus construct but is under-utilised in the field at this time, in particular as μ-CT data is often generated during *in vivo* studies for the measurement of other parameters.

Non-invasive methods to quantify bone formation within a defect site based on imaging method such as X-ray and μ-CT have been developed to in order to provide clinicians with a means to make informed decisions regarding the removal of external fixation. These methods have been developed primarily for treatment of distraction osteogenesis, a surgical technique used to lengthen long bones, however many similarities exist between the defect type created for distraction osteogenesis and a critical-sized defect with an implanted scaffold. In both cases, a gap in the length of the bone is created and new bone is allowed to form within the gap, with or without the addition of a scaffold, and the defect is stabilised with external fixation during the treatment. In the treatment of such defects, the timely removal of external fixation is a critical factor as early removal can result in re-fracture and additional pain for the patient. Late removal of the external fixator results in additional patient pain and increased risk of infection.

The clinical decision to remove external fixation is currently informed by X-ray and μ-CT imaging and callus measurement parameters that can be calculated from these.

The most common criterion for the removal of fixation is the measurement of the thickness of continuous cortices of bone bridging a defect using X-rays. A thickness of 2 mm in three bridging cortices has been reported as sufficient for removal of fixation, with reported re-fracture rates of 4% (Skaggs et al. 1999) and 3% (Fischgrund et al. 1994). This method is advantageous due to the availability and relatively low cost of X-ray imaging, but is of limited value as a result of user subjectivity. It is also based on 2D defect images and the visibility and dimensions of the cortices may be dependent on the angle at which the X-ray is taken. Despite these limitations, a pixel value ratio (P_r), evaluated from X-ray images, has been used as a guide for fixation removal, with re-fractures reported in defects with $P_r < 0.8$ (Song et al. 2005) and a suggested optimal P_r value of 1 (Zhao et al. 2009). The 2D nature of these quantitative callus assessment methods is a limiting factor as they do not account for 3D variations in callus density or continuous loading paths of bone.

Other measurements such as bone mineral density, a scalar value from a DEXA scan (Hazra et al. 2008; Song et al. 2012), and a strength–strain index (SSI), defined as the cross-sectional moment of inertia ($CSMI$) weighted by density distribution (Kokoroghiannis et al. 2009; Lind et al. 2001), have also been identified as useful measurements of callus integrity. Cross-sectional moment of inertia ($CSMI$) was found to have high correlation with bending breaking force determined using three-point bending (Jamsa et al. 1998). While the 3D nature of these assessment methods gives a more complete picture of overall callus mechanical integrity than the 2D methods above, the presence of continuous loading paths within the bone callus is still not accounted for. This means that a good $CSMI$ or P_r value may be predicted

even in cases where cracks or gaps that would affect the load-bearing abilities of the callus are present.

The primary objective of the study in this chapter is to develop anatomically-accurate finite element models of ovine tibia with two types of implanted scaffold and to assess the mechanical stability of each individual defect. Models are constructed from μ-CT scan images of each defect region, and include both the new bone callus and scaffold geometries. The accuracy of each model geometry is verified by comparing computationally-evaluated bending stiffness with experimentally determined stiffness values for the same defects that were reported in a previous study (Lohfeld et al. 2012). The stability of each defect, and in particular the ability to withstand realistic compressive loading, is evaluated using bending and compression simulations, along with stress distribution analyses. The secondary objective of this study is to evaluate two clinically-used callus-evaluation parameters, P_r (2D) and $CSMI$ (3D), to predict the safety of removing the external fixator device for each individual defect. Comparisons are made with the results of computational simulations of bending and compressive loading to make conclusions on the suitability of the use of these callus-evaluation parameters.

6.3 Methods

6.3.1 Summary of Model Development

A flowchart outlining the individual steps in the present study is shown in Figure 6.1, for the case of PCL/β-TCP scaffolds, and in Figure 6.2, for the case of β-TCP scaffolds. The context for this study is described in Section 6.3.2 with reference to an *in vivo* study in which scaffolds were implanted in tibial defects. The methods by which FE model geometries are generated are described for intact tibiae in Section 6.3.3 and for tibial defects with implanted scaffolds in Section 6.3.4.

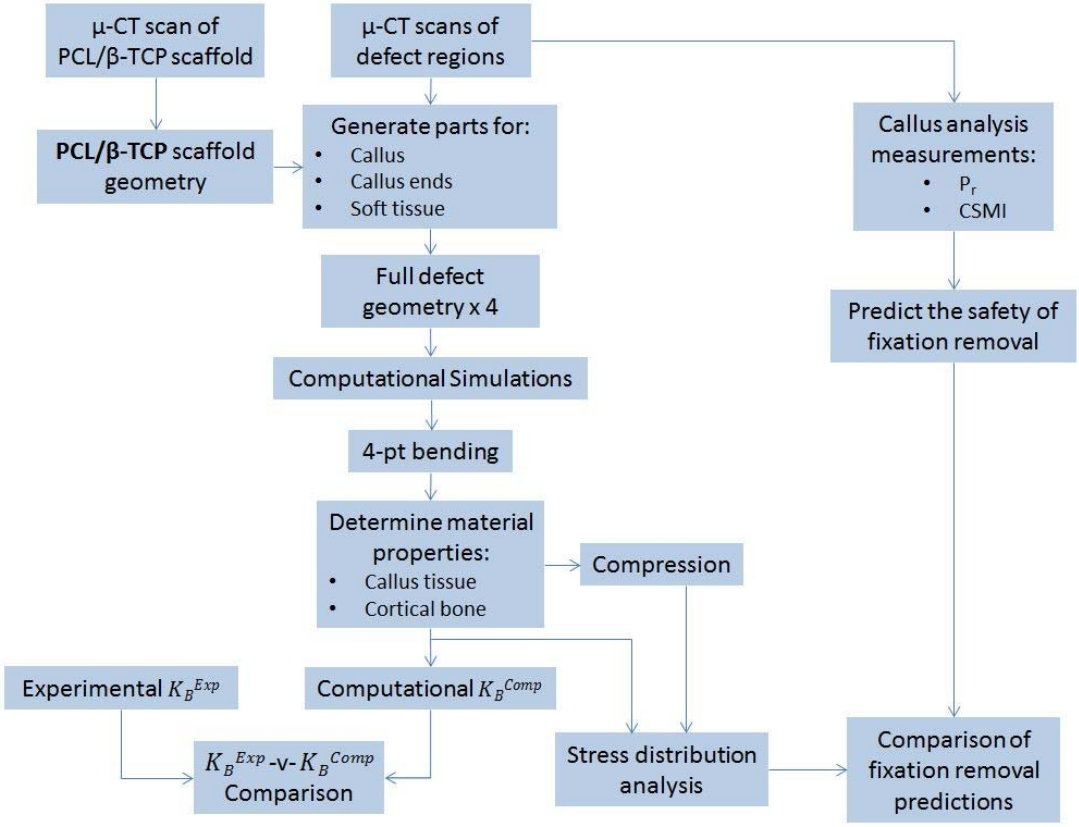

Figure 6.1: Flowchart outlining the individual steps in the study presented in this chapter for the case of PCL/β-TCP scaffolds.

The development of four-point bending simulations to replicate an experimental test set-up is described in Section 6.3.5, and the specification of the mechanical properties that are used in FE simulations is detailed in Section 6.3.6. Simulations of compressive loading that is representative of *in vivo* loading are described in Section 6.3.7. The mechanical performance of these tibial defects is evaluated using stress distribution analysis in Section 6.3.8. The calculation of two types of callus assessment measurements that are used to evaluate the safety of external fixation removal is outlined in Section 6.3.9.

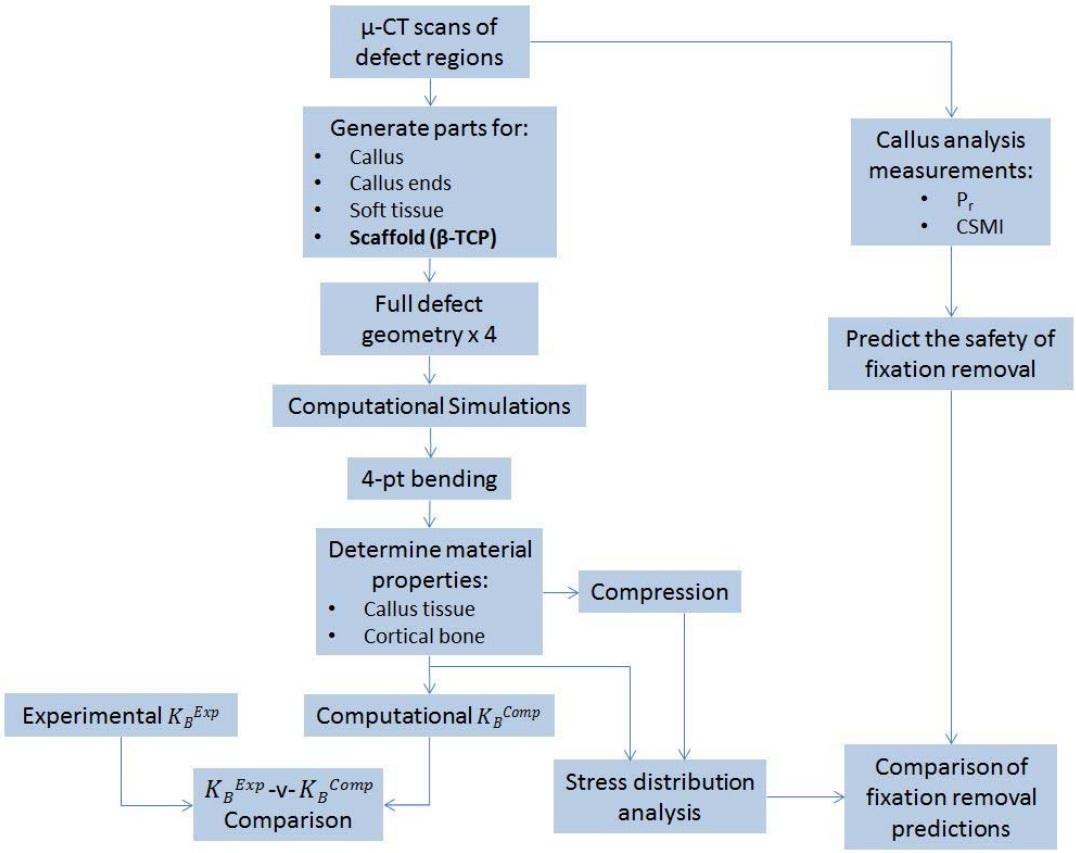

Figure 6.2: Flowchart outlining the individual steps in the study presented in this chapter for the case of β-TCP scaffolds.

6.3.2 *In Vivo* Study Data

This study is based around an *in vivo* study of scaffolds implanted in critical-sized ovine tibial defects as part of the STEPS EU-FP6 project (Lohfeld et al. 2012). To give a brief summary of the *in vivo* study, two types of scaffold were implanted (Figure 6.3): PCL/β-TCP scaffolds fabricated from a 90/10wt% blend of PCL and β-TCP powders using SLS and commercially available β-TCP scaffolds (Biovision, Illmenau, Germany). Scaffolds were implanted in 20 mm mid-shaft defects in the right tibia, leaving the left tibia intact, and stabilised using a titanium plate and fixation screws. After 14 weeks, both the right and left tibiae were extracted, and X-ray imaging and μ-CT imaging was carried out.

Four-point bend testing was carried out on both left and right tibiae, as per Figure 6.3, to a maximum load of 40 N with a 40 mm distance between loading points and a total unsupported length of 160 mm. Each tibia was incrementally rotated 30° about the longitudinal axis to determine the bending stiffness in 360°. The equivalent bending stiffness, K_B, was calculated using Equation (6.1) (ISO 1990):

$$K_B = \frac{(2b + 3a)b^2k}{12} \tag{6.1}$$

where b is the unsupported length between the two outermost supports, a is the distance between the loading supports and k is the slope of the load-deflection curve, as indicated in Figure 6.4. An average experimental bending stiffness, $K_B{}^{Exp}$, was calculated for each of the four samples from the full set of experimental bending

stiffness data (i.e. 0° - 360°) for comparison with the predictions of the computational models in the present study.

For the purposes of the present study, two defect samples for each scaffold type were selected from the full set of data generated in the STEPS *in vivo* study (Lohfeld et al. 2012), giving a total of four samples. High-resolution computational model geometries for FE modelling in the present study were generated from the μ-CT scan data that was generated in the STEPS study, as described below in Section 6.3.3 and 6.3.4.

6.3.3 Generation of Model Geometries: Intact Tibiae

The real geometry of the intact tibia for each sample was not available as only μ-CT scans of the callus/defect region and no μ-CT scans of the full tibia were obtained at the time of the *in-vivo* study. Instead, an idealised tibial geometry was generated for each individual defect by extracting the tibia cross-section geometry from the uppermost image of the scan of the callus region, in which the tibial cross-section is visible, as per Figure 6.5. An idealised tibia with constant cross-section and a length of 80 mm was constructed by extruding this cross-section along the longitudinal axis.

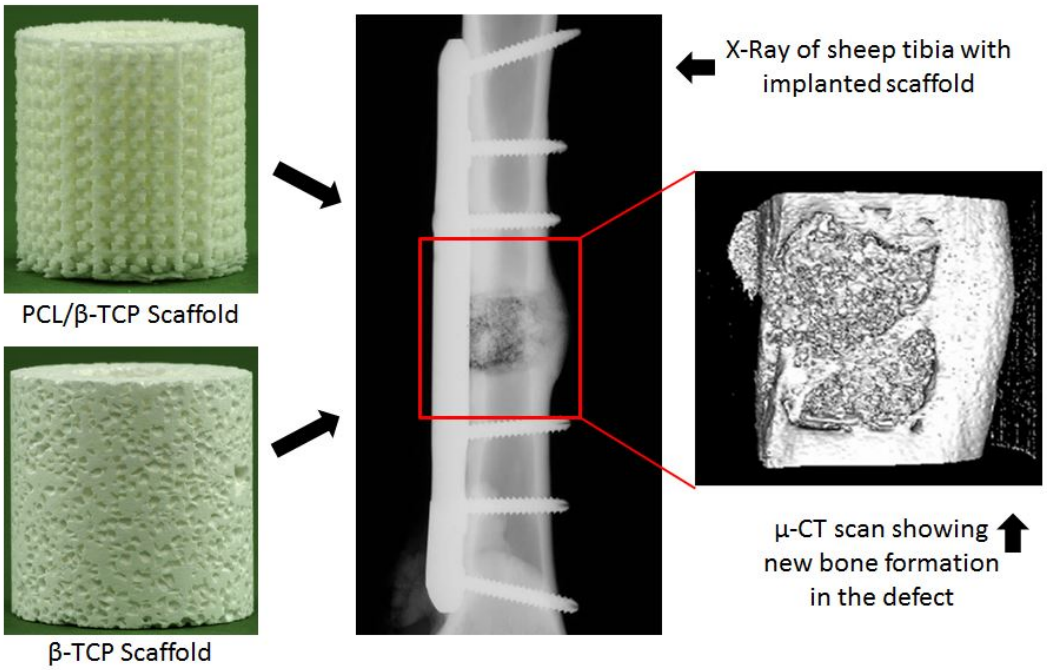

Figure 6.3: PCL/β-TCP scaffolds and β-TCP scaffolds were implanted in critical-sized defects in ovine tibiae as part of the STEPS EU-FP6 project (Lohfeld et al. 2012). New bone formation was evaluated by X-ray and μ-CT scanning

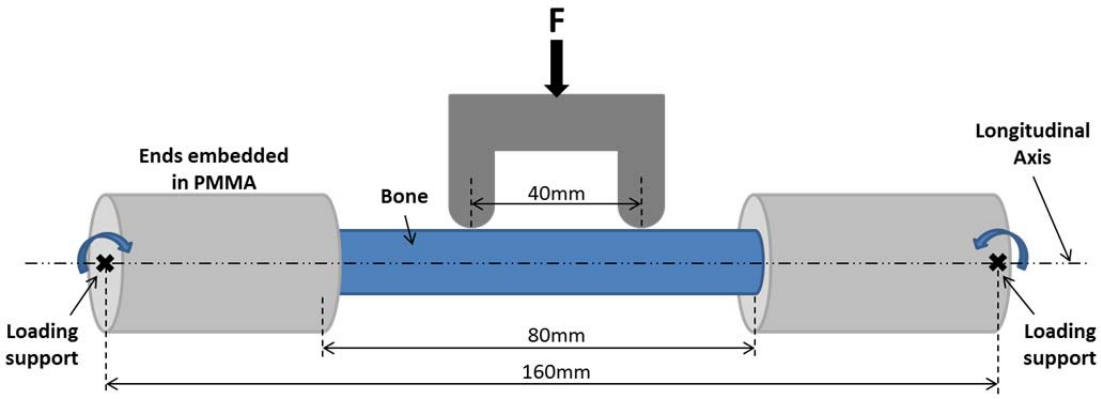

Figure 6.4: Schematic diagram of the experimental four-point bending test set-up used to evaluate tibial bending stiffness by Lohfeld et al. (Lohfeld et al. 2012).

6.3.4 Generation of Model Geometries: Tibiae with Scaffold and Callus

FE models of the tibial defect were constructed from μ-CT scans of each defect area. Each full model consists of the real bony callus tissue geometry, the implanted tissue engineering scaffold, the tibia and soft tissue. Idealised geometries for soft tissue and the portion of the callus that is outside of the scanned volume were generated. The model generation process is described in detail below for defects with both scaffold types.

For the defects with implanted β-TCP scaffolds, both scaffold and callus are visible in the μ-CT scans, as shown in Figure 6.6. The scaffold and callus model geometries were generated directly from the μ-CT scans, and were combined with the idealised tibia geometry. The β-TCP scaffold geometry could not be separated from the surrounding bone automatically using grey-value as there was very little difference between the grey-value of the scaffold and the grey-values of the surrounding tissue in some regions of the scan. The β-TCP scaffold geometry was extracted from the μ-CT scan manually in MIMICS (Materialise, Belgium) by selecting individual scaffold regions and using the region-growing function. The callus tissue geometry was generated by segmenting tissue with grey-values ranging from 40 to 90, based on visible tissue regions, and removing any overlaps with the β-TCP scaffold geometry using Boolean subtraction. In order to account for material property heterogeneity in callus tissue regions, each callus region was separated into five separate parts to represent five ranges of grey-value, each with an average grey-value of 45, 55, 65, 75 and 85, respectively.

For the defects with implanted PCL/β-TCP scaffolds, the callus tissue geometry was generated by segmenting tissue with grey-values ranging from 40 to 180, based on visible tissue regions. Similar to the β-TCP scaffold case, callus regions were separated into five separate parts to represent five ranges of grey-value, each with an average grey-value of 54, 82.5, 110.5, 138.5 and 166.5, respectively. Only the callus geometry is visible in the μ-CT scans as the grey-values of the scaffold are too low to be visible at the settings used to scan bone (see Figure 6.6). This is due to the low density of the scaffold material in comparison to bone. The PCL/β-TCP scaffold geometry was obtained from a separate scan of the scaffold. The scaffold geometry was then imported and aligned within each defect in the callus model using MIMICS. Any scaffold material intersecting the surrounding bone callus region was removed using Boolean subtraction.X-ray images of the tibial defects indicate that the callus has a rounded shape and extends above and below the scaffold region visible in the μ-CT scans shown in Figure 6.7. In order to represent this portion of the callus, extra material (named 'callus ends') was generated by interpolating between the tibia geometry and each end of the callus using MIMICS. In this way, a part specific to each defect, and to each end of the callus defect, was generated for each sample to replicate the shape of the callus as seen on the X-ray images. Some interpretation was required here as the X-ray images are 2D and only one was available per tibia, but the shape of the extra added callus material adheres as closely as possible to measurements of the callus from the X-rays.

Soft tissues, such as fibrous or granulation tissue within the defect regions, are not visible on the CT scans due to the low density of these tissue types. Idealised

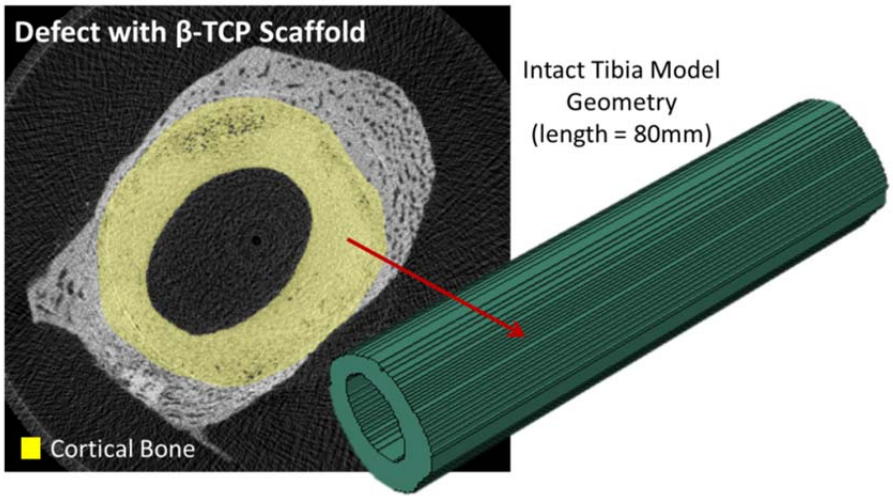

Figure 6.5: Generation of intact tibia model geometries from defect μ-CT scan images. This example is illustrated using μ-CT scan images for a defect with an implanted β-TCP scaffold.

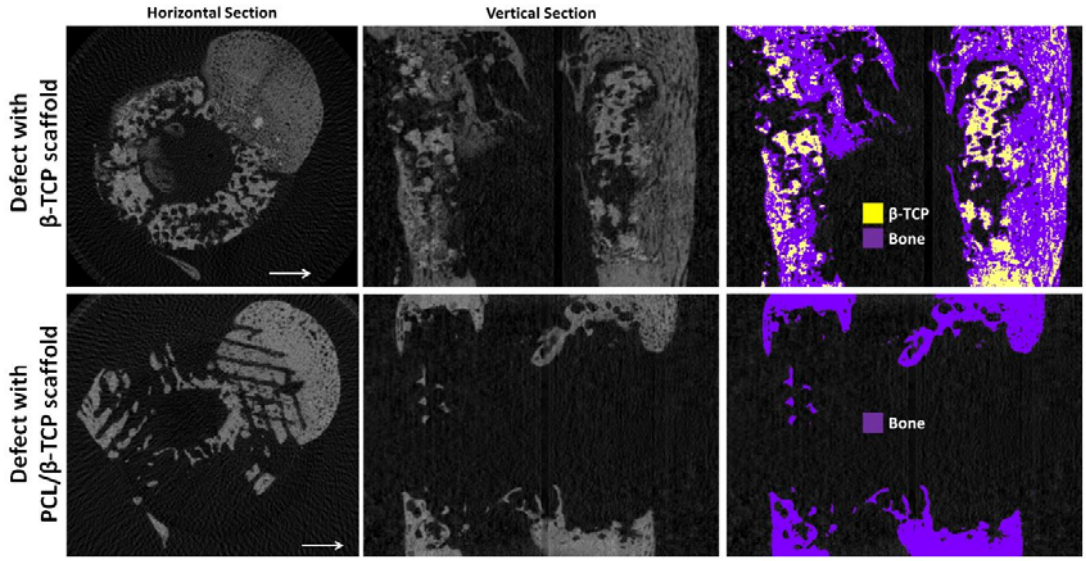

Figure 6.6: Sections of μ-CT scans of *in-vivo* callus with an implanted β-TCP scaffold (top) and PCL/β-TCP scaffold (bottom): (L-R) horizontal section, vertical section and vertical section showing new bone formation (purple) and regions of high density indicating scaffold location for β-TCP scaffolds (yellow). No scaffold is visible in the defect with an implanted PCL/β-TCP scaffold due to low material density relative to that of bone.

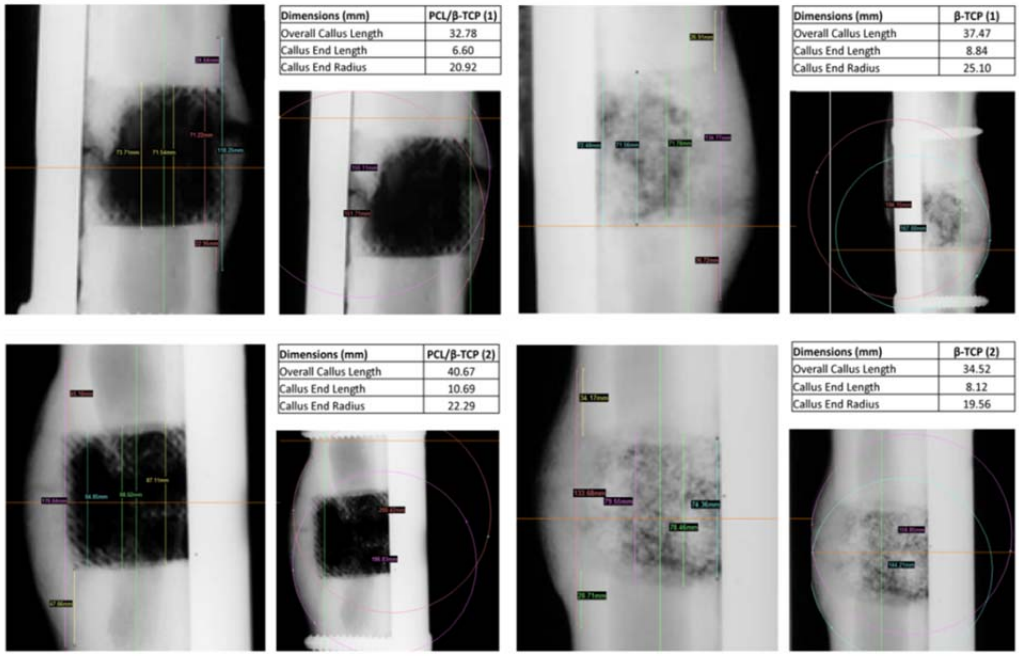

Figure 6.7: Measurement of the dimensions of each end of the callus geometry from X-ray images of four tibial defects.

representations of the soft tissue geometries were generated manually for each individual defect model using MIMICS. Firstly, the outer geometry of the overall defect region was selected and a mask was created that filled this volume. Secondly, the volume of the callus tissues and scaffold geometries were removed from this region using Boolean subtraction. The remaining region represents the volume of soft tissue within the defect.

Individual FE meshes were generated and exported from MIMICS for each tissue type and scaffold, where each is a separate 'part' of the overall assembly. Voxel meshes were used for each part, with reduced integration 8-noded hexahedral brick elements. Models were imported to Abaqus/Standard V6.13 (DS SIMULIA, USA) and output files (.odb) for each part were generated. All part geometries were then imported from .odb files into a single model, and the full model geometries were

assembled using the merge mesh tool in Abaqus/CAE. Infinitesimal deformation kinematics was assumed (NLGEOM turned off) to simplify the simulations, within Abaqus/Standard.

When merging parts using this tool within Abaqus/CAE, it was found that selecting the option to remove duplicate elements (referred to here as option 1) resulted in some changes in element set assignment, resulting in changes to material section assignment. In order to rectify this, the elements in the set for each section were reselected manually. Note that this was not observed when the option to remove duplicate elements (referred to here as option 2) was not selected; however when using option 2 it is possible for the operation of merging two meshes to result in two elements being present in the same location with merged nodes, and in this case it is then unclear which element material properties are used. On this basis, option 1 was used for all model assembly in this study; however negligible differences between model results were found when option 1 and option 2 were compared. Boolean subtraction tools were used to ensure there is no overlap between individual parts in MIMICS, therefore any overlap in mesh elements was a result of pixel averaging during mesh generation in MIMICS.

The full model assembly process for defects with β-TCP scaffolds is illustrated in Figure 6.8 and in Figure 6.9 for defects with β-TCP scaffolds. Each of the four model geometries was assigned a label (β-TCP (1), β-TCP (2), PCL/β-TCP (1) and PCL/β-TCP (2)), corresponding to the scaffold material type, and this is shown in Figure 6.10 alongside the X-ray image of the corresponding defect. Each defect is referred to using these labels from this point onwards.

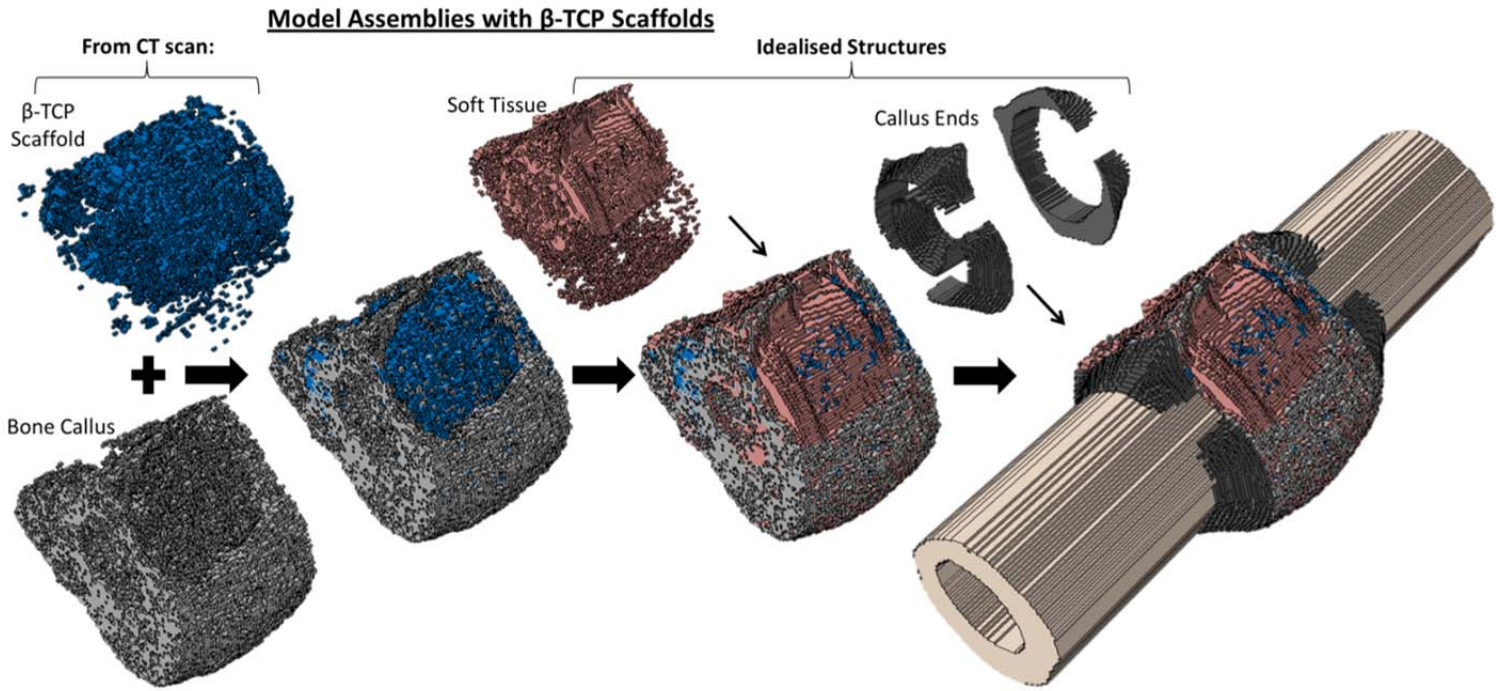

Figure 6.8: Schematic diagram illustrating the assembly of model geometries for tibial defects with β-TCP scaffolds. In this case, the β-TCP scaffold and bone callus geometries are obtained directly from one μ-CT scan; soft tissue and callus ends parts are idealised structures generated based on the μ-CT scan geometries.

Figure 6.9: Schematic diagram illustrating the assembly of model geometries for tibial defects with PCL/β-TCP scaffolds. In this case, the PCL/β-TCP scaffold geometry is obtained from a separate μ-CT scan from the bone callus geometries as it is not visible in this scan (Figure 6.6), and is carefully positioned to fit the regions containing scaffold struts visible in bone callus scan images. Soft tissue and callus ends parts are idealised structures generated based on the μ-CT scan geometries.

6.3.5 Four-Point Bending Test Model Development

Simulations of four-point bending were carried out to assess the bending stiffness of both intact tibiae and tibial defects with implanted scaffolds. A schematic diagram of the experimental four-point bending test set-up is shown in Figure 6.4, as per Lohfeld et al. (Lohfeld et al. 2012). The computational model implementation of this is illustrated in Figure 6.11. For each model, the mid-point of the tibial cross-section was calculated in the 1- and 2-directions to give the centroid and the location of the longitudinal axis. The tibia was positioned such that the centroid of the tibial cross-section lies at zero on both the 1- and 2-axis, and that the longitudinal axis is aligned with the 3-axis. The mid-point of the tibia was positioned at x_3 = 0, leaving a 40 mm length at either side. Reference Points (RPs) for boundary conditions were positioned at (0, 0, 80) and (0, 0, -80), giving an unsupported span of 160 mm. Boundary conditions were applied to each RP to restrict motion to rotation about the 1-axis. Each end of the tibia was constrained to the closest RP using *MPC Beam constraints. A loading node was selected from the top layer of nodes at both x_3 = 20 mm and at x_3 = -20 mm to give a loading span of 40 mm. *MPC Tie constraints were created between each loading node and the remaining nodes at the top surface at the same x_3-position to replicate the deformation of the tibia due to the displacement of the loading supports in the experimental test set-up. A force of 20 N was applied to each loading node with a smooth step amplitude (load = 0 N at step time = 0, load = 20 N at step time = 1). The average displacement at the loaded nodes was recorded and the slope of the load-deflection curve (k) was calculated.

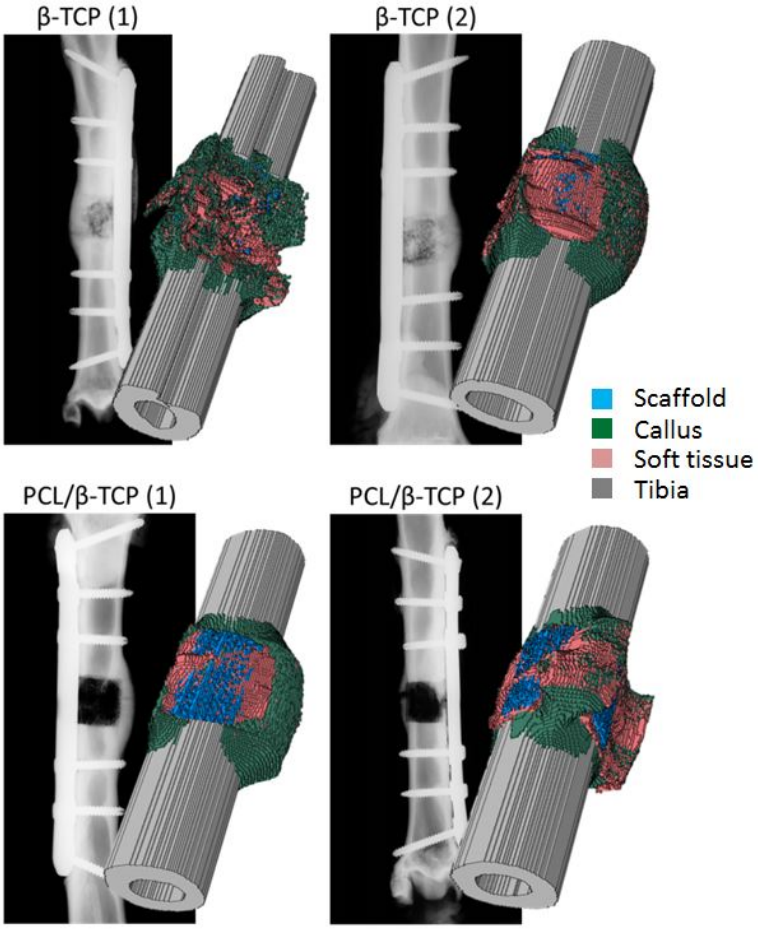

Figure 6.10: Illustration of the full tibia, callus and scaffold model assembly that is used for each case (β-TCP (1), β-TCP (2), PCL/β-TCP (1) and PCL/β-TCP (2)), along with the corresponding X-ray image.

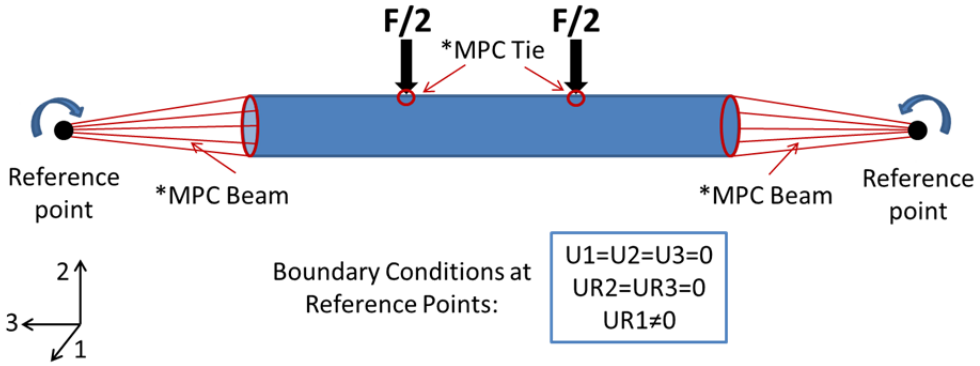

Figure 6.11: Schematic diagram of computational model implementation of the four-point bending set-up.

Each model was incrementally rotated 30° about the longitudinal axis and loading was repeated to determine the bending stiffness at angles 0° to 330° to replicate the experimental testing, giving a total of 12 individual loading configurations per sample, noting that the 360° case is identical to the 0° case. The equivalent bending stiffness (K_B) was calculated for each angular configuration, as per Equation (6.1). It was not possible to align the 0° position of the simulation geometries with the 0° position from the experimental testing (Lohfeld et al. 2012) due to lack of orientation information in the μ-CT scans, therefore bending stiffness evaluated from the simulations at any individual angle could not be compared directly with the corresponding experimental value. Instead, an average bending stiffness ${K_B}^{Comp}$, evaluated by averaging over the 12 angular configurations, was determined for each of the four sample models.

The statistical difference between experimental average bending stiffness, ${K_B}^{Exp}$, and ${K_B}^{Comp}$ was evaluated for each model using an unpaired T-test. The correlation between ${K_B}^{Exp}$ and ${K_B}^{Comp}$ was evaluated using the Pearson's correlation coefficient, r, which is calculated using Equation (6.2), where n is the sample number, x is the value of ${K_B}^{Exp}$ and y is the value of ${K_B}^{Comp}$.

$$r = \frac{n(\sum xy) - (\sum x)(\sum y)}{\sqrt{[n\sum x^2 - (\sum x)^2][n\sum y^2 - (\sum y)^2]}} \tag{6.2}$$

6.3.6 Elastic Property Assignment

6.3.6.1 Cortical Bone Elastic Properties

Four-point bending simulations of intact tibiae using the idealised intact tibia model geometries described in Section 6.3.3 above were carried out to determine the elastic modulus of cortical bone specific to the specimens used in this study. Experimental data for the bending stiffness of intact tibiae that was generated as part of the STEPS project was used for comparison and model verification (Lohfeld et al. 2012). The values of ovine cortical bone elastic modulus reported in the literature are summarised in Table 6.1 and vary between 15 and 24.6 GPa. Bending simulations were carried out with values of cortical bone elastic modulus representative of this range of properties as described above and the bending stiffness of each tibia was calculated as per Equation (6.1). The results of these models (Figure 6.12), which are discussed in further detail in Section 6.4.1 below, indicate that these values of elastic modulus overestimate bending stiffness, therefore simulations with lower values of elastic moduli were carried out. An elastic modulus of 11 GPa was found to give the best approximation of the experimentally reported values (n = 4) for these specific FE models of intact tibiae (n = 4). This value of elastic modulus was then used for cortical bone in subsequent simulations of tibial defects with implanted scaffolds.

Note that a homogeneous elastic modulus is assigned in these intact tibia models and that anisotropy was not accounted for. This modulus represents an average cortical bone elastic modulus. Regional variations in material density and pixel grey-value in cortical bone are known to exist, and are visible in the top slices of μ-CT scans of the

defect regions. However, as only idealised tibial geometries are available for this study, these variations cannot

Table 6.1: Summary of values for elastic modulus (E) and ultimate strength (σ_U) of cortical bone reported in the literature.

Animal	Location	Test method	E (GPa)	σ_U (MPa)	Reference
Sheep	Tibia	FEA (2D)	15.75	-	(Steiner et al. 2012)
	Tibia	Nanoindentation	20.8	-	(Cipitria et al. 2012)
	Tibia	Nanoindentation	15-25	-	(Grant et al. 2014)
	Tibia	3-Point Bending	25.6	-	(Schorlemmer et al. 2005)
	Tibia	3-Point Bending	-	110-124	(Malizos et al. 2006)
	Tibia	3-Point Bending	-	289	(Schorlemmer et al. 2005)
	Femur	3-Point Bending	-	136-201	(Wallace et al. 2013)
Human	Tibia	FEA	20	-	(Gardner et al. 2000)
	Tibia	FEA	15.75	-	(Smit et al. 2002)
	Tibia	Compression	-	200	(Kemper et al. 2007)
	Femur	Tension	-	10.27	(Evans 1976)
	Femur	Tension Compression	-	50-160 160-240	(Hansen et al. 2008)
Pig	Femur	Tension	-	96.7-119.2	(Feng and Jasiuk 2011)
Dog	Tibia	Torsion	-	28.5	(Markel et al. 1990)
Rabbit	Tibia	Nanoindentation	20.66	-	(Vayron et al. 2012)
Rat	Femur	FEA	15	-	(Shefelbine et al. 2005)
	Femur	Nanoindentation	7.2	-	(Leong and Morgan 2009)

be accounted for. The values of cortical bone elastic modulus reported in the literature and in Table 6.1, in some cases evaluated using nanoindentation on regions of fully-dense cortical bone, represent the upper bounds of cortical bone elastic modulus. It is expected that average values of cortical bone across a cross-section of a long bone would be lower than the values reported in Table 6.1, due to microporosity and local variations in density.

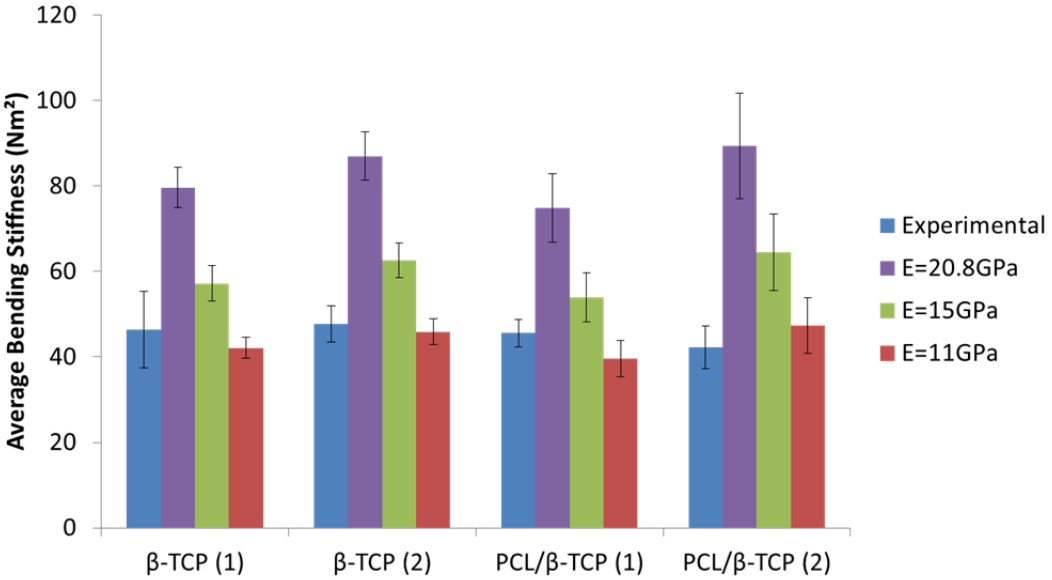

Figure 6.12: Bending stiffness calculated from four-point bending simulations of idealised intact tibia geometries with varied input elastic modulus (E), showing best fit for E = 11 GPa (red). Mean values for each data set are shown and error bars represent standard deviation. Experimentally-evaluated average bending stiffness for each specific tibial defect (blue), evaluated from data generated in previous study (Lohfeld et al. 2012), are included for comparison purposes.

6.3.6.2 Scaffold Elastic Properties

Linear elastic properties and a Poisson's ratio of 0.3 were assumed for both scaffold types, as per previous chapters in this thesis. A homogeneous elastic modulus was assumed for the β-TCP scaffolds with E = 24.6 GPa (Wang et al. 2004).

The PCL/β-TCP scaffolds are known to have heterogeneous mechanical properties at the element level, as a result of the presence of β-TCP particles and the sintering process, as discussed in Chapters 3, 4 and 5. However, in order to generate FE meshes of the tibial defects with PCL/β-TCP scaffolds, the scaffold part had to be generated in a separate μ-CT scan (as discussed in Section 6.3.4 above). The scaffold part was then imported into a second set of μ-CT scan data of the defect region for alignment and model assembly. Due to the fundamental limitations of combining parts from two different sets of μ-CT scans in this way, only geometrical information and no grey-value information can be retained from the part that is being added to the second μ-CT scan. As a result, only homogeneous elastic property assignment can be used for the PCL/β-TCP scaffolds. In order to determine the appropriate value of scaffold elastic modulus for this study, the average grey-value of individual 90/10wt% PCL/β-TCP scaffold struts (that were fabricated for the study presented in Chapter 4 of this thesis) was evaluated. The average value of strut grey-value for the four struts considered in Chapter 4 was found to be 101.51. The relationship between elastic modulus and grey-value that was established for the 90/10wt% PCL/β-TCP material in Chapter 4 was then used to determine the strut elastic modulus, giving a value of 250.37 MPa. This value of elastic modulus is assigned to PCL/β-TCP scaffold geometries in all simulations using undegraded material properties.

The elastic modulus of degraded PCL/β-TCP scaffolds was estimated from the results of Chapter 5, in which *in vitro* degradation of PCL/β-TCP scaffold materials was carried out. In Chapter 5, accelerated ageing methods were used to simulate ageing to an equivalent of 14 weeks *in vivo.* The elastic modulus of the PCL/β-TCP scaffold materials at this point was 37.43% of the original material elastic modulus. The elastic modulus of the degraded scaffold material, for use in the present study, was then estimated from this result giving a value of 93.71 MPa. Bending test simulations using this value were carried out in order to evaluate the influence of scaffold degradation on the mechanical performance of the scaffold-callus construct.

6.3.6.3 Callus Elastic Properties

The exact elastic properties of the defect callus materials specific to the defects used in this study are not known as no mechanical testing of callus tissues was carried out at the end of the *in-vivo* study. As the constructed model geometries for the defects with β-TCP scaffolds are arguably more accurate due to the visibility of the scaffold in μ-CT scan images, these models were used to determine appropriate callus elastic modulus values. Simulations were carried out with typical ranges of elastic properties, as listed in Table 6.2, and compared with experimental results (Lohfeld et al. 2012) in order to establish a suitable range of properties for callus tissues. Representative results for defects with each scaffold type (rather than an average of the full set of 12), shown in Figure 6.13 and discussed in further detail below in Section 6.4.2, indicate that the use of properties from (Claes and Heigele 1999) give the best fit for both model types. These values of callus tissue properties were used in all defect models from this point onwards. An elastic modulus value of 2 MPa and

a Poisson's ratio of 0.167 were assumed for soft tissue (Hori and Lewis 1982). These values have previously been used in FE defect modelling (Vetter et al. 2011; Lacroix and Prendergast 2002).

Due to differences in scan settings, the overall range of grey-values differed between µ-CT scans of defects with each scaffold type. The range of grey-values was high in

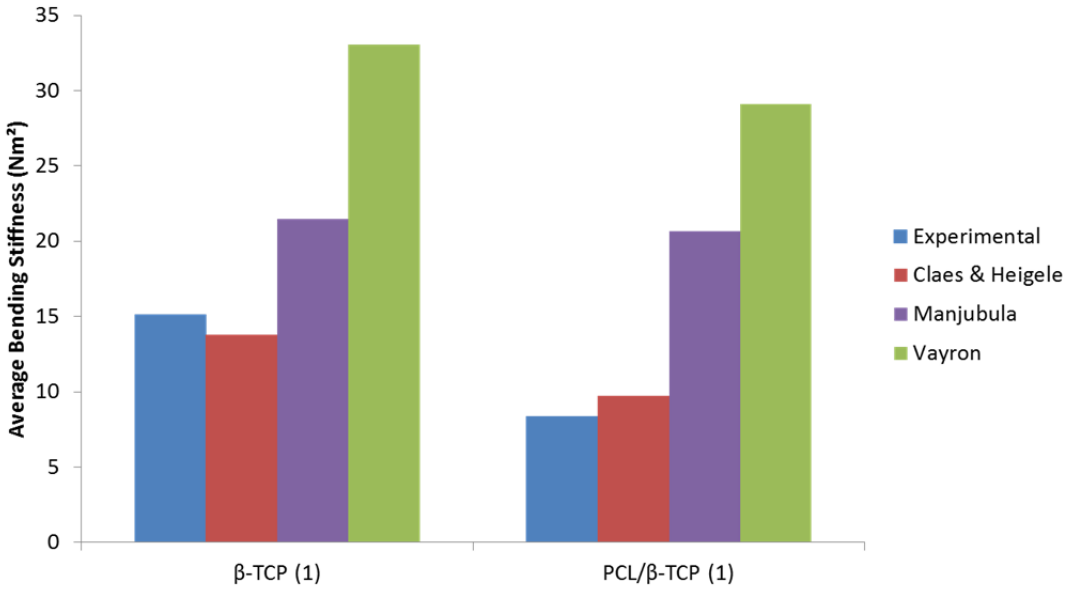

Figure 6.13: Bending stiffness calculated from four-point bending simulations of tibial defects with a range of input material properties in the callus parts, for one defect with each scaffold type. Mean values for each data set are shown and error bars represent standard deviation. Simulations using callus properties from (Claes and Heigele 1999) are shown in red, from (Manjubala et al. 2009) in purple and from (Vayron et al. 2012) in green. Experimentally-evaluated average bending stiffness for each specific tibial defect (blue), evaluated from data generated in a previous study (Lohfeld et al. 2012), are included for comparison purposes with material properties from (Claes and Heigele 1999) showing the best fit with experimental data.

the μ-CT scans of defects with PCL/β-TCP scaffolds (callus grey-values range from 40 to 180) in comparison to μ-CT scans of defects with β-TCP scaffolds (callus grey-values range from 40 to 90). The callus elastic modulus values, as determined for models of defects with β-TCP scaffolds were then scaled for use in the models of defects with PCL/β-TCP scaffolds. A scaling factor was calculated using the average grey-values of cortical bone in each defect scan. For the purposes of this scaling it was assumed that the density of cortical bone in each animal was uniform. Average values of grey-values of cortical bone for defects with β-TCP scaffolds were found to be 82.117 and 86.81, giving an average of 84.49. Average values of grey-values of cortical bone for defects with PCL/β-TCP scaffolds were found to be 134.18 and 133.87, giving an average of 134.03. Taking the grey-value of cortical bone in scans with β-TCP scaffolds as a baseline, the scaling factor (s) was calculated as per Equation (6.3).

$$s = \frac{84.49}{134.03} = 0.63 \tag{6.3}$$

This scaling factor was applied to all elastic modulus values for the callus region in models of defects with PCL/β-TCP scaffolds, in order to evaluate the elastic modulus values for each region. In all cases, the elastic modulus of the 'Range 3' callus section appropriate to each model type was assigned to the callus ends part (see Figure 6.9). The material properties assigned in each model type is summarised in Table 6.3.

Table 6.2: Summary of values for elastic modulus (E) and ultimate strength (σ_U) of bone callus tissues reported in the literature.

Animal	Test method	E (GPa)	σ_U (MPa)	Weeks Post-Fracture	Reference
Sheep	3-Point Bending	-	14.6 - 24	14.29	(Malizos et al. 2006)
	Nanoindentation	3.6-6.6	-	2	(Manjubala et al. 2009)
		3.8-8.4	-	3	
		9.5-12	-	6	
		10.4-13.5	-	9	
	FEA (2D)	1	-	Soft Callus	(Claes and Heigele 1999)
		6	-	Stiff Callus	
Dog	Torsion	-	3.6-15.6	4-12	(Markel et al. 1990)
Rabbit	Nanoindentation	15.35	-	4	(Vayron et al. 2012)
		15.85	-	7	
		17.82	-	13	
	Nanoindentation	2.36	-	7	(Guo et al. 2001)
Rat	Nanoindentation	$0.5x10^{-3}$-1.68	-	3.4	(Leong and Morgan 2009)
	3-Point Bending	-	5	3	(Ulrich-Vinther and Andreassen 2005)
			48	8	

Table 6.3: List of mechanical properties, elastic modulus (E) and Poisson's ratio (υ), for tibial callus defect simulations (bending and compression).

Material		E (MPa)	υ	Reference
β-TCP Scaffold		24.6×10^3	0.3	(Wang et al. 2004)
90/10wt% PCL/β-TCP Scaffold	Undegraded	250.37	0.3	Calculated from Experimental Results of Chapter 4 and Chapter 5
	Degraded	93.71	0.3	
Cortical Bone		11×10^3	0.3	Section 6.3.6.1
Soft Tissue		2	0.167	(Hori and Lewis 1982)
Callus Tissues (Models with β-TCP Scaffolds)	Range 1	1×10^3	0.3	Upper and lower values reported in (Claes and Heigele 1999)
	Range 2	2.23×10^3	0.3	
	Range 3	3.61×10^3	0.3	
	Range 4	4.76×10^3	0.3	
	Range 5	6×10^3	0.3	
Callus Tissues (Models with PCL/β-TCP Scaffolds)	Range 1	630.42	0.3	Based on results from values reported in (Claes and Heigele 1999), scaled as per Section 6.3.6.3
	Range 2	1.43×10^3	0.3	
	Range 3	2.21×10^3	0.3	
	Range 4	3×10^3	0.3	
	Range 5	3.78×10^3	0.3	

6.3.7 Compression Test Model Development

Compression simulations to replicate the axial loading experienced by the scaffold-callus construct *in vivo* were carried out to give a snapshot of the load-bearing abilities of each individual defect at 14 weeks post-implantation. Peak axial tibio-femoral contact forces in sheep of 2.12 x body weight were recorded by Taylor et al.

(Taylor et al. 2006), and an average body weight for sheep of 647.5 N can be calculated from values reported by Bergmann et al. (Bergmann et al. 2001). The axial contact force, F, can then be calculated as per Equation (6.4).

$$F = 2.12 \times 647.5\ N = 1.3727kN \tag{6.4}$$

Compression simulations were carried out using the model geometries generated in Section 6.3.4. A constant, compressive force of 1.3727 kN was applied to one end of the tibia. The displacement of all nodes on this end of the tibia were constrained to a loading node in the 3-direction using a *EQUATION constraint. The displacement of nodes on the opposite end of the tibia was fixed in the 3-direction, with one node fixed in all directions. The compressive stress (σ_C) was calculated as per Equation (6.5) where F is the compressive force and A_{tibia} is the cross-sectional area of the tibia. The compressive elastic modulus (E_C) of the full model was calculated as per Equation (6.6), where the compressive strain (ε_c) was calculated as the change in length over the original length in the 3-direction of the full model.

$$\sigma_c = \frac{F}{A_{\text{tibia}}} \tag{6.5}$$

$$E_c = \frac{\sigma_c}{\varepsilon_c} \tag{6.6}$$

6.3.8 Stress Distribution Analysis

The maximum stress fracture criterion was used to assess the failure of materials in each simulation. The maximum stress failure criterion assumes that failure will occur when the maximum principal stress (σ_{Max}) in a material exceeds the ultimate tensile strength (σ_{UT}) of the material, or when the minimum principal stress (σ_{Min}) is less than the ultimate compressive strength (σ_{UC}) of the material. The safe region for the material is then described as:

$$\sigma_{UC} < \sigma_{Min} < \sigma_{Max} < \sigma_{UT} \tag{6.7}$$

The ultimate tensile strength (σ_{UT}) of ovine callus tissue, evaluated using 3-pt bending, has been reported as between 14.6 and 25 MPa (Malizos et al. 2006); the lower value of 14.6 MPa was chosen for the purposes of this study to give a conservative estimation of σ_{UT}. Note that the values of σ_{UT} for callus tissues reported in Table 6.3 are significantly lower than the values reported for cortical bone in Table 6.1. A compressive to tensile strength ratio of 1.21 has been reported for human cortical bone (Kemper et al. 2007). As the compressive strength (σ_{UC}) of callus tissues were not available in the literature, this ratio was used to estimate a compressive strength for callus tissues giving a value of 17.7 MPa. The value of σ_{UC} for compacted, sintered β-TCP has been reported as 315 MPa (Metsger et al. 1999), and σ_{UT}, evaluated using 3-pt bending, was reported as 181 MPa (Boilet et al. 2013). The value of σ_{UT} for undegraded 90/10wt% PCL/β-TCP scaffold material was found to be 2.01 MPa in Chapter 4 of this thesis. The value of σ_{UC} for the exact scaffold

material used in this study was unavailable, therefore the value of σ_{UC} reported for a similar material (90/10wt% PCL/HA, solid cylinder fabricated using SLS) is used with a value of 33.7 MPa (Eshraghi and Das 2012).

While it is known that bone is a relatively brittle material, as is β-TCP, the failure behaviour of callus tissues has not been extensively studied and brittle failure is assumed for the purposes of this study. The results of experimental testing of 90/10wt% PCL/β-TCP scaffolds in Chapters 4 and 5 in this thesis reveal that the failure behaviour is dominated by the PCL phase, resulting in ductile behaviour. For the purposes of comparing the failure of callus tissues and scaffold materials in each of the simulations in this chapter, a brittle failure criterion is assumed. Note that this likely results in an over-conservative estimation of failure within the PCL/β-TCP scaffold materials, and potentially in the callus tissues.

The principal stress distribution for all elements in each part was then analysed using a code written in Matlab (Mathworks, UK). The total range of stress values in each model was divided into sub-ranges (increments of 1 MPa) and the number of elements with stress values within each range was calculated. Increments of 10 MPa were used for stress distribution analysis of compression simulations due to the greater distribution of stresses in the models. The percentage of elements in which material failure is predicted to occur, i.e. the percentage of elements outside of the safe zone according to Equation (6.7), is calculated as a function of the total defect volume (callus, scaffold and soft tissue). Failure in compression is calculated from the minimum principal stresses and with σ_{UC} as a threshold for failure using

Equation (6.8). Failure in tension is calculated from the maximum principal stresses and with σ_{UT} as a threshold for failure using Equation (6.9).

$$\%\ Failure\ in\ Compression = \frac{\sum elements\ with\ \sigma_{MIN} < \sigma_{UC}}{\sum elements\ in\ the\ defect\ region} \tag{6.8}$$

$$\%\ Failure\ in\ Tension = \frac{\sum elements\ with\ \sigma_{MAX} > \sigma_{UT}}{\sum elements\ in\ the\ defect\ region} \tag{6.9}$$

6.3.9 Callus Assessment Measurements

The pixel value ratio (P_r) (Hazra et al. 2008) for each individual defect was calculated using Equation (6.10). Measurements of mean pixel value were taken from X-ray images of each defect at 14 weeks *in vivo* by importing each X-ray into MIMICS. For each defect, three regions of bone were selected using the measurements tool in MIMICS to analyse the mean pixel value: within the bone callus, above the bone callus and below the bone callus (Figure 6.14). The mean pixel value of intact bone was taken to be the average of pixel value calculated above and below the defect. The value of P_r for each defect was calculated using Equation (6.10). A pixel value of 1 corresponds to intact bone, and is considered the threshold above which removal of external fixation is safe (Zhao et al. 2009).

$$P_r = \frac{mean\ pixel\ value\ of\ callus\ bone}{mean\ pixel\ value\ of\ intact\ bone(distal\ and\ proximal)} \tag{6.10}$$

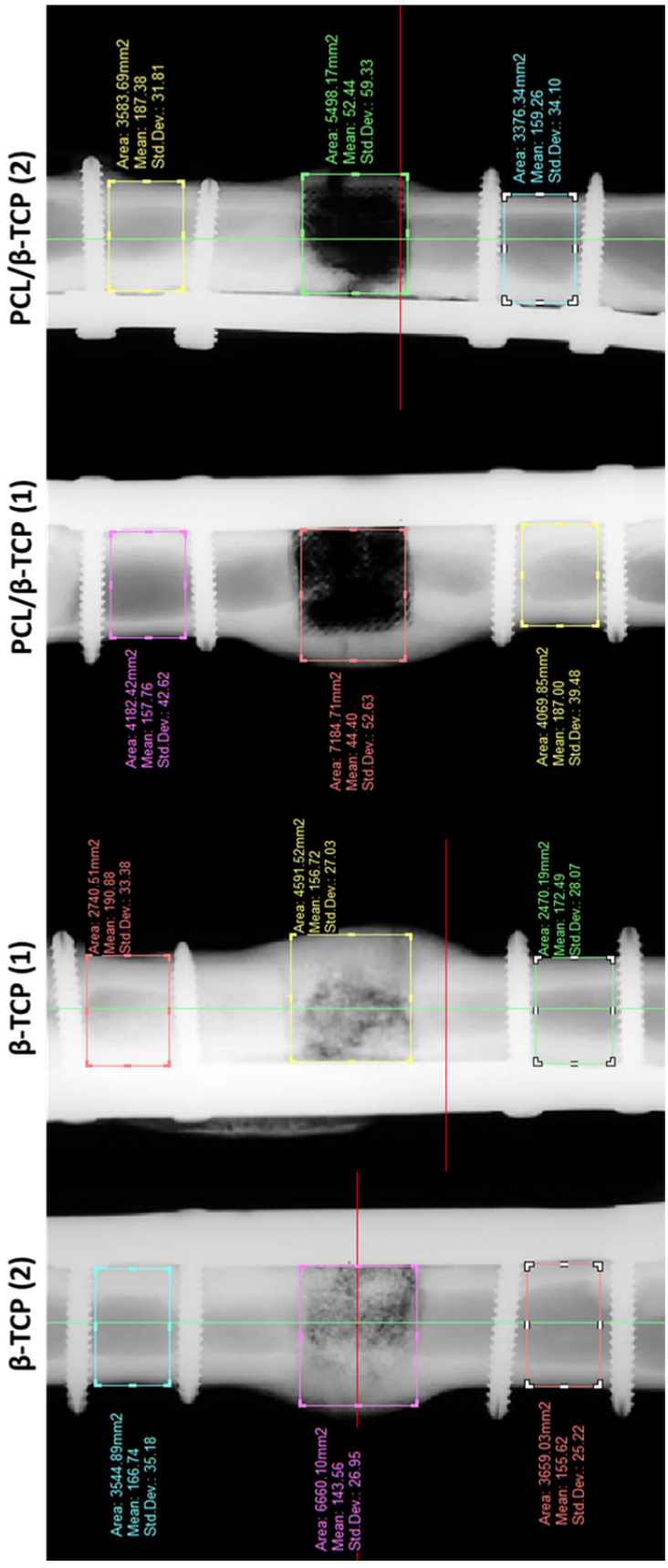

Figure 6.14: Evaluation of regional average pixel values for the calculation of pixel ratio values for each defect.

The cross-sectional moment of inertia ($CSMI$) of each individual defect was calculated using Equation (6.11), where a_i is the area of one voxel and (y_i - y_c) is the distance of a voxel (i) to the central axis (y_c). The BoneJ plugin for ImageJ software was used to calculate the value of $CSMI$ for each defect. The μ-CT scan of each defect was loaded in the software and the Moments3D function within the BoneJ plugin was used to calculate the $CSMI$ in the 1-, 2- and 3-directions. For the purposesof this study, the 3-direction is the direction of the central tibial axis in the bending simulations (Section 6.3.5) and the loading direction in the compression simulations (Section 6.3.7).

$$CSMI = \sum a_i \, (y_i - y_c)^2 \tag{6.11}$$

6.4 Results

6.4.1 Four-Point Bending Simulations: Intact Tibia

The bending stiffness of idealised intact tibia geometries was evaluated using four-point bending simulations. The results for simulations with a range of values of cortical bone elastic modulus are shown in Figure 6.12 in comparison with experimental data for intact tibiae generated as part of the STEPS project (Lohfeld et al. 2012). Higher values of elastic modulus (15 to 24.6 GPa) were found to overestimate the bending stiffness of the intact tibiae. An elastic modulus of 11 GPa was found to give the best approximation of the experimentally reported values for

intact tibiae (Figure 6.12) and is used in subsequent simulations of each tibia with callus and scaffold model (as described in Section 6.3.6). The correlation between $K_B{}^{Exp}$ and $K_B{}^{Comp}$ was evaluated, with r-values of 0.9991 and 0.9843 for tibiae generated from μ-CT scans of defects with β-TCP scaffolds and PCL/β-TCP scaffolds, respectively, indicating good correlation. No significant difference between $K_B{}^{Exp}$ and $K_B{}^{Comp}$ was found for the β-TCP (1), (2) and PCL/β-TCP (2) models with P values of 0.12, 0.23 and 0.05, respectively (n = 12), while a P value of 0.0007 was calculated for PCL/β-TCP (1) (n = 12). It was not possible to find a value of cortical bone elastic modulus to fit all tibiae due to the necessity of using homogeneous assignment of elastic properties and idealised tibial geometries. The difference between $K_B{}^{Exp}$ and $K_B{}^{Comp}$ was 4.35, 1.84, 5.98 and -5.01 Nm^2 for β-TCP (1), β-TCP (2), PCL/β-TCP (1) and PCL/β-TCP (2), respectively. This value of elastic modulus gives a good fit between models in which $K_B{}^{Comp}$ results in an overestimation of $K_B{}^{Exp}$ and those in which it results in an underestimation of $K_B{}^{Exp}$.

6.4.2 Four-Point Bending Simulations: Tibia with Callus and Scaffold

Bending simulations of computational model geometries of tibiae with defects containing β-TCP scaffolds and PCL/β-TCP scaffolds (Section 6.3.4) were carried out as per Section 6.3.5. Four-point bending simulations were carried out with typical ranges of elastic properties for callus tissue, as listed in Table 6.3, in order to establish a suitable range of properties for callus tissues. The results of these models are shown in comparison with experimental results (Lohfeld et al. 2012) in Figure 6.13, indicating that the use of properties from (Claes and Heigele 1999) give the

best fit for both model types. These properties were used to generate a full set of $K_B{}^{Comp}$ data. The bending stiffness for each angular configuration and average bending stiffness were calculated and are shown in comparison to experimental data from (Lohfeld et al. 2012) in Figure 6.15. The correlation between $K_B{}^{Exp}$ and $K_B{}^{Comp}$ was evaluated using the Pearson's correlation coefficient, giving a value of 0.9 showing good correlation. Bending stiffness for simulations with the β-TCP scaffolds correlate best with the experimental data with a Pearson's correlation coefficient of 0.9987, compared to a value of 0.9461 for the PCL/β-TCP scaffolds. No significant difference between $K_B{}^{Exp}$ and $K_B{}^{Comp}$ was found for defects with the β-TCP scaffolds, with P values of 0.16 and 0.46 for β-TCP (1) and β-TCP (2), respectively (n = 12) showing a good fit between experimental and computational measurements of bending stiffness. Significant differences between $K_B{}^{Exp}$ and $K_B{}^{Comp}$ were found with P values of 0.002 and 0.0001 for PCL/β-TCP (1) and PCL/β-TCP (2), respectively (n = 12).

The bending stiffness of callus defects with degraded PCL/β-TCP scaffolds was evaluated and results are shown in comparison with the bending stiffness of defects calculated from simulations using undegraded PCL/β-TCP material properties, as well as with experimental data, in Figure 6.16. The use of degraded elastic modulus values for PCL/β-TCP scaffolds resulted in a 3% reduction in bending stiffness for PCL/β-TCP (1) and a 39.3% reduction for PCL/β-TCP (2), as shown in Figure 6.16. This indicates that the role of scaffold stiffness is dependent on callus volume, as the volume of the callus region in the finite element mesh of PCL/β-TCP (1) is 3.5 times larger than for PCL/β-TCP (2).

Contour plots illustrating the distribution of von Mises stresses in the callus and scaffold parts of each model are shown in Figure 6.17. Greatest stresses are shown for the PCL/β-TCP (1) simulations, in which a low volume of callus material is visible. The principal stress distribution in the callus and scaffold parts of each four-point bending simulation is shown in Figure 6.18, where shaded regions represent stresses between σ_{UC} and σ_{UT}, in red for the callus region and blue for each scaffold type. Approximated values of σ_{UC} are indicated with an asterix, and -σ_{UT} for both scaffold and callus are included as solid lines to indicate conservative values of σ_U. Elements with stresses outside these limits indicate predicted material failure; less than 0.01% failure is found in scaffold or callus parts for models β-TCP (1), β-TCP (2) and PCL/β-TCP (1). Compressive failure (0.1%) and 21% failure in tension was predicted in the scaffold part of the PCL/β-TCP (2) model. Contour plots showing maximum and minimum principal strains for the case of the PCL/β-TCP (1) simulation are shown in Figure 6.19.

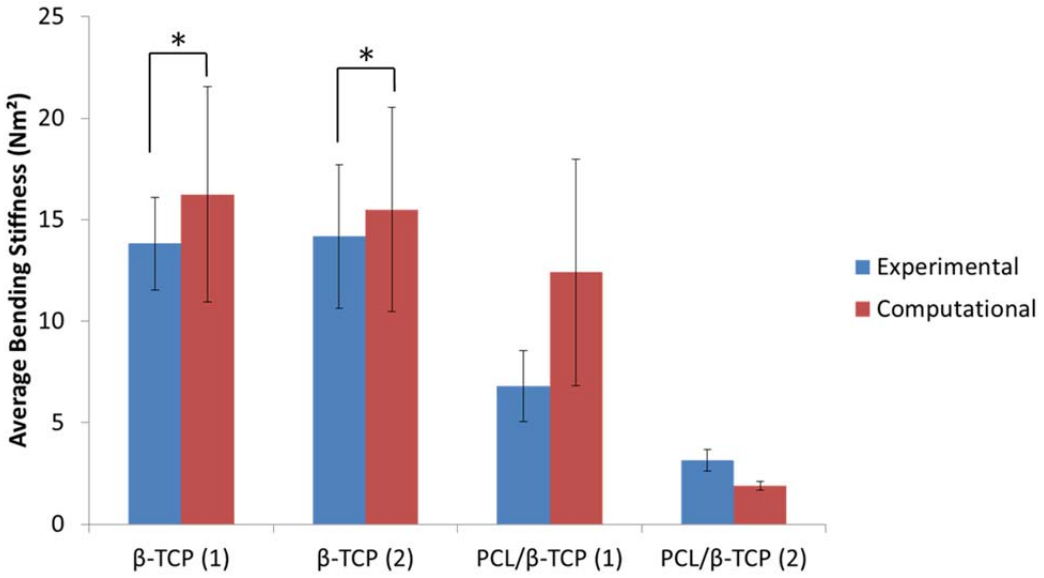

Figure 6.15: Bending stiffness calculated from four-point bending simulations of tibial defects (red). Experimentally-evaluated average bending stiffness for each specific tibial defect (blue), evaluated from data generated in a previous study (Lohfeld et al. 2012), are included for comparison purposes. Mean values for each data set are shown and error bars represent standard deviation. *p > 0.05.

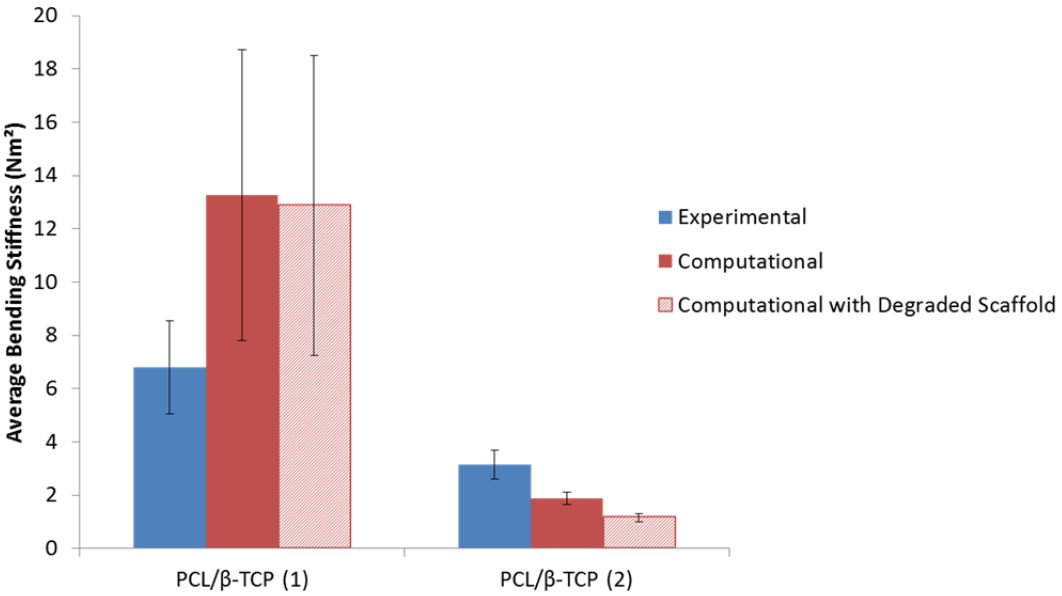

Figure 6.16: Bending stiffness calculated from four-point bending simulations of tibial defects implanted PCL/β-TCP using undegraded (red) and degraded (pink) PCL/β-TCP scaffold elastic modulus values. Experimentally-evaluated average bending stiffness for each specific tibial defect (blue), evaluated from data generated in a previous study (Lohfeld et al. 2012), are included for comparison purposes. Mean values for each data set are shown and error bars represent standard deviation.

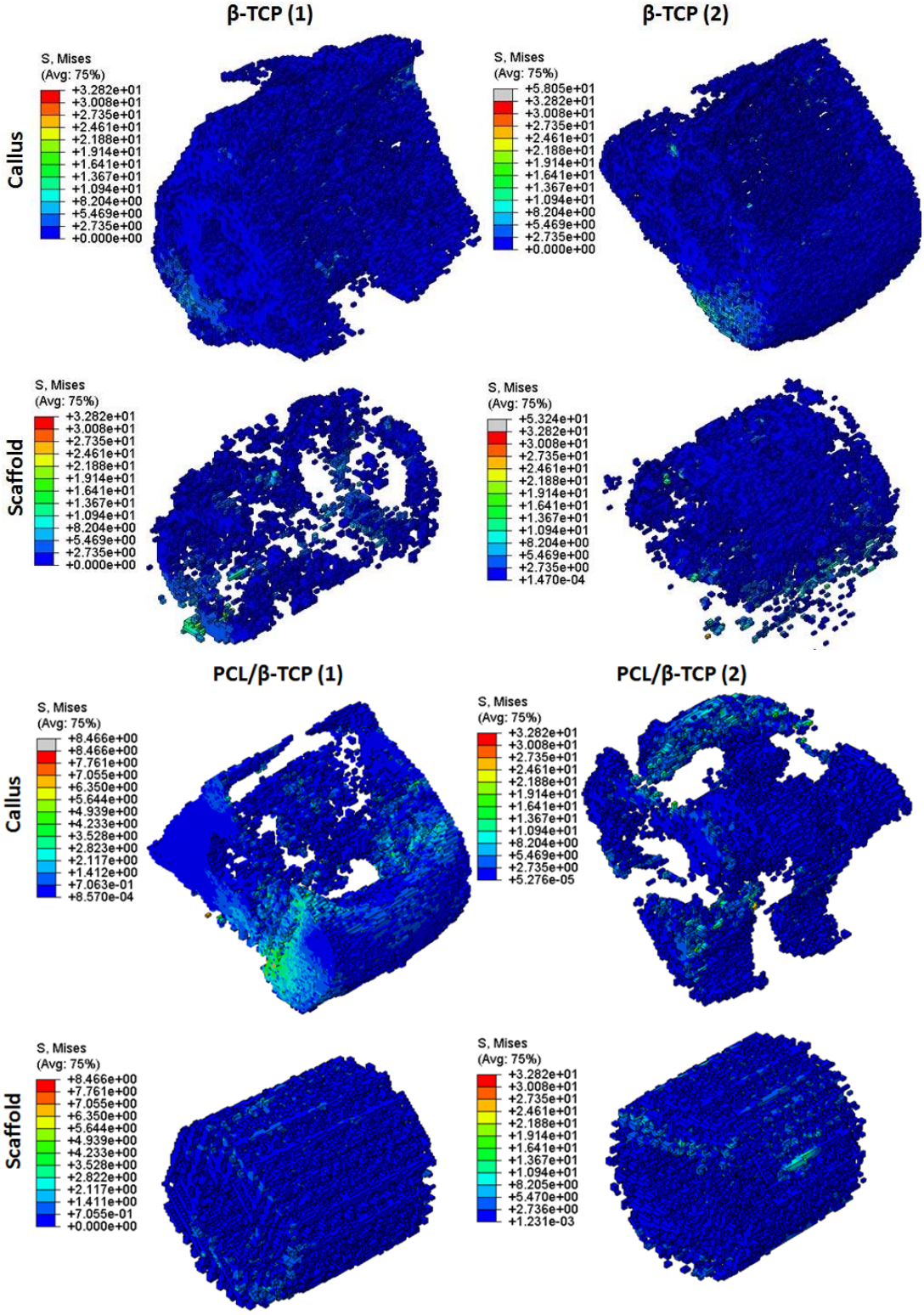

Figure 6.17: Contour plots showing von Mises stress distribution (MPa) in the callus and scaffold parts for each model under four-point bending.

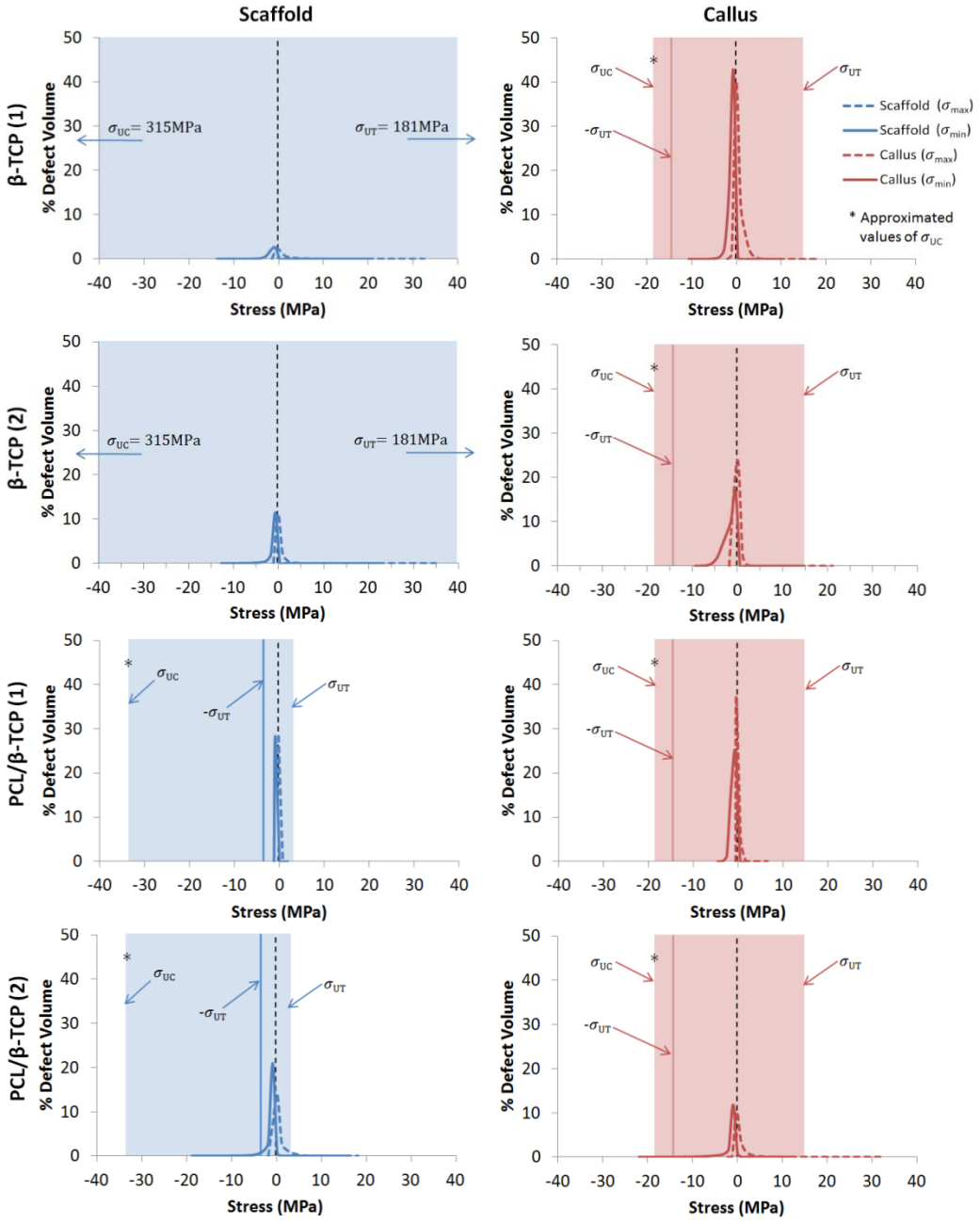

Figure 6.18: Principal stress distributions for four-point bending simulations of tibiae with scaffolds and defects. The shaded regions represent stresses between the compression and tensile ultimate strength values (σ_{UC}, σ_{UT}) of the scaffold materials (blue) and callus tissue (red). Stars indicate values of σ_{UC} that are approximated from the literature. Solid lines indicating values of -σ_{UT} are included to indicate conservative values of ultimate strength.

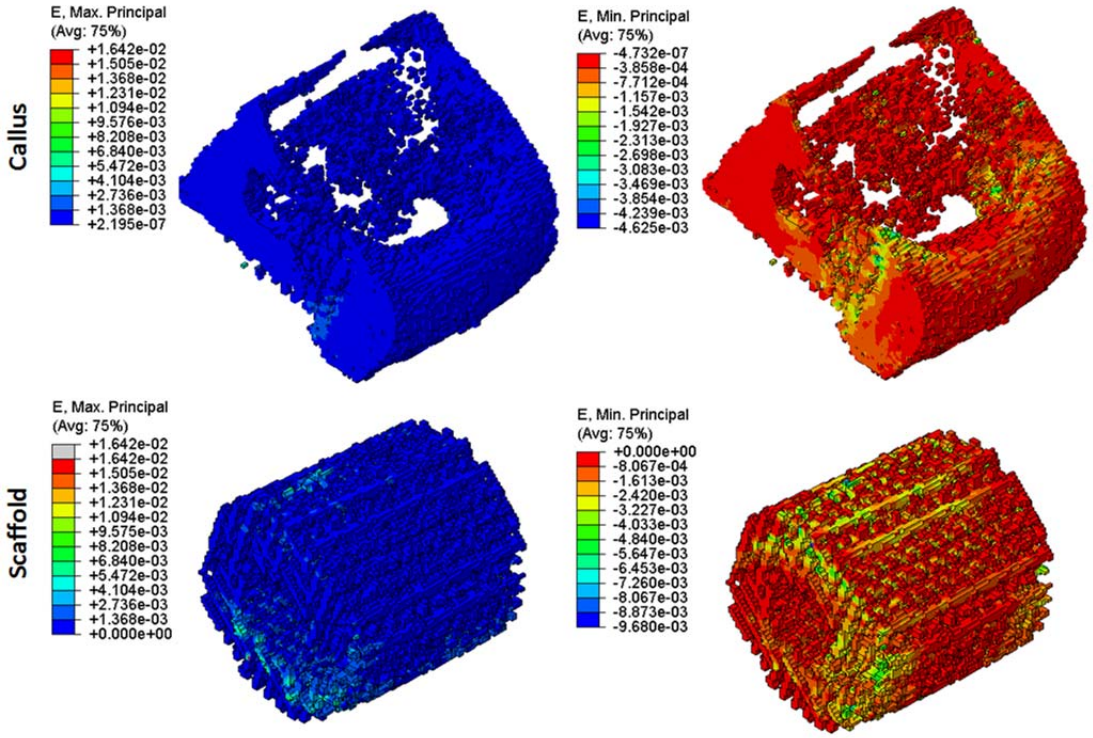

Figure 6.19: Contour plots showing maximum and minimum principal strain distribution in the callus part (top) and the scaffold part (bottom) for each model assembly under four-point bending loading.

6.4.3 Compression Simulations: Tibia with Callus and Scaffold

Compression simulations of computational model geometries of tibiae with defects containing β-TCP scaffolds and PCL/β-TCP scaffolds (described in Section 6.3.4) with compressive forces representative of *in vivo* loading during normal gait were carried out as per Section 6.3.7. The effective compressive elastic modulus for each model was calculated, shown in Figure 6.20, with maximum value of 1.64 GPa for β-TCP (2) and lowest value of 0.288 GPa for PCL/β-TCP (2).

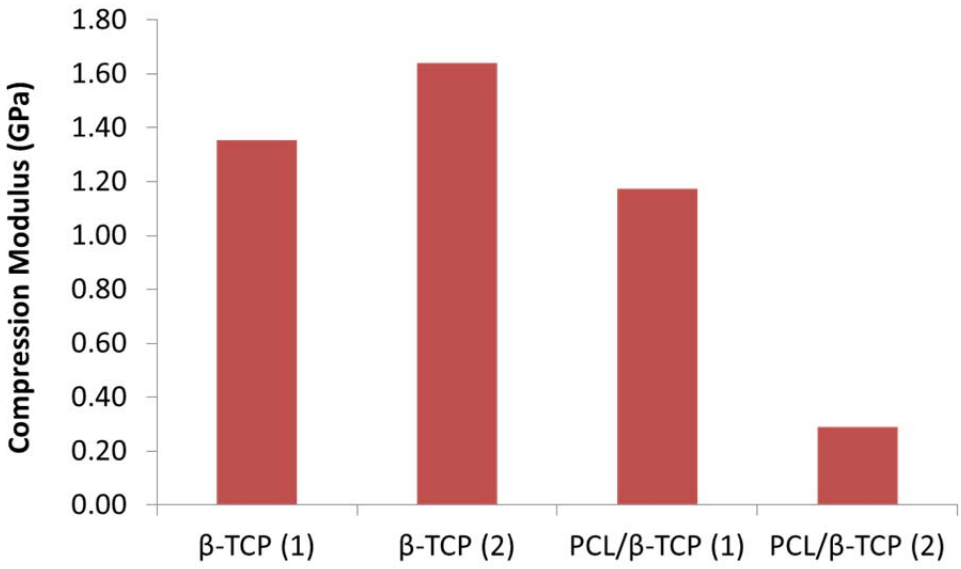

Figure 6.20: Tibial defect stiffness calculated from compression simulations of tibial defects with two types of implanted scaffolds.

Contour plots illustrating the distribution of von Mises stresses in the callus and scaffold parts of each model are shown in Figure 6.21. The principal stress distribution in the callus and scaffold parts of each compression simulation is shown in Figure 6.22, where shaded regions represent stresses between σ_{UC} and σ_{UT}, in red for the callus region and blue for each scaffold type. Elements with stresses outside of these limits indicate predicted fracture of material; the volume of material in which failure is predicted is shown for each model in Figure 6.23 as a percentage of the total callus volume. Compressive failure is predicted in a greater volume of the callus tissues in defects with β-TCP scaffolds (22% and 15% for β-TCP (1) and β-TCP (2), respectively) than in defects with PCL/β-TCP scaffolds (4% and 5% for PCL/β-TCP (1) and PCL/β-TCP (2), respectively). The same result was observed for predicted tensile failure, with values of 6%, 0.5%, 0.08% and 0.34% for β-TCP (1),

β-TCP (2), PCL/β-TCP (1) and PCL/β-TCP (2), respectively. The opposite result was found in the case of the scaffold materials, with compressive failure only predicted for the PCL/β-TCP (2) model. No tensile failure was predicted within either β-TCP scaffold volume, however tensile failure is predicted in 1.6% and 18.3% of the scaffold volume in models PCL/β-TCP (1) and PCL/β-TCP (2), respectively.

Contour plots showing maximum and minimum principal strains for the case of the PCL/β-TCP (1) simulation under compressive loading are shown in Figure 6.24. The maximum and minimum strain distribution for both cases with implanted PCL/β-TCP scaffolds under compressive loading is presented in Figure 6.25. Some regions of relatively high strain magnitudes can be seen in the contour plots (Figure 6.24), however the results in Figure 6.25 show that these strain magnitudes are generally experienced only by a very small percentage of the elements. In fact, for the compressive loading shown here, which is the more severe of the two loading scenarios, only one case, namely the scaffold material in the PCL/β-TCP model, in terms of minimum principal strain only, experiences strain magnitudes greater than 5% in a substantial volume of the material. The presence of high strain magnitudes does indicate that the use of the non-linear geometry (NLGEOM) option in Abaqus is advisable during these simulations. This option was not used in these simulations due to practical complications encountered in running models with these very complex model geometries. For future studies, it is recommended that the NLGEOM option is used to ensure the most accurate possible solution.

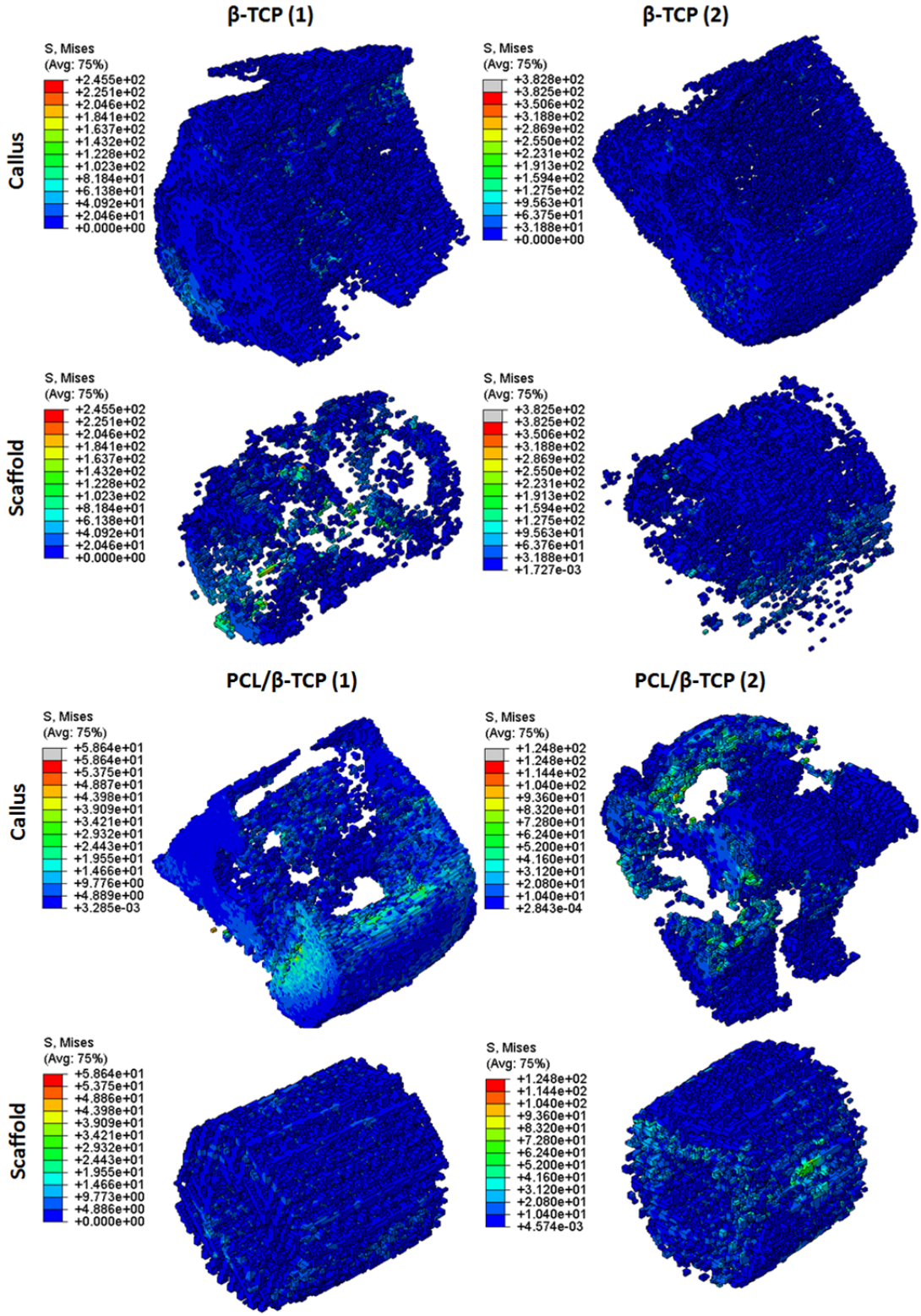

Figure 6.21: Contour plots showing von Mises stress distribution (MPa) in the callus part (top) and the scaffold part (bottom) for each model assembly under compressive loading.

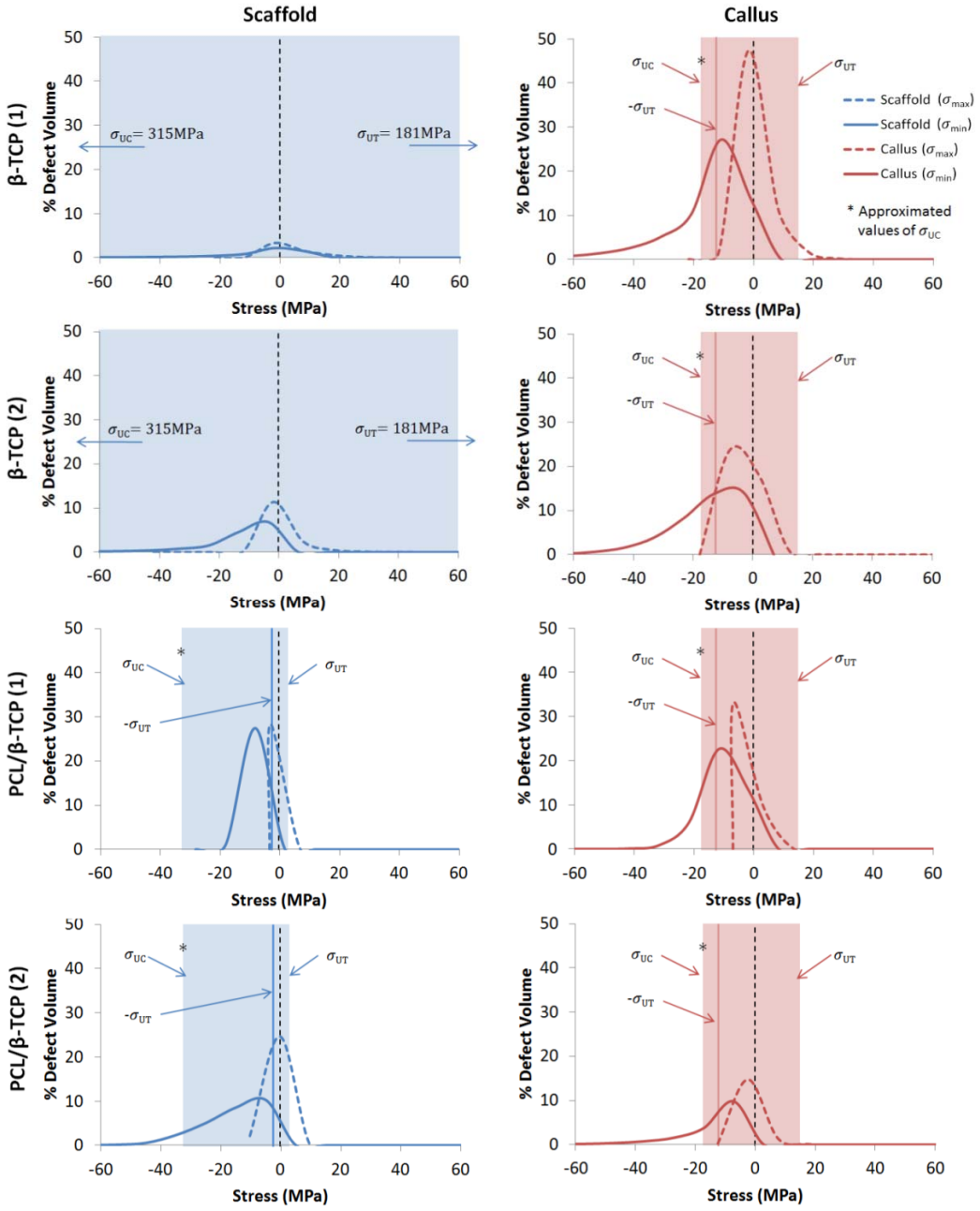

Figure 6.22: Principal stress distribution for compression simulations of tibiae with scaffolds and defects. The shaded regions represent stresses between the compression and tensile ultimate strength values (σ_{UC}, σ_{UT}) of the scaffold materials (blue) and callus tissue (red). Stars indicate values of σ_{UC} that are approximated from the literature. Solid lines indicating values of -σ_{UT} are included to indicate conservative values of ultimate strength.

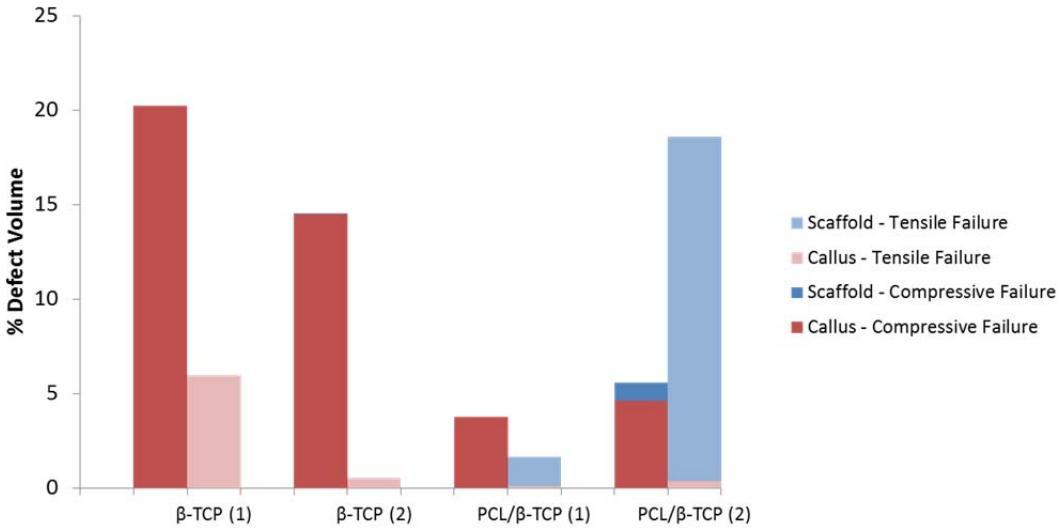

Figure 6.23: Percentage volume of each defect in which compressive or tensile failure has occurred due to simulated *in vivo* compressive loading. Results for callus tissues are shown in red and for scaffold material in blue, with compressive results in bold colours and tensile results in faded colours.

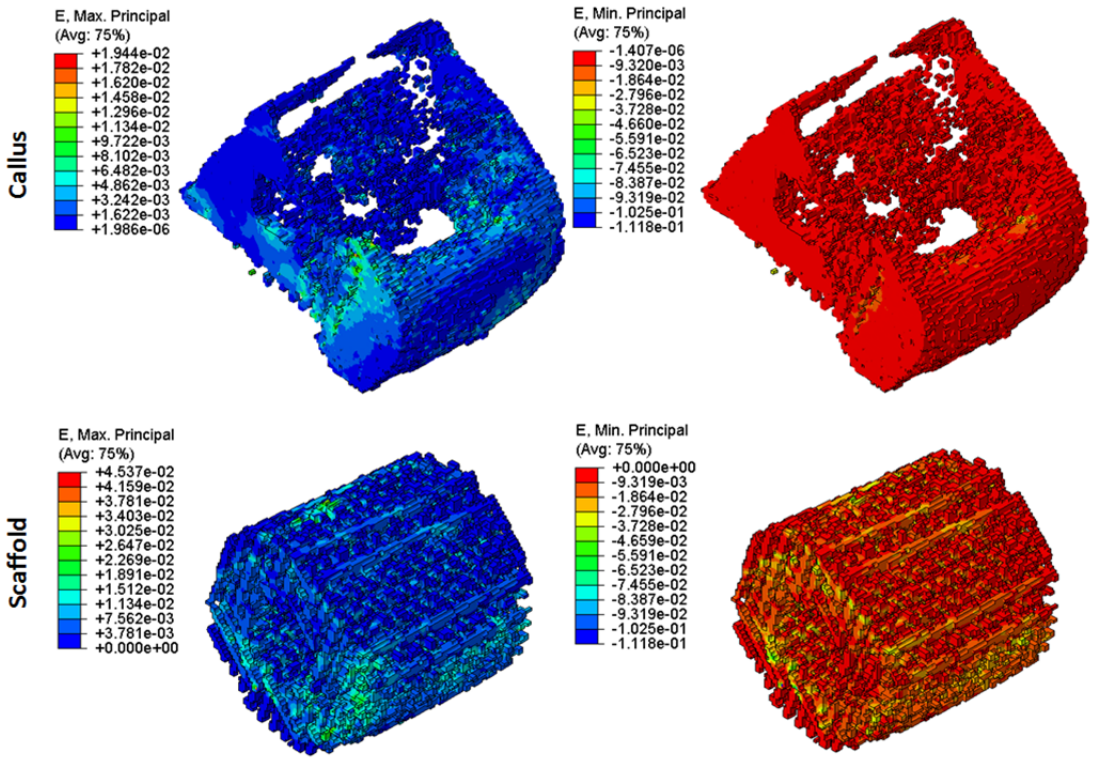

Figure 6.24: Contour plots showing maximum and minimum principal strain distribution in the callus part (top) and the scaffold part (bottom) for each model assembly under compressive loading.

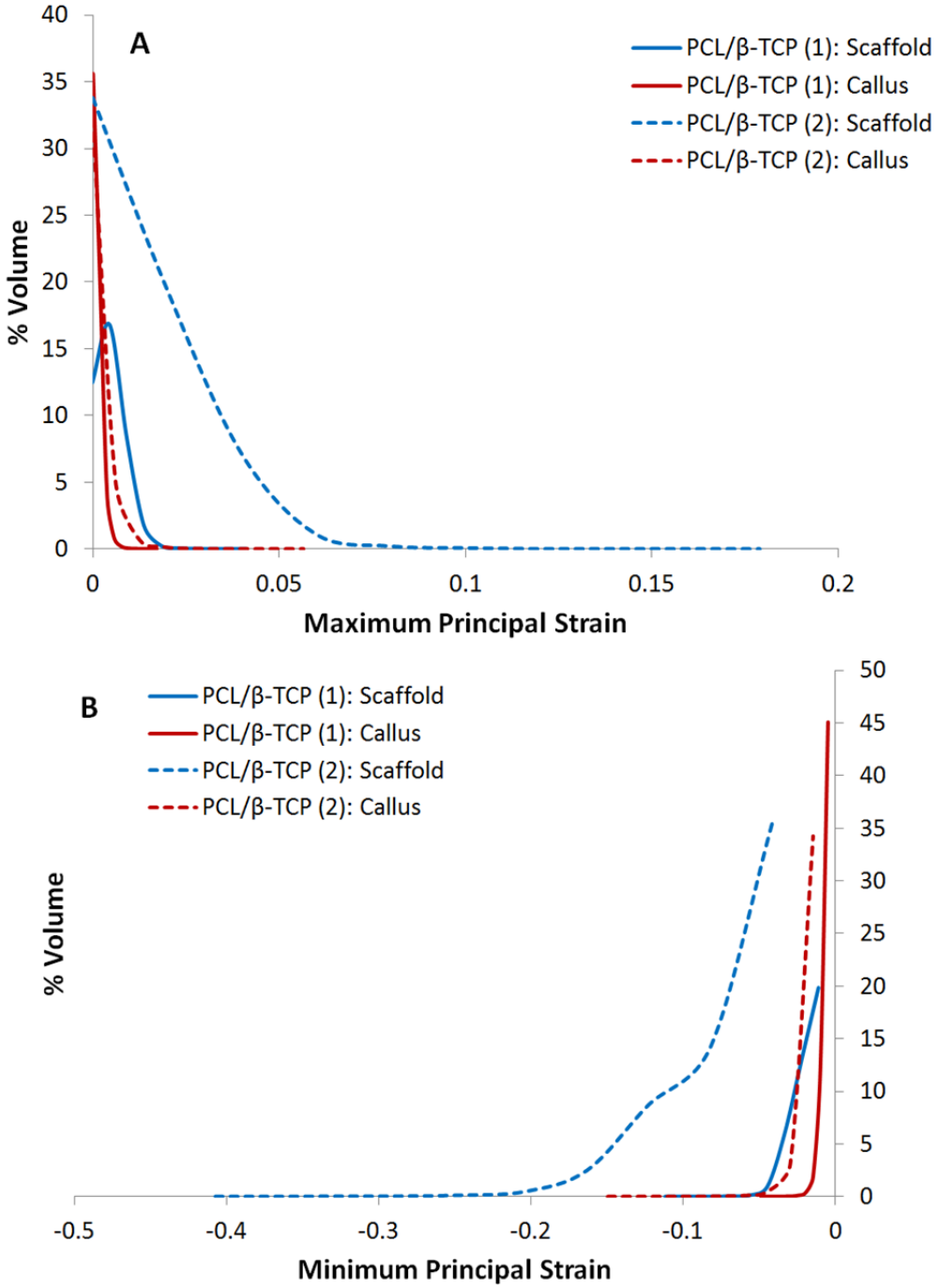

Figure 6.25: Maximum principal strain distribution (A) and minimum principal strain distribution (B) for compressive loading of both model geometries with implanted PCL/β-TCP scaffolds.

6.4.4 Callus Assessment Methods

In order to assess the correlation between P_r and bending stiffness the value of P_r for each defect is shown with respect to $K_B{}^{Exp}$ and $K_B{}^{Comp}$ in Figure 6.26. A Pearson's coefficient value of 0.95 was determined for P_r and $K_B{}^{Exp}$, and a value of 0.72 was determined for P_r and $K_B{}^{Comp}$, indicating that P_r is a better predictor of $K_B{}^{Exp}$ than of $K_B{}^{Comp}$. Using a linear fit between bending stiffness and P_r, the value of E_B corresponding to a P_r of 1 was calculated, giving threshold bending stiffness values of 16.5 Nm² and 22.7 Nm² for experimental and computational results respectively. This indicates that the predicted value of bending stiffness required for fixation removal is greater for computational modelling than for experimental evaluation, and that the computationally-evaluated threshold for fixation removal is more conservative than the experimentally-evaluated threshold.

$CSMI$ is shown with respect to $K_B{}^{Exp}$ and $K_B{}^{Comp}$ in Figure 6.27. A Pearson's coefficient value of 0.92 was determined for $CSMI$ and $K_B{}^{Exp}$, and a value of 0.82 was determined for $CSMI$ and $K_B{}^{Comp}$, indicating that $CSMI$ is a better predictor of experimentally evaluated bending stiffness. Using a linear fit between bending stiffness and $CSMI$, the predicted threshold values of $CSMI$ for fixation removal, corresponding to E_B values of 16.5 Nm² and 22.7 Nm², were calculated. This generated threshold values of $CSMI$ of 334 x 10^9 kg.mm² and 353 x 10^9 kg.mm² for experimental and computational results, respectively. Again, the use of computational modelling provides a more conservative threshold for fixation removal.

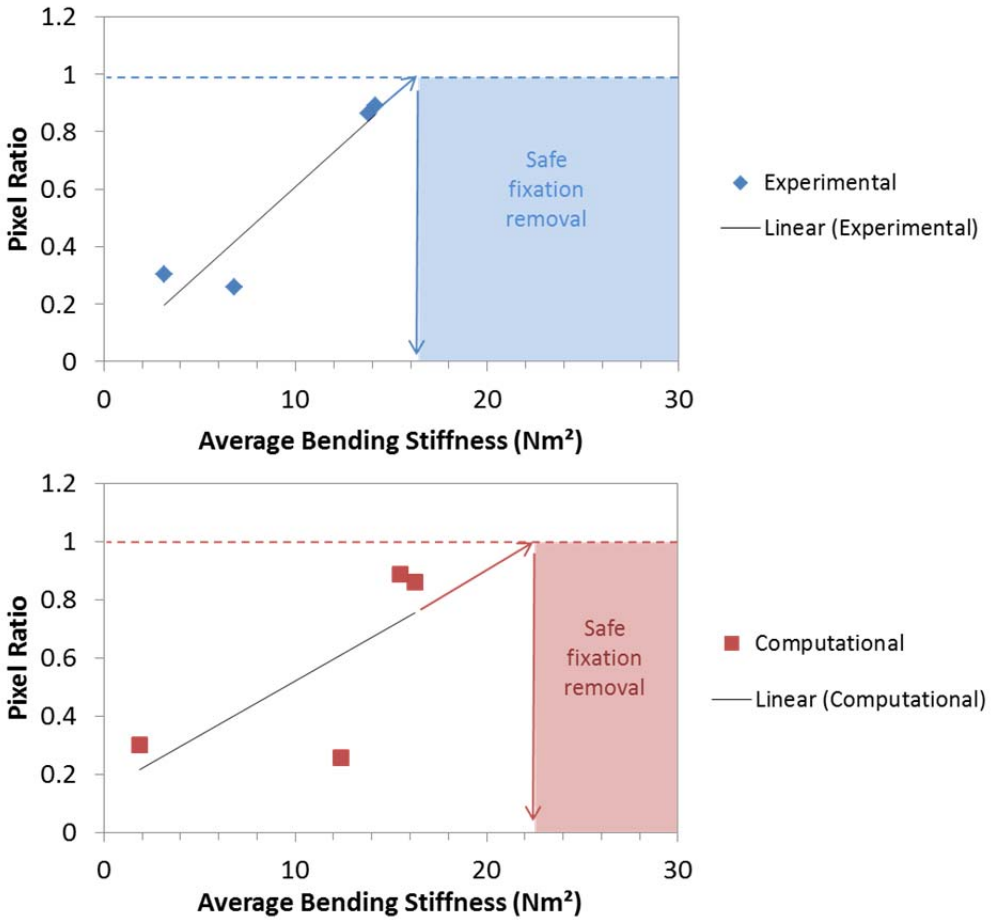

Figure 6.26: Pixel ratio (P_r) versus average bending stiffness for experimentally evaluated bending stiffness (above, blue) and computationally evaluated bending stiffness (below, red). A pixel ratio value of 1 has been suggested for safe fixation removal. A linear fit is shown for each data set, and is used to determine the value of average bending stiffness corresponding to a pixel value of 1 for safe fixation removal. Values of 16.5 and 22.7Nm² were determined from the experimental and computational data sets, respectively.

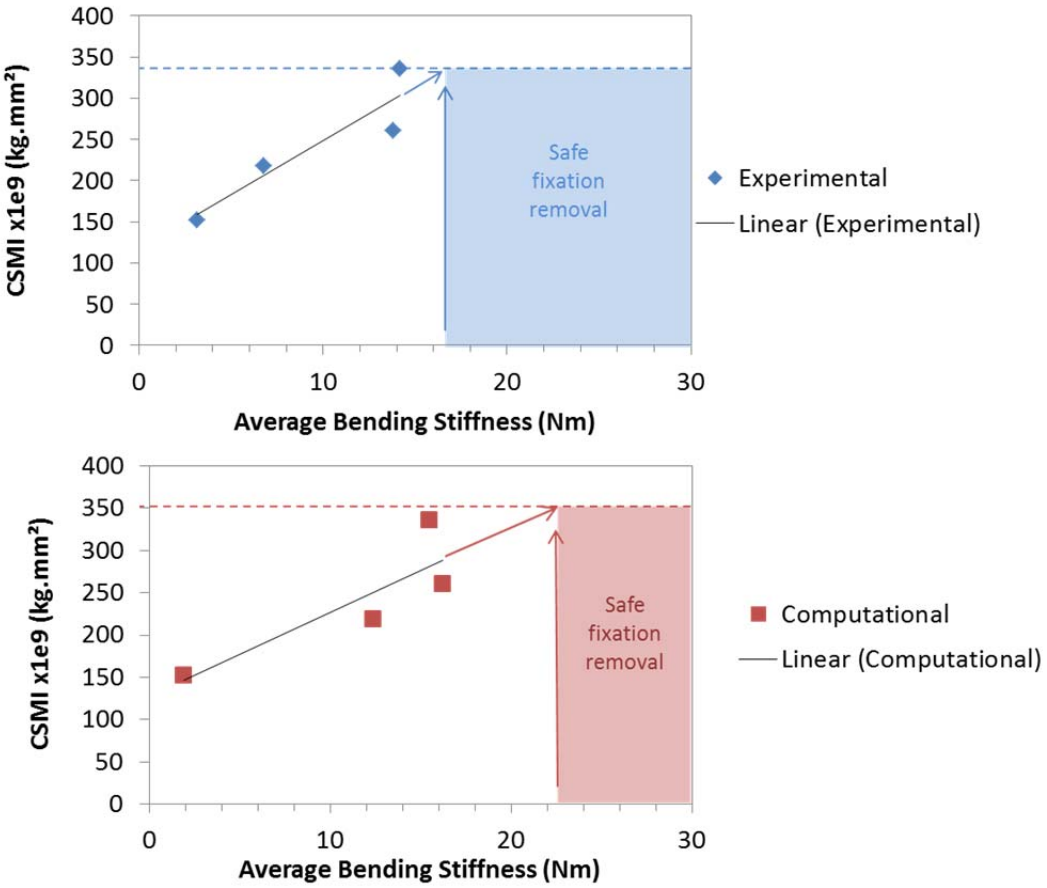

Figure 6.27: Cross-sectional moment of inertia ($CSMI$) versus average bending stiffness for experimentally evaluated bending stiffness (above, blue) and computationally evaluated bending stiffness (below, red). Average bending stiffness values of 16.5 and 22.7Nm² for safe fixation removal were determined for the experimental and computational data sets, respectively from Figure 6.26. A linear fit is shown for each data set, and is used to determine corresponding values of $CSMI$ for safe fixation removal, giving values of $334 \times 10^9 Nm^2$ and $353 \times 10^9 Nm^2$ for the experimental and computational data sets, respectively.

6.5 Discussion

Finite element mesh geometries were constructed for both idealised, intact tibiae and for tibiae with callus and scaffold geometries from μ-CT scans of ovine tibial defect regions that were taken 14 weeks post-implantation of scaffolds. The elastic modulus values of cortical bone were determined using four-point bending simulations of idealised, intact tibiae and calibrating against experimental data giving a value of 11 GPa. The good fit between experimental and computational results confirms the suitability of these idealised tibia geometries for use in full tibial defect simulations. FE model geometries for tibiae with implanted scaffolds and new bone callus geometries were successfully generated from the defect region μ-CT scan images. The model generation process was simplest for defects with implanted β-TCP scaffolds as the geometry of both scaffold and bone callus visible on the same scan images and as the scaffold density was greater than that of the surrounding bone tissue (Figure 6.6). A large degree of β-TCP scaffold degradation, i.e. regions where material removal has occurred, is visible inthe μ-CT scan images. Idealised parts were generated for the tibia and for the portion of callus joining the callus region in the μ-CT scans to the tibia. The results of four-point bending simulations show that the simulations accurately predict tibial bending stiffness for defects with implanted β-TCP scaffolds. This verifies the material properties used in these simulations as well as the method of model generation.

The process of model generation was more complex for defects with implanted PCL/β-TCP scaffolds as the scaffold was not visible in the same μ-CT scan as the bone callus (Figure 6.6), meaning that information regarding scaffold geometry and

material loss through degradation is not available. The bone scaffold geometry was obtained from a separate scan of an intact scaffold, and this was then fitted to the callus geometry manually. While not as anatomically accurate as models for defects with implanted β-TCP scaffolds, the results show that these models give a reasonable estimate of tibial bending stiffness, both overestimating and underestimating with predicted bending stiffness values that are 195% and 60% of the experimentally evaluated values for PCL/β-TCP (1) and PCL/β-TCP (2), respectively. The callus tissue volume in the PCL/β-TCP (1) model is 3.5 times greater than the callus volume in the PCL/β-TCP (2) model. The relative trend of bending stiffness is preserved however; the bending stiffness of PCL/β-TCP (1) is greater than the bending stiffness of PCL/β-TCP (2) for both experimental and computational results.

Generating model geometries directly from μ-CT scans as for the β-TCP scaffolds is a more accurate method, and the results presented here (Figure 6.15) suggest that this method should be employed, where possible. In cases where the scaffold is not visible in μ-CT scans, a secondary scan taken with scan settings optimal for the scaffold material should be taken in order to obtain the real scaffold geometry. It is not possible to tell from the scans used in this study whether or not any material removal has occurred in the PCL/β-TCP scaffolds during the 14 weeks implantation *in vivo* and it is likely that the use of idealised scaffold geometries overestimates the amount of scaffold material present at this point in time. It is also worth noting that the results above indicate that the accuracy of these computational models is highest for defects where a large volume of callus tissue has formed. Taking the PCL/β-TCP

(1) model geometry as an example, it is possible that some material removal had occurred. An accurate computational model geometry that accounts for material removal, in combination with reduced elastic modulus due to degradation of the material, would result in a lower overall bending stiffness that would give an improved prediction of the experimental bending stiffness.

The tibia geometries used here are idealised; while the cross-section matches the cross-section visible in the μ-CT scan of the defect region in each individual case, in reality the cross-section is unlikely to be constant along a 80 mm length of the tibia as assumed here. The use of the real tibia geometries, which could be obtained using CT scanning but were not available for the present study, would result in more accurate model geometries. However, the region of interest in the present study is the scaffold-callus region; as the tibia geometries used are most accurate closest to this region the errors resulting from the use of idealised tibia models for this study are not expected to be significant.

The use of computational modelling to simulate four-point bending enables the generation of additional information to bending stiffness to give a more complete picture of defect mechanical behaviour. The evaluation of maximum and minimum principal stress distribution (Figure 6.18) gives a useful insight into load distribution within each individual defect. In the case of defects with β-TCP scaffolds, loading is primarily supported by the callus tissue, with the majority of loading in β-TCP (1) supported by the callus compared to a more even distribution between scaffold and callus in β-TCP (2). The volume of scaffold in the β-TCP (2) model is approximately 3 times greater than in the β-TCP (1) model, therefore it is expected that a greater

portion of the bending loading would be supported by the greater volume of the stiffer scaffold material.

In the case of defects with PCL/β-TCP scaffolds, loading is either primarily supported by the scaffold (PCL/β-TCP (2)) or more evenly distributed between scaffold and callus (PCL/β-TCP (1)). It should be noted that failure was predicted in a greater volume of the scaffold in PCL/β-TCP (2) than in PCL/β-TCP (1), with 0.1% failure in compression and 21% failure in tension. This model geometry has by far the lowest volume of callus tissue, which indicates that that load bearing capacity provided by the larger volumes of callus tissue in each of the other models is required in order to provide defect stability and that the scaffolding abilities of the PCL/β-TCP scaffolds alone may not be sufficient without the use of an external fixator device.

The computational model geometries that have been developed for four-point bending simulations provide a facility to assess the ability of each defect to support other types of loading. Compressive loading that is representative of the magnitude of compressive forces experienced in sheep tibia was simulated using these geometries. Analysis of the stress distribution in each of the compression simulations (Figure 6.22) shows similar results to the bending simulations, with loading supported by the callus tissue in the β-TCP (1) model, a more even distribution of loading between scaffold and callus in β-TCP (2) and in PCL/β-TCP (1). The primary load-bearing material in the PCL/β-TCP (2) model under compressive loading is the scaffold material in the PCL/β-TCP (2) model, similar to under bending loading, due to the lower volume of stiffer callus material.

The percentage volume of material within each defect in which failure is predicted under *in vivo* loading is worrying. For defects with the β-TCP scaffolds, failure is predicted in 26.2% and 15% (tensile and compressive) of the callus tissues and no failure of the scaffold material is predicted. In contrast, 3.9% and 5% failure is predicted in the callus region in defects with PCL/β-TCP scaffolds along with 1.6% and 19.2% failure in the PCL/β-TCP scaffolds. These results indicate that the magnitudes of loading that are estimated to be experienced *in vivo* in sheep tibiae during normal gait would result in failure of the tibia-callus-scaffold assembly, and that removal of external fixation at this time would not be appropriate for any defect. The high volume of predicted failure in the scaffold material in the PCL/β-TCP (2) model, compared to each of the other models, which all have greater callus volume, again indicates that significant volumes of mineralised callus are required in this type of critical-sized defect in order to support *in vivo* loading.

It is also worth noting that the use of values of σ_U evaluated using tensile or bending methods, indicated by solid, vertical lines in Figure 6.18 and Figure 6.22, give a more conservative estimation of failure compared to those evaluated using compression testing for each of the scaffold types as well as the callus tissue. *In vivo* loading of callus tissues in particular is predominantly compressive; however there is a lack of information in the literature regarding the compressive properties of callus tissues. Mechanical testing of callus tissues reported in the literature (Table 6.3**:**) is generally performed using bending test methods; however as the primary failure mechanism in bending is tensile cracking the data produced by these methods alone may not be sufficient. More information regarding the compressive properties of

callus tissues, as well as the evaluation of increasing callus stiffness and strength as healing progresses, would be very valuable for the field of computational modelling of bone callus defects.

Clinical measures of parameters such as pixel value ratio and cross-sectional moment of inertia using imaging methods have been correlated with re-fracture rates (Song et al. 2005) and mechanical integrity of fracture calluses (Jamsa et al. 1998). Here, both of these parameters have been evaluated for each individual defect (Figure 6.26 and Figure 6.27). Using the suggested threshold of P_r = 1 for the safe removal of external fixation (Zhao et al. 2009), none of the four defects studied here qualify for removal of external fixation. Both of the defects with implanted β-TCP scaffolds fall very close to this threshold with values of 0.89 and 0.86. This is somewhat surprising given that the results above indicate that these defects are not capable of supporting *in vivo* compressive loading. The computational and experimental results considered here both have good correlation with P_r, and the relationship between P_r and bending stiffness was used to calculate a value of bending stiffness that correlates to P_r = 1. Good correlation was also observed between $CSMI$ and bending stiffness, and the relationship between $CSMI$ and bending stiffness was used to calculate values of $CSMI$ that correlate to P_r = 1. In this way, values of bending stiffness and $CSMI$ that correlate with safe removal of external fixation can be calculated. Note that both P_r and $CSMI$ are evaluated directly from X-ray and μ-CT scan images, respectively, in which the PCL/β-TCP scaffolds are not visible. When this is considered, the methods above do not account for the presence of the scaffold or its contribution to the load-bearing abilities of the

scaffold-callus construct, therefore limiting the accuracy of these evaluation methods for defects containing this type of scaffold.

It is interesting to note that threshold values of each measure (P_r and $CSMI$) that have been calculated to predict the safe removal of fixation are not significantly greater than the predicted values for defects with β-TCP scaffolds, suggesting that these defects are relatively close to what would be considered full healing by these measurements. However, the results of the *in vivo* compressive loading simulations presented here predict failure in large volumes of callus material (in the case of defects with β-TCP scaffolds) and in both callus and scaffold materials (in the case of defects with PCL/β-TCP scaffolds). This indicates that the threshold levels of bone formation that are required for fixation removal are underestimated by P_r, leading to the calculation of a non-conservative threshold value of $CSMI$. In order to reduce the predicted volumes of failed material to safer levels, the results above suggest that increased callus tissue volumes, increased callus tissue mechanical properties or reduced degradation of the β-TCP scaffolds would be required for defects with β-TCP scaffolds. Similar changes of increased callus tissue volumes and increased callus tissue mechanical properties would be required for defects with PCL/β-TCP scaffolds. These results suggest that the use of these measures (P_r and $CSMI$) may need to be treated carefully, as the results call into question how appropriate they are as predictors for safe fixation removal. It is accepted that the compression simulations presented in this chapter are not directly supported by experimental testing, however the results presented here do point to the need for experimentation to explore the issue further.

A major advantage of the methods that are presented here is that a non-invasive method to assess the mechanical integrity of the scaffold-callus construct is provided. This can be combined with repeated μ-CT scanning during longitudinal *in vivo* studies to assess the development of a new bone callus and its contribution to the overall mechanical performance of the scaffold-callus construct. The results presented above, for defects with β-TCP scaffolds in particular, demonstrate that generic material properties from the literature can be used in anatomically accurate models to accurately predict bending stiffness when carefully calibrated as in this study. The load-bearing abilities of the defect can be evaluated using failure criteria, and the safety of removing external fixation can be evaluated. The models that are generated are also anatomically accurate and defect-specific, or patient-specific, and provide individualised information for live subjects for the clinician that would otherwise be unavailable.

6.6 Conclusions

Computational model geometries of tibial defects that include the implanted scaffold and bone callus geometries were carefully constructed from μ-CT scan images that were generated during a previously conducted animal trial study. The accuracy of these models was assessed by comparing the predicted bending stiffness of each defect with experimentally-evaluated bending stiffness data that was generated as part of the previous animal trial. The mechanical integrity of defects with two types of implanted scaffold, β-TCP and PCL/β-TCP, was analysed using computational simulations of both bending and compression loading and stress distribution

analysis. The results of these analyses highlight the influence of callus volume and scaffold volume on the load-bearing abilities of these defects.

Clinically-used measures to predict the safety of removing external fixation were used to analyse these defects with implanted β-TCP and PCL/β-TCP scaffolds. These measurements confirm results of computational simulations and stress distribution analyses which suggest that removal of external fixation would be premature. The calculated values of these measures for defects with β-TCP scaffolds, while predicting that fixation removal would indeed be premature, are very close to the threshold values for fixation removal. Care must be taken in the interpretation of these measures, as this result is contrary to large volumes of tissue failure predicted by simulations of compressive loading representative of *in vivo* loading, which suggests that significant changes in the mechanical properties of the scaffold-callus construct, specifically through increased callus volume and mineralisation, would be required for safe fixation removal.

The methods presented here have potential for the development of a non-invasive computational assessment of defect stability. While current μ-CT scan technology cannot facilitate μ-CT scanning of live human or large animal subjects, the methodology presented in this chapter can still be used to generate FE model geometries from CT scan images (with much larger pixel sizes) for the type of study presented here, although decreased accuracy would be expected. Analysis of the scaffold-callus construct at successive time-points during the course of fracture callus healing would provide insight into the transfer of load-bearing from scaffold to callus as scaffold degradation increases and as callus formation progresses and

mineralisation increases. The load-bearing abilities of the entire defect (callus and scaffold) as healing progresses can be assessed using both bending and compression loading simulations and compared with clinically-used measurements to evaluate the suitability of fixation removal. In this way, patient-specific computational modelling can inform decision making in a clinical setting by providing additional information about the load-bearing abilities of any defect at any point in time.

6.7 References

Bergmann, G., Deuretzbacher, G., Heller, M., Graichen, F., Rohlmann, A., Strauss, J. and Duda, G.N. 2001. Hip contact forces and gait patterns from routine activities. *Journal of Biomechanics* 34(7), pp. 859–71.

Bhumiratana, S., Grayson, W.L., Castaneda, A., Rockwood, D.N., Gil, E.S., Kaplan, D.L. and Vunjak-Novakovic, G. 2011. Nucleation and growth of mineralized bone matrix on silk-hydroxyapatite composite scaffolds. *Biomaterials* 32(11), pp. 2812–20.

Boerckel, J., Kolambkar, Y., Stevens, H., Lin, A., Dupont, K. and Guldberg, R. 2012. Effects of in vivo mechanical loading on large bone defect regeneration. *Journal of Orthopaedic Research* 30(7), pp. 1067–1075.

Boilet, L., Descamps, M., Rguiti, E., Tricoteaux, A., Lu, J., Petit, F., Lardot, V., Cambier, F. and Leriche, A. 2013. Processing and properties of transparent hydroxyapatite and β tricalcium phosphate obtained by HIP process. *Ceramics International* 39(1), pp. 283–288.

Cancedda, R., Cedola, a, Giuliani, a, Komlev, V., Lagomarsino, S., Mastrogiacomo, M., Peyrin, F. and Rustichelli, F. 2007. Bulk and interface investigations of scaffolds and tissue-engineered bones by X-ray microtomography and X-ray microdiffraction. *Biomaterials* 28(15), pp. 2505–24.

Cipitria, A., Lange, C., Schell, H., Wagermaier, W., Reichert, J.C., Hutmacher, D.W., Fratzl, P. and Duda, G.N. 2012. Porous scaffold architecture guides tissue formation. *Journal of Bone and Mineral Research* 27(6), pp. 1275–88.

Claes, L.E. and Heigele, C. a 1999. Magnitudes of local stress and strain along bony surfaces predict the course and type of fracture healing. *Journal of Biomechanics* 32(3), pp. 255–66.

Eshraghi, S. and Das, S. 2012. Micromechanical finite-element modeling and experimental characterization of the compressive mechanical properties of polycaprolactone-hydroxyapatite composite scaffolds prepared by selective laser sintering for bone tissue engineering. *Acta Biomaterialia* 8(8), pp. 3138–43.

Evans, F.G. 1976. Mechanical properties and histology of cortical bone from younger and older men. *The Anatomical Record* 185(1), pp. 1–11.

Feng, L. and Jasiuk, I. 2011. Multi-scale characterization of swine femoral cortical bone. *Journal of Biomechanics* 44(2), pp. 313–320.

Fischgrund, J., Paley, D. and Suter, C. 1994. Variables affecting time to bone healing during limb lengthening. *Clinical Orthopaedics and Related Research* 301, pp. 31–37.

Freeman, T. a, Patel, P., Parvizi, J., Antoci, V. and Shapiro, I.M. 2009. Micro-CT analysis with multiple thresholds allows detection of bone formation and resorption during ultrasound-treated fracture healing. *Journal of Orthopaedic Research* 27(5), pp. 673–9.

Gao, J., Gong, H., Huang, X., Fang, J., Zhu, D. and Fan, Y. 2013. Relationship between microstructure, material distribution, and mechanical properties of sheep tibia during fracture healing process. *International Journal of Medical Sciences* 10(11), pp. 1560–9.

Gardner, T.N., Evans, M. and Simpson, H. 1998. Temporal variation of applied inter fragmentary displacement at a bone fracture in harmony with maturation of the fracture callus. *Medical Engineering & Physics* 20(6), pp. 480–4.

Gardner, T.N., Stoll, T., Marks, L., Mishra, S. and Knothe Tate, M. 2000. The influence of mechanical stimulus on the pattern of tissue differentiation in a long bone fracture--an FEM study. *Journal of Biomechanics* 33(4), pp. 415–25.

Geris, L., Gerisch, A., Maes, C., Carmeliet, G., Weiner, R., Vander Sloten, J. and Van Oosterwyck, H. 2006. Mathematical modeling of fracture healing in mice: comparison between experimental data and numerical simulation results. *Medical & Biological Engineering & Computing* 44(4), pp. 280–9.

Grant, C. a, Wilson, L.J., Langton, C. and Epari, D. 2014. Comparison of mechanical and ultrasound elastic modulus of ovine tibial cortical bone. *Medical Engineering & Physics* 36(7), pp. 869–74.

Guo, L., Guo, X., Leng, Y., Cheng, J.C. and Zhang, X. 2001. Nanoindentation study of interfaces between calcium phosphate and bone in an animal spinal fusion model. *Journal of Biomedical Materials Research* 54(4), pp. 554–9.

Hansen, U., Zioupos, P., Simpson, R., Currey, J.D. and Hynd, D. 2008. The effect of strain rate on the mechanical properties of human cortical bone. *Journal of Biomechanical Engineering* 130(1), p. 011011.

Hazra, S., Song, H.-R., Biswal, S., Lee, S.-H., Lee, S.H., Jang, K.-M. and Modi, H.N. 2008. Quantitative assessment of mineralization in distraction osteogenesis. *Skeletal Radiology* 37(9), pp. 843–7.

Hori, R.Y. and Lewis, J.L. 1982. Mechanical properties of the fibrous tissue found at the bone-cement interface following total joint replacement. *Journal of Biomedical Materials Research Part A* 16(6), pp. 911–927.

ISO 1990. Implants for surgery - Determination of bending strength and stiffness of bone plates. *ISO 9585:1990*.

Jamsa, T., Jalovaara, P., Peng, Z., Ams, T.J. and Tuukkanen, J. 1998. Comparison of Three-Point Bending Test and Peripheral. *Bone* 23(2), pp. 155–161.

Jones, A.C., Arns, C.H., Hutmacher, D.W., Milthorpe, B.K., Sheppard, A.P. and Knackstedt, M. a 2009. The correlation of pore morphology, interconnectivity and physical properties of 3D ceramic scaffolds with bone ingrowth. *Biomaterials* 30(7), pp. 1440–51.

Jones, A.C., Milthorpe, B., Averdunk, H., Limaye, A., Senden, T.J., Sakellariou, A., Sheppard, A.P., Sok, R.M., Knackstedt, M. a, Brandwood, A., Rohner, D. and Hutmacher, D.W. 2004. Analysis of 3D bone ingrowth into polymer scaffolds via micro-computed tomography imaging. *Biomaterials* 25(20), pp. 4947–54.

Kemper, A., Mcnally, C., Kennedy, E., Manoogian, S., Tech, V., Forest, W. and Biomechanics, I. 2007. The material properties of human tibia cortical bone in tension and compression: implications for the tibia index. In: *Proceedings of the 20th Enhanced Safety of Vehicles Conference*.

Kokoroghiannis, C., Charopoulos, I., Lyritis, G., Raptou, P., Karachalios, T. and Papaioannou, N. 2009. Correlation of pQCT bone strength index with mechanical testing in distraction osteogenesis. *Bone* 45(3), pp. 512–6.

Lacroix, D. and Prendergast, P.J. 2002. A mechano-regulation model for tissue differentiation during fracture healing: analysis of gap size and loading. *Journal of Biomechanics* 35(9), pp. 1163–71.

Lee, S.J., Lim, G.J., Lee, J.-W., Atala, A. and Yoo, J.J. 2006. In vitro evaluation of a poly(lactide-co-glycolide)-collagen composite scaffold for bone regeneration. *Biomaterials* 27(18), pp. 3466–72.

Van Lenthe, G.H., Hagenmüller, H., Bohner, M., Hollister, S.J., Meinel, L. and Müller, R. 2007. Nondestructive micro-computed tomography for biological imaging and quantification of scaffold-bone interaction in vivo. *Biomaterials* 28(15), pp. 2479–90.

Leong, P.L. and Morgan, E.F. 2009. Correlations between indentation modulus and mineral density in bone-fracture calluses. *Integrative and Comparative Biology* 49(1), pp. 59–68.

Lind, P.M., Lind, L., Larsson, S. and Orberg, J. 2001. Torsional testing and peripheral quantitative computed tomography in rat humerus. *Bone* 29(3), pp. 265–70.

Lohfeld, S., Cahill, S., Barron, V., McHugh, P., Dürselen, L., Kreja, L., Bausewein, C. and Ignatius, A. 2012. Fabrication, mechanical and in vivo performance of polycaprolactone/tricalciumphosphate composite scaffolds. *Acta Biomaterialia* 8(9), pp. 3446–3456.

Malizos, K.N., Papachristos, A. a, Protopappas, V.C. and Fotiadis, D.I. 2006. Transosseous application of low-intensity ultrasound for the enhancement and monitoring of fracture healing process in a sheep osteotomy model. *Bone* 38(4), pp. 530–9.

Manjubala, I., Liu, Y., Epari, D.R., Roschger, P., Schell, H., Fratzl, P. and Duda, G.N. 2009. Spatial and temporal variations of mechanical properties and mineral content of the external callus during bone healing. *Bone* 45(2), pp. 185–192.

Markel, M.D., Wikenheiser, M. a and Chao, E.Y. 1990. A study of fracture callus material properties: relationship to the torsional strength of bone. *Journal of Orthopaedic Research* 8(6), pp. 843–50.

Mehta, M., Checa, S., Lienau, J., Hutmacher, D. and Duda, G.N. 2012. In vivo tracking of segmental bone defect healing reveals that callus patterning is related to early mechanical stimuli. *European Cells & Materials* 24(0), pp. 358–71.

Metsger, D.S., Rieger, M.R. and Foreman, D.W. 1999. Mechanical properties of sintered hydroxyapatite and tricalcium phosphate ceramic. *Journal of Materials Science. Materials in Medicine* 10(1), pp. 9–17.

Rai, B., Lin, J.L., Lim, Z.X.H., Guldberg, R.E., Hutmacher, D.W. and Cool, S.M. 2010. Differences between in vitro viability and differentiation and in vivo bone-forming efficacy of human mesenchymal stem cells cultured on PCL-TCP scaffolds. *Biomaterials* 31(31), pp. 7960–70.

Roshan-Ghias, A., Lambers, F.M., Gholam-Rezaee, M., Müller, R. and Pioletti, D.P. 2011. In vivo loading increases mechanical properties of scaffold by affecting bone formation and bone resorption rates. *Bone* 49(6), pp. 1357–64.

Schlichting, K., Schell, H., Kleemann, R.U., Schill, A., Weiler, A., Duda, G.N. and Epari, D.R. 2008. Influence of scaffold stiffness on subchondral bone and subsequent cartilage regeneration in an ovine model of osteochondral defect healing. *The American Journal of Sports Medicine* 36(12), pp. 2379–91.

Schorlemmer, S., Ignatius, A., Claes, L. and Augat, P. 2005. Inhibition of cortical and cancellous bone formation in glucocorticoid-treated OVX sheep. *Bone* 37(4), pp. 491–6.

Schulte, F. a, Lambers, F.M., Kuhn, G. and Müller, R. 2011. In vivo micro-computed tomography allows direct three-dimensional quantification of both bone formation and bone resorption parameters using time-lapsed imaging. *Bone* 48(3), pp. 433–42.

Shefelbine, S.J., Simon, U., Claes, L., Gold, A., Gabet, Y., Bab, I., Müller, R. and Augat, P. 2005. Prediction of fracture callus mechanical properties using micro-CT images and voxel-based finite element analysis. *Bone* 36(3), pp. 480–8.

Skaggs, D., Leet, A., Money, M., Shaw, B., Hale, J. and Tolo, V. 1999. Secondary fractures associated with external fixation in pediatric femur fractures. *Journal of Pediatric Orthopedics.* 19(5), pp. 582–6.

Smit, T.H., Huyghe, J.M. and Cowin, S.C. 2002. Estimation of the poroelastic parameters of cortical bone. *Journal of Biomechanics* 35(6), pp. 829–35.

Song, H., Oh, C., Mattoo, R., Park, B., Kim, S., Park, I., Jeon, I. and Ihn, J. 2005. Femoral lengthening over an intramedullary nail using the external fixator: risk of infection and knee problems in 22 patients with a follow-up of 2 years or more. *Acta Orthopaedica* 76(2), pp. 245–252.

Song, S.-H., Agashe, M., Kim, T.-Y., Sinha, S., Park, Y.-E., Kim, S.-J., Hong, J.-H., Song, S.-Y. and Song, H.-R. 2012. Serial bone mineral density ratio measurement for fixator removal in tibia distraction osteogenesis and need of a supportive method using the pixel value ratio. *Journal of Pediatric Orthopedics. Part B* 21(2), pp. 137–45.

Steiner, M., Claes, L., Simon, U., Ignatius, A. and Wehner, T. 2012. A computational method for determining tissue material properties in ovine fracture calluses using electronic speckle pattern interferometry and finite element analysis. *Medical Engineering and Physics* 34(10), pp. 1521–1525.

Taylor, W.R., Ehrig, R.M., Heller, M.O., Schell, H., Seebeck, P. and Duda, G.N. 2006. Tibio-femoral joint contact forces in sheep. *Journal of Biomechanics* 39(5), pp. 791–8.

Ulrich-Vinther, M. and Andreassen, T.T. 2005. Osteoprotegerin treatment impairs remodeling and apparent material properties of callus tissue without influencing structural fracture strength. *Calcified Tissue International* 76(4), pp. 280–6.

Vayron, R., Barthel, E., Mathieu, V., Soffer, E., Anagnostou, F. and Haiat, G. 2012. Nanoindentation measurements of biomechanical properties in mature and newly formed bone tissue surrounding an implant. *Journal of Biomechanical Engineering* 134(2), p. 021007.

Vetter, a, Liu, Y., Witt, F., Manjubala, I., Sander, O., Epari, D.R., Fratzl, P., Duda, G.N. and Weinkamer, R. 2011. The mechanical heterogeneity of the hard callus influences local tissue strains during bone healing: a finite element study based on sheep experiments. *Journal of Biomechanics* 44(3), pp. 517–23.

Vetter, A., Epari, D.R., Seidel, R., Schell, H., Fratzl, P., Duda, G.N. and Weinkamer, R. 2010. Temporal tissue patterns in bone healing of sheep. *Journal of Orthopaedic Research* 28(11), pp. 1440–7.

Vijayakumar, V., Marks, L., Bremmer-Smith, A., Hardy, J. and Gardner, T. 2006. Load transmission through a healing tibial fracture. *Clinical Biomechanics* 21(1), pp. 49–53.

Wallace, R.J., Pankaj, P. and Simpson, a H.R.W. 2013. The effect of strain rate on the failure stress and toughness of bone of different mineral densities. *Journal of Biomechanics* 46(13), pp. 2283–7.

Wang, C., Zhou, X. and Wang, M. 2004. Influence of sintering temperatures on hardness and Young's modulus of tricalcium phosphate bioceramic by nanoindentation technique. *Materials Characterization* 52(4-5), pp. 301–307.

Yao, D., Smith, A., Nagarajan, P., Vasquez, A., Dang, L. and Chaudhry, G.R. 2006. Fabrication of polycaprolactone scaffolds using a sacrificial compression-molding process. *Journal of Biomedical Materials Research. Part B, Applied Biomaterials* 77(2), pp. 287–95.

Zhao, L., Fan, Q., Venkatesh, K.P., Park, M.S. and Song, H.R. 2009. Objective guidelines for removing an external fixator after tibial lengthening using pixel value ratio: a pilot study. *Clinical Orthopaedics and Related Research* 467(12), pp. 3321–6.

7 Conclusions and Recommendations

7.1 Chapter Summary

This chapter summarises and discusses the outcomes of the work in this thesis. A summary of the work presented in Chapters 3 to 6 of this thesis is given in Section 7.2. The main limitations of this work are summarised in Section 7.3. Possibilities for future work stemming from the research presented in this thesis are outlined in Section 7.4.

7.2 Thesis Summary

A method to accurately predict the real elastic properties of a 90/10wt% PCL/β-TCP sintered scaffold material was developed in **Chapter 3**. Macro-scale FE models of individual struts were generated from high-resolution μ-CT scans. A range of methods was then explored to determine the most appropriate and most practical way to assign the elastic constants in the high resolution models. Micro-scale FE segments models were generated from XMT scans of the real material microstructure, with sufficient resolution to capture the individual β-TCP particles within the material. Effective elastic constants were determined using micromechanical modelling approaches and the relationship between elastic

properties and grey-value was determined. Element-specific assignment of elastic properties based on element grey-value in macro-scale models, using the micro-scale results, was shown to accurately predict macro-scale strut elastic modulus when compared with experimentally-evaluated strut elastic modulus, while also accounting for the real material microstructure. In comparison, homogeneous assignment of PCL elastic properties gave a good prediction of strut elastic modulus; however it is not representative of the real material as it does not account for the presence of the β-TCP phase in the material. Homogeneous assignment of elastic properties derived using the rule of mixtures significantly overestimated strut elastic modulus. By including both real micro- and macro-scale geometries and locally-varying mechanical properties, the microstructure-based method that has been developed is capable of accounting for the influence of both the influence of microstructural geometries and stiffness on the macro-scale behaviour of this sintered PCL/β-TCP scaffold material. Note that this methodology is dependent on XMT scan resolution, which must be sufficient to capture the real geometry and distribution of the smaller ceramic particles in the material.

As the microstructure-based method discussed above involves generating micro-scale material properties from the real material microstructure, in theory this method should be capable of predicting the macro-scale elastic properties of other multi-phase materials with complex microstructures. The capabilities of this method and the dependence of the micro-scale properties on the material microstructure are evaluated in **Chapter 4** for a similar SLS material, with a lower volume of ceramic and visibly different microstructure. The relationship between the material elastic modulus and average grey-value on the microscale was not found to be the same for

SLS materials with different ceramic content, i.e. a material-specific relationship between elastic modulus and average grey-value is required. The ability of the multiscale modelling methodology developed in Chapter 3 to predict the elastic properties of this 90/10wt% material was evaluated and macroscale strut models were assessed by comparing the predicted macroscale strut effective modulus with the experimentally evaluated strut modulus. The results of this chapter demonstrate that this methodology can accurately predict the macroscale elastic properties of SLS materials when a material-specific definition of the relationship between elastic modulus and grey-value is used and when XMT scans that capture the real material microstructure are used.

Microstructural analysis of two SLS materials with different volumes of incorporated ceramic particles, evaluated in Chapters 3 and 4, highlighted differences in material microstructure. The influence of these ceramic particles on the macro-scale elastic properties of these materials is of critical importance, specifically for the application of orthopaedic scaffolds in load-bearing defects. The impact of increasing the volume of ceramic in SLS materials on material microstructure and elastic properties was evaluated in **Chapter 5**. SLS scaffold materials were fabricated from PCL and from 90/10wt% PCL/β-TCP and 50/50wt% PCL/β-TCP. The results of this study show that increasing ceramic content results in a slight increase in stiffness but significant reductions in strength. The changes in mechanical properties and material microstructure of these materials under simulated physiological degradation conditions were evaluated. Differences in the microstructure of materials with increasing ceramic content were observed in both undegraded and degraded states, as were resulting differences in material elastic properties. The reduction in strut

stiffness and in strength due to degradation was greater for struts containing β-TCP than for PCL struts. The results of this study highlight the effect that incorporating ceramic particles has on the mechanical properties of these materials, in both undegraded and degraded states. These effects must be considered for the design of orthopaedic scaffolds.

Computational model geometries of four tibial defects with implanted scaffolds that were carefully constructed from μ-CT scan images, generated during a previously conducted animal study, (Lohfeld et al. 2012), are presented in **Chapter 6**. The accuracy of these models was assessed by comparing the predicted bending stiffness of each defect with experimentally-evaluated bending stiffness data from (Lohfeld et al. 2012). Models of defects with β-TCP scaffolds were found to have greater accuracy than models of defects with PCL/β-TCP scaffolds due to the greater complexity in constructing the latter set of model geometries. The mechanical integrity and load-sharing within defects with each type of implanted scaffold was analysed using stress distribution analysis for computational simulations of bending and compression loading. The results of these analyses highlight the influence of callus volume and of both scaffold volume and stiffness on the load-bearing abilities of these defects.

Clinically-used methods to predict the safety of removing external fixation were also calculated for each defect in **Chapter 6**. These measurements confirm results of computational simulations and stress distribution analyses that suggest that removal of external fixation would be premature. The calculated values of these measures for defects with β-TCP scaffolds, while predicting that fixation removal would indeed

be premature, are very close to the threshold values for fixation removal. Care must be taken in the interpretation of these measures, as this result is contrary to large volumes of tissue failure predicted by simulations of compressive loading representative of *in vivo* loading, which suggests that significant changes in the mechanical properties of the scaffold-callus construct would be required for safe fixation removal. While these measures do have some value for predicting safe removal of external fixation, the results of this chapter indicate that they are insufficient when used alone.

7.3 Limitations

Microstructural models of 50/50wt% and of 90/10wt% PCL/β-TCP scaffold materials were generated from high resolution μ-CT scans of the materials, as described in Chapter 3 and 4. A large quantity of noise was present in the regions surrounding the material in both sets of scans due to the low density of the PCL phase in each material. This meant that thresholding of the scans based on grey-value was not an acceptable method of separating the PCL volume from the surrounding volume as pixels in the (empty) region surrounding the scaffold material were also selected. Instead, the regions of material were selected from the scans manually with the help of the region-growing tool within MIMICS (Materialise, Belgium). The PCL and β-TCP phases within each material were then separated by thresholding based on grey-value.

The PCL/β-TCP scaffold materials that were studied in parallel with the PCL scaffold material in Chapter 5 were fabricated using different PCL particle sizes. This was necessary in order to achieve a 50/50wt% PCL/β-TCP material with sufficient mechanical integrity for use in this study, as described by (Lohfeld et al. 2012). The use of different particle sizes is a limitation of this study as it results in the addition of a second variable between the two PCL/β-TCP materials: β-TCP content and particle size. However, the PCL scaffold material that was included in this study was fabricated with the same PCL particle size as the 90/10wt% PCL/β-TCP scaffold material; therefore conclusions regarding the influence of β-TCP particles can be made by comparing these two materials. When these effects are considered, reasonable conclusions can be made regarding differences between the 90/10wt% and the 50/50wt% PCL/β-TCP materials, as detailed above.

The degradation of SLS materials was studied using accelerated degradation methods in Chapter 5 of this thesis. Accelerated degradation methods were used due to time constraints and the long degradation time of PCL. Such methods are intended for use below the glass transition temperature (T_g) of the polymer, however PCL has a T_g of -60°C and a melt temperature (T_m) of 60°C (Woodruff and Hutmacher 2010). While this means that the degradation conditions presented here are above the T_g of PCL, so too are physiologically representative degradation conditions at 37°C. An accelerated degradation temperature of 47°C was chosen in order to maintain a temperature well below the T_m of the material. The use of real-time degradation would provide a more accurate prediction of *in vivo* material degradation, and is the preferable method in general.

The computational modelling of real tibial defects with implanted scaffolds is presented in Chapter 6. The primary limitation of this section is limited to defects containing a PCL/β-TCP scaffold. The density of the bony callus is far greater than that of the polymeric scaffold, therefore only a faint outline of the PCL/β-TCP scaffold was visible in μ-CT scans of the defect. As discussed in Section 7.4 below, a potential solution to this is the use of two separate scans of the same defect region, one to capture the real geometry of the scaffold and one to capture the real geometry of the callus. The data available for this study was limited to the μ-CT scan data that was generated as part of an earlier animal study (Lohfeld et al. 2012), and the generation of new scans of the defects was not possible. In order to overcome this issue, a separate scan of a PCL/β-TCP scaffold that was fabricated as part of the same overall study was obtained. The scaffold geometry was generated from this scan and was manually fitted into the defect geometry that was generated from the defect μ-CT scans. Any scaffold material that overlapped with the callus tissue was removed using Boolean subtraction; however additional material removal due to degradation may have occurred *in vivo*. μ-CT scan data for intact tibiae was also not available, therefore idealised structures with constant cross-section that are specific to each defect were generated from the cross-section of cortical bone that were visible in the μ-CT scan of each defect. Only four defect model geometries were considered in this case due to limited availability of experimental and CT scan data; for future studies it is recommended that greater number of cases should be considered for the generation of more conclusive results.

The computational modelling of tibial defects is also limited by the lack of available subject-specific micro-scale material properties for use in FE modelling. This has

been generated in other studies using nanoindentation of callus tissues (Manjubala et al. 2009), however no data was generated for these specific defects as part of the earlier animal study. Instead, the elastic properties of cortical bone were carefully deduced using computational modelling of intact tibiae and calibrating against data for the macro-scale bending stiffness of intact tibiae that was generated as part of the earlier animal study. The elastic properties of β-TCP reported in the literature were assumed (Wang et al. 2004) and the elastic properties of the PCL/β-TCP scaffold material were established in Chapter 4 using a rigorous multi-scale modelling approach. The remaining unknown values are those of the callus tissues, and a trial and error approach using values reported in the literature was adopted. A good fit between computational and experimental bending stiffness values was reported for defects with β-TCP scaffolds, thus validating the use of the final material properties. While the use of the real material elastic properties would be preferable, the results of this study show that the use of values reported in the literature is acceptable, when used carefully, for cases where this information is not available.

7.4 Future Research

The multi-scale modelling methodology presented in Chapter 3 was shown to accurately predict the macro-scale elastic modulus of 50/50wt% PCL/β-TCP struts when compared with experimentally-evaluated strut elastic modulus. The result of analysis in Chapter 4 indicates that a material-specific relationship between micro-scale elastic modulus and grey-value is required, but verifies that this multi-scale modelling methodology also accurately predicts the macro-scale elastic modulus of

90/10wt% PCL/β-TCP struts. As this methodology generates a material-specific relationship between micro-scale elastic modulus and grey-value, there are numerous possibilities for the application of this method. Materials fabricated using SLS have a highly complex microstructure by nature, as discussed in Chapter 5. This is also the case for other SLS materials, in particular polymer-ceramic composite materials (Eshraghi and Das 2012; Zhang et al. 2008; Jain et al. 2010), and is not limited to orthopaedic applications. The methodology presented here can be used to predict the macro-scale elastic properties of various types of materials with complex microstructures as it is specific to the real material microstructure through the use of high resolution 3D scan images of that material.

Callus tissues are highly heterogeneous in nature (Leong and Morgan 2009) and the elastic properties of newly-formed callus tissues are dependent on numerous factors including time and the degree of mineralisation (Manjubala et al. 2009; Cipitria et al. 2012). As grey-value is related to material density the multi-scale modelling methodology presented in this thesis has potential for the generation of grey-value specific elastic properties for callus tissues. Once calibrated against experimental testing of tissue, this method would enable the use of defect-specific material properties in high-resolution computational modelling of callus tissues without the need for invasive mechanical testing for each specific sample, for the case of small animals.

The degradation of biodegradable polymeric biomaterials is most commonly assessed by immersion in simulated physiological conditions (pH 7.4, 37°C), (ISO 2010). This results in full exposure of all surfaces of the test material to the

surrounding liquid. This is reasonably realistic for the case of polymeric implants in vascular applications where the device is immersed in blood flow *in vivo*. The 3D models generated from μ-CT scans in Chapter 6 of this thesis indicate that large portions of the scaffold surface are covered with bone callus tissue at 14 weeks post-implantation, for both PCL/β-TCP and β-TCP scaffold types. It is understood that callus tissues are somewhat porous in comparison to cortical bone and that the permeability of callus tissues is varied but low ($5x10^{-15} – 3.7x10^{-13}$ m^4/Ns) (Lacroix and Prendergast 2002). However the *in vivo* environment of implanted scaffolds is no doubt very different to the *in vitro* test environment that is generally used, which suggests that the *in vitro* degradation behaviour may overestimate the extent of *in vivo* degradation. This raises the question of whether or not immersion in physiological fluids is the best method to simulate *in vivo* degradation of polymeric implants for orthopaedic applications, and suggests that it is worth investigating alternative methods for *in vitro* evaluation of the degradation behaviour of these materials.

In Chapter 6, one of the major difficulties was the construction of a finite element model for a tibial defect containing new bone formation and a PCL/β-TCP scaffold, as discussed in Section 7.3. The results of FE modelling of defects with two types of implanted scaffold, one type visible in μ-CT scans of the defect and one type not visible, in Chapter 6 indicate that the use of the real scaffold geometry in defects containing β-TCP scaffold generates more accurate predictions of bending stiffness. This suggests that future research should focus on the generation of μ-CT scan data for defects that capture both the bony callus geometry and the real scaffold geometry. One possible method to achieve this is use of two scans, one at optimal

settings for the bony callus and a second scan at optimal settings for the polymer-based scaffold, which can then be combined to generate a data-set containing the real geometry of both the scaffold and callus. Increasing the number of bits used in the scan may also improve the visibility of both material types in the scan, i.e. 16-bits versus 8-bits.

It is also recommended that a CT scan is taken of the entire bone in order to generate accurate full bone bone geometries for this type of FE modelling. The availability of CT scan data for the full tibia would also enable simulations of the real, *in vivo* loading. Realistic loading consists of both axial loading and loading through muscle attachments (Taylor et al. 2006). While the use of approximated values of axial loading forces used in Chapter 6 gives a good estimation of the ability of each defect to withstand *in vivo* loading, simulations that account for realistic loading through muscle attachments would provide a more complete picture.

The results of Chapter 6 indicate that FE models of the scaffold-callus construct generated from μ-CT scans have the ability to predict the bending stiffness of the real defect. The FE models also generate stress-distribution data that indicates the load-sharing between scaffold and callus. These methods have significant potential for non-invasive monitoring of the progression of bone formation in a longitudinal animal study, where FE modelling can be used to evaluate the contribution of the bone callus to load-bearing within the defect. The ability to predict load-bearing within the defect has significant value in a clinical setting. The data generated from this type of study would provide clinicians with additional information to that on raw X-ray images and μ-CT scans, thus enabling them to make decisions regarding the

removal of external fixator devices based on predicted mechanical properties, load-bearing and load-sharing within the real defect.

7.5 Conclusion

In conclusion, the use of both mechanical testing methods and computational modelling in this thesis has led to an improved understanding of the influence of ceramic content on mechanical properties of SLS fabricated scaffold materials as well as the development of a multi-scale modelling methodology for the prediction of macro-scale mechanical properties. Computational modelling of real defect and scaffold geometries has resulted in a non-invasive method to generate useful information regarding stability and load-bearing within each defect, providing a framework for the assessment of the safety of external fixator removal.

7.6 References

Cipitria, A., Lange, C., Schell, H., Wagermaier, W., Reichert, J.C., Hutmacher, D.W., Fratzl, P. and Duda, G.N. 2012. Porous scaffold architecture guides tissue formation. *Journal of Bone and Mineral Research* 27(6), pp. 1275–88.

Eshraghi, S. and Das, S. 2012. Micromechanical finite-element modeling and experimental characterization of the compressive mechanical properties of polycaprolactone-hydroxyapatite composite scaffolds prepared by selective laser sintering for bone tissue engineering. *Acta Biomaterialia* 8(8), pp. 3138–43.

ISO 2010. *ISO 10993-13:2010: Biological evaluation of medical devices - Part 13: Identification and quantification of degradation products from polymeric medical devices*.

Jain, P.K., Pandey, P.M. and Rao, P.V.M. 2010. Selective Laser Sintering of Clay-Reinforced Polyamide. *Polymer Composites* 31(4), pp. 732–743.

Lacroix, D. and Prendergast, P.J. 2002. A mechano-regulation model for tissue differentiation during fracture healing: analysis of gap size and loading. *Journal of Biomechanics* 35(9), pp. 1163–71.

Leong, P.L. and Morgan, E.F. 2009. Correlations between indentation modulus and mineral density in bone-fracture calluses. *Integrative and comparative biology* 49(1), pp. 59–68.

Lohfeld, S., Cahill, S., Barron, V., McHugh, P., Dürselen, L., Kreja, L., Bausewein, C. and Ignatius, A. 2012. Fabrication, mechanical and in vivo performance of polycaprolactone/tricalciumphosphate composite scaffolds. *Acta Biomaterialia* 8(9), pp. 3446–3456.

Manjubala, I., Liu, Y., Epari, D.R., Roschger, P., Schell, H., Fratzl, P. and Duda, G.N. 2009. Spatial and temporal variations of mechanical properties and mineral content of the external callus during bone healing. *Bone* 45(2), pp. 185–192.

Taylor, W.R., Ehrig, R.M., Heller, M.O., Schell, H., Seebeck, P. and Duda, G.N. 2006. Tibio-femoral joint contact forces in sheep. *Journal of Biomechanics* 39(5), pp. 791–8.

Wang, C., Zhou, X. and Wang, M. 2004. Influence of sintering temperatures on hardness and Young's modulus of tricalcium phosphate bioceramic by nanoindentation technique. *Materials Characterization* 52(4-5), pp. 301–307.

Woodruff, M.A. and Hutmacher, D.W. 2010. The return of a forgotten polymer—Polycaprolactone in the 21st century. *Progress in Polymer Science* 35(10), pp. 1217–1256.

Zhang, Y., Hao, L., Savalani, M.M., Harris, R. a and Tanner, K.E. 2008. Characterization and dynamic mechanical analysis of selective laser sintered hydroxyapatite-filled polymeric composites. *Journal of Biomedical Materials Research. Part A* 86(3), pp. 607–16.